



HAL
open science

Spin-orbit torque and spin dependent transport in magnetic nano-heterostructures

Tianyi Ma

► **To cite this version:**

Tianyi Ma. Spin-orbit torque and spin dependent transport in magnetic nano-heterostructures. Quantum Physics [quant-ph]. Université de Lorraine; University of Chinese academy of sciences, 2023. English. NNT : 2023LORR0148 . tel-04286181

HAL Id: tel-04286181

<https://theses.hal.science/tel-04286181>

Submitted on 15 Nov 2023

HAL is a multi-disciplinary open access archive for the deposit and dissemination of scientific research documents, whether they are published or not. The documents may come from teaching and research institutions in France or abroad, or from public or private research centers.

L'archive ouverte pluridisciplinaire **HAL**, est destinée au dépôt et à la diffusion de documents scientifiques de niveau recherche, publiés ou non, émanant des établissements d'enseignement et de recherche français ou étrangers, des laboratoires publics ou privés.



**UNIVERSITÉ
DE LORRAINE**

**BIBLIOTHÈQUES
UNIVERSITAIRES**

AVERTISSEMENT

Ce document est le fruit d'un long travail approuvé par le jury de soutenance et mis à disposition de l'ensemble de la communauté universitaire élargie.

Il est soumis à la propriété intellectuelle de l'auteur. Ceci implique une obligation de citation et de référencement lors de l'utilisation de ce document.

D'autre part, toute contrefaçon, plagiat, reproduction illicite encourt une poursuite pénale.

Contact bibliothèque : ddoc-theses-contact@univ-lorraine.fr
(Cette adresse ne permet pas de contacter les auteurs)

LIENS

Code de la Propriété Intellectuelle. articles L 122. 4

Code de la Propriété Intellectuelle. articles L 335.2- L 335.10

http://www.cfcopies.com/V2/leg/leg_droi.php

<http://www.culture.gouv.fr/culture/infos-pratiques/droits/protection.htm>



UNIVERSITÉ
DE LORRAINE

C2MP



中国科学院大学
University of Chinese Academy of Sciences

Spin-orbit torque and spin dependent transport in magnetic nano-heterostructures

Pour l'obtention du titre de:

DOCTEUR DE L'UNIVERSITÉ DE LORRAINE ET
DE L'UNIVERSITÉ DE L'ACADÉMIE CHINOISE DES SCIENCES
en Physique

Tianyi MA

Composition du Jury:

Directeur de thèse:	M. Yuan LU	Chargé de Recherche CNRS, Université de Lorraine, FRANCE
Co-directeurs de thèse:	M. Michel VERGNAT	Professeur, Université de Lorraine, FRANCE
	M. Xiufeng HAN	Professeur, Institute of Physics, Chinese Academy of Sciences, CHINE
Président de jury:	MME. Jianhua ZHAO	Professeur, Institute of Semiconductors, Chinese Academy of Sciences, CHINE
Rapporteurs:	M. Haifeng DING	Professeur, Nanjing University, CHINE
	M. Henri JAFFRES	Directeur de recherche CNRS, Unité de mixte de physique CNRS/Thales, FRANCE

Institut Jean Lamour - UMR 7198 - Université de Lorraine

Département de Physique de la Matière et des Matériaux

Equipe Nanomatériaux pour L'Optoélectronique

Ecole doctorale C2MP

13 octobre 2023

Résumé élargi

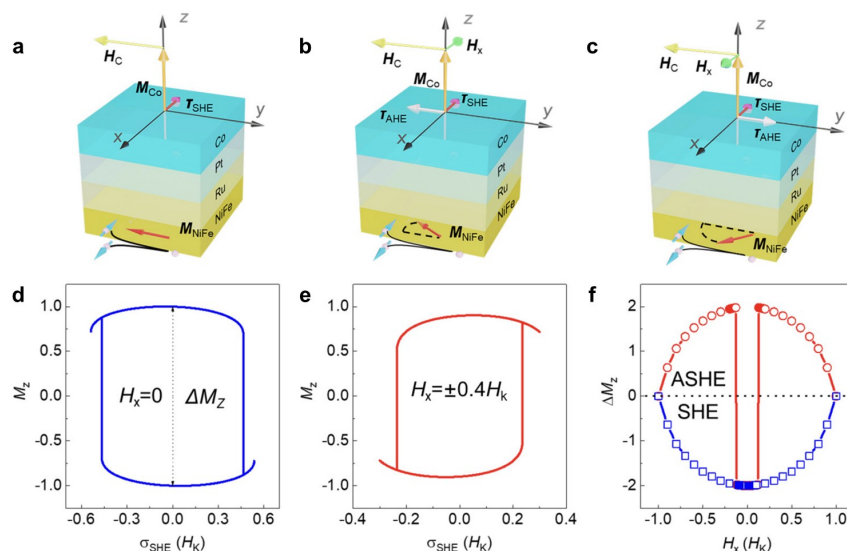
La spintronique est le mariage de l'électronique qui utilise la charge électrique des électrons pour transmettre de l'information, et du spin, une autre propriété intrinsèque des électrons. De nombreux dispositifs pratiques de spintronique ont émergé grâce aux avancées réalisées dans ce domaine. Parmi eux, la jonction tunnel magnétique est un élément clé, car elle est considérée comme un candidat prometteur pour les mémoires non volatiles de prochaine génération. Par conséquent, l'un des sujets de recherche central en spintronique consiste à améliorer les performances de lecture et d'écriture électriques des jonctions tunnel magnétiques. Cette étude examine les deux aspects et mène une série de recherches sur la commutation de l'aimantation perpendiculaire induite par le courant et l'effet de magnétorésistance tunnel dans les jonctions tunnel magnétiques. Les détails sont énumérés ci-dessous:

(1) La génération de courants de spin dans les ferromagnétiques a été étudiée et la commutation de l'aimantation perpendiculaire induite par deux courants de spin provenant de l'effet Hall de spin et de l'effet Hall anormal dans un ferromagnétique a été réalisée. Un modèle de macrospin concerne l'hétérostructure avec une couche d'aimantation dans le plan et une couche d'aimantation perpendiculaire, c'est-à-dire une multicouche magnétique de type T. Supposons que deux courants de spin sont générés par l'effet Hall de spin et l'effet Hall anormal lorsqu'un courant est appliqué, l'absorption de ces deux courants de spin par l'aimantation perpendiculaire entraîne alors sa commutation. La polarité de commutation est codéterminée par la polarisation du courant de spin et la direction du champ magnétique effectif dans le plan et cela permet de différencier la contribution de l'effet Hall de spin de celle de l'effet Hall anormal. Ainsi, l'existence de ces deux mécanismes de génération de courant de spin dans les

ferromagnétiques est confirmée.

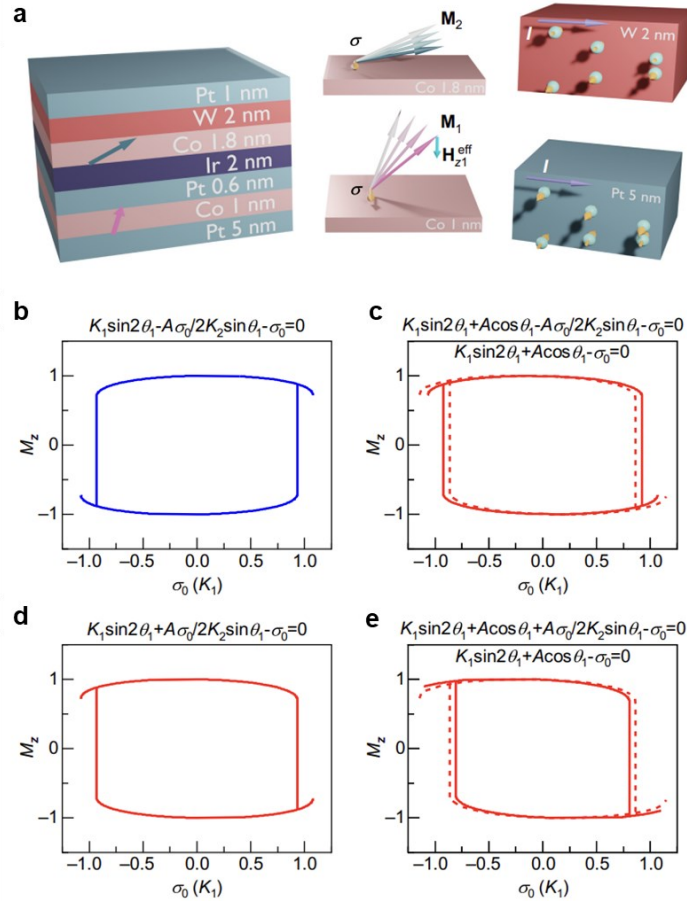
La figure R1 illustre la commutation de l'aimantation perpendiculaire induite par les couples de spin-orbite générés dans un ferromagnétique NiFe. Dans la figure R1(a), les électrons circulent dans la direction y , parallèle à l'aimantation de NiFe. Seul l'effet Hall de spin peut générer des courants de spin, et grâce au champ de couplage brisant la symétrie, une commutation déterministe de l'aimantation perpendiculaire induite par l'effet Hall de spin est obtenue. Pendant ce temps, dans les figures R1(b-c), un champ magnétique externe dirigé selon l'axe x est appliqué, ce qui incline l'aimantation de NiFe vers la direction x . Maintenant, à la fois l'effet Hall de spin et l'effet Hall anormal peuvent générer des courants de spin. Avec l'aide du champ magnétique dirigé selon l'axe x , une commutation déterministe de l'aimantation perpendiculaire induite par l'effet Hall anormal peut également être obtenue. Il est important de noter que la figure R1(f) démontre qu'avec la présence du couple de l'effet Hall anormal, la polarité de commutation est déterminée par le champ dirigé selon l'axe x . Ce changement de polarité de commutation devient le critère de validation expérimentale de cette idée.

Ensuite, des expériences ont été menées pour concevoir une multicouche magnétique de type T. L'existence de ces deux courants de spin est validée par des mesures de commutation de l'aimantation perpendiculaire induite par le courant. Cette partie du travail ouvre la voie au développement de dispositifs de spintronique exempts de métaux lourds et à faible coût.



Figures R1 la commutation de l'aimantation perpendiculaire induite par les couples de spin-orbite générés dans un ferromagnétique. Les schémas du système sans champ magnétique, avec un champ magnétique dirigé vers la gauche (-x) et avec un champ magnétique dirigé vers la droite (+x) sont montrés respectivement dans les figures (a-c). Les figures (d-e) présentent les calculs du modèle de macrospin simulant ces trois situations. La figure (f) montre la dépendance du champ magnétique sur la polarité de commutation de l'aimantation perpendiculaire.

(2) Un champ magnétique perpendiculaire efficace est obtenu dans une multicouche magnétique de type T, ce qui permet une commutation efficace de l'aimantation perpendiculaire induite par le couple spin-orbite. Tout d'abord, un modèle de macrospin de type T est établi, dans lequel nous avons constaté que l'aimantation dans le plan s'oriente vers la direction perpendiculaire sous l'effet du couple spin-orbite lorsqu'un courant est appliqué. La figure R2 illustre que, grâce au couplage intercouche entre l'aimantation dans le plan et l'aimantation perpendiculaire, l'aimantation perpendiculaire subit un champ perpendiculaire effectif supplémentaire, ce qui facilite (entrave) la commutation de l'aimantation perpendiculaire et réduit (augmente) la densité de courant critique lorsque deux couches subissent des courants de spin de même (opposée) polarité.

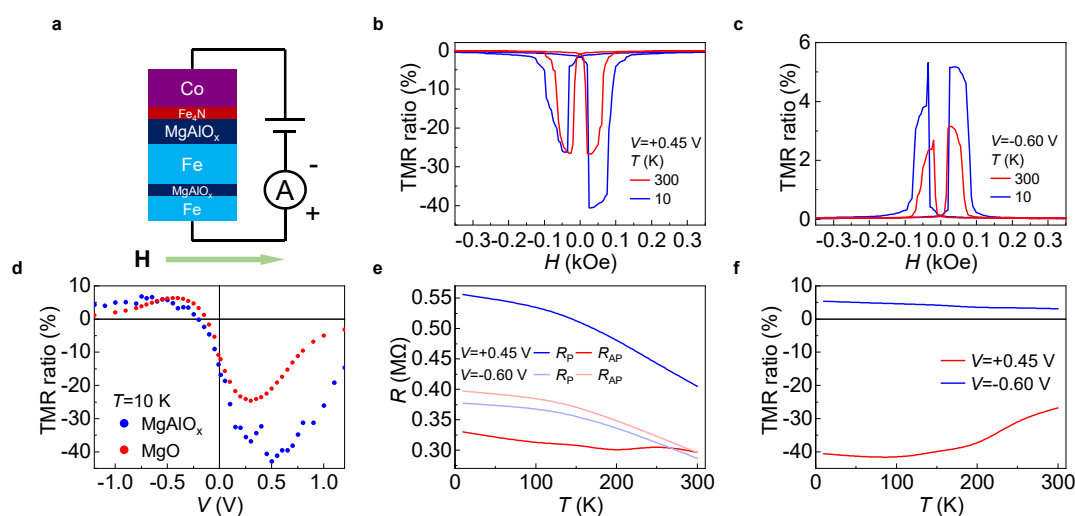


Figures R2 Création d'un champ perpendiculaire effectif dans le tricouche magnétique de type T. (a) L'aimantation dans le plan s'incline vers la direction z sous l'effet du couple spin-orbite. Le cobalt perpendiculaire subit un champ perpendiculaire effectif supplémentaire sous l'effet du couplage intercouche. (b-c) Simulations du modèle de macrospin lorsque les deux couches magnétiques subissent des couples spin-orbite de direction opposée ; (d-e) Simulation du modèle de macrospin lorsque les deux couches magnétiques subissent des couples spin-orbite de même direction.

La présence d'un champ magnétique perpendiculaire effectif est confirmé grâce à des expériences de commutation de l'aimantation perpendiculaire induite par un champ perpendiculaire. Cette partie du travail contribue à la réalisation d'une commutation efficace de la magnétisation perpendiculaire dans les multicouches de type T.

(3) Réalisation d'une magnétorésistance tunnel contrôlable par tension dans les jonctions tunnel magnétiques Fe_4N . Des jonctions tunnel magnétiques de haute

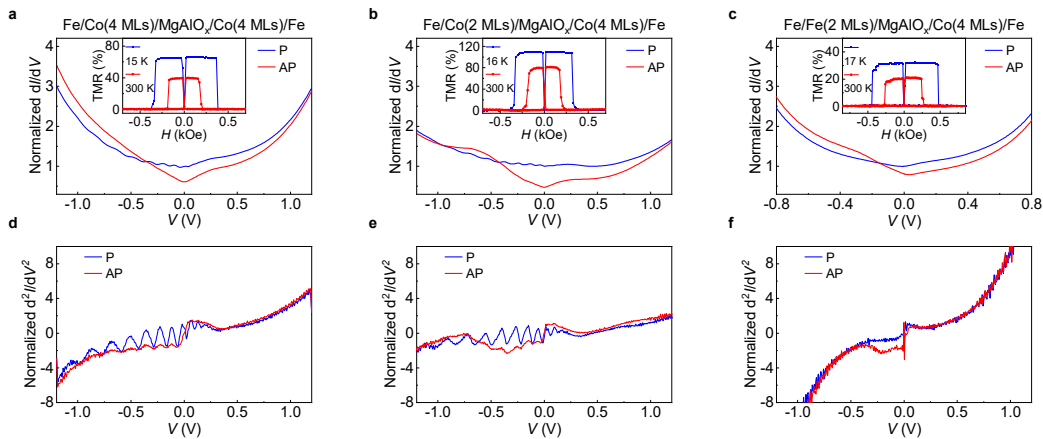
qualité Fe/MgAlO_x/Fe/MgAlO_x/Fe₄N ont été fabriquées sur un substrat monocristallin MgO(001) par épitaxie par jets moléculaires. Une magnétorésistance tunnel dépendante de la polarisation a été obtenue expérimentalement. Comme illustré dans la figure R3, lorsqu'une tension de polarisation positive (négative) est appliquée, les électrons se trouvant dans l'électrode Fe (Fe₄N) se déplacent par effet tunnel vers l'électrode Fe₄N (Fe), la résistance de l'état antiparallèle est inférieure (supérieure) à celle de l'état parallèle, ce qui entraîne un rapport de magnétorésistance tunnel négatif (positif). À l'aide d'un calcul ab initio, il est démontré que cet effet est causé par le changement des canaux de « tunnellation », qui est lié à la structure de bande de Fe₄N près du niveau de Fermi. Cette partie du travail ouvre la voie au développement de nouveaux dispositifs logiques à spin.



Figures R3 Résultats de mesure de la magnétorésistance tunnel (TMR) de la jonction tunnel magnétique Fe₄N. (a) Schéma de l'installation de mesure. (b-c) Courbes de TMR mesurées à température ambiante et à 10 K pour une tension de polarisation $V=+0.45$ V et -0.60 V, respectivement. (d) Dépendance de la tension des rapports de TMR des jonctions tunnel Fe₄N avec une barrière de MgAlO_x et de MgO à 10 K. (e) Dépendance de la température de la résistance de l'état P et AP lorsque $V=+0.45$ V et -0.60 V. (f) Dépendance de la température des rapports de TMR lorsque $V=+0.45$ V et -0.60 V.

(4) Étude de l'influence du désordre interfacial sur l'amplitude des oscillations résonantes dans les jonctions tunnel magnétiques à double barrière et puits quantiques.

Les états du puits quantique formés dans les jonctions tunnel magnétiques à double barrière permettent une tunnelisation cohérente résonante des électrons, ce qui pourrait être exploité pour atteindre un rapport de magnétorésistance par effet tunnel plus élevé. Nous avons fabriqué par épitaxie une série de DMTJ Fe/MgAlO_x/Fe/MgAlO_x/Fe et avons étudié systématiquement la dépendance de l'amplitude des oscillations en fonction des désordres introduits par l'insertion de Co aux interfaces supérieure et intermédiaire Fe/MgAlO_x. Comme illustré dans la Figure R4, il devient évident que l'amplitude des oscillations reste stable lorsque le Co est inséré en dehors du puits quantique, tandis qu'elle peut être considérablement réduite par le désordre chimique introduit par l'insertion de Co à l'intérieur du puits quantique. Elle peut même être détruite par le désordre structural provoqué par l'insertion de Fe à l'intérieur du puits quantique. Notre découverte met en évidence et explique le rôle des désordres structuraux et chimiques interfaciaux sur l'amplitude des oscillations et ouvre la voie au développement de dispositifs DMTJ polyvalents qui présentent simultanément un rapport TMR élevé et une amplitude d'oscillation élevée.



Figures R4 Dépendance en fonction de la polarisation, de la conductance différentielle dI/dV et de la conductance différentielle secondaire d^2I/dV^2 des échantillons avec insertion interne.

Abstract

Spintronics focuses on exploiting both the spin and charge freedom of electrons. Tremendous of practical spintronics devices have emerged with the advance of spintronics. Among them, magnetic tunnel junction is the cornerstone since it is a promising candidate as next-generation non-volatile memories. Therefore, one central research subject of spintronics is to enhance the electrical reading and writing performance of magnetic tunnel junctions. This study concerns both sides and carries out a series of researches on current-induced perpendicular magnetization switching and tunnel magnetoresistance effect in magnetic tunnel junctions. Details are listed below:

(1) Generation of spin currents in ferromagnets has been studied. And switching of perpendicular magnetization driven by two spin currents originated from the spin Hall effect and the anomalous Hall effect in a ferromagnet has been realized. A macrospin model concerns the heterostructure with both an in-plane magnetization layer and a perpendicular magnetization layer, i.e., a Type-T magnetic multilayer, is established. Suppose two spin currents are generated through the spin Hall effect and the anomalous Hall effect when a current is applied. Consequently, the absorption of these two spin currents by the perpendicular magnetization leads to its switching. The switching polarity is co-determined by the spin current polarization and the in-plane effective magnetic field direction. And by which the spin Hall effect contribution and the anomalous Hall effect contribution can be differentiated. Thus, the existence of these two spin current generation mechanisms in ferromagnets is confirmed. Next, experiments are carried out to obtain a well-designed Type-T magnetic multilayer. The existence of these two spin currents is validated by the current-induced perpendicular

magnetization switching measurements. This part of work paves ways for the development of heavy-metal free, low cost spintronics devices.

(2) An effective perpendicular magnetic field is obtained in a Type-T magnetic multilayer, which leads to an efficient spin-orbit torque induced perpendicular magnetization switching. Firstly, a Type-T macrospin model is established, in which we found that the in-plane magnetization tilts toward the perpendicular direction under the spin-orbit torque when a current is applied. With the interlayer coupling between the in-plane magnetization and the perpendicular magnetization, the perpendicular magnetization experiences an additional effective perpendicular field, which facilitates (hampers) the switching of perpendicular magnetization and reduces (increases) the critical current density when two layers experience spin currents with same (opposite) polarity. Next, experiments are carried out to obtain a well-designed Type-T magnetic multilayer. And the effective perpendicular magnetic field is confirmed through perpendicular field-driven perpendicular magnetization switching experiments. This part of work contributes to the realization of efficient perpendicular magnetization switching in T-type multilayers.

(3) Realization of voltage-controllable tunnel magnetoresistance in Fe_4N magnetic tunnel junctions. High-quality $\text{Fe}/\text{MgAlO}_x/\text{Fe}/\text{MgAlO}_x/\text{Fe}_4\text{N}$ magnetic tunnel junctions are grown on a single crystal $\text{MgO}(001)$ substrate via molecular beam epitaxy. And a bias-dependent tunnel magnetoresistance is experimentally obtained. When a positive (negative) bias voltage is applied, the electrons tunneling from the Fe (Fe_4N) electrode to the Fe_4N (Fe) electrode, the resistance of antiparallel state is lower (higher) than that of parallel state, which leads to a negative (positive) TMR ratio. Through an *ab initio* calculation, it is demonstrated that this effect is caused by the change of tunneling channels, which related to the band structure of Fe_4N near the Fermi level.

This part of work paves ways for the development of new spin logic devices.

(4) Investigation on the influence of interfacial disorder on the amplitude of resonant oscillation in double-barrier quantum well magnetic tunnel junctions. Quantum well states formed in double-barrier magnetic tunnel junctions enables coherent resonant tunneling of electrons, which could be utilized for achieving higher tunneling magnetoresistance ratio. We epitaxially fabricated a series of Fe/MgAlO_x/Fe/MgAlO_x/Fe DMTJs, and systematically investigated the oscillation amplitude dependence of the disorders introduced by inserted Co at the top and middle Fe/MgAlO_x interfaces. It becomes clear that the oscillation amplitude remains stable when inserting Co out of the QW, while it can be greatly reduced by the chemical disorder introduced by Co insertion within the QW. And even be eliminated by the structural disorder introduced by Fe insertion within the QW. Our discovery highlights and elucidates the role of interfacial structural and chemical disorders on the oscillation amplitude and paves ways for the development of versatile DMTJ devices which simultaneously poses high TMR ratio and high oscillation amplitude.

Key Words: spin Hall effect, anomalous Hall effect, perpendicular magnetic anisotropy, tunnel magnetoresistance, magnetic tunnel junction, quantum well

Contents

Résumé élargi.....	I
Abstract	VII
Contents	XI
List of figures.....	XIII
1 Introduction.....	1
1.1 Introduction of spintronics	1
1.2 Tunneling magnetoresistance	5
1.3 Spin transfer torque.....	12
1.4 Spin-orbit torque	13
1.4.1 Spin Hall effect and anomalous Hall effect	14
1.4.2 Field-free perpendicular magnetization switching induced by SOTs.....	19
1.5 Spintronics devices in advanced computing	36
1.6 Structure of this dissertation	47
2 Methods.....	50
2.1 Growth techniques of magnetic multilayers	50
2.1.1 Magnetron sputtering	50
2.1.2 Molecular beam epitaxy.....	52
2.2 Fabrication of magnetic devices	55
2.2.1 Ultraviolet lithography	55
2.2.2 Argon-ion etching	56
2.2.3 Photoresist removal and lift-off	58
2.2.4 MTJ processing flow.....	59
2.3 Characterization of magnetic and electrical properties.....	61
2.3.1 Vibrating sample magnetometry	61
2.3.2 Physical property measurement system	62
2.3.3 Three-dimensional magnetic field probe station.....	63
3 Field-free perpendicular magnetization switching induced by AHE torque in NiFe	64
3.1 Research background	64
3.2 Experimental and simulate methods	66
3.2.1 Fabrication and measurement of samples	66
3.2.2 Construction and analyses of the macrospin model.....	67
3.3 Experimental results and discussions.....	73
3.4 Chapter summary	86
4 Effective perpendicular field induced by SOT in a magnetic trilayer ...	88

4.1 Research background	88
4.2 Experimental and simulate methods	89
4.2.1 Construction and analyses of the macrospin model.....	89
4.2.2 Sample fabrication and measurements.....	96
4.3 Experimental results and discussions.....	97
4.4 Chapter summary	107
5 Sign-changeable TMR effect in magnetic tunnel junctions	109
5.1 Research background	109
5.2 Experimental and simulate results	112
5.2.1 Growth of high-quality multilayers	112
5.2.2 Structure analysis	114
5.2.3 Transport measurements	117
5.2.4 <i>Ab initio</i> calculations.....	121
5.3 Discussions	124
5.4 Chapter summary	125
6 Impact of interfacial structural and chemical disorders on the resonant oscillation in QW based MTJs.....	127
6.1 Research background	127
6.2 Experimental results.....	129
6.2.1 Sample preparation	129
6.2.2 Structural and chemical characterization	133
6.2.3 Magneto-transport measurements	136
6.2.4 <i>Ab initio</i> calculations.....	141
6.3 Discussions	142
6.4 Chapter Summary	144
7 Summary	146
7.1 Conclusion of the dissertation.....	146
7.2 Future research outlook	148
Bibliography	151
Acknowledgements.....	171
Curriculum vitae and list of publications.....	175

List of figures

Figure 1-1	Comparison between conventional computing and in-memory computing	2
Figure 1-2	The roadmap of the development of MRAMs	3
Figure 1-3	Evolution of MRAM capacity	5
Figure 1-4	Schematic of the Jullière model of TMR	6
Figure 1-5	Measurements of TMR in MTJs with Al_2O_3 barrier at room temperature	7
Figure 1-6	Tunneling in Fe/MgO/Fe MTJ for electrons with different symmetry	8
Figure 1-7	TEM images of high-quality MTJs	9
Figure 1-8	Dependence of TMR on the proportion of Co in FeCo_x alloy and its mechanism	9
Figure 1-9	Realization of a ultrahigh TMR ratio in Fe/ Mg_4AlO_x /Fe MTJ	11
Figure 1-10	QW states in the double-barrier MTJ	11
Figure 1-11	Dependence of the STT direction on current direction	13
Figure 1-12	Schematic of SHE, AHE and ISHE	15
Figure 1-13	Three origins of SHE and AHE	16
Figure 1-14	Electrical switching and measurements in the MTJ with SOT	18
Figure 1-15	Schematic of torques in the Landau-Lifshitz-Gilbert-Slonczewski equation	20
Figure 1-16	SOT-induced perpendicular magnetization switching	22
Figure 1-17	Schemes of SOT-induced magnetization switching	23
Figure 1-18	A symmetry-based analysis of SOT-induced perpendicular magnetization switching	25
Figure 1-19	Field-free perpendicular magnetization switching by SOTs in an epitaxial CoPt/CuPt bilayer	27
Figure 1-20	Field-free perpendicular magnetization switching in an antiferromagnetic/ferromagnetic bilayer	28
Figure 1-21	Field-free perpendicular magnetization switching in the CoFeB/Ti/CoFeB multilayer	29
Figure 1-22	Field-free perpendicular magnetization switching in a system with interlayer coupling	31
Figure 1-23	Polarity-changeable field-free perpendicular magnetization switching in a Type-T magnetic multilayer	32
Figure 1-24	Field-free perpendicular magnetization switching with interlayer DMI	34

Figure 1-25	Field-free perpendicular magnetization switching with the starry field in the industry	35
Figure 1-26	Programmable spin logic device based on single magnetic tunnel junction	37
Figure 1-27	NAND gate and NOR gate based on the domain wall motion [275]....	39
Figure 1-28	Construction of artificial neuron and artificial synapse in spiking neural networks.....	41
Figure 1-29	Principal and realization of spoken-digit recognition with single nanoscale spintronic oscillator.....	43
Figure 1-30	Principal and realization of vowel recognition based on a spintronic-oscillator network	45
Figure 1-31	Principal and realization of integer factorization based on stochastic computing	46
Figure 2-1	Principle of magnetron sputtering.....	51
Figure 2-2	Magnetron sputtering equipment	52
Figure 2-3	Measurement setup and principles of RHEED	53
Figure 2-4	Ultra-high vacuum transfer tunnel at Institut Jean Lamour, Université de Lorraine-France	54
Figure 2-5	UV exposure equipment.....	56
Figure 2-6	Ion etching equipment.....	58
Figure 2-7	Detailed mechanical design of vibrating sample magnetometry	62
Figure 2-8	Three-dimensional magnetic field probe station.....	63
Figure 3-1	Spin currents generated in ferromagnets.....	65
Figure 3-2	Magnetization switching through spin currents generated in magnetic layers.....	65
Figure 3-3	Perpendicular magnetization switching induced by SOTs generated in a ferromagnet.....	67
Figure 3-4	Optimization of the coupling layer thickness.....	74
Figure 3-5	Structure and magnetization of the sample	75
Figure 3-6	Perpendicular magnetization switching induced by SHE	76
Figure 3-7	Perpendicular magnetization switching induced by SHE under 100 Oe magnetic field	78
Figure 3-8	Perpendicular magnetization switching induced by SHE under 50 Oe magnetic field	79
Figure 3-9	Perpendicular magnetization switching induced by AHE.....	80
Figure 3-10	Reproducibility test of the AHE-induced perpendicular magnetization switching.....	81
Figure 3-11	SHE-induced perpendicular magnetization switching of the sample with 5 nm NiFe	83

Figure 3-12	AHE-induced perpendicular magnetization switching of the sample with 5 nm NiFe	83
Figure 3-13	SHE-induced perpendicular magnetization switching of the sample with 1 nm NiFe	84
Figure 3-14	AHE-induced perpendicular magnetization switching of the sample with 1 nm NiFe	84
Figure 4-1	Effective perpendicular fields generated on Néel-type domain walls by SOT.....	89
Figure 4-2	Creation of perpendicular effective field in the Type-T magnetic trilayer	91
Figure 4-3	Calculations of the generation efficiency of the effective perpendicular field.....	96
Figure 4-4	Atomic and magnetic structures of the Type-T magnetic multilayers	98
Figure 4-5	Optimization of sample magnetic structures.....	99
Figure 4-6	SOT-induced perpendicular magnetization switching in sample <i>A</i> , <i>B</i> and <i>C</i>	100
Figure 4-7	SOT-induced perpendicular magnetization switching in sample <i>A</i> and <i>B</i>	101
Figure 4-8	Measurements of the effective perpendicular field in <i>A</i> and <i>B</i>	103
Figure 5-1	Tunnel magnetoresistance effect in MFTJ	111
Figure 5-2	RHEED patterns of the MgAlO _x Fe ₄ N MTJ.....	113
Figure 5-3	RHEED patterns of the MgO Fe ₄ N MTJ	113
Figure 5-4	Atomic structures and chemical maps of the MgAlO _x Fe ₄ N MTJ.....	115
Figure 5-5	Atomic structures and chemical maps of the MgO Fe ₄ N MTJ.....	116
Figure 5-6	TMR measurement results of the MgAlO _x Fe ₄ N MTJ.....	117
Figure 5-7	<i>R-H</i> measurements of the MgAlO _x Fe ₄ N MTJ under different bias at 10 K	119
Figure 5-8	<i>R-H</i> measurements of the MgO Fe ₄ N MTJ under different bias at 10 K	119
Figure 5-9	Bias dependence of the differential conductance dI/dV of the MgAlO _x Fe ₄ N MTJ.....	120
Figure 5-10	TMR measurements of the MgO Fe ₄ N MTJ at different temperatures	121
Figure 5-11	<i>Ab initio</i> calculations of bulk Fe and Fe ₄ N	123
Figure 6-1	Resonant oscillation of conductance in the QW MTJ.....	127
Figure 6-2	Schematics of samples' structure	130
Figure 6-3	RHEED patterns of Sample <i>D</i> in different growth steps	131
Figure 6-4	RHEED patterns of Sample <i>D</i> in different growth steps along the [100] azimuths of MgO substrate.....	132

Figure 6-5	RHEED patterns and intensity oscillation of Sample <i>F</i> in different growth steps along the [100] azimuths of MgO substrate	132
Figure 6-6	RHEED patterns of the control stack in different growth steps along the [100] azimuth of MgO substrate.....	133
Figure 6-7	Interfacial structures and chemical maps of MTJ stacks	134
Figure 6-8	STEM-HAADF images and elements maps extracted from STEM-EELS measurements of Sample <i>B</i>	135
Figure 6-9	STEM-HAADF images and elements maps extracted from STEM-EELS measurements of Sample <i>D</i>	135
Figure 6-10	STEM-HAADF images and elements maps extracted from STEM-EELS measurements of Sample <i>E</i>	136
Figure 6-11	Bias dependence of differential conductance dI/dV and secondary differential conductance d^2I/dV^2 of samples with outer insertion.....	137
Figure 6-12	Bias dependence of differential conductance dI/dV and secondary differential conductance d^2I/dV^2 of samples with inner insertion	137
Figure 6-13	Bias dependence of d^2I/dV^2 of MTJs fabricated on the same control stack	139
Figure 6-14	QW states formed in Fe and Fe/Co	142

1 Introduction

1.1 Introduction of spintronics

This century heralds the dominance of high-performance computers, with classical computing rooted in von Neumann architecture and the emerging trend of neuromorphic computing significantly transforming our daily lives. Notably, in 1997, IBM's Deep Blue surpassed the World Chess Champion, Garry Kasparov, followed by Google's AlphaGo defeating the 9-dan professional Go player, Lee Sedol, in 2016. These achievements vividly illustrate the immense computational power harnessed. However, it is important to acknowledge that both Deep Blue and AlphaGo exhibit larger footprints and demand greater power compared to their human counterparts. To further propel the advancements in general computing, it is imperative to pursue enhanced efficiency and reduced power consumption.

In classical von Neumann architecture, computing units and storage units exist as separate entities, necessitating constant information exchange between them, as depicted in Figure 1-1. However, this process incurs significant energy and time consumption. Storage units typically operate at a slower speed compared to computing units, exacerbating the efficiency challenges. Consequently, the prevailing approach is to focus on the development of faster and more efficient storage units or explore the integration of computing units and storage units into cohesive entities, such as in-memory computing [1,2].

In comparison to electronics, which solely focus on the charge freedom of electrons, spintronics encompasses both charge and spin freedom. This field serves as a fundamental pillar in computer science, offering an economical and efficient means

to transfer a vast amount of information between computable electrical signals and non-volatile magnetization orientations, and vice versa. A significant milestone in spintronics occurred in 1998 when Albert Fert and Peter Grünberg discovered the giant magnetoresistance (GMR) effect [3,4], leading to their subsequent Nobel Prize in Physics in 2007. The advent of hard disks based on GMR and tunneling magnetoresistance (TMR) has revolutionized computer storage, providing vast and cost-effective storage capacities. This development propelled computers into the hands of the general public and laid the foundation for the era of big data [5–13].

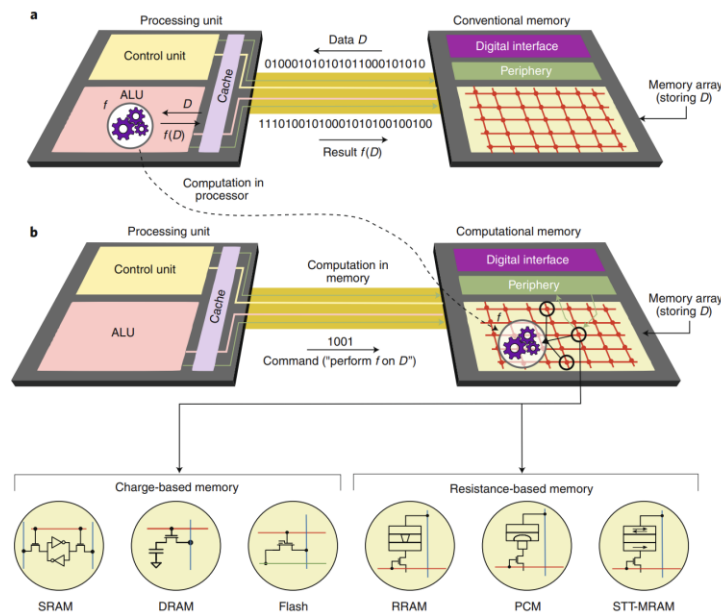


Figure 1-1 Comparison between conventional computing and in-memory computing. (a) Von-Neumann architecture. Computing happens in the processor; (b) In-memory computing architecture. Computing happens in the memory [1].

Today, with the maturation of techniques such as spin transfer torque (STT) and spin-orbit torque (SOT), it is now possible to directly manipulate the magnetization orientation using electrical currents, eliminating the need for magnetic fields. This advancement has greatly accelerated the evolution of magnetic random-access memories (MRAMs). STT-MRAM and SOT-MRAM exhibit ultralow standby power consumption, high endurance, rapid operating speeds, high density, and compatibility

with the back end of line (BEOL) process of complementary metal oxide semiconductor (CMOS) technology. These exceptional characteristics position STT-MRAM and SOT-MRAM as promising candidates for the next generation of non-volatile storage [2,14].

The core building blocks of MRAM are magnetic tunnel junctions (MTJs). The resistance of an MTJ is determined by the tunnel magnetoresistance (TMR) effect, whereby the resistance is lower (higher) when the two layers within the MTJ are aligned in a parallel (antiparallel) configuration. The TMR ratio is commonly defined as $(R_{AP} - R_P)/R_P \times 100\%$. MTJs can be classified into two main types based on their magnetic anisotropy: in-plane MTJs [15–17] and perpendicular MTJs [18–21].

The evolution of MRAM is illustrated in Figure 1-2. During the initial stages, such as the Asteroid-MRAM and Toggle-MRAM era, the magnetization in MTJ is switched by the Oersted field generated by currents. However, this approach poses a significant drawback when it comes to downsizing and integration. Subsequently, the discovery of the STT effect allowed for magnetization switching by applying currents through two magnetic layers, eliminating the need for an external magnetic field. This breakthrough simplified the device structure and facilitated the development of smaller devices and larger-scale integration.

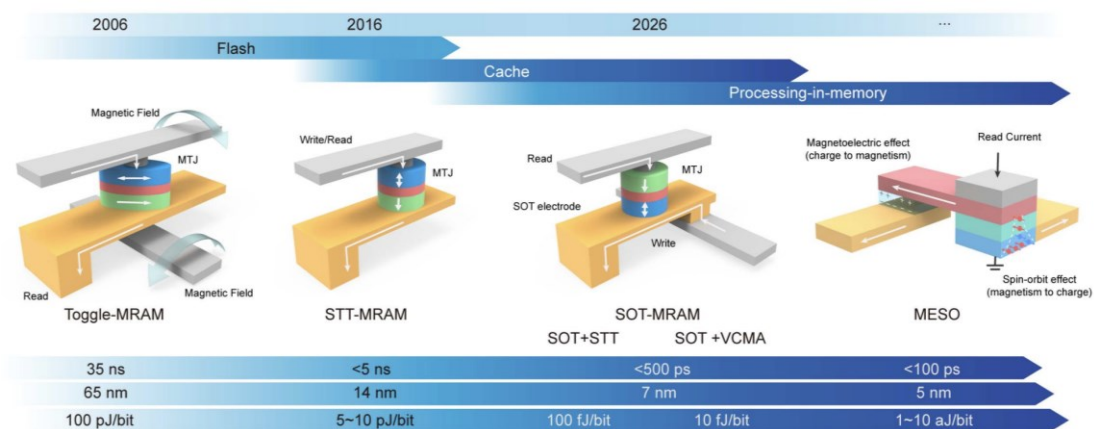


Figure 1-2 The roadmap of the development of MRAMs [2].

However, the utilization of STT effect in MRAM introduces a significant

challenge as currents inevitably flow through the insulating layer positioned between the two magnetic layers. This leads the risk of voltage breakdown when large writing currents are employed, resulting in endurance issues for STT-MTJ. This dilemma is addressed through the discovery of SOT effect, wherein a transverse spin current is generated by passing electrons through heavy metals. The absorption of this spin current enables the magnetization switching of adjust layer, effectively separating the writing currents from the reading current and eliminating the needs of passing large currents through the insulating layer. Thus, the endurance of SOT-MTJ is significantly enhanced.

Furthermore, the time required for SOT switching falls within the sub-nanosecond to sub-picosecond range, making it highly suitable for the development of in-memory computing. This enables the simplification of computing architectures and reduces power consumption based on SOT-MTJ. Additionally, recent advancements in MRAM development involve the incorporation of ferroelectric materials, van der Waals materials, and topological materials, which offer lower critical current density and versatile functionality, further enhancing the potential of MRAM.

The industry also plays a huge role in the development of MRAM [22–30]. As shown in Figure 1-3, the leading companies such as IBM and Motorola have been investing MRAM since early 2000s. Over time, there has been a shift in focus from Toggle-MRAM to STT-MRAM, alongside with the increasing of integration scale. Nowadays, to further enhance the storage density and the operating speed, the mainstream research is shifting towards the developments of perpendicular STT-MRAM and even SOT-MRAM.

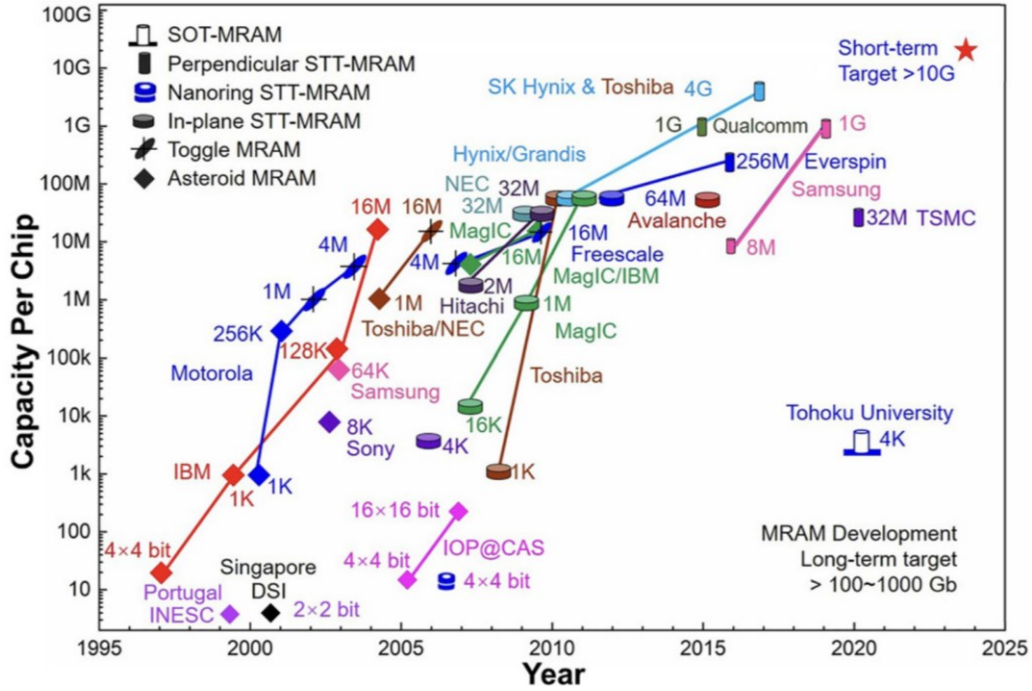


Figure 1-3 Evolution of MRAM capacity [31].

1.2 Tunneling magnetoresistance

MTJ typically consists two magnetic layers, and it exhibits a high (low) resistance state corresponding to the antiparallel (parallel) alignment of these two layers. This phenomenon is referred as the TMR effect. The TMR effect is directly linked with density of states (DOS) of magnetic electrodes near the Fermi level, as depicted in Figure 1-4. When a bias voltage is applied, electrons in the left magnetic electrode (FM_1) have higher energy, can tunnel into the right magnetic electrode (FM_2). DOS with the opposite spin polarization is different near the Fermi level due to the band splitting effect in magnetic metals. We note spin-up (spin-down) DOS_{\uparrow} (DOS_{\downarrow}) in FM_1 as a_1 ($1-a_1$), and DOS_{\uparrow} (DOS_{\downarrow}) in FM_2 as a_2 ($1-a_2$). Therefore, the spin polarization of FM_1 $P_1 = (DOS_{\uparrow} - DOS_{\downarrow}) / (DOS_{\uparrow} + DOS_{\downarrow}) = 2a_1 - 1$. Similarly, the spin polarization of FM_2 $P_2 = 2a_2 - 1$. The TMR ratio can be expressed as $(G_{AP} - G_P) / G_{AP}$, in which $G_P = a_1 a_2 + (1 - a_1)(1 - a_2)$, and $G_{AP} = a_1(1 - a_2) + a_2(1 - a_1)$, respectively. Finally,

we obtain the TMR ratio as $2P_1P_2/(1-P_1P_2)$, which is determined by the DOS polarization of electrodes near the Fermi level. Electrodes with higher spin polarization leads to higher TMR ratio. This simple model is known as the Jullière model [32], while a more precise model is proposed by Slonczewski in 1989 [33].

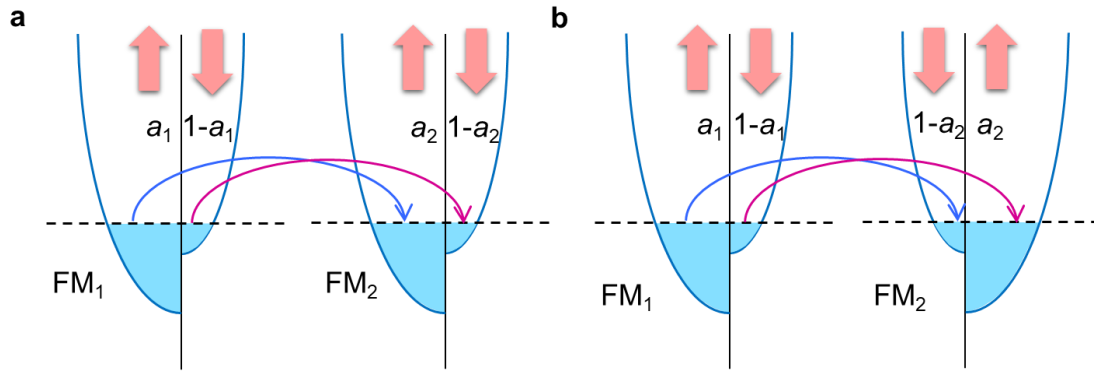


Figure 1-4 Schematic of the Jullière model of TMR. Tunneling process when in the parallel state and antiparallel state is shown in (a) and (b), respectively.

In 1995, Miyazaki et al. and Moodera et al. made significant breakthroughs by achieving substantial TMR ratio at room temperature. A TMR ratio of 18% at room temperature was realized in a Fe/Al₂O₃/Fe MTJ [34], while a TMR ratio of 11.8% at room temperature was achieved in CoFe/Al₂O₃/Co MTJ [35], as depicted in Figure 1-5. The observation of TMR effect at room temperature accelerated researches of MRAM. In 2007, Wei et al. further observed a TMR ratio of 81% at room temperature in a CoFeB/AlO_x/CoFeB MTJ [36]. Worth of noting, all aforementioned studies were conducted on non-crystalline Al₂O₃ barrier. To achieve even higher TMR ratios, the optimization of barriers becomes crucial.

Early to 2001, Butler et al. [37] and Mathon et al. [38] already predicted a potential TMR ratio up to 1000% in a Fe/MgO/Fe MTJ based on *ab initio* calculations. This remarkable phenomenon arises from the filtering effect of electrons with different symmetry induced by the single crystalline MgO barrier. As shown in Figure 1-6. The electrons in electrodes are in Bloch states. Meanwhile, in the barrier, there are

evanescent states due to the band gap between the conduction band and valence band. The energy dispersion depends on the symmetry of electrons for both the Bloch and evanescent states which coupled at the interface.

The Δ_1 electrons are all spin majority in Fe at the Γ point near the Fermi level. Therefore, the spin polarization of Fe is 100% if only consider Δ_1 electrons, which indicates a very high TMR ratio. As shown in Figure 1-6, *ab initio* calculations reveal that the decay length of Δ_1 electrons in single crystalline MgO is significantly longer compared to Δ_2 , Δ_2' , and Δ_5 electrons. In the case of coherent tunneling, where the momentum of electrons remains unchanged during the tunneling process, the Δ_1 electrons dominate the tunneling process. Complemented with band structures of Fe, a remarkably high TMR ratio can be achieved. Notice that the quality of interface has a substantial impact on the TMR ratio. Defects [39], impurities [40], oxidation [41,42] and other factors can lead to incoherent tunneling of electrons, thereby reducing the TMR ratio. Therefore, one must improve the crystal quality to obtain higher TMR ratio [37,38,43].

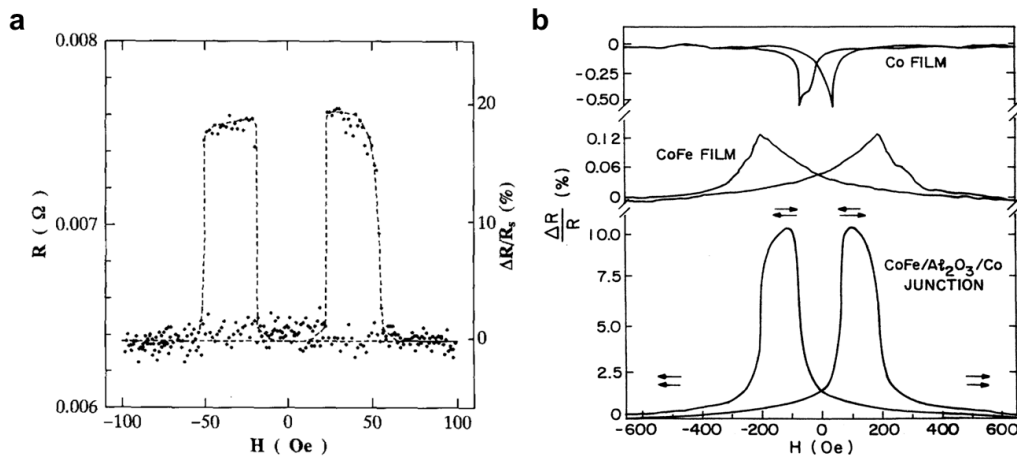


Figure 1-5 Measurements of TMR in MTJs with Al₂O₃ barrier at room temperature. (a) Fe/Al₂O₃/Fe MTJ [34]; (b) CoFe/Al₂O₃/CoFe MTJ [35].

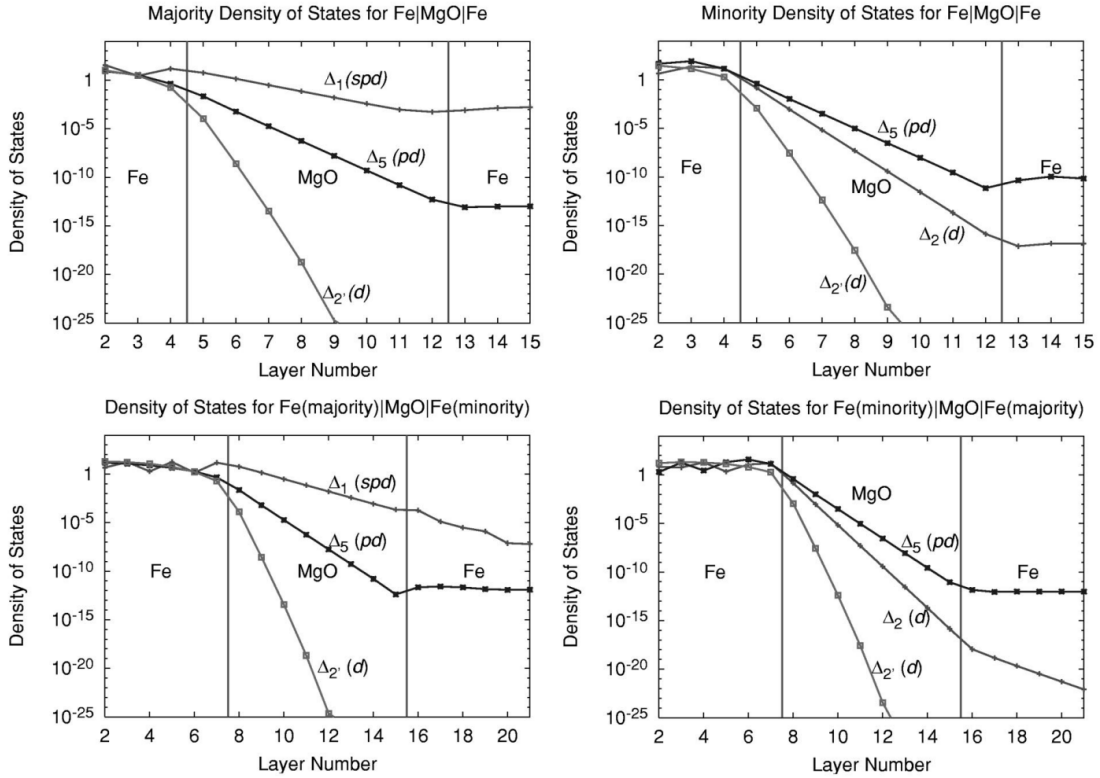


Figure 1-6 Tunneling in Fe/MgO/Fe MTJ for electrons with different symmetry. Top two figures and bottom two figures represent situations of tunneling process in the parallel state and antiparallel state, respectively [37].

In 2004, Parkin et al. [45] and Yuasa et al. [44] fabricated high-quality MTJs with MgO barrier and observed significantly higher TMR ratio compared to those with Al_2O_3 barrier. At room temperature, TMR ratio up to 220% is obtained in CoFe/MgO/CoFe MTJ, while TMR ratio up to 180% is obtained in Fe/MgO/Fe MTJ. As shown in Figure 1-7, the excellent crystal quality and interfaces between the electrode and MgO played a crucial role in achieving these high TMR ratios.

It is worth noting that the utilization of FeCo alloy as electrodes usually yields higher TMR ratios comparing to pure Fe in experiments. As illustrated in Figure 1-8, the TMR ratio exhibits an initial increase followed by a decrease as the Co proportion in the FeCo alloy is increased. The maximum TMR ratio is achieved at approximately 25% Co proportion. This phenomenon can be attributed to the shifting of the Fermi level resulting from the increasing Co proportion and the consequent alterations in

tunneling channels. Moreover, the contribution of non- Δ tunneling, Δ_5 electrons tunneling and interfacial minority states are should be noticed [46,47].

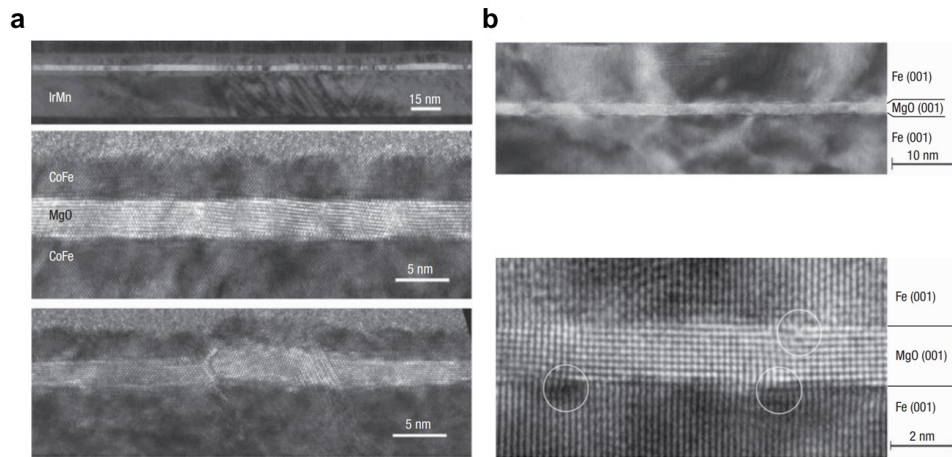


Figure 1-7 TEM images of high-quality MTJs. CoFe/MgO/CoFe MTJ and Fe/MgO/Fe MTJ is shown in (a) and (b), respectively [44,45].

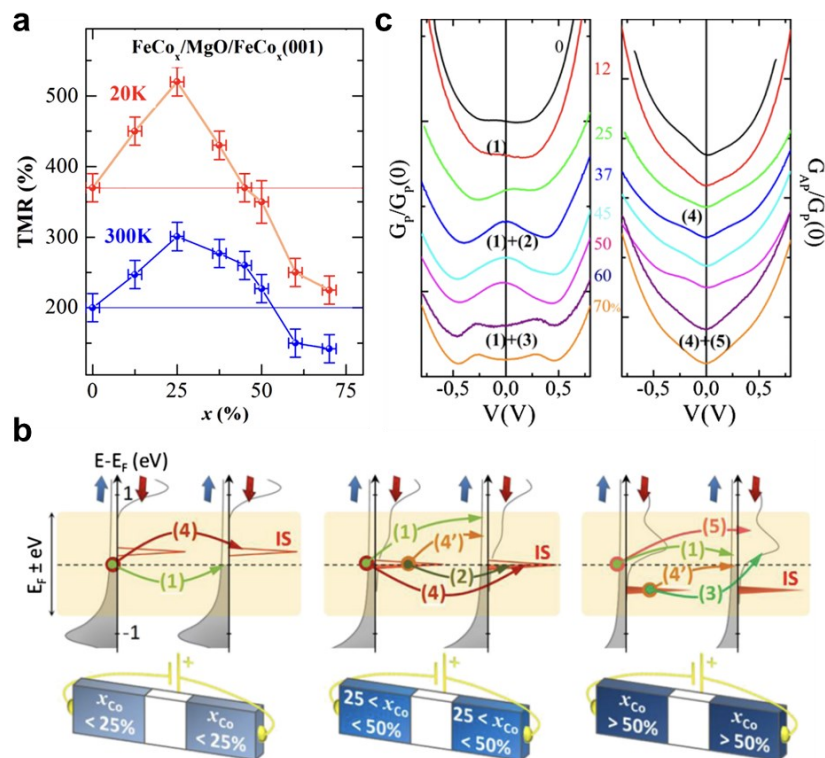


Figure 1-8 Dependence of TMR on the proportion of Co in FeCo_x alloy and its mechanism. (a) Dependence of TMR ratio on the Co proportion in FeCo electrode at 20 K and 300 K. (b) Dependence of band structures and tunneling channels on the Co proportion. (c) Dependence of the conductance of parallel state and antiparallel state on the Co proportion [46].

The lattice mismatch between bulk MgO and bcc Fe is 3.8% [48]. In contrast, the mismatch between bulk MgAl₂O₄ (MAO) and bcc Fe is less than 1% [49]. Figure 1-9 illustrates the remarkable achievements in interface engineering by optimizing the MAO barrier in Fe/Mg₄AlO_x/Fe MTJ. At room temperature, a TMR ratio up to 429%, and an impressive 1034% at 10 K is achieved [48].

The presence of this ultra-flat interface also enables the formation of quantum wells (QWs), where resonant tunneling effects can be observed [50–55]. In Figure 1-10, it is depicted that QW states are formed by Δ_1 majority electrons in Fe between two MAO layers. The tunneling probability increases as the bias voltage elevates the Fermi level of left Fe electrode to match with the QW states. The period of QW states corresponds to the differential conductance period [56]. Additionally, researchers have successfully achieved a double QWs structure in Fe/MAO/Fe/MAO/Fe/MAO/Fe MTJ [57]. Related *ab initio* calculations can be found in the work conducted by Wang et al. [58]

Due to the significantly high TMR ratios observed in MTJs, various non-volatile MRAM have been developed based on this technology. In earlier generations of MRAM, magnetization switching was achieved through the Oersted field induced by currents [59–67]. However, this approach posed challenges on devices intergradation and called for a pure electrical method of writing data. At the same time, extensive research efforts have been devoted to developing perpendicular MTJ to achieve higher storage density. Perpendicular magnetic anisotropy is commonly induced by interfaces between magnetic and oxide materials [68], such as Ta/CoFeB/MgO [20,69–71], Fe/MgO [72–75], Co/AlO_x [76], CoFe/AlO_x [77]. It also arises from interfaces between magnetic materials and heavy metals, such as Co/Pt [78,79], CoFe/Pd [80]. Notice that for the CoFeB electrode, additional annealing process is indispensable to obtain the

perpendicular magnetic anisotropy, where B atoms are driven away from CoFeB and accumulate in the heavy metal [68].

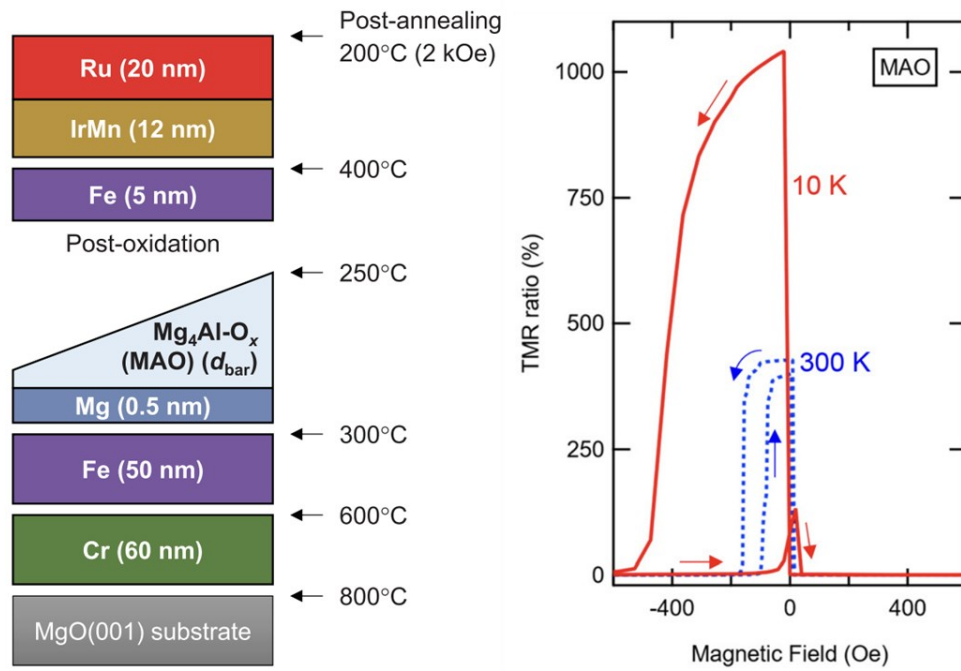


Figure 1-9 Realization of a ultrahigh TMR ratio in Fe/Mg₄AlO_x/Fe MTJ [48].

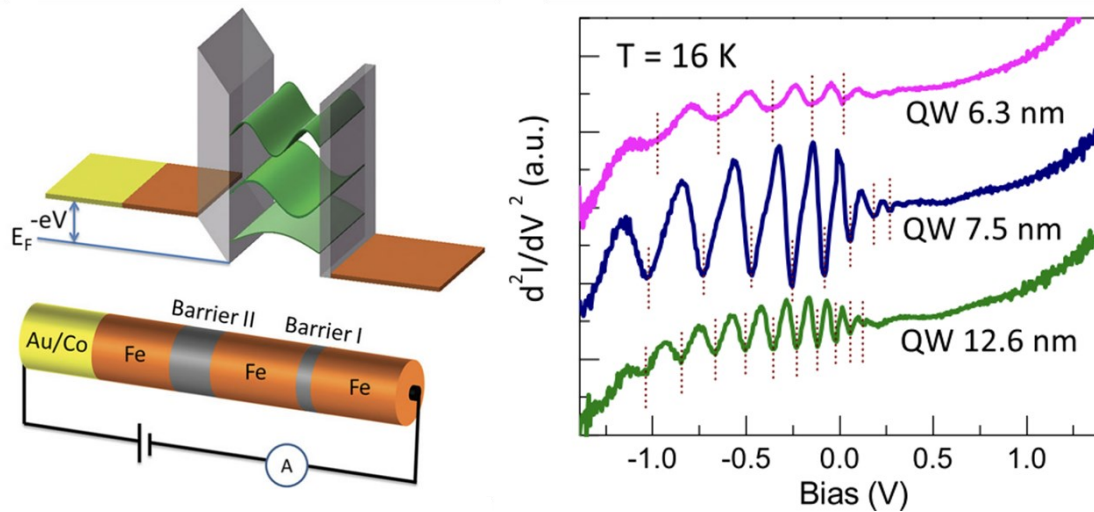


Figure 1-10 QW states in the double-barrier MTJ [56].

Recent studies have revealed the existence of magnetism in van der Waals materials such as CrI₃ [81,82], Cr₂Ge₂Te₆ [83], Fe₃GeTe₂ [84]. In 2019, Wang et al. and Alghamdi et al. [85,86] successfully switched magnetization of Fe₃GeTe₂ by SOT. In the same year, Song et al. [87] reported an astonishingly high TMR ratio up to 57000%

in the graphene/CrI₃/graphene heterostructure. Additionally, multiferroic tunnel junctions (MFTJs) have garnered significant attention [88,89]. In 2012, Pantel et al. [90] observed the coupling of ferromagnetic and ferroelectric interactions in a Co/PbZr_{0.2}Ti_{0.8}O₃(PZT)/LSMO MFTJ, achieving four stable states in this system. Moreover, the sign of TMR ratio is modified by a presetting bias voltage. These researches lay the foundation for MTJs with versatile functionality.

1.3 Spin transfer torque

In 1996, Slonczewski [91] and Berger [92] predicted that a spin polarized current passing through a magnetic multilayer would transfer angular momentum, exerting torques on the magnetization. This phenomenon is known as the STT effect. In 1999, Myers et al. [93] experimentally demonstrated magnetization switching induced by STT in a Co/Cu/Co spin valve. Subsequently, in 2004, Huai et al. [15] reported the magnetization switching induced by STT in a CoFe/Al₂O₃/CoFe MTJ. The discovery of STT opened up a new realm of research of current-induced magnetization switching and significantly accelerated the development of MRAM.

Figure 1-11 illustrates the effect of STT on the free layer magnetization when a current passes through the magnetic multilayer. The STT experienced by the free and reference layer can be described by $\boldsymbol{\tau}_{1,2} \propto I \mathbf{s}_{1,2} \times (\mathbf{s}_1 \times \mathbf{s}_2)$ based on theoretical calculations. Here, I , \mathbf{s}_1 and \mathbf{s}_2 represent the current, the free layer unit magnetization vector and the reference layer unit magnetization vector, respectively. The STT tilts the direction of free layer magnetization parallel (antiparallel) to reference layer magnetization when electrons inject from the reference (free) layer into the free (reference) layer [91–93].

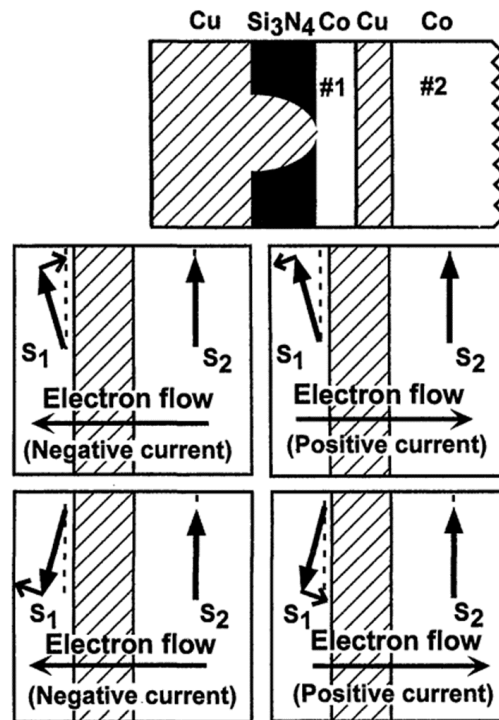


Figure 1-11 Dependence of the STT direction on current direction. Magnetization of the free layer is set parallel (antiparallel) to reference layer when electrons injects from the reference (free) layer to free (reference) layer [93].

The discovery of STT effect has revolutionized the MRAM technology by eliminating the need for magnetic fields. It enables the switching of magnetization in MTJ using only a current. This breakthrough has made the large-scale integration of STT-MTJ possible, marking the ear of STT-MRAM [19,94–99]. However, the STT scheme presents some challenges. Firstly, the relatively large writing currents have to pass through the insulating barrier, which raises endurance concerns. Additionally, STT-induced magnetization switching is realized by directly overcoming the damping torque, leading to a relatively long precession process during switching. This, in turn, slows down the operating speed [100].

1.4 Spin-orbit torque

The angular and orbital momentum of electrons in the lattice are coupled. When

an electron moves relative to the nucleus, an equivalent relative motion of the nucleus with respect to the electron occurs. This motion of the nucleus, which possesses charges, generates an effective magnetic field. This effective magnetic field interacts with the electron's spin, leading to the coupling of the electron's motion (or orbital momentum) with its own spin momentum. This phenomenon is referred to as spin-orbit coupling.

When electrons passing through heavy metals with strong spin-orbit coupling or magnetic multilayers, transverse spin currents can be generated through the spin Hall effect (SHE) [101–103] or interfacial Rashba effect [104–113]. By absorbing these spin currents, magnetization of the adjacent layer experiences a torque, i.e., the SOT. SOT offers a means of a high speed, low power consumption and insulator-protected magnetization switching [101,103,105]. Therefore, it is now widely applied in the development of MRAM and spin logic devices [105,114–121].

1.4.1 Spin Hall effect and anomalous Hall effect

Figure 1-12 illustrates the schematic of the SHE, inverse spin Hall effect (iSHE) and anomalous Hall effect (AHE). When a current passes through heavy metals or doped semiconductors with the spin-orbit coupling, a transverse spin current is generated to the electric field. The polarization of the spin current, the direction of the spin current and the direction of the electric field are mutually orthogonal, i.e., $\mathbf{J}_S = \hbar/2e \cdot \theta_{SH}(\mathbf{J}_C \times \boldsymbol{\sigma})$, where θ_{SH} represents the spin Hall angle of the material, representing the efficiency of the spin current convention. This phenomenon is known as SHE; Similarly, when a current passing through magnetic materials, a spin current is generated. And the magnetization orientation leads to a difference in spin accumulation along the edge, resulting in an observable voltage difference. This effect is referred as AHE; Furthermore, injecting a spin current into non-magnetic materials induces an electric current transverse to the spin current, which is known as ISHE [122].

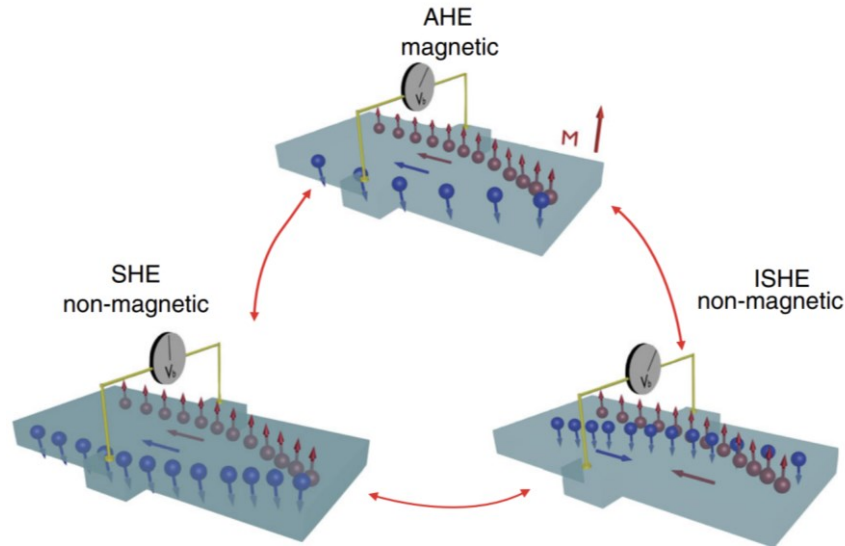


Figure 1-12 Schematic of SHE, AHE and ISHE [122].

The origins of SHE and AHE share similar mechanisms, as depicted in Figure 1-13, which involve three mechanisms: the intrinsic mechanism [123,124], the side jump mechanism [125] and the skew scattering mechanism [126,127]. From an experimental perspective, the primary objective is to identify material systems with larger SOT since the ultimate goal of utilizing of SHE and AHE is to manipulate and probe magnetization.

Commonly used spin-source materials include heavy metals such as Pt [101,128–131], Pt alloy [132–135], Ta [103,128], W [136–140], Pd [141], Hf [142], Rh [143], Ir [144]. Antiferromagnet materials such as PtMn [145], IrMn [146,147]. Van der Waals materials such as WTe₂ [148,149], PtTe₂ [150], MoS₂ [151], NbSe₂ [152], MoTe₂ [153]. And topological materials such as Bi₂Se₃ [154–161]. In terms of heavy metal and antiferromagnets, the magnitudes of their θ_{SH} are approximately 0.1, with β -W exhibiting the highest value of -0.5 [138,162]. Meanwhile, the magnitudes of θ_{SH} of van der Waals materials are also range from 0.01 to 0.1. Notably, with spin-momentum locking surface states in the topological insulators, their magnitudes of θ_{SH} are up to 10 even 100. For instance, $(\text{Bi}_{0.5}\text{Sb}_{0.5})_2\text{Te}_3$ has a θ_{SH} of 450 [163]. However, topological

insulators usually function at low temperature, and have much higher resistance comparing with magnetic metals, which can lead to large shutting currents in the ferromagnet/topological insulator heterostructure. For the later problem, one solution is to utilize magnetic insulators with similarly high resistance [163]. Another approach involves fabricating conducting topological materials, such as $\text{Bi}_{0.9}\text{Sb}_{0.1}$ [164].

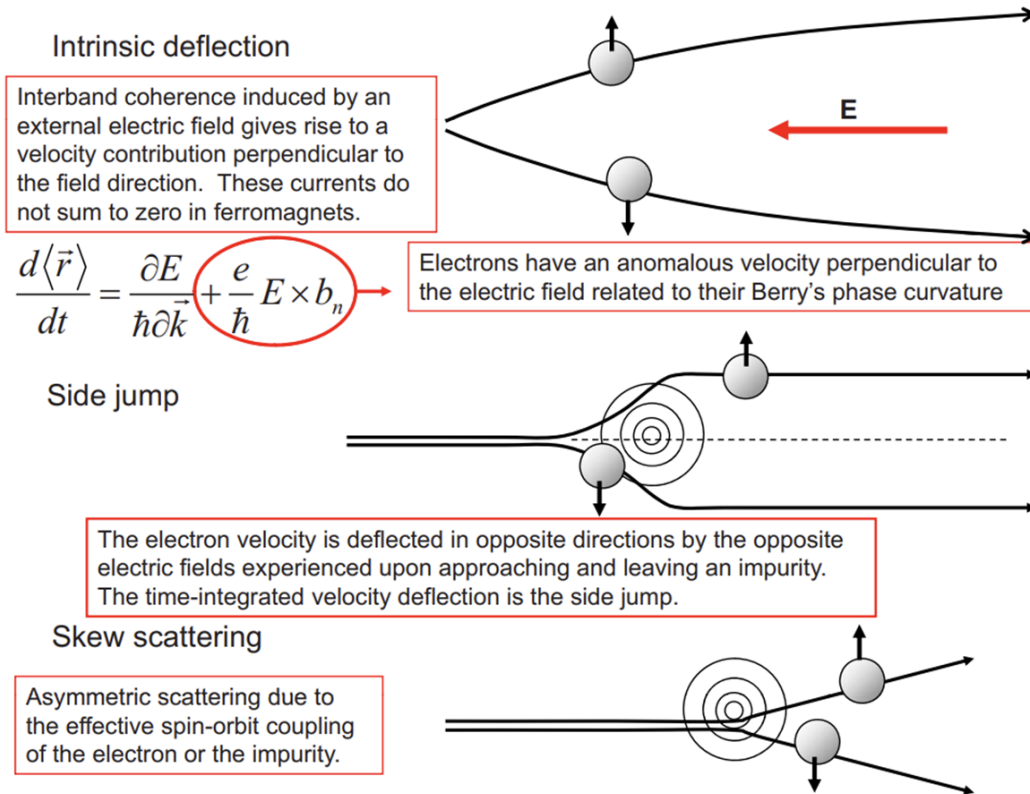


Figure 1-13 Three origins of SHE and AHE [165].

Notice that, SOT in heavy metals and antiferromagnets arises from SHE, where the polarization is predetermined by the geometry. In contrast, the AHE, planar Hall effect (PHE) [166,167] and interfacial spin-processional scattering can generate spin currents with flexible polarizations [168]. Specifically, the polarization of spin currents generated by AHE is parallel to the magnetization, while the direction of spin currents is determined by $\mathbf{m} \times \mathbf{J}_C$. These mechanisms offer means to alter the polarization of spin currents and enable more flexible manipulation of magnetization [169–174].

To achieve more efficient magnetization switching, it is crucial to characterize SOT in various material systems. Several commonly employed methods for this purpose include loop-shift measurements, second harmonic measurements, spin torque-ferromagnetic resonance (ST-FMR) measurements, and spin pumping measurements. These techniques offer valuable insights into the generation of SOTs, enabling a better understanding and optimization of magnetization switching processes.

Loop-shift measurement is a direct mean of quantifying the effective perpendicular field induced by SOT through measure the horizontal shifts of R_{xy} - H_z loops. During the measurements, both an in-plane magnetic field and a perpendicular magnetic field are usually required simultaneously. Meanwhile, such method cannot be applied to measure SOTs in systems with in-plane magnetization since it is based on AHE of perpendicular magnetization [85,175–177].

Second-harmonic measurement involves utilizing a small AC to generates an AC SOT at the same frequency. As a result, the magnetization undergoes oscillations at the same frequency, leading to variations in AHE resistance and PHE resistance. One advantage of this method is that it has no requirement for magnetic orientations, making it applicable to wider range of systems [178]. However, this method is based on the first and second harmonic voltage signal and a lock-in amplifier is needed. Additionally, during the measurement, the application and rotation of an external magnetic field are necessary [85,179–181].

Similarly, the ST-FMR method quantifies the variations in anisotropy magnetoresistance to observe SOTs-induced magnetization processions [102,182–186]; while spin pumping involves the induction of magnetization procession by an oscillating magnetic field, followed by the measurement of electric signals converted from the spin current through ISHE. This process allows for the interpretation of the

SHE efficiency [187–189]. For a comprehensive understanding of the evolutions of SHE and AHE and the relevant material systems, please refer to the following references [122,165].

In contrast to STT, the spin currents induced by SHE and AHE is transverse to the direction of electric fields, allowing for the separation of the read-line and write-line, which provides MTJ with significantly enhanced endurance. As shown in Figure 1-14, an in-plane CoFeB/MgO/CoFeB MTJ is grown on Ta. When a current is portrait applied, a spin current perpendicular to films is generated, with its polarization along the transverse direction. Upon absorption by top CoFeB layer, its magnetization is switched, which can be observed through TMR measurements. Thus, both electrical switching and probing of magnetization are achieved, marking a true milestone in the development of SOT-MRAM [103].

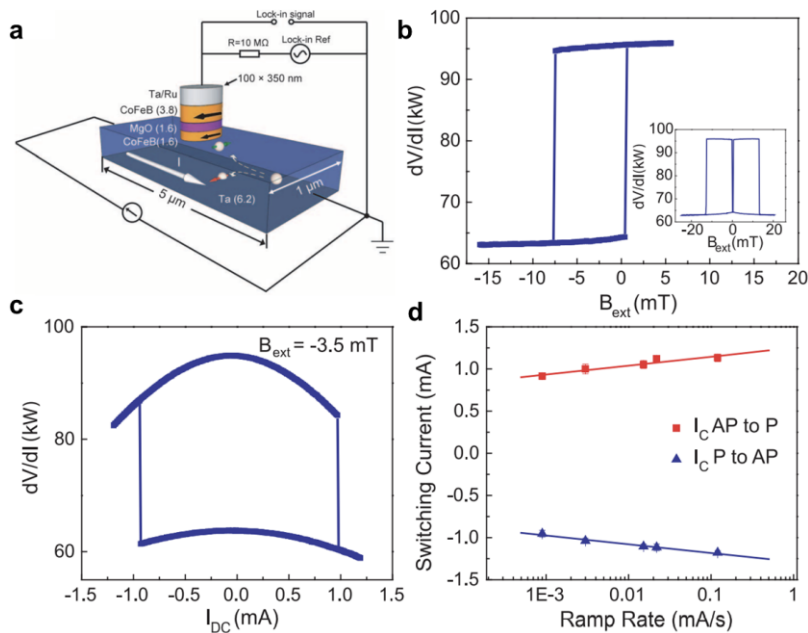


Figure 1-14 Electrical switching and measurements in the MTJ with SOT. (a) Schematic of the structure of MTJ, the magnetization and spin current direction and the measurement setup. (b) Dependence of the differential resistance on the applied magnetic field. (c) Current dependence of the differential resistance. (d) Dependence of the critical current on the ramp rate [103].

1.4.2 Field-free perpendicular magnetization switching induced by SOTs

In the realm of hard disk drive development, it has been discovered that perpendicular magnetic domains offer significant improvements in storage density while maintaining thermal stability, surpassing their in-plane counterparts. Similar considerations have guided the evolution of MRAM, transitioning from utilizing in-plane magnetization to employing perpendicular magnetization. The STT mechanism functions equally effectively for both in-plane and perpendicular magnetization systems. Therefore, the primary challenge in developing perpendicular STT-MRAM lies in inducing perpendicular magnetic anisotropy. After conducting a series of explorations, it is successfully achieved at the CoFeB/MgO interface. Additionally, the MgO barrier exhibits a high TMR ratio, further enhancing its appeal. Consequently, CoFeB/MgO/CoFeB and its derivative structures have become the predominant design choice for perpendicular STT-MRAM [2]. Nevertheless, unlike the STT mechanism, switching perpendicular magnetization via SOT requires an additional symmetry-breaking in-plane magnetic field, posing integration challenges. For the sake of convenience in subsequent discussions, we present a brief introduction to the dynamic equations governing magnetization under magnetic fields and current-induced torques.

The dynamic equation governing the behavior of magnetization in the presence of magnetic fields is described by the Landau-Lifshitz-Gilbert (LLG) equation [190]

$$\frac{\partial \mathbf{M}}{\partial t} = -\gamma \mathbf{M} \times \mathbf{H} - \frac{\alpha}{M} \mathbf{M} \times \frac{\partial \mathbf{M}}{\partial t}. \quad (1-1)$$

Here, γ represents the gyromagnetic ratio while α is the Gilbert damping factor. This equation describes the rotational motion of magnetization \mathbf{M} when subjected to an external magnetic field \mathbf{H} . The \mathbf{M} rotates around \mathbf{H} and eventually aligns parallel to \mathbf{H} , taking into account the dissipation of energy into the lattice. To incorporate the influence of currents, the LLG equation is further modified by introducing the STT term,

leading to the Landau-Lifshitz-Gilbert-Slonczewski (LLGS) equation

$$\frac{\partial \mathbf{m}}{\partial t} = -\gamma \mathbf{m} \times \mathbf{H} + \alpha \mathbf{m} \times \frac{\partial \mathbf{m}}{\partial t} + \lambda_D \mathbf{m} \times \boldsymbol{\sigma} \times \mathbf{m} + \lambda_F \boldsymbol{\sigma} \times \mathbf{m}. \quad (1-2)$$

Here, the first term represents the field term, which induces the rotation of \mathbf{m} around \mathbf{H} . The second term corresponds to the damping term, causing \mathbf{m} to gradually align with \mathbf{H} . The third term, $\mathbf{m} \times \boldsymbol{\sigma} \times \mathbf{m}$, known as the Slonczewski term or damping-like term, emerges when currents are applied. As depicted in Figure 1-15, if the spin polarization vector $\boldsymbol{\sigma}$ is antiparallel to \mathbf{H} , the damping-like term will be antiparallel to the damping term. This configuration allows the current to provide additional energy to \mathbf{m} , enabling it to sustain precession around \mathbf{H} and even undergo a magnetic switching. The term $\boldsymbol{\sigma} \times \mathbf{m}$ is the field-like term, while λ_D and λ_F are coefficients proportional to the spin current density. It is important to note that, for the sake of derivation convenience, we employ the normalized magnetization, $\mathbf{m} = \mathbf{M}/M$, in the equation.

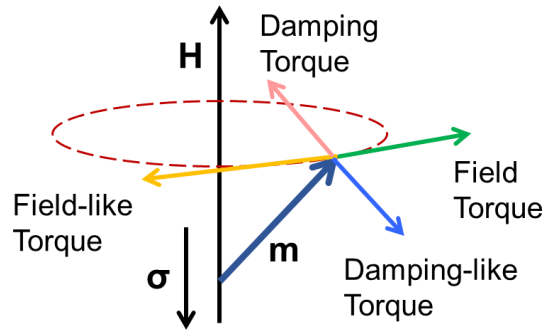


Figure 1-15 Schematic of torques in the Landau-Lifshitz-Gilbert-Slonczewski equation.

In 2012, Liu et al. conducted a study where they observed the perpendicular magnetization switching in Pt/Co multilayers and identified the SOT generated through SHE as the underlying mechanism [101]. As illustrated in Figure 1-16, the presence of SHE results in a spin current $\boldsymbol{\sigma}$, polarized along the $+x$ direction, being injected into the upper layer of Co when a current flows through Pt in the $+y$ direction. This $\boldsymbol{\sigma}$ acts on the magnetization \mathbf{m} of Co in the form of $\boldsymbol{\tau}_{\text{ST}} = \tau_{\text{ST}}^0 (\mathbf{m} \times \boldsymbol{\sigma} \times \mathbf{m})$. The \mathbf{m} experiences

an anisotropy field \mathbf{B}_{an} , exerting a torque of $\boldsymbol{\tau}_{\text{an}} = -\mathbf{m} \times \mathbf{B}_{\text{an}}$. It should be noted that when the SOT is small, \mathbf{B}_{an} lies in the yz plane, and its y component is opposite to the y component of \mathbf{m} . Additionally, the magnitude of \mathbf{B}_{an} should be zero when \mathbf{m} aligns with its easy axis and reaches its maximum when \mathbf{m} is perpendicular to the easy axis. Therefore, we can represent the anisotropy field as $\mathbf{B}_{\text{an}} = -B_{\text{an}}^0 m_y \mathbf{y}$. Substituting this into the torque equation, we obtain $\boldsymbol{\tau}_{\text{an}} = -\mathbf{m} \times [-B_{\text{an}}^0 (\mathbf{m} - m_z \mathbf{z})] = -\mathbf{m} \times (B_{\text{an}}^0 m_z \mathbf{z})$. The \mathbf{m} is also influenced by the external magnetic field \mathbf{B}_{ext} , resulting in a torque of $\boldsymbol{\tau}_{\text{ext}} = -\mathbf{m} \times \mathbf{B}_{\text{ext}}$. It is important to note that the dominant torque driving SOT switching is the Slonczewski-like term, while the field-like term is often neglected (including this dissertation). However, the field-like term does exist and impacts the switching process. Its presence can be characterized through second harmonic measurements [179].

In the scenario where the external magnetic field lies in the yz plane and the SOT is small, the three torques exerted on \mathbf{m} align along the x -direction and balance each other, resulting in a stable \mathbf{m} position. This equilibrium can be expressed as $\tau_{\text{tot}} = \tau_{\text{ST}}^0 + B_{\text{ext}} \sin(\theta - \beta) - B_{\text{an}}^0 \sin \theta \cos \theta = 0$, where θ and β are defined as depicted in Figure 1-16. However, when the current reaches the threshold and the SOT becomes strong enough, the \mathbf{m} can be switched from one stable state to another. The polarity of this switching, either from $\mathbf{m} > 0$ to $\mathbf{m} < 0$ or vice versa, is determined by the direction of the in-plane magnetic field. It is important to note that, unlike in STT-induced perpendicular magnetization switching, the presence of a symmetry-breaking in-plane magnetic field is indispensable in SOT-induced perpendicular magnetization switching. Without this magnetic field, deterministic perpendicular magnetization switching cannot be achieved.

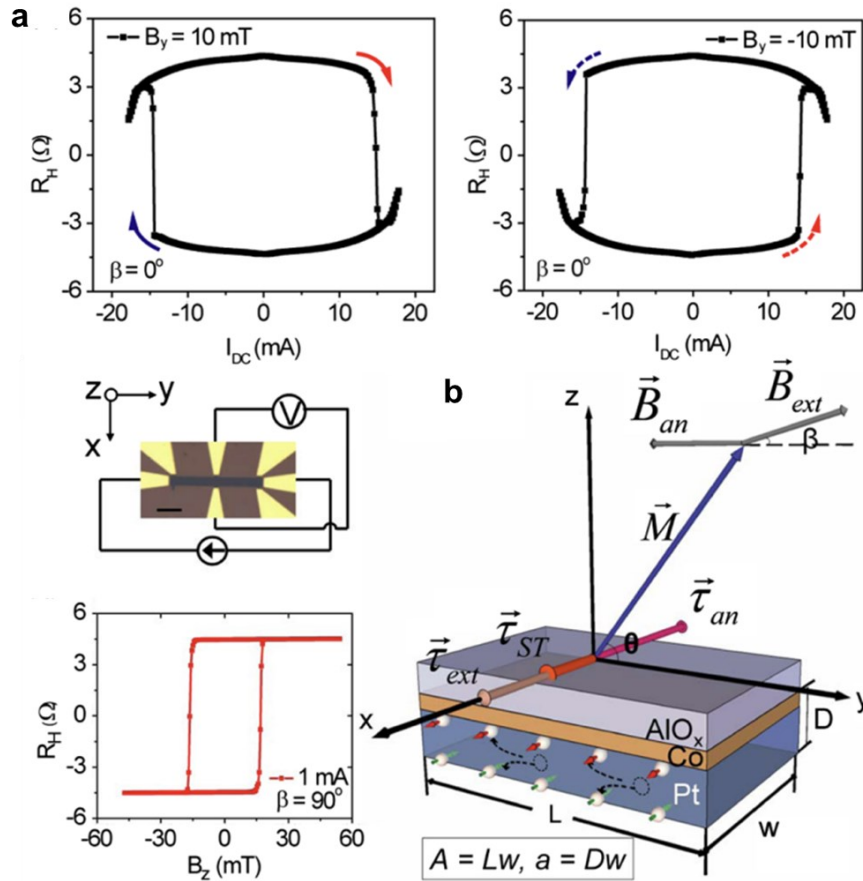


Figure 1-16 SOT-induced perpendicular magnetization switching. (a) Measurements of switching of perpendicular magnetization. Directions of magnetization, torques and effective fields are given in (b) [101].

With the advancement of SOT research, Fukami et al. proposed a classification for SOT-induced magnetization switching, identifying three distinct types [191]. As illustrated in Figure 1-17, when electrons are injected into a heavy metal in the $+x$ direction, SHE generates a spin current in the $+z$ direction with polarization along the $-y$ direction. Consequently, when the magnetic easy axis is along the z direction, deterministic perpendicular magnetization switching can be achieved by applying an auxiliary magnetic field in the x direction, known as Type-Z switching. In contrast, when the easy axis is along the y direction, in-plane magnetization switching can be accomplished without the need for an external magnetic field, referred to as Type-Y switching. Lastly, when the easy axis lies in the x direction, deterministic in-plane

magnetization switching requires the application of an auxiliary magnetic field in the z direction, termed Type-X switching.

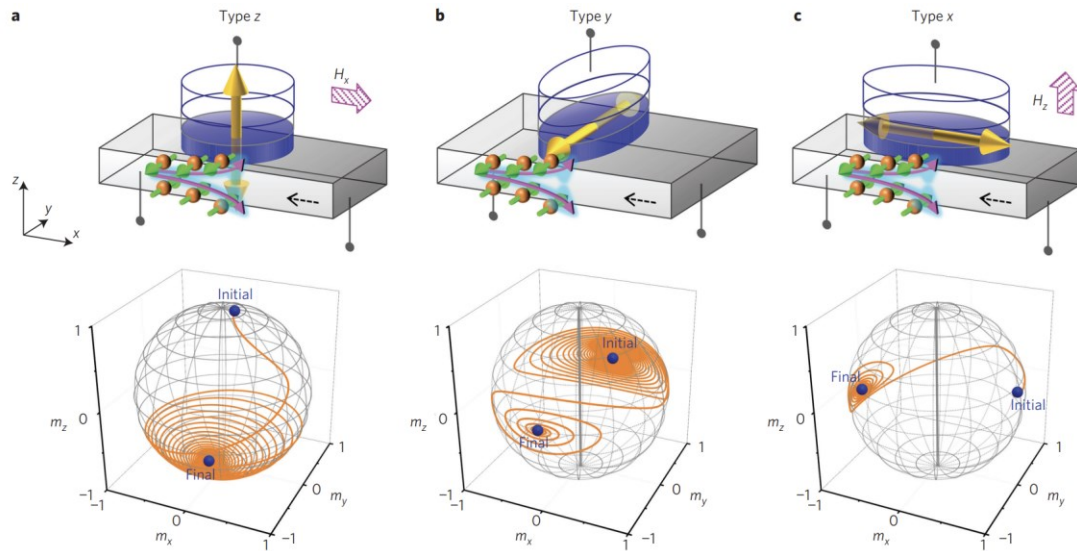


Figure 1-17 Schemes of SOT-induced magnetization switching. (a-c) represent the Type-Z, Type-Y and Type-X switching, respectively [191].

It is worth noting that Type-Z and Type-X switching belong to the same category in terms of symmetry. In both cases, the spin polarization is perpendicular to the magnetization, necessitating an auxiliary magnetic field perpendicular to both the magnetization and the spin polarization direction for switching. Only Type-Y differs, as the spin polarization is parallel to the magnetization, allowing for deterministic switching similar to the STT mechanism without the need for an additional magnetic field. However, this parallel configuration leads to a direct competition between the damping term and the SOT in the LLGS equation, resulting in prolonged precession at the onset of the switching process [100]. Consequently, Type-Y switching is typically slower in terms of switching speed [192], while Type-X and Type-Z switching exhibit similar and faster dynamics [193].

In 2014, Yu et al. conducted an analysis on the necessity of an additional magnetic field in Type-Z and Type-X switching from a symmetry perspective, and proposed a method to achieve field-free Type-Z switching [137]. As depicted in Figure

1-18, the magnetization \mathbf{m} , is oriented along the z direction, while the current \mathbf{J} , flows in the x direction. Due to the SHE, the \mathbf{m} experiences a field-like torque and a Slonczewski-like torque. For the sake of convenience in discussions, these two torques can be considered equivalent to field-like effective magnetic fields, namely $\mathbf{H}_y^{\text{FL}} = H_y^{\text{FL}}\mathbf{y}$ and Slonczewski-like effective magnetic field, $\mathbf{H}_y^{\text{DL}} = H_y^{\text{DL}}\mathbf{m} \times \mathbf{y}$, respectively.

Firstly, in the absence of magnetic fields, we performed a mirror operation along the xz plane on the multilayer system. The multilayer material possesses inherent symmetry to the xz plane, thus remaining unchanged. The \mathbf{J} aligned with the $+x$ direction, also remains unaffected. However, the pseudovector \mathbf{m} , initially oriented along the $+z$ direction, is inverted towards $-z$. Similarly, the effective magnetic fields, being pseudovectors, exhibit a reversal in \mathbf{H}_y^{DL} while \mathbf{H}_y^{FL} remains unaltered. Due to the symmetric nature of the multilayer with respect to the xz mirror, both states are equivalent. Consequently, the direction of \mathbf{m} , whether up or down, does not exhibit a preference with respect to \mathbf{J} or the induced torques. Thus, the attainment of deterministic Type-Z switching is unattainable.

However, the introduction of an in-plane magnetic field \mathbf{H}_{ap} along the $+x$ direction alters the scenario. Upon performing the xz mirror operation, the direction of \mathbf{H}_{ap} changes to $-x$. If we consider the state where the \mathbf{m} is aligned with the $+z$ direction and \mathbf{H}_{ap} is along the $+x$ direction, the equivalent state after the xz mirror operation would feature \mathbf{m}' directed towards $-z$ and \mathbf{H}'_{ap} along $-x$. Given that we can directly control the direction of the applied magnetic field \mathbf{H}_{ap} , we can simultaneously determine the direction of \mathbf{m} . This leads to the realization of field-assisted deterministic perpendicular magnetization switching.

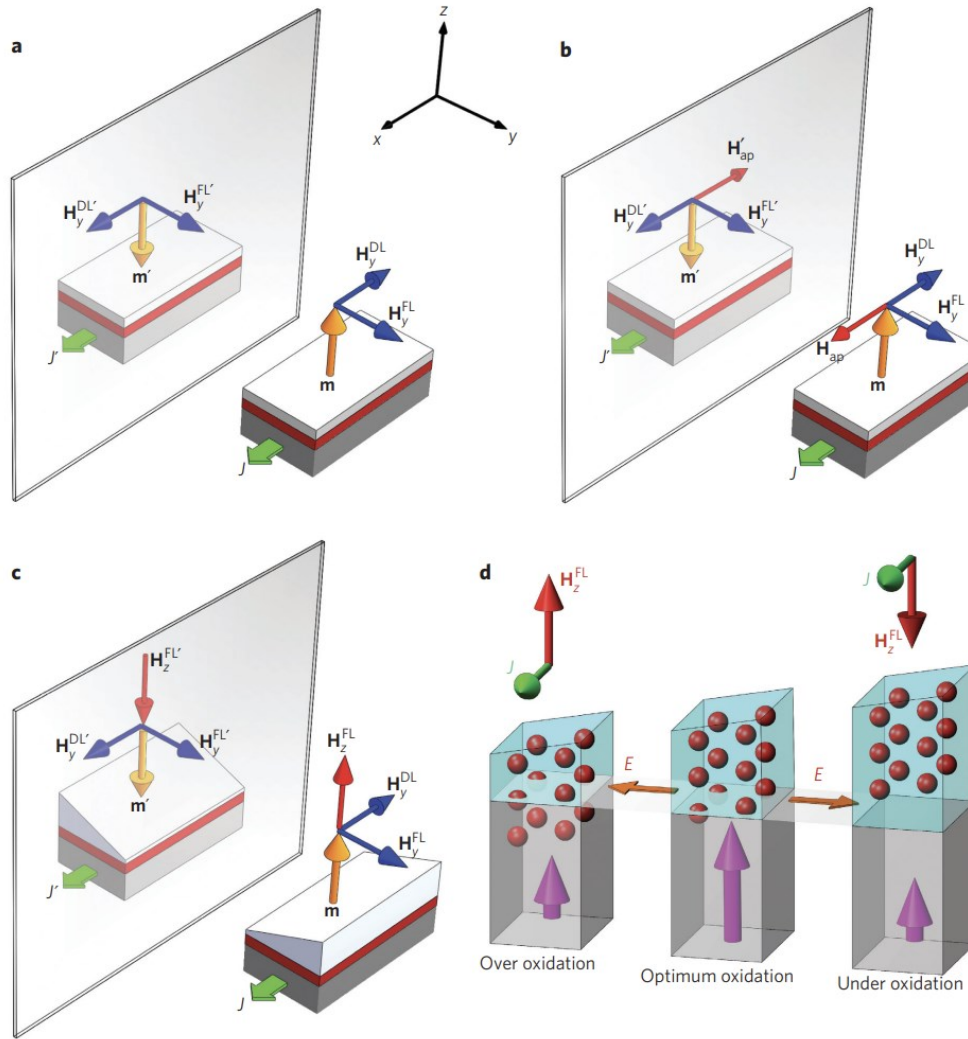


Figure 1-18 A symmetry-based analysis of SOT-induced perpendicular magnetization switching. Directions of the current, magnetization and effective fields are shown in the figure. (a) Without magnetic fields, it is equivalent for the magnetization-up state and magnetization-down state. Deterministic switching of magnetization by the current is prohibited. (b) The mirror symmetry is broken by introducing an x -direction magnetic field. Current induced deterministic switching is possible. (c) The mirror symmetry is broken by the thickness gradient. An effective perpendicular field is induced by the current and deterministic switching is possible. (d) Generation of the effective perpendicular field by current [137].

Alternatively, by modifying the structure of the multilayer to intentionally break its xz mirror symmetry, the direction of \mathbf{m} can be determined by \mathbf{J} . In this case, an effective field \mathbf{H}_z^{FL} along the $+z$ direction, may be generated to facilitate magnetization switching. This additional field may arise from the presence of a built-in electric field

within the wedge film.

Essentially, achieving Type-Z switching necessitates the breaking of xz mirror symmetry, which is parallel to the current flow. This symmetry breaking enables the generation of torques or effective fields along the z direction. However, the mass production of homogeneous wedge films poses a significant challenge for the industry. As a result, researchers have investigated numerous methods to break the symmetry and accomplish field-free Type-Z switching [194,194–200]. In the following sections, we will discuss several classical mechanisms in detail.

In 2016, MacNeill et al. conducted an investigation on the WTe_2 /Permalloy bilayer and observed the emergence of a perpendicular damping-like torque in the material with reduced symmetry [148]. The mirror symmetry along the ac plane in WTe_2 is naturally broken, allowing for the generation of a damping-like torque along the c -axis when a current is injected along the a -axis. This phenomenon was experimentally detected through ST-FMR measurements. Similarly, in 2021, Liu et al. achieved field-free perpendicular magnetization switching by utilizing an perpendicular damping-like torque in an epitaxial $CuPt/CoPt$ bilayer [201]. As illustrated in Figure 1-19, while the mirror symmetry is preserved along three planes, it is broken along the other three. By altering the angle of the injected current, it becomes possible to generate and control the perpendicular damping torque.

In 2016, Fukami et al. demonstrated field-free perpendicular magnetization switching in an antiferromagnetic/ferromagnetic bilayer by leveraging the exchange bias effect originating from the antiferromagnetic layer [145]. As depicted in Figure 1-20, when the $PtMn$ antiferromagnetic layer reaches a sufficient thickness, the perpendicular magnetization becomes tilted towards the in-plane direction due to the presence of the exchange bias. Subsequently, when a current is applied, an effective

perpendicular field is generated, with its direction determined by the current flow. By employing a sufficiently large current, the perpendicular magnetization can be switched. Remarkably, the antiferromagnetic layer serves a dual role as both a symmetry-breaking agent and a spin source, thereby simplifying the design of MTJ in this context. Similarly, in 2016, van den Brink et al. [202] and W. J. Kong et al. [147] also employed an antiferromagnetic IrMn layer, to provide an exchange bias field, leading to field-free switching of the perpendicular Co layer.

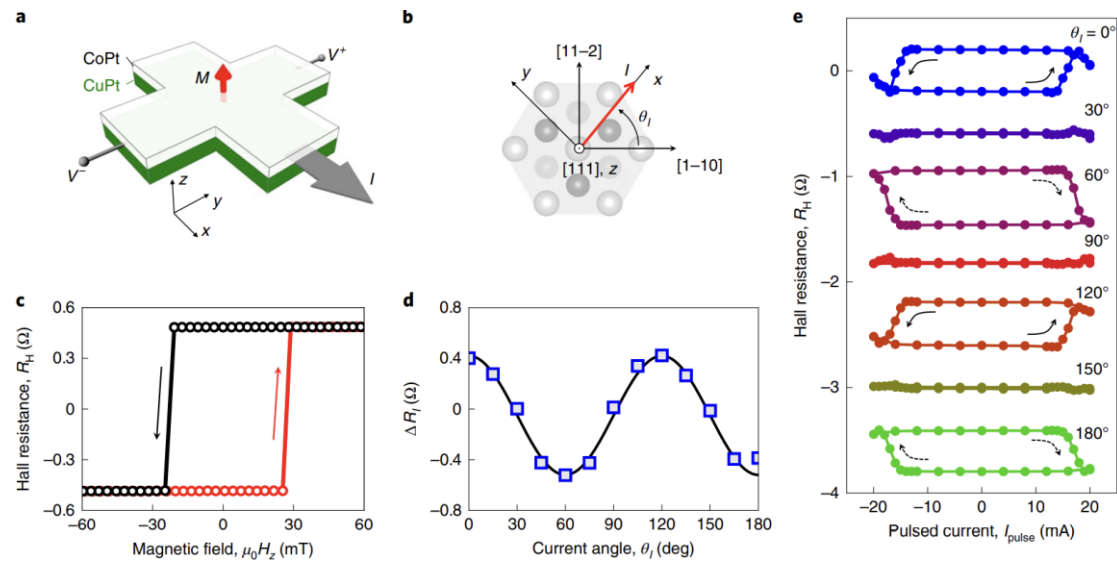


Figure 1-19 Field-free perpendicular magnetization switching by SOTs in an epitaxial CoPt/CuPt bilayer. (a) Schematic of the measurement setup. (b) Definition of the angle between the current and the lattice direction. (c) AHE when the angle is zero. (d) Current angle dependence of the amplitude of current-induced magnetization switching. (e) Current-induced magnetization switching [201].

In 2018, Baek et al. achieved field-free perpendicular magnetization switching in a Type-T magnetic multilayer with both in-plane and perpendicular magnetization [171]. As depicted in Figure 1-21, in the CoFeB/Ti/CoFeB multilayer, when the in-plane CoFeB magnetization is oriented along the $+x$ and $-x$ directions, the switching polarity of the perpendicular CoFeB magnetization is clockwise and counterclockwise, respectively. Notably, in this system, SOTs arise not only from the SHE in the bulk in-plane CoFeB layer but also from spin filtering and spin precessional

scattering at the CoFeB/Ti interface, which stem from the interfacial spin-orbit coupling. Due to the presence of spin precessional scattering, SOTs experienced by the perpendicular CoFeB magnetization exhibit a component along the z -direction.

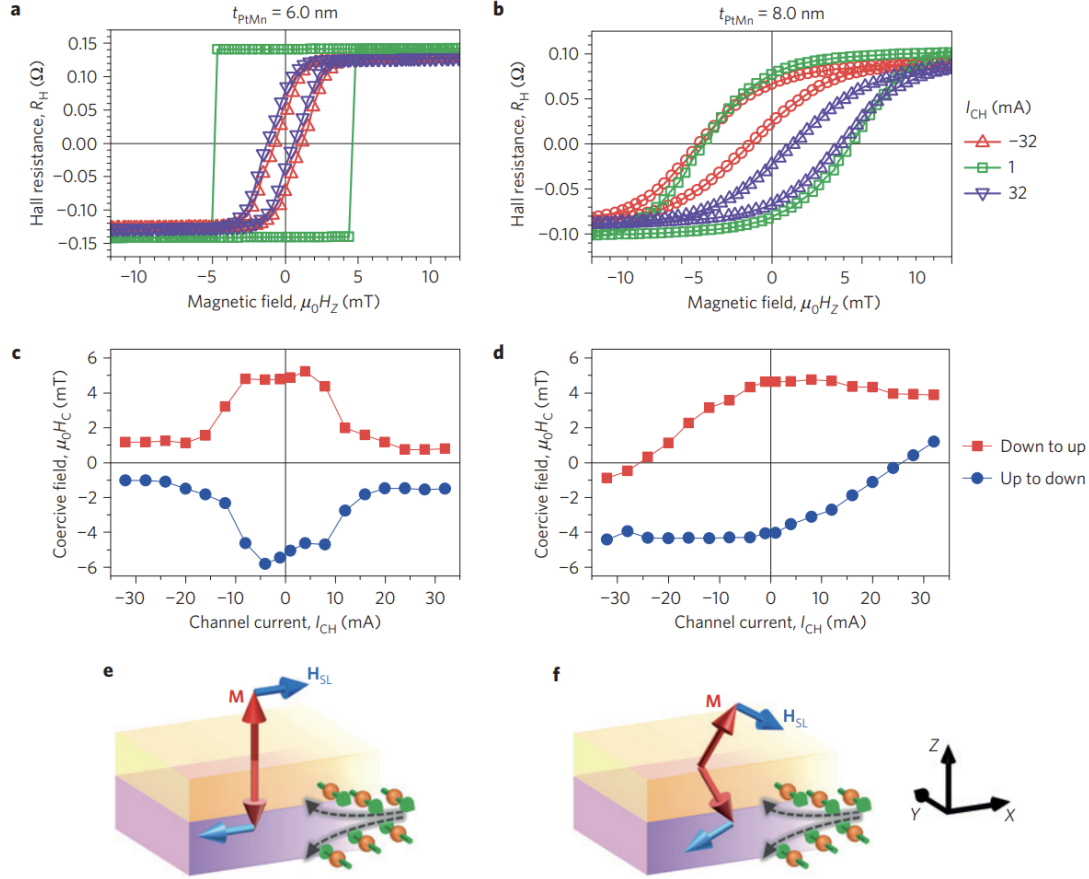


Figure 1-20 Field-free perpendicular magnetization switching in an antiferromagnetic/ferromagnetic bilayer. Current dependence of AHE when PtMn is 6 nm and 8 nm is shown in (a) and (b), respectively. Current dependence of the coercive field when the PtMn is 6 nm and 8 nm is shown in (c) and (d), respectively. Schematics of current-induced magnetization switching when the PtMn is 6 nm and 8 nm is shown in (e) and (f), respectively [145].

In 2020, Hibino et al. also observed a similar perpendicular SOT term induced by spin precessional scattering at the Pt/Co interface in the NiFe/Pt/Co system, highlighting the influence of the nonmagnetic material [203]. For more detailed theoretical insights into interface spin filtering and spin precessional scattering, refer to the articles by Amin et al. [168,204]. However, it is important to note that there is still

ongoing debate regarding the mechanisms underlying spin generation at interfaces. In 2021, Zhu et al. reported a strong interface spin-orbit coupling in the Ti/CoFeB bilayer, confirmed by the presence of perpendicular magnetic anisotropy in CoFeB. However, no spin current generated by spin filtering or the Rashba effect was observed [205]. Further research is necessary to elucidate the underlying mechanism of interfacial spin currents.

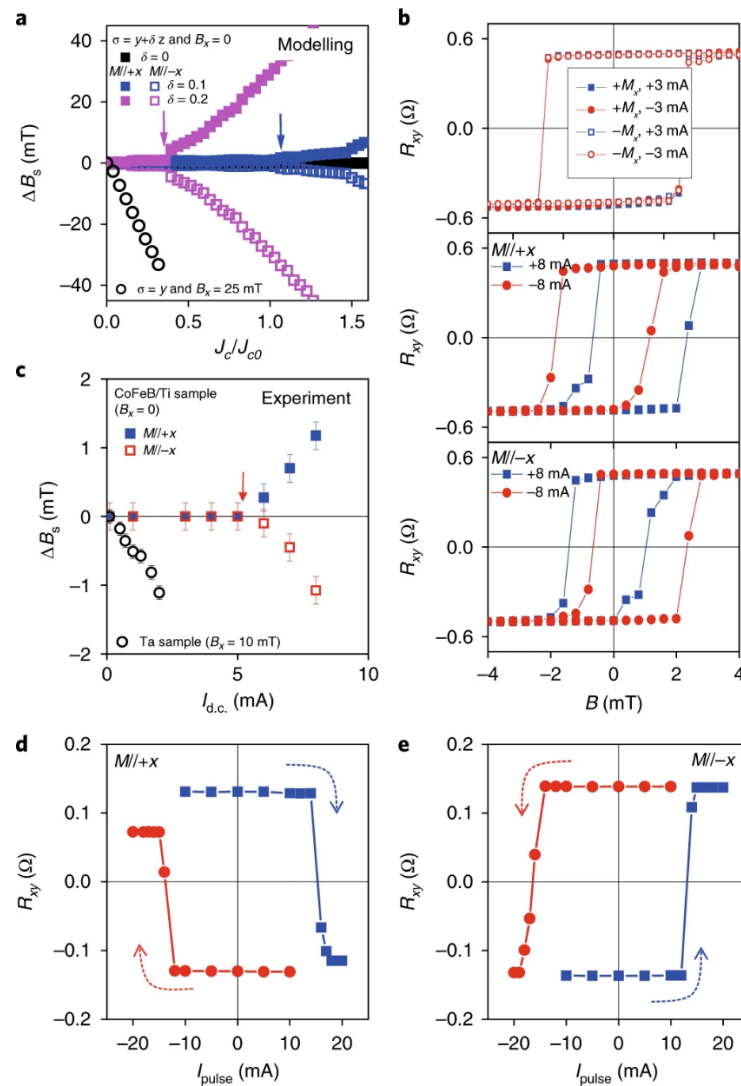


Figure 1-21 Field-free perpendicular magnetization switching in the CoFeB/Ti/CoFeB multilayer. (a) Simulation of current dependence of loop shifts with and without the z-torque. (b) Loop shifts with different currents when in-plane magnetization is along different directions. (c) Experimental results of current dependence of loop shifts. Field-free perpendicular magnetization switching when in-plane magnetization is along the +x and -x direction is shown in (d) and (e), respectively [171].

In 2016, Lau et al. achieved field-free perpendicular magnetization switching in a Type-T magnetic multilayer by exploiting the interlayer coupling between in-plane and perpendicular magnetization [206]. The system consists of both an in-plane CoFe layer and a perpendicular CoFe layer, as illustrated in Figure 1-22. The in-plane CoFe magnetization is fixed by the antiferromagnetic IrMn, while the interlayer Ruderman-Kittel-Kasuya-Yosida (RKKY) coupling is mediated by Ru. Through this interlayer coupling, the perpendicular magnetization experiences an in-plane effective field generated by the in-plane magnetization, enabling field-free switching. Furthermore, the direction of this effective field can be adjusted by varying the thickness of the Ru layer. As a result, the polarity of switching can be modified. This effect is not only observed in the chirality of current-induced magnetization switching but also in the horizontal loop shifts observed during field-driven magnetization switching. This approach, which utilizes interlayer coupling to achieve field-free switching, is compatible with existing MRAM fabrication technologies, providing a convenient tool for the development of future spin logic devices [207].

Building upon the same principle, in 2018, Wang et al. achieved field-free perpendicular magnetization switching and current-controlled polarity in a Type-T magnetic multilayer [119]. In the Pt/Co/Ru/Co/Pt stack depicted in Figure 1-23, the two Co layers, sandwiched by the two Pt layers, are coupled through the intermediate Ru layer via RKKY mechanism [208]. When a current is injected in the y -direction, the lower perpendicular Co magnetization experiences a SOT in the x -direction from the bottom Pt layer, as well as an in-plane effective field in the y -direction from the upper in-plane Co magnetization. This leads to Type-Z switching of the perpendicular Co magnetization. Notably, the in-plane Co magnetization cannot be switched due to its larger magnetic moment.

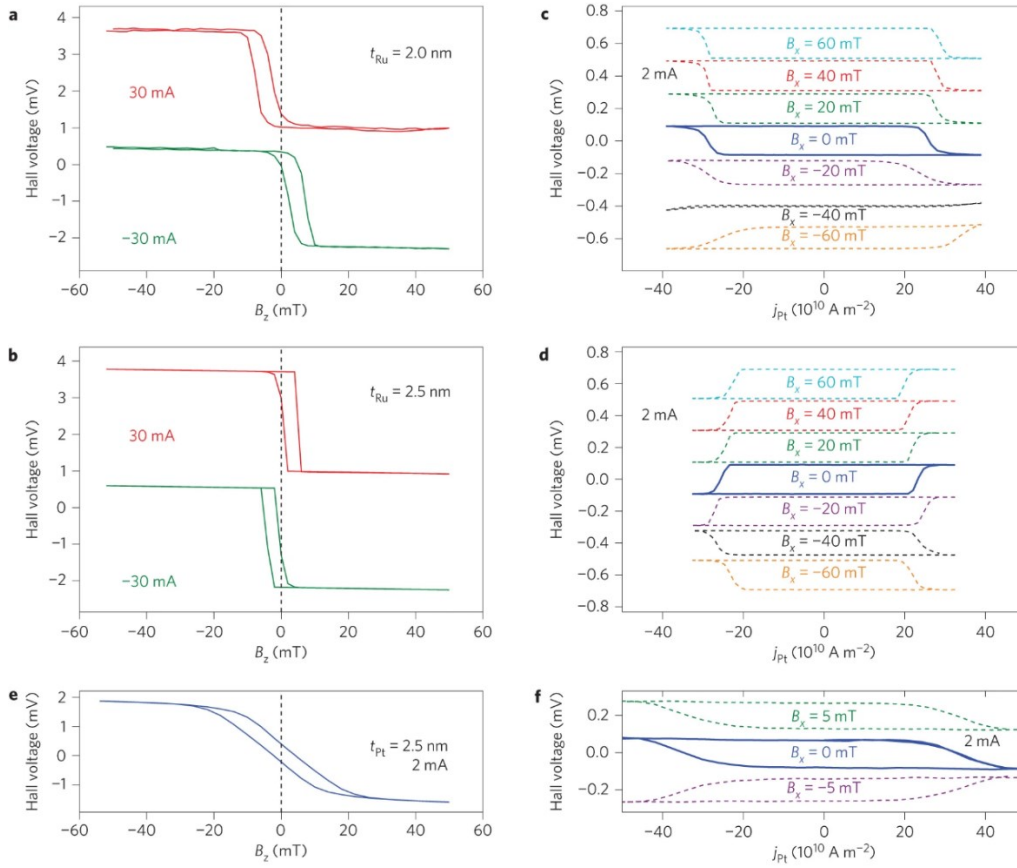


Figure 1-22 Field-free perpendicular magnetization switching in a system with interlayer coupling. The thickness of Ru is 2 nm and the interlayer coupling is AFM in (a) and (c). The thickness of Ru is 2.5 nm and the interlayer coupling is FM in (b) and (d). AHE and the current-induced perpendicular magnetization switching when the interlayer is 2.5 nm Pt is shown in (e) and (f), respectively [206].

Conversely, when a current is injected in the x -direction, the perpendicular Co magnetization experiences an SOT in the y -direction, while the in-plane effective field also aligns with the y -direction. Thus, Type-Z switching of the perpendicular Co magnetization cannot be achieved. Simultaneously, the in-plane Co magnetization experiences an SOT in the y -direction from the top Pt layer, enabling its Type-Y switching when the SOT is sufficiently large. As a result, the orientation of the in-plane Co magnetization and the polarity of perpendicular magnetization switching can be determined by the x -directional current. Based on this concept, a multifunctional logic gate can be constructed by defining the y -directional current as the input and utilizing

the AHE resistance as the output. Moreover, the functionality of the logic gate can be altered by applying an x -directional current.

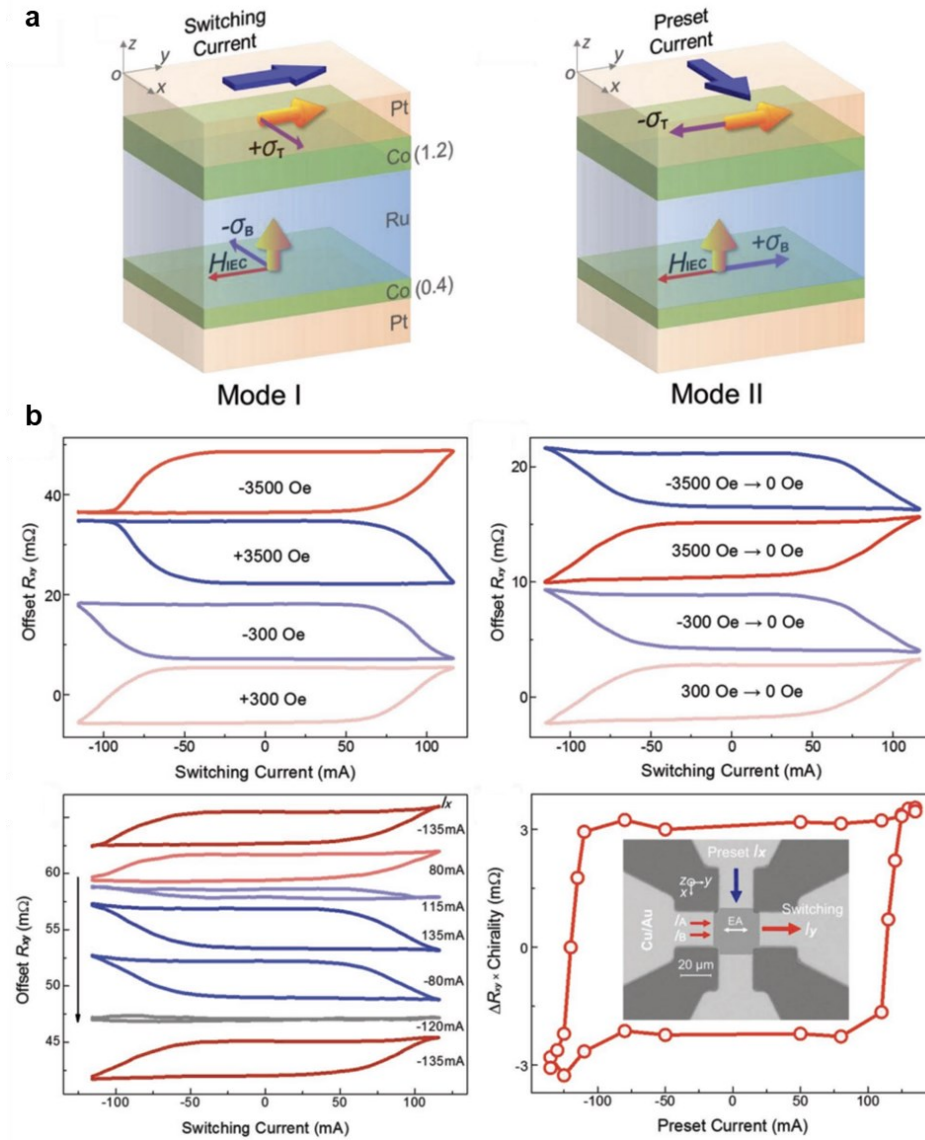


Figure 1-23 Polarity-changeable field-free perpendicular magnetization switching in a Type-T magnetic multilayer. (a) Two modes of the current-induced magnetization switching. (b) Polarity-tunable current-induced perpendicular magnetization switching [119].

In addition to the RKKY coupling, the Dzyaloshinskii-Moriya interaction (DMI) between magnetic moments plays a crucial role in breaking mirror symmetry and enabling field-free perpendicular magnetization switching [199,209,210]. In materials or interfaces with broken spatial inversion symmetry, neighboring spins have a tendency to be mutually orthogonal due to the presence of DMI [211–216]. This effect

can even give rise to the formation of topological structures such as skyrmions [217–219], which have been extensively studied for their potential applications in spin logic devices [220–222]. More recently, researchers have discovered that DMI can also exist between two ferromagnetic layers separated by an intermediate layer, known as interlayer Dzyaloshinskii-Moriya interaction (iDMI) [223–227]. This phenomenon has opened up new possibilities for designing chiral spintronic devices with unique functionalities and characteristics, offering new avenues for the development of advanced spintronic devices.

In 2022, He et al. demonstrated field-free perpendicular magnetization switching of in a ferromagnetic multilayer by harnessing iDMI [209]. The system depicted in Figure 1-24 consists of two perpendicular magnetic layers. The presence of iDMI introduces an additional energy term, $E_{DM} \equiv -\mathbf{D} \cdot (\mathbf{S}_T \times \mathbf{S}_B)$, where \mathbf{D} represents the amplitude of iDMI, and its direction is dictated by the specific multilayer structure.

By performing a mirror operation along the direction of \mathbf{D} , it is observed that the two states corresponding to magnetization pointing up and down exhibit distinct E_{DM} values, indicating a broken mirror symmetry. Consequently, field-free perpendicular magnetization switching can be achieved by applying an electric current along the direction of \mathbf{D} . This study highlights the significance of iDMI in enabling efficient and energy-saving manipulation of perpendicular magnetization in multilayer systems.

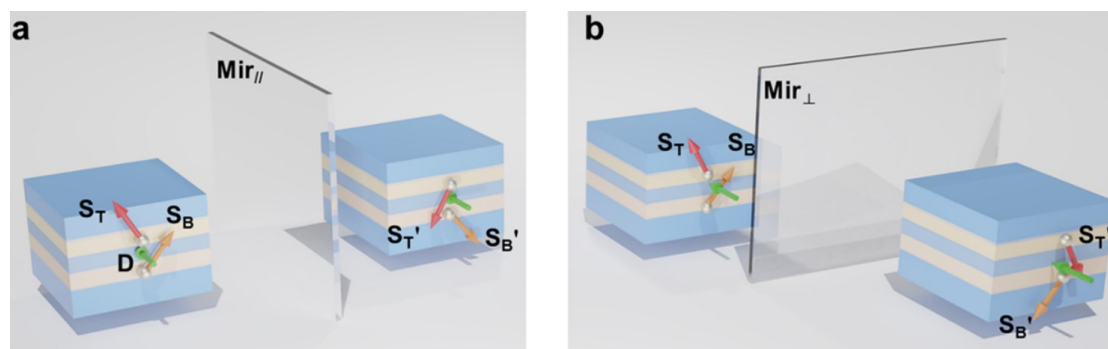


Figure 1-24 Field-free perpendicular magnetization switching with interlayer DMI. Schematics of scenarios when the mirror is parallel to the D vector and perpendicular to D is shown in (a) and (b), respectively. Notice that D is a polar vector. The DMI energy of the two states obtained by mirroring process are different in (a) while remains same in (b) [209].

Furthermore, extensive research has been conducted to enhance the performance of SOT-MRAMs, leading to the development of novel devices and mechanisms. Recent advancements include: (1) Simultaneous utilization of STT and SOT to achieve field-free perpendicular magnetization switching [228–231]. (2) Implementation of voltage-controlled magnetic anisotropy (VCMA) to reduce the critical current density [116,232,233]. (3) Simplification of device structures by utilizing SOT switching in a single layer of Tb-Co without heavy metals [234]. (4) Efficient field-free perpendicular magnetization switching in Fe_4N with unique magnetic structures [235,236]. (5) Suppression of field-like terms in SOTs by utilizing the Oersted field generated by currents to improve the efficiency of perpendicular magnetization switching [237]. (6) Manipulation of field-like torque through stress generated by piezoelectric materials [238]. (7) Realization of 16 basic logic operations in a single MTJ with non-symmetric shape [239]. (8) Creation of unclonable functions through the uncertainty introduced during annealing processes [240,241].

These advancements not only contribute to improving the performance and functionality of SOT-MRAM but also pave the way for the development of innovative spintronic devices with enhanced capabilities and novel functionalities.

In the industry, multiple technical approaches are being pursued simultaneously to achieve field-free switching in SOT-MTJ. These include: (1) Type-Y switching of in-plane SOT-MTJ: This approach offers a simple structure and inherent field-free switching but is associated with slower switching speeds [242–244]. (2) Type-Y/Type-X hybrid switching of in-plane SOT-MTJ: This approach enables field-free switching with relatively faster speeds [157,245]. (3) Field-free Type-Z switching of perpendicular SOT-MTJ: This approach offers the highest storage density and fastest switching speeds but requires additional design considerations to break mirror symmetry. As depicted in Figure 1-25, a thick in-plane layer is grown on top of the Type-Z perpendicular MTJ, and the stray field generated by the in-plane magnetization serves as the required in-plane field for switching [114,246,247]. Furthermore, Kong et al. have demonstrated field-free perpendicular magnetization switching by utilizing the interlayer coupling between in-plane and perpendicular magnetizations. This approach has shown promising results, achieving a TMR ratio of up to 50% [248].

These different approaches offer trade-offs in terms of device complexity, switching speed, and storage density. Continued research and development in these areas contribute to the advancement of SOT-MRAM technology, enabling the realization of efficient and high-performance spintronic devices for various applications.

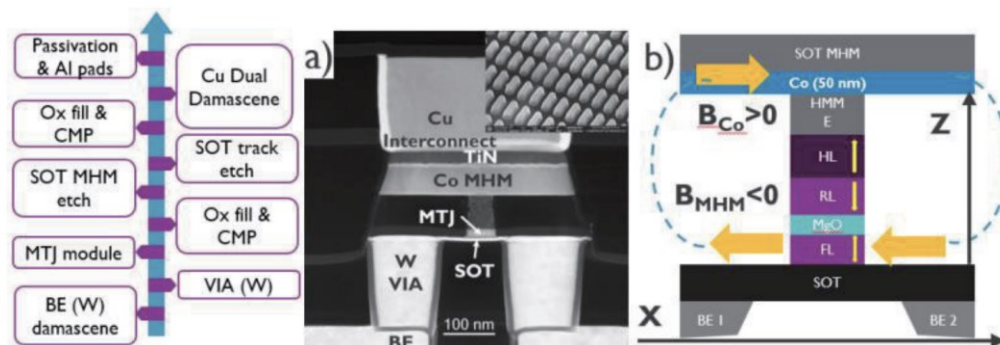


Figure 1-25 Field-free perpendicular magnetization switching with the stray field in the industry. (a) TEM image of the SOT-MTJ. (b) Schematic of SOT-MTJ stack with top-pinned design [246].

1.5 Spintronics devices in advanced computing

The development of spintronics has not only contributed to fundamental scientific understanding but has also led to the emergence of numerous practical devices [14]. For instance, the discovery of GMR and TMR has greatly advanced the development of hard disk drives and magnetic sensors, enabling higher storage capacities and improved sensing capabilities [249–251]. The maturation of electrical writing techniques, such as STT and SOT, has revolutionized the field of MRAM. STT-MRAM and SOT-MRAM have overcome the limitations of the Oersted field and offer faster operating speeds, making them highly promising for all memory hierarchy levels [252]. Additionally, these advancements have spurred research on spin nano-oscillators, including mutually coupled oscillator networks, which have potential applications in areas such as microwave communication and neuromorphic computing [253–260].

Furthermore, spintronics has found applications beyond traditional memory and computing devices. It has been successfully integrated into the construction of neural networks, opening up new possibilities for neuromorphic computing and artificial intelligence [261–263]. Spin logic circuits have also been explored, aiming to develop alternative computing architectures based on spintronic principles [264,265].

The continuous advancement of spintronics research not only expands our understanding of fundamental physics but also drives the development of practical devices and extends the boundaries of its applications, creating exciting possibilities at the intersection of spintronics with other scientific disciplines such as superconductivity [266–270] and optics [271,272].

In 2003, Ney et al. proposed a design for programmable spin logic devices based on a single MTJ [273]. As shown in Figure 1-26, the key idea is to control the

magnetization of two in-plane layers (\mathbf{M}_1 and \mathbf{M}_2) in the MTJ using input currents (I_A , I_B , and I_C). \mathbf{M}_1 and \mathbf{M}_2 have different coercivity fields, meaning they require different magnetic fields for switching. By defining the input current magnitudes, desired magnetization states can be achieved.

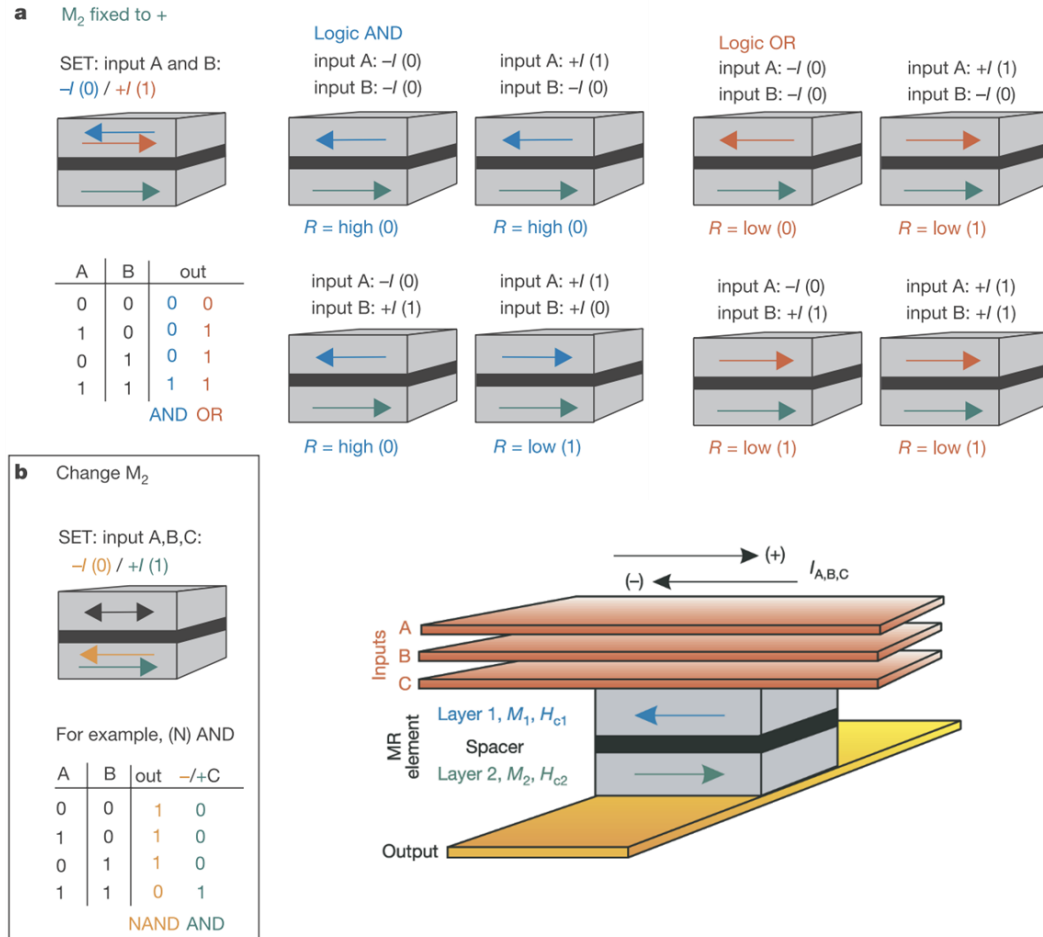


Figure 1-26 Programmable spin logic device based on single magnetic tunnel junction. Realization of the AND and OR gate. (b) Realization of the NAND and AND gate [273].

The input currents I_A and I_B alone should not generate sufficient Oersted field to switch \mathbf{M}_1 . Only when I_A and I_B are applied together, creating a combined field, will switch \mathbf{M}_1 but not \mathbf{M}_2 . Only when I_A , I_B , and I_C are all applied, \mathbf{M}_2 can be switched. The current flowing in the positive (negative) direction is defined as input 1 (0). The output is the TMR of MTJ, with low-resistance (high-resistance) state defined as 1 (0). The functionality is changeable by presetting the magnetic orientations. Before

performing logic operations, if the system is first preset to keep \mathbf{M}_1 towards the left and \mathbf{M}_2 to the right using I_A , I_B , and I_C . Thus, the input-output relationship of MTJ satisfies the AND logic. Similarly, when the system is preset to keep both \mathbf{M}_1 and \mathbf{M}_2 to the right (left), now the input-output relationship satisfies the OR (NAND) logic.

Hence, the pure electrical programmable logic gate is realized in a single MTJ. Future integration of STT or SOT techniques to switch the magnetization of the MTJ makes it more promising for device integration.

In 2019, Luo et al. utilized a selective oxidation process to create a sample with both an in-plane magnetic anisotropy region and a perpendicular magnetic anisotropy region. And based on this sample, the field-free perpendicular magnetization switching is achieved [274]. In 2020, with the same technic, Luo et al. further fabricated logic gates based on the SOT-induced domain-wall motion. Both a XOR gate and a full-adder gate are created by cascaded NAND gates [275]. As shown in Figure 1-27, Pt/Co/ AlO_x nanowires are used in the experiments, and the selective oxidation is performed to create in-plane magnetic anisotropy in the selected blue area, while perpendicular magnetic anisotropy remains in the other pink area. Due to the presence of DMI at the Pt/Co interface and the long length of the nanowire, magnetic domains are naturally formed to minimize the system's energy.

The SOT-induced domain-wall motion is as follow. First, an external magnetic field is applied to induce $+z$ domain on the left side of the nanowire, resulting in the formation of a domain wall between $+z$ and $-z$ domains. Then when a current is applied, the $+z$ domain keeps expanding while the $-z$ domain keeps contracting under SOT. Until the $+z$ domain reaching the in-plane region, which causes switching of in-plane magnetization, and forming a $-z$ domain on the other side. Thus, the perpendicular regions on either side of the in-plane region are always in opposite directions. This

process works as a NOT gate, by defining $+z$ and $-z$ magnetization as 0 and 1, respectively,

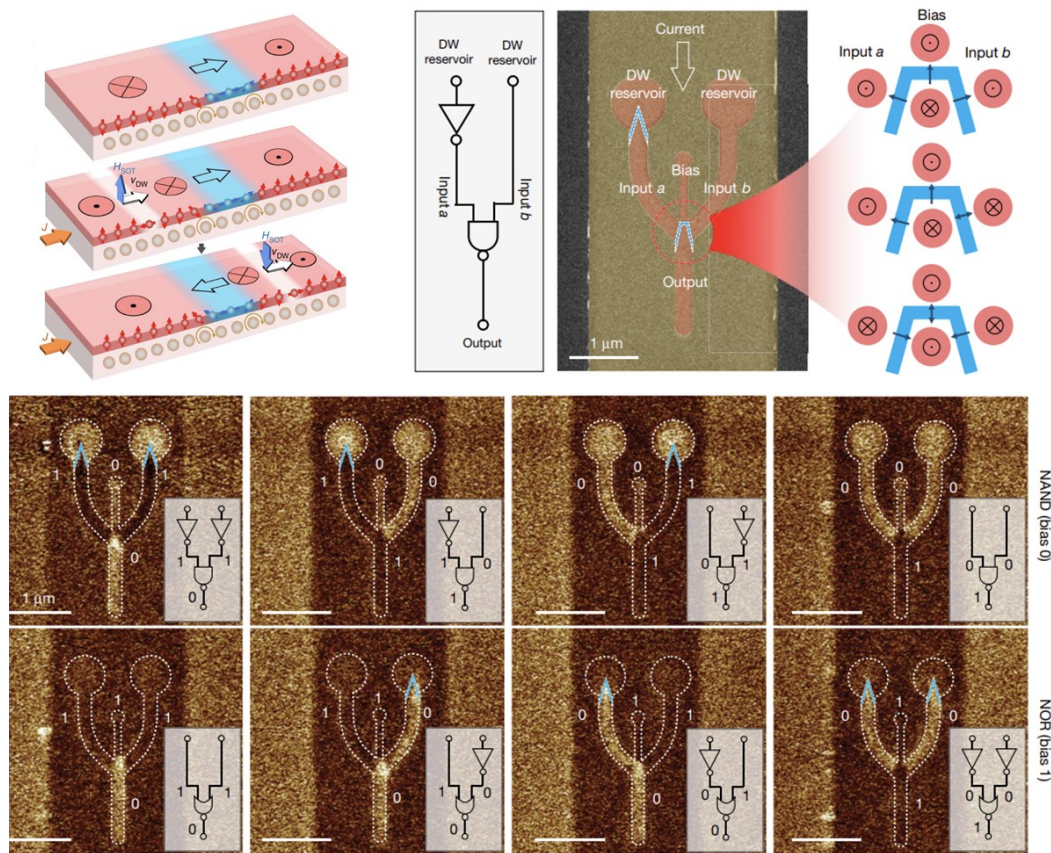


Figure 1-27 NAND gate and NOR gate based on the domain wall motion [275].

Furthermore, the cascading of these race-track-type domain-wall motion devices is convenient, allowing more complex functions to be realized by combining simple logic gates, as shown in Figure 1-27, where NOT gates are employed first to output the necessary 0 and 1 states, which are inputs for the succeeding NAND and NOR gates. In 2021, based on the same principle, Luo et al. proposed a design for a unidirectional domain-wall diode [276].

In recent years, the development of neural networks has solved increasingly difficult problems, encouraging for deeper researches. Neural networks are constructed by artificial synapses and artificial neurons. Artificial synapses connect the neurons and store connection weights, which are often real numbers with high precision and occupy

a large number of traditional binary storage units. Artificial neurons provide nonlinear output based on the input, and this task executed through traditional binary logic devices is also less efficient. Therefore, to achieve larger-scale and more efficient neural networks, the fabrication of non-volatile memristor and nonlinear logic devices as artificial synapses and neurons is a necessity. In this research area, resistive random-access memory [277–279] and spintronics devices [280–285] have both achieved considerable success.

In 2019, Kurenkov et al. fabricated a Hall bar device based on a Ta/Pt/PtMn/Pt/[Co/Ni]₂/Co/MgO/Ru multilayer. And in a single device, both artificial neuron and synapse functionalities in spiking neural networks (SNNs) are demonstrated through SOT-induced perpendicular magnetization switching [286]. As shown in Figure 1-28, when a pair of current pulses with equal amplitude, opposite directions and a time interval of $\Delta\tau$ are applied to the device, the perpendicular magnetization is switched by SOT. Notably, the switching amplitude ΔR is determined by $\Delta\tau$, which is consistent with the biological synaptic weight dependence on the signals receiving from two neurons. Hence, this device can function as an artificial synapse in SNNs. On the other hand, when a set of current pulses with equal amplitude and the same direction are applied to the device, the probability of perpendicular magnetization switching is determined by both the number and frequency of the pulses. Moreover, whether fix the number of pulses and change the frequency or vice versa, the dependence of the switching probability are always sigmoid-shaped, which is in consistent with the biological neuron excitation dependence on the strength of input pulses. Therefore, this device can also functions as an artificial neuron in SNNs.

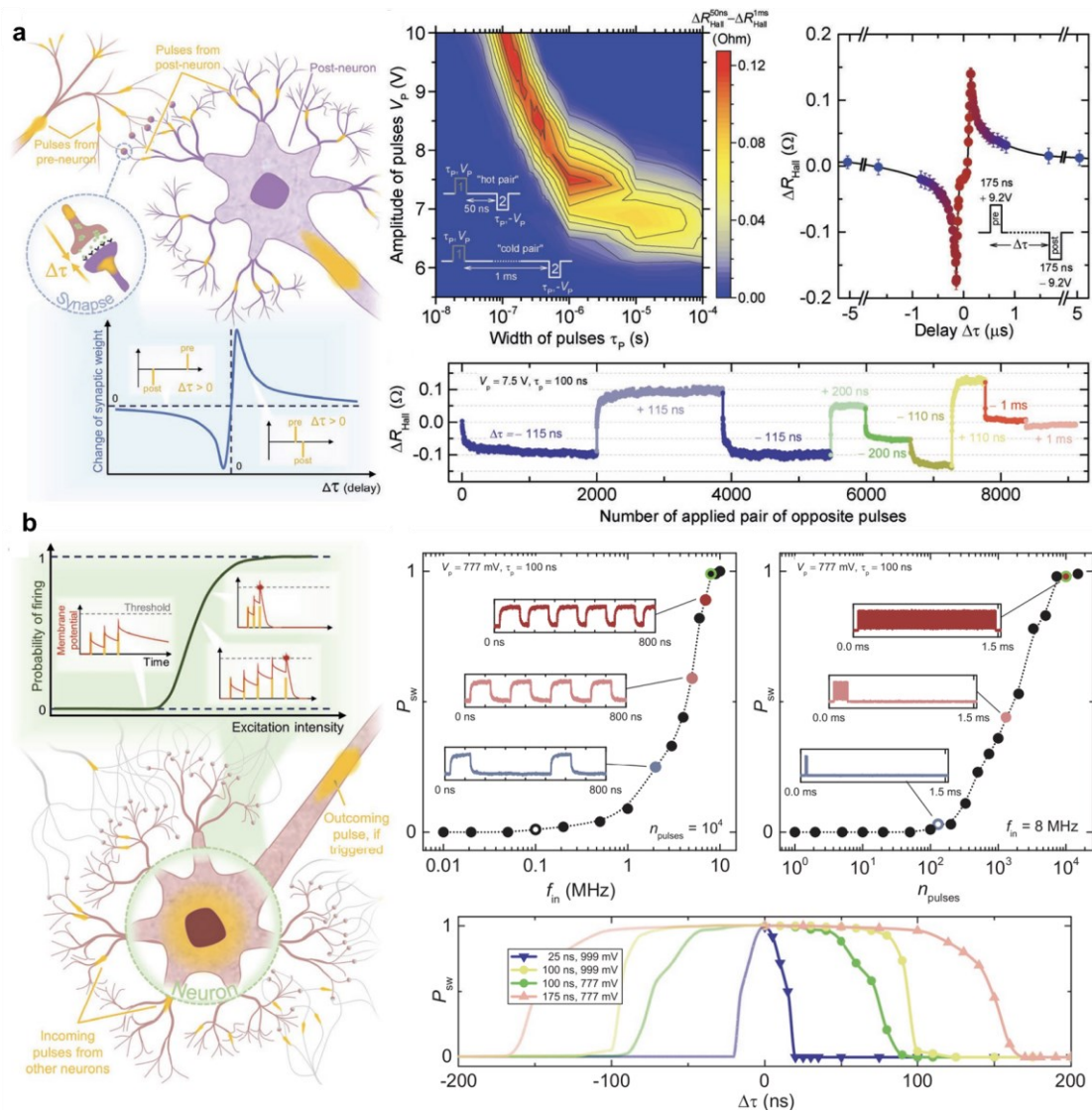


Figure 1-28 Construction of artificial neuron and artificial synapse in spiking neural networks. The principal and characterization of the artificial synapse and artificial neuron are shown in (a) and (b), respectively [286].

In addition to Hall-bar devices, spin nano-oscillators are also used as neural network devices and have been successfully applied in speech recognition. In 2017, Torrejon et al. fabricated a single spin nano-oscillator based on MTJ and achieved a 99.6% accuracy rate in spoken-digit recognition [287]. The average output voltage of the spin nano-oscillator is stable under the input current, but its response to the history of the input current is nonlinear, which is a necessary feature of neurons in the reservoir computing [287–289].

The process of spoken-digit recognition is shown in Figure 1-29. First, a spoken-digit audio file, for example, "1," is taken from the dataset and divided into N_τ small sections with a duration of τ . Each section is then filtered into N_f frequency channels, to obtain N_f amplitude-time functions. These functions are multiplied by a randomly generated binary $N_f \times N_\theta$ mask matrix, resulting in a single discrete and recombined amplitude-time function with N_θ points, which correspond to the number of neurons. Notice the duration of each point is θ , so that $\tau = N_\theta \theta$ is maintained. The voltage corresponding to each recombined function is the input of the spin nano-oscillator, resulting in N_θ envelope output voltages V for each section. Finally, the computer is employed to construct 10 sets of specific linear combination parameters $\omega_{i,\theta}$ of V , by which each section corresponding to 10 outputs. The 10 outputs of each section are then averaged, resulting in 10 outputs for each spoken-digit audio file, with only the correct output being 1 and the rest being 0. Here, i represents the 10 digits from 0 to 9. The memory-effect of spin nano-oscillator plays a crucial role in this network. Its output is not only nonlinear dependent on the applied currents, but also determined by the previous inputs. This process allows the transformation of the complex speech recognition problem a simple linear classification problem in a high-dimensional space. Without this process, it is impossible to realize speech recognition based on random 0/1 numbers which introduced in this recognition procedure. As shown in Figure 1-29, without the spin nano-oscillator leads to a 10% recognition rate. Based on this work, in 2019, Riou et al. introduced an additional delay feedback loop to the spin nano-oscillator, greatly enhancing its response to the input history and further improving its recognition rate [288].

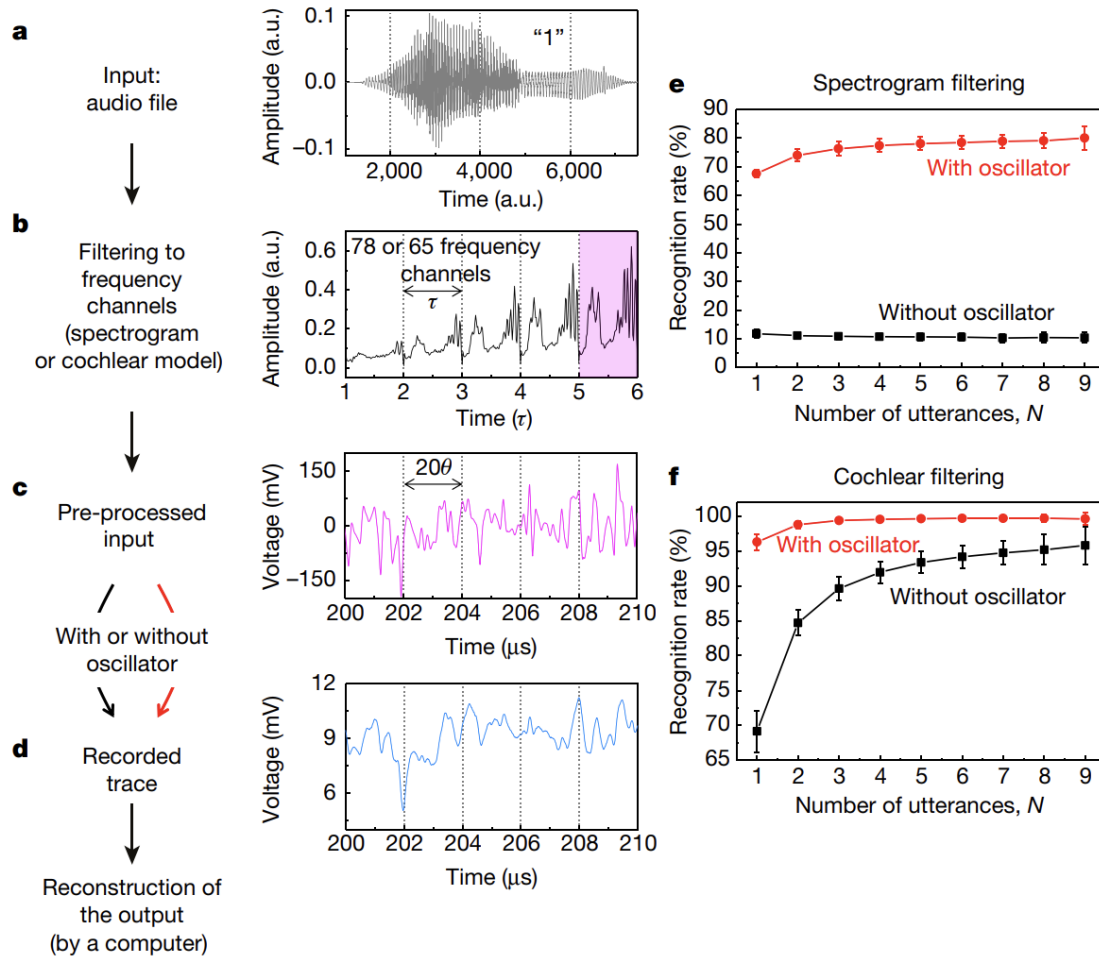


Figure 1-29 Principal and realization of spoken-digit recognition with single nanoscale spintronic oscillator. Step-by-step process and results of the recognition are shown in (a-d). Comparison of the recognition rate between cases with oscillator and without oscillator when in the spectrogram filtering and the cochlear filtering are shown in (e) and (f), respectively [287].

The oscillation frequency of a spin nano-oscillator is not only depended on the amplitude of the input current, but also modulated by the external oscillating magnetic field. This characteristic can also be utilized to construct networks for speech recognition. In 2018, Romera et al. realized vowel recognition by using a network consisting of four serially connected spin nano-oscillators [290], as shown in Figure 1-30. Firstly, vowel utterances are decomposed by frequency and linearly recombined. As a result, each vowel utterance is represented by a combination of two frequencies, which forms the input of the network. The network itself comprises four serially

connected spin nano-oscillators (labeled 1, 2, 3 and 4), with each of the output current of one oscillator is fed as input to the next one, and also has independent circuit to control their oscillation frequency. Additional circuits are placed above the four oscillators, which generate two oscillating magnetic fields (labeled A and B) of various frequencies. When the oscillation frequency of one oscillator is close to that of one magnetic field, its frequency is modulated to synchronize with the field. As a result, the system can achieve various resonance states, for instance, oscillator 1 synchronize with magnetic field A, oscillator 2 synchronize with magnetic field A, or oscillator 1 synchronize with magnetic field A while oscillator 2 synchronize with magnetic field B simultaneously. By continuously adjusting input currents, the resonance states of the system can be tuned till and each vowel corresponds to a specific resonance state, thereby achieving vowel recognition. Experiments show that stronger mutual coupling between the spin nano-oscillators leads to wider resonance locking range and higher recognition rate. Comparing to traditional neural networks, the construction of spin nano-oscillator network is structurally simpler, and the number of parameters that needs for optimizing is greatly reduced, owing to the complex dynamical behavior of the spin nano-oscillators themselves.

In the development of MRAMs, achieving long-term data retention, necessitates the stability of MTJ to remain its state, such that there exists a sufficiently high energy barrier between the two states to prevent unexpected magnetization switching induced by thermal disturbance. On the other hand, if the energy barrier is lowered sufficiently, the MTJ will rapidly switch between the parallel and antiparallel states under thermal disturbance, and the probability of being in each state can be modulated by applying an external STT or VCMA, allowing the random MTJ to be used as a probabilistic-bit (p-bit). Building upon this concept, probability computing has been proposed as a potential

avenue for further advancements.

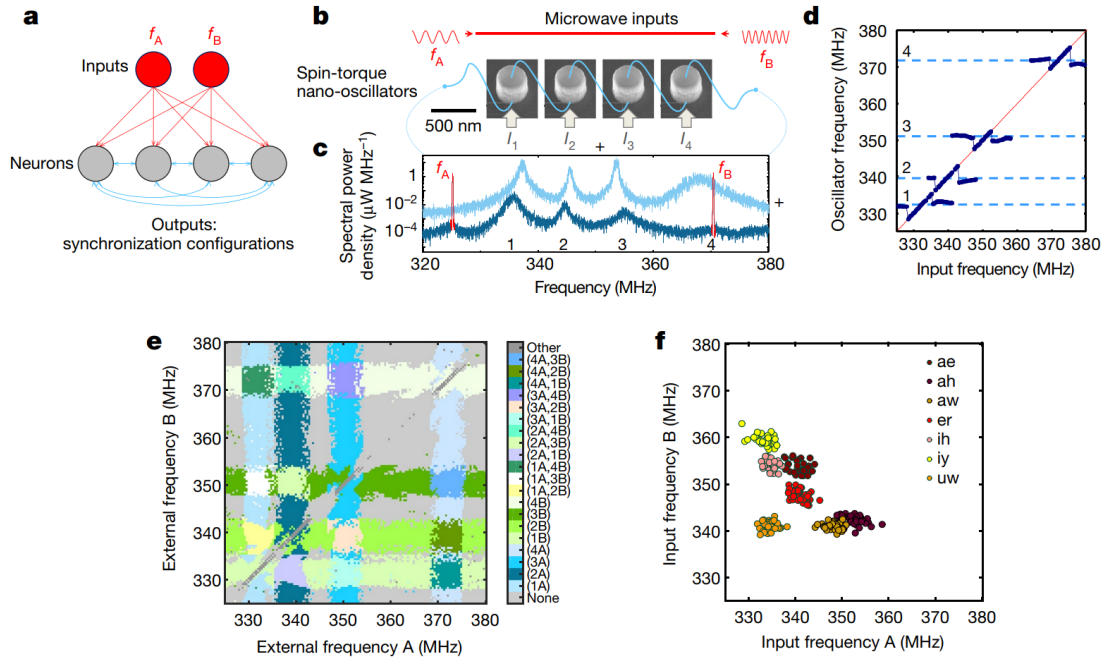


Figure 1-30 Principal and realization of vowel recognition based on a spintronic-oscillator network. (a) Schematic of the network structure. (b-c) Measurement setup and results. (d) Input frequency dependence of the oscillator frequency. (e) Combination of the frequency A and B. (f) Convention from the utterance to the input frequency A and B [290].

In 2019, Borders et al. used stochastic MTJs to construct eight p-bits and formed a network to implement integer factorization. This vividly demonstrated the superiority of probability computing in solving complex problems and realization of reverse logic [262]. As shown in Figure 1-31, the principle of integer factorization is as follows: First, a cost function $E = (A \cdot B - F)^2$ is constructed, where A and B are the two factors to be obtained and F is the number to be factorized. When E is minimized, the product of A and B is equal to F . Then, given the initial A_0 and B_0 , the initial E_0 is obtained. To reduce E , a new $A' = A_0 - \eta \partial E / \partial A$ and a new $B' = B_0 - \eta \partial E / \partial B$ are set, where η is the learning rate which can be adjusted according to conditions.

It should be noted that in experiments, the p-bits are binary, so the decimal numbers need to be expanded in binary to obtain the practical update conditions. Here, the number to be factorized is 35, so each factor requires four p-bits to be expanded.

Because the energy barrier is so low in these p-bits, they traverse the 0/1 states continuously, which is equivalent to randomly selecting all the numbers between 0-15. The probability of a p-bit being in the 1 state increases with the increase of the external voltage, so by applying a voltage to the p-bit as the aforementioned update condition, the probability of the p-bit being in the 1 state can be updated, leading to the system naturally evolve toward the direction of energy reduction, eventually stabilizing in the state of minimum energy, i.e., $A \cdot B = F$, achieving factorization.

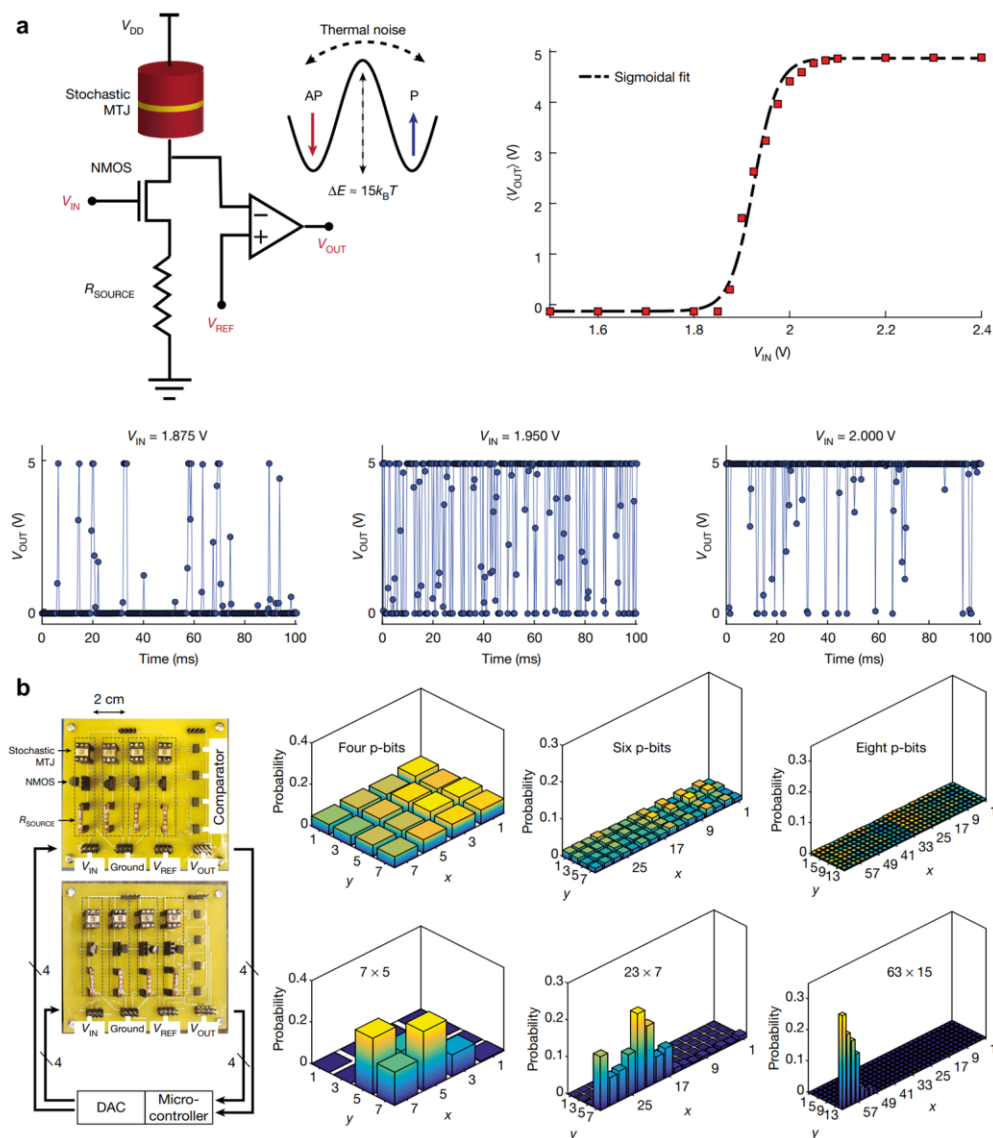


Figure 1-31 Principal and realization of integer factorization based on stochastic computing. (a) Construction and characterization of the unit p-bit. (b) Building of the stochastic circuit and the realization of the integer factorization [262].

This design cleverly set the conditions of system evolution, achieved complex logic functionality without the need for complex external circuits, laying the foundation for future probability computing. It should be noted that the speed of system evolution depends on the speed of stochastic MTJ switching between the parallel and antiparallel states. To achieve faster computation, the energy barrier of the MTJ needs to be further reduced to increase its switching speed. In the same year, Cai et al. constructed artificial neurons based on p-bits to and used VCMA to update the probability, successfully achieved handwritten digit recognition by construction such artificial neural network [280]. These works demonstrate the broad application prospects of MTJ-based p-bits in future advanced computing schemes [291].

1.6 Structure of this dissertation

This dissertation primarily explores two closely related fields in spintronics: SOT effect and TMR effect. By utilizing SOT, the magnetization direction of the free layer in MTJ can be electrically controlled, while TMR effect enable the electrical detection of the relative orientation of the free layer's magnetization. By combining SOT with TMR effect, the core unit of next generation of MRAM is constructed. In order to develop high-speed and high-density perpendicular SOT-MRAM, an additional in-plane ferromagnetic layer is introduced to assist field-free perpendicular magnetization switching. Additionally, it has been discovered that the spin current generated by the in-plane ferromagnetic layer can drive the perpendicular magnetization switching itself, providing a foundation for developing low-cost, heavy-metal free spintronics devices. However, the clarification of spin currents origin in the ferromagnetic layer is still needed, which lay the groundwork for improving SOT efficiency and developing novel spin logic devices.

This dissertation first investigates the mechanism of spin current generation in the ferromagnetic material NiFe, achieving perpendicular magnetization switching driven by both SHE and AHE torques in NiFe. The AHE-generated spin current, which is polarized parallel to the magnetization direction, significantly increases the degrees of freedom in SOTs, providing a basis for developing efficient spintronics devices without heavy metals. Subsequently, the dissertation continues to study the perpendicular magnetization switching in Type-T magnetic multilayers with both an in-plane magnetic layer and a perpendicular magnetic layer, where the presence of the in-plane layer breaks the mirror symmetry of the system, resulting in field-free perpendicular magnetization switching. Moreover, due to the coupling between the in-plane and perpendicular layers, the perpendicular layer experiences an additional perpendicular effective field provided by the in-plane layer when a current is passed through it, thereby reducing the critical current density required for magnetization switching and further improving the switching efficiency. Next, the TMR effect in epitaxial Fe/MgAlO_x/Fe₄N MTJs is investigated, revealing that the TMR ratio can be continuously tuned from negative to positive by applying an external bias voltage. This phenomenon is attributed to the band structure of Fe₄N. These variable TMR MTJs lay the foundation for the development of novel spin logic devices. Finally, the resonant oscillation in epitaxial Fe/MgAlO_x/Fe/MgAlO_x/Fe quantum well MTJ with Co insertion is investigated. It becomes clear that the oscillation amplitude is heavily influenced by the structural and chemical disorder at the interface within the QW. This finding remains us extra consideration must be taken during the material optimization to fabricate quantum well MTJs with both high TMR ratio and high oscillation amplitude.

This dissertation consists of three main sections: the research background, fabrication and characterization methods, and experimental results and discussions.

Chapter 1 introduces the historical background of spintronics, methods for electrically driving perpendicular magnetization switching, and their applications in novel spin logic devices. Chapter 2 describes the experimental instruments, fabrication techniques, and characterization methods employed in this dissertation, including magnetron sputtering, molecular beam epitaxy, ultraviolet exposure, argon ion etching, and others. Chapter 3 demonstrates the achievement of field-free magnetization switching in the Type-T magnetic multilayers by utilizing the AHE effect in the in-plane magnetic layer. Chapter 4 explores the efficient SOT-induced field-free perpendicular magnetization switching in another Type-T magnetic multilayers, utilizing the tilting of in-plane magnetization under SOT and its coupling with the perpendicular magnetization. Chapter 5 discusses the rare sign-changeable TMR effects observed in Fe₄N MTJs grown by molecular beam epitaxy. Chapter 6 discusses the influence of Co insertion on the oscillation amplitude in epitaxial Fe/MgAlO_x/Fe/MgAlO_x/Fe quantum well MTJs. Finally, Chapter 7 summarizes all the work presented in the dissertation and provides an outlook for future research.

2 Methods

The primary research focuses of this dissertation encompass magnetization switching propelled by SOT in Hall-bar devices and TMR effects in MTJs, all employing magnetic multilayers as the material systems. This chapter serves as an introduction to the experimental instruments and methodologies employed for the growth, fabrication, and measurement of the magnetic multilayers investigated in this study.

2.1 Growth techniques of magnetic multilayers

2.1.1 Magnetron sputtering

Magnetron sputtering is a widely employed technique in industry for large-scale fabrication of thin films due to its notable advantages, including rapid growth rate and high film quality. The underlying principle of magnetron sputtering is illustrated in Figure 2-1. Initially, a noble gas, such as Argon (Ar), is introduced into a vacuum chamber, while a high voltage is applied between the substrate and the target material, leading to the generation of plasma near the target region. The bombardment of ions facilitates the ejection of target atoms, which subsequently deposit onto the substrate, forming a thin layer. Simultaneously, the presence of magnetic fields confines secondary electrons to the target surface. These secondary electrons, in turn, undergo collisions with the noble gas, generating additional ions. This cascade of electron-ion interactions enhances the plasma density, reduces the required gas pressure and voltage for sustaining the plasma, and ultimately improves the sputtering efficiency [292,293].

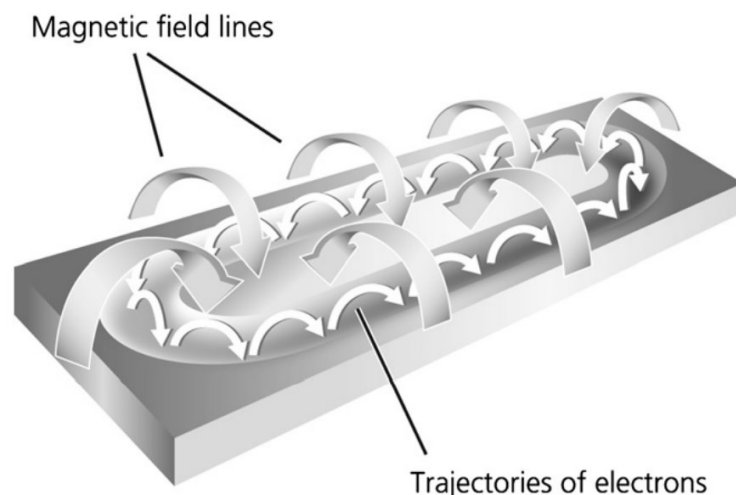


Figure 2-1 Principle of magnetron sputtering [292].

In the case of depositing metal materials, it suffices to apply a DC voltage between the substrate and the target. The positive charges accumulated on the target surface due to ion bombardment naturally dissipate, thereby not significantly impacting the sputtering process. However, when depositing insulating materials, positive charges tend to accumulate on the surface of the insulating target, hindering the continuous bombardment of ions and diminishing the sputtering rate. To address this challenge, an AC voltage is employed between the substrate and the target. Consequently, when a positive voltage is applied, ions effectively bombard the target material, leading to the ejection of target atoms onto the substrate. Conversely, when the voltage becomes negative, electrons impinge upon the target, neutralizing the accumulated positive charges on the target surface and facilitating the continuation of the sputtering process.

In this study, three magnetron sputtering systems were utilized for the growth of magnetic multilayers. Two ULVAC sputtering systems (MPS-4000-HC7 and MB06-9305) were employed at the State Key Laboratory of Magnetism, Institute of Physics, Chinese Academy of Sciences (IOP, CAS), China, as depicted in Figure 2-2. Additionally, a Kenosistec KS400HR sputtering system was utilized at the Micro and Nanotechnologies Competence Center (CC Minalor) of the Institute Jean Lamour,

Centre national de la recherche scientifique (CNRS-IJL), France.

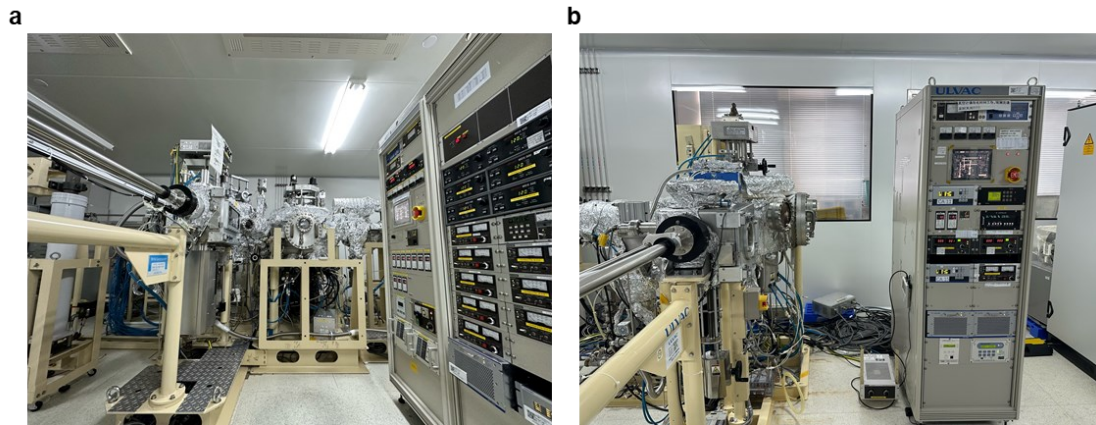


Figure 2-2 Magnetron sputtering equipment. (a) ULVAC MPS-4000-HC7. (b) ULVAC MB06-9305.

The MPS-4000-HC7 system operates at a base pressure below 10^{-6} Pa and features multiple target positions specifically designed for the growth of magnetic multilayers. Notably, it incorporates a permanent magnet capable of generating a magnetic field of 300 Oe during the deposition process, thereby inducing in-plane magnetic anisotropy.

On the other hand, the MB06-9305 system operates at a base pressure of approximately 5×10^{-6} Pa and is primarily employed for the growth of insulating layers and metal electrodes.

2.1.2 Molecular beam epitaxy

Molecular beam epitaxy (MBE) is a well-established technique extensively employed in research laboratories for the fabrication of ultrahigh-quality thin films. Essentially, MBE comprises a comprehensive system that integrates ultra-high vacuum thermal evaporation, electron beam evaporation, *in-situ* annealing, and reflection high-energy electron diffraction (RHEED). Both thermal evaporation and electron beam evaporation in MBE operate at extremely low energies and beam currents, facilitating

the deposition of atomically precise layers onto the substrate in a layer-by-layer growth mode. This precise control ensures the high quality of the deposited thin films. Following the growth process, RHEED is utilized as a direct means to observe the surface roughness of the sample. Additionally, *in-situ* annealing can be performed when necessary to further enhance the crystal quality of the deposited films. By iteratively executing these steps, it is possible to obtain multilayer samples characterized by exceptional quality and uniformity.

The setup, principles, and results of the RHEED measurement are illustrated in Figure 2-3. High-energy electron beams, ranging from 10 to 100 keV, are calibrated using coils and directed towards the surface of the sample, causing a pattern to form on the fluorescent screen. This measurement process can be performed without removing the sample from the high-vacuum chamber, making it compatible with MBE systems.

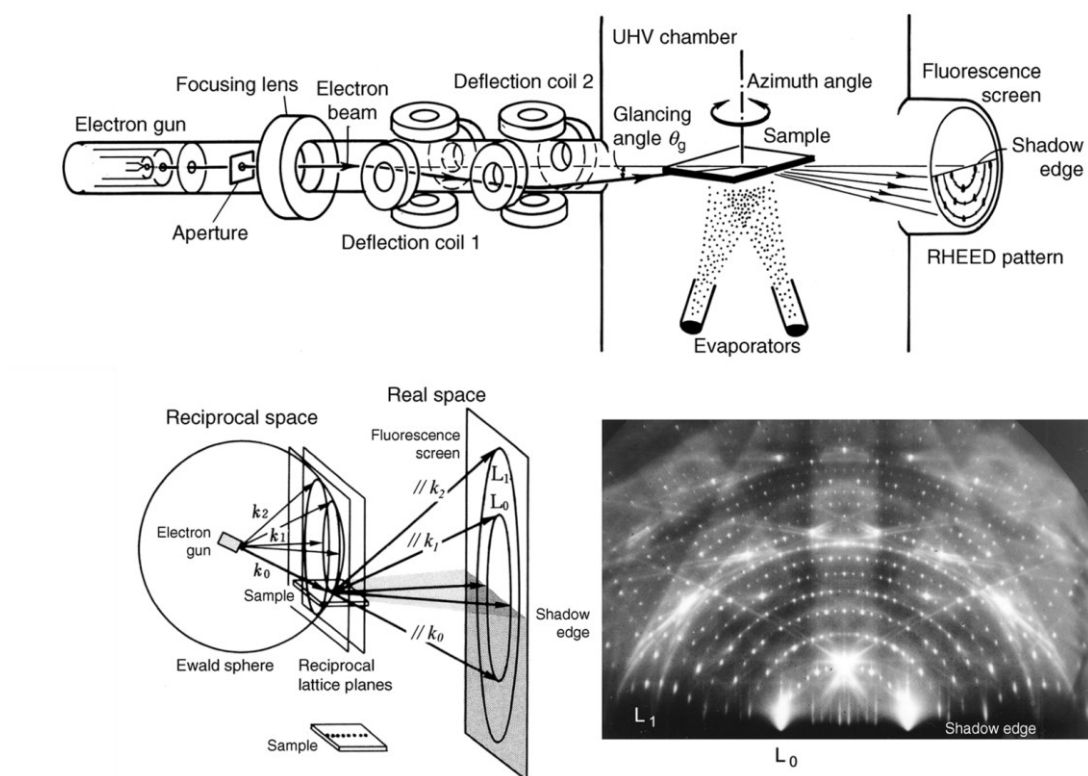


Figure 2-3 Measurement setup and principles of RHEED [294].

In a single crystal sample, the atoms are arranged in a periodic manner. Electron

diffraction within the lattice follows the Laue equation, $\Delta\mathbf{k} = \mathbf{G}$, where \mathbf{G} represents the reciprocal lattice vector and \mathbf{k} denotes the wave vector of the electron. Consequently, by visualizing a sphere centered around the electron gun with k as the radius, the sphere intersects a series of lattice planes (for a one-dimensional atomic chain) or a series of rods (for a two-dimensional atomic lattice) in the reciprocal space of the crystal. These intersection points satisfy the Laue condition and generate diffraction patterns. This construction method is known as the Ewald construction. The morphology of the diffraction pattern provides insights into the quality of the sample. For further detailed discussions on this topic, it is recommended to refer to the works of Hasegawa [294] and Kittel [295].

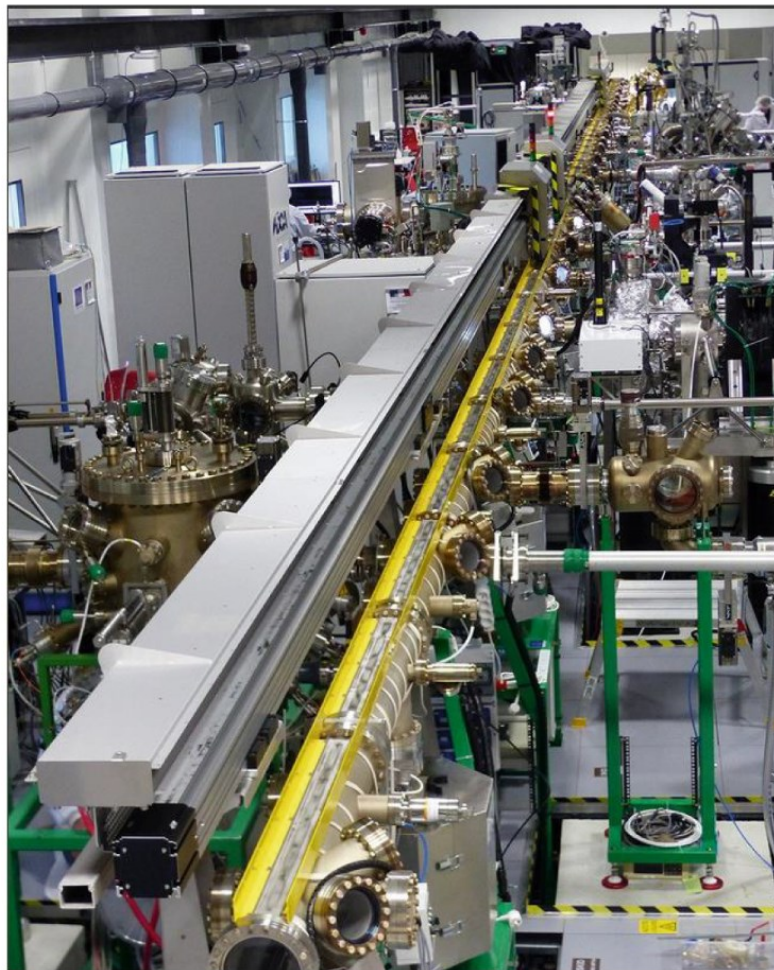


Figure 2-4 Ultra-high vacuum transfer tunnel at Institut Jean Lamour, Université de Lorraine-France [14].

The MBE system utilized in this research is located at the CNRS-IJL Deposits and Analysis under Ultra-high Vacuum of Nanomaterials Competence Center (CC D.A.U.M.). The MBE system operates at a base pressure of 10^{-8} Pa, and further pressure reduction can be achieved by injecting liquid nitrogen into the chamber walls. The chamber is equipped with several metal and oxide targets, enabling the epitaxial growth of high-quality MTJ. Moreover, the introduction of nitrogen gas into the chamber facilitates the growth of metal nitrides, such as Fe_4N . As depicted in Figure 2-4, this MBE system is interconnected with other growth and characterization equipment via a vacuum tube spanning a length of 70 meters.

2.2 Fabrication of magnetic devices

After the growth of magnetic multilayers, additional processing steps are frequently required to fabricate micro- or nano-sized devices for subsequent electrical transport measurements. These steps encompass ultraviolet (UV) lithography, argon-ion etching, photoresist removal, and the deposition of electrode or insulation layers. Each step will be systematically introduced in the subsequent sections, and a comprehensive processing flow for a MTJ will be presented at the conclusion.

2.2.1 Ultraviolet lithography

UV lithography is a crucial process employed to transfer micro-scale patterns from a mask to a photoresist, utilizing UV light. The photoresist, an organic material, can be categorized into positive and negative types based on its reaction to UV light. Positive photoresists exhibit a photochemical reaction upon exposure to UV light, causing the exposed areas to dissolve in the developer during the developing phase. Conversely, negative photoresists undergo a cross-linking reaction upon UV exposure, rendering the exposed areas less soluble in the developer.

The mask, comprising a transparent quartz plate partially coated with opaque chromium, plays a pivotal role during exposure. Positioned between the sample and the UV light source, it determines the irradiation area of the photoresist on the sample surface by virtue of the chromium coverage. Subsequent to exposure, development, and fixation, the pattern present on the mask is transferred to the photoresist. It is noteworthy that a clean mask and uniform coverage of the photoresist on the sample surface are vital factors for achieving optimal exposure outcomes.

The UV lithography systems employed in this study consist of the G-25 contact-type UV lithography equipment, manufactured by Chengdu Xinnanguang Mechanical Equipment Co., Ltd., located in IOP, CAS (Figure 2-5), and the Suss MicroTec MJB4 Mask Aligner for Optical Lithography, situated in CC Minalor, IJL. The G-25 system utilizes a mercury lamp as its UV source, emitting light at a wavelength of 365 nm. Notably, the minimal achievable exposure line width using this system is approximately 2 μm .

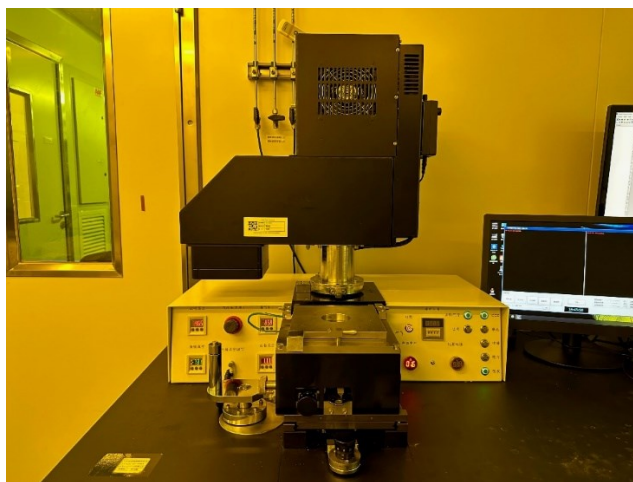


Figure 2-5 UV exposure equipment.

2.2.2 Argon-ion etching

Following UV lithography, the transferred patterns on the photoresist need to be further transferred onto the sample through an etching process. Etching processes can

be broadly categorized as physical or chemical etching. Physical etching exhibits a lower etching rate, limited element selectivity, but superior verticality in pattern transfer. On the other hand, chemical etching demonstrates a faster reaction rate, high element selectivity, but inferior verticality. Therefore, in the fabrication of Hall-bar devices and MTJs, physical etching, specifically argon-ion etching, is the preferred and commonly employed method.

The principle underlying argon-ion etching closely resembles that of magnetron sputtering, as both methods employ argon ions to bombard the material. In argon-ion etching, the sample is subjected to a stream of accelerated argon ions, resulting in the removal of the exposed regions while preserving the parts protected by the photoresist.

Care must be taken to avoid excessive etching duration, as prolonged exposure can lead to carbonization of the photoresist due to overheating. Carbonized photoresist poses challenges during the subsequent removal process. Furthermore, during the etching process, some of the etched atoms may redeposit onto the sample surface, potentially causing short circuits between the magnetic layers on either side of the insulating layer in MTJ fabrication. Therefore, it is crucial to prevent such occurrences.

To mitigate the risk of redeposition and address the potential short circuit issue, it is common practice to tilt the sample normal with respect to the ion beam at the end of the etching process. This tilting aids in the cleanup of the sidewalls of the junction pillar, minimizing the likelihood of unwanted secondary deposition in MTJ fabrication.

The equipment employed in this study comprises an argon-ion etching machine in IOP, CAS, manufactured by Beijing Advanced Company (Figure 2-6), and an IBE 4Wave Ion Beam Etching Equipment, supplemented by a Hidden Secondary Ion Mass Spectrometer system in CC Minalor, IJL. The argon-ion etching machine from Beijing Advanced Company operates at a base pressure of 4×10^{-4} Pa and a working pressure

of 2×10^{-2} Pa. To prevent carbonization of the photoresist, the substrate of this machine is equipped with a cooling water system. Additionally, the substrate can rotate at a specific speed to ensure uniform etching across the sample. The IBE 4Wave etching system features a secondary electron spectrometer, enabling real-time monitoring of the etching progress. This capability greatly facilitates the fabrication of MTJs, ensuring precise control and optimization of the etching process.



Figure 2-6 Ion etching equipment.

2.2.3 Photoresist removal and lift-off

After the etching process, the remaining photoresist on the sample surface necessitates removal. One approach is to immerse the sample in a sequence of acetone, alcohol, and deionized water for ultrasonic cleaning, followed by drying with nitrogen gas. However, in cases where an insulator (e.g., SiO_2) or metal is present on the residual photoresist during the lift-off process, it becomes essential to eliminate the attached insulator or metal while removing the photoresist.

Lifting off metal is relatively straightforward and can be achieved by prolonging the soaking and ultrasonic time in acetone. On the other hand, lifting off insulator is more challenging. To address this, a method provided by CC Minalor, IJL involving several steps can be employed. Initially, the sample is soaked in Remover 1165 at 80°C

for 30 minutes. Subsequently, it undergoes ultrasonic cleaning, followed by rinsing with deionized water and drying with nitrogen gas. The successful lift-off of the insulator is contingent upon the quality of the coated photoresist. With a well-established notch of bilayer resist, the insulator lift-off can generally be accomplished successfully.

2.2.4 MTJ processing flow

MTJ serves as fundamental components within MRAM. Its fabrication entails multiple intricate steps, encompassing the definition of bottom electrodes, junction region delineation, and top electrode definition. Due to the considerable length and complexity of this process, we present a comprehensive account of the fabrication procedure employed in the case of MTJ at CC Minalor, IJL, serving as an illustrative example.

2.2.4.1 Define bottom electrodes

- (1) Clean the sample and spin coat it with positive photoresist S1813 by a spin coater.
- (2) Place the sample on a hot plate and bake it.
- (3) Expose the sample to UV light with an UV lithography system.
- (4) Develop the sample in MF319 developer solution with agitation.
- (5) Rinse the sample in deionized water with agitation and dry it with nitrogen gas.
- (6) Etch the sample with an argon-ion etching machine. At the same time record the variation of secondary electron elements, especially Mg, with time for the next etching process which define the junction region.
- (7) Immerse and ultrasonicate the sample in acetone, rinse it with alcohol, and dry it with nitrogen gas.

2.2.4.2 Define junction regions

- (1) Clean the sample and spin coat it with LOR3A positive photoresist by a spin coater.
- (2) Place the sample on a hot plate and bake it.
- (3) Spin coat the sample again with S1813 positive photoresist with a spin coater.
- (4) Place the sample on a hot plate and bake it again.
- (5) Expose the sample to UV light with an UV lithography system.
- (6) Develop the sample in MF319 developer solution with agitation.
- (7) Rinse the sample in deionized water with agitation and dry it with nitrogen gas.
- (8) Inspect the sample under a microscope to confirm the presence of obvious steps formed by two layers of photoresist.
- (9) Etch the sample with an argon-ion etching machine until reaching the middle of the barrier.
- (10) Deposit SiO_2 on the sample by magnetron sputtering.
- (11) Immerse the sample in Remover 1165 at 80°C for 30 minutes, ultrasonicate and rinse it with deionized water, and dry it with nitrogen gas.
- (12) Inspect the sample under a microscope to confirm the presence of clean and complete junction regions.

2.2.4.3 Define the top electrode

- (1) Clean the sample and spin coat it with S1813 positive photoresist by a spin coater.
- (2) Place the sample on a hot plate and bake it.
- (3) Expose the sample to UV light with an UV lithography system.
- (4) Develop the sample in MF319 developer solution with agitation.

- (5) Rinse the sample in deionized water with agitation and dry it with nitrogen gas.
- (6) Deposit Ta/Pt electrodes on the sample by magnetron sputtering.
- (7) Immerse and ultrasonicate the sample in acetone, rinse it with alcohol, and dry it with nitrogen gas.
- (8) Inspect the sample under a microscope to confirm the presence of clean and complete MTJs.

2.3 Characterization of magnetic and electrical properties.

In spintronics research, our focus lies in studying the magnetic properties of magnetic multilayers, including magnetic anisotropy, coercivity, and exchange bias. Additionally, we investigate their magneto-transport properties under the influence of electric fields, such as SHE, AHE, and TMR effects. In this segment, we will present the measurement instruments and characterization techniques commonly employed in these investigations.

2.3.1 Vibrating sample magnetometry

In 1995, Foner invented the vibrating sample magnetometer (VSM) as a crucial tool for quantifying the magnetic moment of thin films under varying magnetic fields [296]. Figure 2-7 illustrates its mechanical setup, wherein a non-magnetic rod holds the sample positioned between two electromagnets. During measurement, the magnetic field is incrementally scanned between the electromagnets while the rod vibrates along the z -axis. Consequently, the sample's stray field vibrates synchronously, inducing a corresponding change in the sensed magnetic flux by the stationary measuring coils. The resultant flux alteration generates an electrical current that can be isolated through lock-in amplifiers, effectively measuring the sample's magnetization

in response to the evolving magnetic fields. This technique enables the determination of magnetic anisotropy, coercivity, and exchange bias parameters, which are of particular interest in the study.

In this dissertation, the primary instrument employed is the EZ VSM manufactured by MicroSense, located at IOP, CAS. The EZ VSM offers a magnetic field range of ± 2.2 T and exhibits a measurement accuracy of 10^{-6} emu.

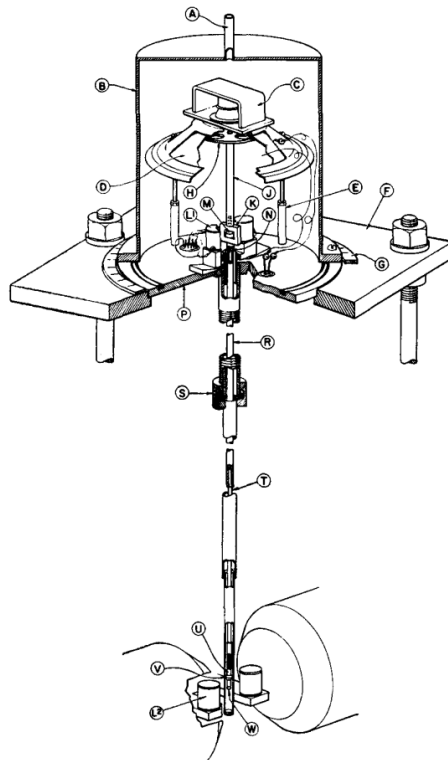


Figure 2-7 Detailed mechanical design of vibrating sample magnetometry [296].

2.3.2 Physical property measurement system

The Physical Property Measurement System (PPMS), an experimental platform developed by Quantum Design, offers a high-magnetic-field and low-temperature measurement environment. It is designed with superconducting coils to generate the magnetic field, while the superconducting state is maintained through the use of liquid helium, which is also used for sample cooling. The sample, positioned on a sample rod, is connected to external instruments to facilitate electrical measurements. In our study,

we primarily utilize the PPMS located at IOP, CAS. This particular PPMS model features a maximum magnetic field capability of ± 9 T, ensuring a magnetic field accuracy of 2 Oe. It enables temperature-dependent measurements within the range of 1.9 K to 400 K. Notably, the system includes an automated sample rotation mechanism, allowing for precise angle measurements.

2.3.3 Three-dimensional magnetic field probe station

Figure 2-8 depicts the three-dimensional magnetic field probe station, developed by Beijing East Changing Company and located at IOP, CAS. This station comprises three mutually orthogonal Helmholtz coils, each capable of independently carrying current and generating a magnetic field. Notably, these coils lack an iron core, resulting in the production of a precise yet relatively small magnetic field. Positioned at the center of the coils, the sample stage and probes are connected to external instruments. By placing the sample on the stage and pressing it with a probe, the electrical transport properties of the sample under varying magnetic fields can be observed. The probe station offers a maximum magnetic field strength of 340 Oe, with an accuracy of 5×10^{-3} Oe.

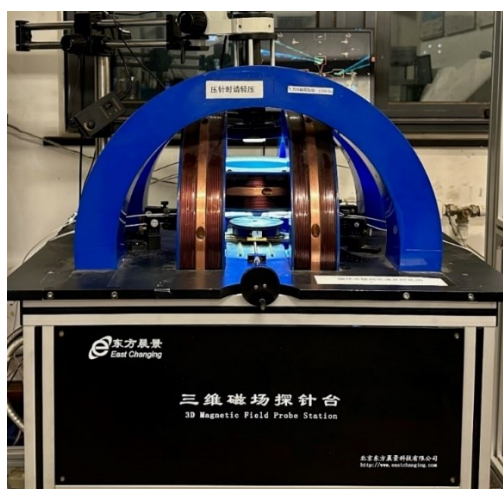


Figure 2-8 Three-dimensional magnetic field probe station.

3 Field-free perpendicular magnetization switching induced by AHE torque in NiFe

3.1 Research background

SOT represents a promising technique for achieving rapid magnetization switching with minimal power consumption. It has gained significant traction in the advancement of MRAM and spin logic devices. In conventional heavy metal/ferromagnet bilayers, the SOT phenomenon arises from the SHE, wherein the spin current's direction, polarization, and the electrical current's direction are mutually orthogonal. Consequently, upon establishing the device structure, the spin polarization direction becomes inherently predetermined.

In recent theoretical research by Amin et al. [297], it was proposed that spin currents could be induced in ferromagnetic metals. Figure 3-1 illustrates the presence of spin currents originating from both SHE and AHE. The SHE-induced spin current exhibits a polarization direction orthogonal to both the spin current direction and the electric field direction, which is similar to heavy metal scenario. In contrast, the AHE-induced spin current exhibit a polarization direction parallel to the magnetization. Notably, the polarization of the AHE-induced spin current can be easily controlled due to the adjustable magnetization in ferromagnets, rendering it a convenient parameter to manipulate.

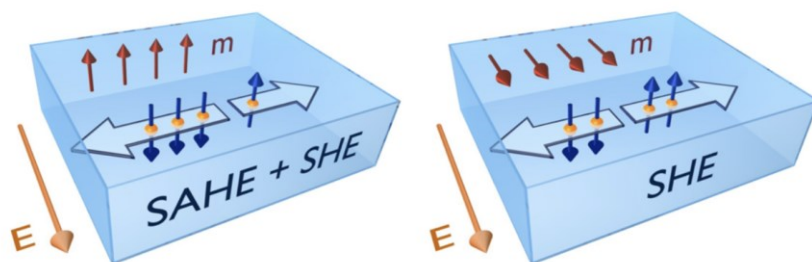


Figure 3-1 Spin currents generated in ferromagnets. Both SHE and AHE contribute to the generation of spin currents when the electric field is perpendicular to the magnetization (Left). Meanwhile, only SHE contributes to the generation of spin current when the electric field is parallel with the magnetization (Right) [297].

Experimental evidence has corroborated the generation of spin currents through both SHE and AHE in ferromagnetic materials, leading to successful magnetization switching. Wu et al. [172] demonstrated this phenomenon by utilizing the SHE-induced spin current in in-plane CoFeB, resulting in perpendicular CoFeB magnetization switching, as depicted in Figure 3-2. Similarly, Seki et al. [173] employed AHE-generated SOT in FePt to achieve in-plane NiFe magnetization switching. However, further investigations are still necessary to elucidate the interplay between AHE-generated SOT and SHE-generated SOT in ferromagnets, particularly in the context of achieving efficient perpendicular magnetization switching.

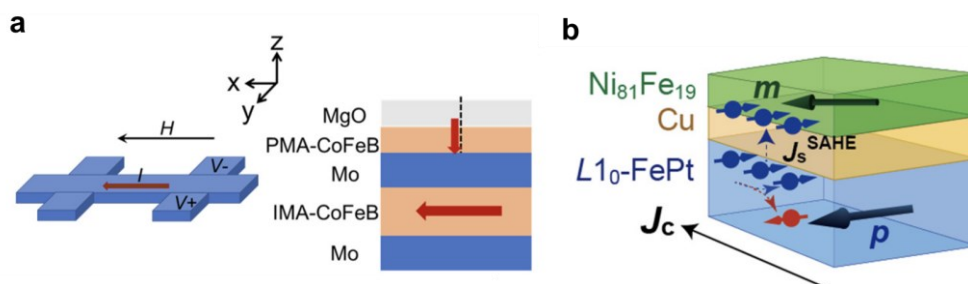


Figure 3-2 Magnetization switching through spin currents generated in magnetic layers. (a) The current is parallel with in-plane CoFeB magnetization. SHE-induced spin current drives perpendicular CoFeB magnetization switching when the current passes through the in-plane layer. (b) The current is perpendicular to in-plane FePt magnetization. AHE-induced spin current drives in-plane NiFe magnetization switching when the current passes through the in-plane layer [172,173].

This chapter presents a novel experimental approach utilizing an in-plane NiFe/Ru/perpendicular ferromagnetic trilayer structure with a carefully designed geometric configuration, and successfully demonstrates the generation of both SHE- and AHE-induced SOTs in NiFe. In this configuration, the current flows parallel to the pinned NiFe magnetization, while the applied magnetic field is transverse to it. The experimental results highlight that NiFe can simultaneously produce SHE- and AHE-SOTs, with the AHE torque exhibiting significant strength, thereby dominating the SOT switching process and leading to a reversal in the switching polarity. This investigation serves as a crucial stepping stone for advancing SOT devices, eliminating the reliance on heavy metals. The primary findings of this chapter have been published in Physical Review B [298].

3.2 Experimental and simulate methods

3.2.1 Fabrication and measurement of samples

Type-T magnetic multilayers comprising both in-plane and perpendicular layers are fabricated using magnetron sputtering (ULVAC MPS-4000-HC7). The film structure of the main sample is $\text{SiO}_2||\text{Ta}(2)/\text{IrMn}(8)/\text{NiFe}(3)/\text{Ru}(2)/\text{Pt}(1)/\text{Co}(1)/\text{Pt}(1)$ (nm). In its as-grown state, the film exhibited an in-plane easy axis along the y -direction. To induce perpendicular magnetic anisotropy, Co is inserted between two Pt layers during the deposition process. As a control sample, a $\text{SiO}_2||\text{Ru}(2)/\text{Pt}(1)/\text{Co}(1)/\text{Pt}(1)$ (nm) film is grown. The magnetic anisotropy of the samples is characterized using a VSM. Subsequently, the samples are patterned into cross-shaped Hall-bar devices with dimensions of 20 μm width and 200 μm length using standard UV lithography and argon-ion etching techniques. Pt(5)/Au(80 nm) electrodes are employed to connect the terminals of the Hall-bar devices. Electrical measurements are carried out with a

Keithley 2400 as the current source and a Keithley 2182 as the Hall voltage detector. To provide the magnetic field during testing, a PPMS and a three-dimensional magnetic field probe station are utilized. All measurements are performed at room temperature.

3.2.2 Construction and analyses of the macrospin model

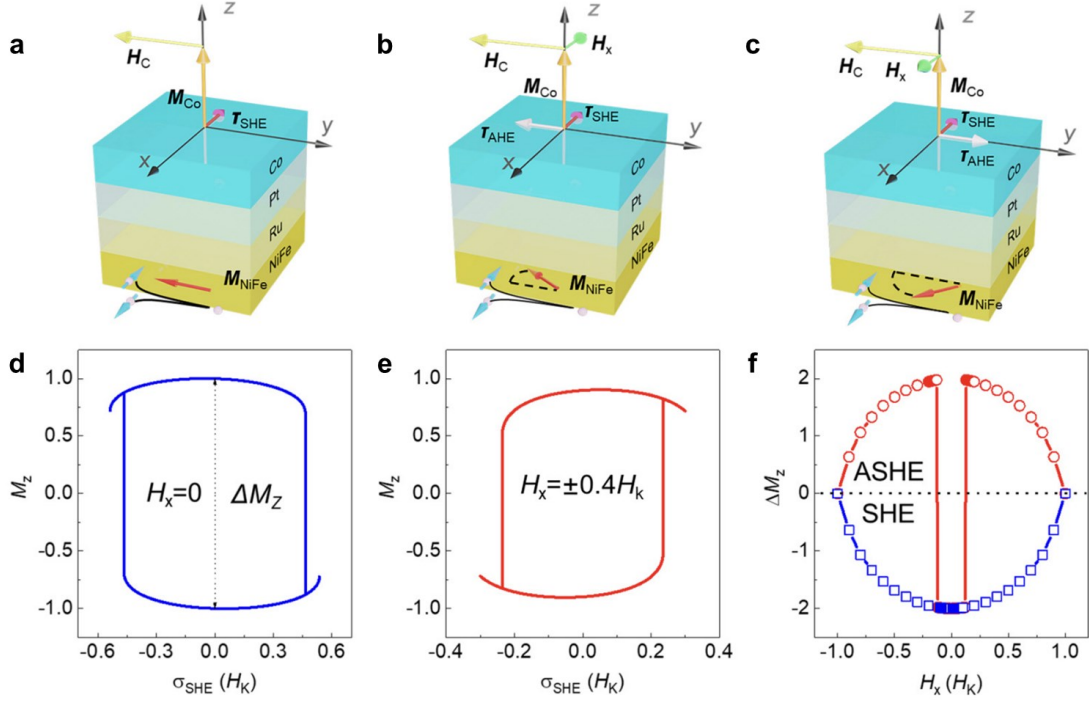


Figure 3-3 Perpendicular magnetization switching induced by SOTs generated in a ferromagnet. Schematics of the system without a magnetic field, with a $-x$ directional field, and with a $+x$ directional field are shown in (a-c), respectively. (d-e) Calculations of the macrospin model simulating these three situations. (f) Magnetic field dependence of the perpendicular magnetization switching polarity [298].

To elucidate the contrasting impact of SHE and AHE on magnetization switching, a macrospin model is employed in our simulation [299]. Figure 3-3 illustrates the influences of SHE torque and AHE torque on perpendicular magnetization switching, supposing a current \mathbf{J}_c flows along the y axis. In the absence of external magnetic fields, the magnetization of \mathbf{m}_{NiFe} is pinned in the y direction, specifically at $\varphi_{NiFe} = 270^\circ$, due to the presence of the exchange bias field \mathbf{H}_{EB} . Here, θ and φ denote the polar and azimuth angles, respectively. The coupling field \mathbf{H}_C

between NiFe and Co, as well as the current \mathbf{J}_c , also in the y direction. Within the SHE mechanism, a spin current $\boldsymbol{\sigma}_{\text{SHE}}$ is generated with polarization along the x direction. Notably, since \mathbf{m}_{NiFe} is parallel to \mathbf{J}_c , the AHE mechanism does not produce a spin current in this specific case. For convenience, the direction of $\boldsymbol{\sigma}$ represents the polarization of the spin current, and its magnitude is proportional to the density of the spin current. Both $\boldsymbol{\sigma}$ and \mathbf{H} are expressed in normalized units. Given our interest in the perpendicular magnetization switching of Co above the NiFe layer, only the spin current flowing along the z -direction is taken into consideration. When the system reaches stability, the torque arising from the effective field \mathbf{H}_{eff} counterbalances the SOT induced by SHE, resulting in

$$\mathbf{m}_{\text{Co}} \times \mathbf{H}_{\text{eff}} + \mathbf{m}_{\text{Co}} \times \boldsymbol{\sigma}_{\text{SHE}} \times \mathbf{m}_{\text{Co}} = 0. \quad (3-1)$$

Here, \mathbf{H}_{eff} is determined by the perpendicular magnetic anisotropy energy E_K , the coupling field \mathbf{H}_C , and the externally magnetic field \mathbf{H}_x (if present). The Type-Z switching indicates that when \mathbf{m}_{Co} , $\boldsymbol{\sigma}_{\text{SHE}}$ and \mathbf{H}_C are mutually orthogonal, the perpendicular \mathbf{m}_{Co} can be switched [191]. By setting $H_x = 0$, the torque balance equation can be simplified to

$$H_K \sin \theta \cos \theta + H_C \cos \theta - \sigma_{\text{SHE}} = 0, \quad (3-2)$$

which bears resemblance to the equation presented in [101]. The left-hand side terms of the equation represent the torques induced by the anisotropy field \mathbf{H}_K , the coupling field \mathbf{H}_C , and the SHE torque, respectively. In particular, $H_K = 2E_K/M_S$, where M_S is the saturated magnetization of Co. Through calculations, we obtain the SOT-induced magnetization switching, as shown in Figure 3-3(d)

When \mathbf{H}_x is applied, \mathbf{m}_{NiFe} deviates from the y direction, i.e., $\varphi_{\text{NiFe}} \neq 270^\circ$. Thus, $\mathbf{m}_{\text{NiFe}} \times \mathbf{J}_c \neq 0$, and the AHE mechanism induces a spin current $\boldsymbol{\sigma}_{\text{AHE}}$ whose polarization is parallel to \mathbf{m}_{NiFe} . Therefore, the torque balance equation becomes

$$\mathbf{m}_{\text{Co}} \times \mathbf{H}_{\text{eff}} + \mathbf{m}_{\text{Co}} \times \boldsymbol{\sigma}_{\text{SHE}} \times \mathbf{m}_{\text{Co}} + \mathbf{m}_{\text{Co}} \times \boldsymbol{\sigma}_{\text{AHE}} \times \mathbf{m}_{\text{Co}} = 0. \quad (3-3)$$

After simplification and rearrangement, it can be written as

$$H_K \sin \theta \cos \theta - \sin \varphi (H_C \sin \varphi_{\text{NiFe}} \cos \theta + \sigma_{\text{SHE}} + \sigma_{\text{AHE}} \cos^2 \varphi_{\text{NiFe}}) - \cos \varphi [(H_x + H_C \cos \varphi_{\text{NiFe}}) \cos \theta - \sigma_{\text{AHE}} \cos \varphi_{\text{NiFe}} \sin \varphi_{\text{NiFe}}] = 0, \quad (3-4a)$$

$$\sin \varphi [-(H_x + H_C \cos \varphi_{\text{NiFe}}) + \sigma_{\text{AHE}} \cos \varphi_{\text{NiFe}} \sin \varphi_{\text{NiFe}} \cos \theta] + \cos \varphi [H_C \sin \varphi_{\text{NiFe}} + (\sigma_{\text{SHE}} + \sigma_{\text{AHE}} \cos^2 \varphi_{\text{NiFe}}) \cos \theta] = 0. \quad (3-4b)$$

Notably, if $H_x = 0$ and $\varphi_{\text{NiFe}} = 270^\circ$, the AHE effect becomes negligible, leading to $\sigma_{\text{AHE}} = 0$. In this case, the torque balance equation restricts \mathbf{m}_{Co} to the yz plane, i.e., $\varphi = 90^\circ$. Consequently, Equation 3-4 simplifies to Equation 3-2.

When $H_C \ll |H_x| \ll H_{\text{EB}}$, $\cos \varphi_{\text{NiFe}} \approx H_x/H_{\text{EB}}$, and $\sin \varphi_{\text{NiFe}} \approx -1$.

Therefore, Equation 3-4 can be further simplified as:

$$H_K \sin \theta \cos \theta + \sin \varphi (H_C \cos \theta - \sigma_{\text{SHE}}) - \cos \varphi (H_x \cos \theta + \sigma_{\text{AHE}} H_x/H_{\text{EB}}) = 0. \quad (3-5)$$

The impact of the AHE torque on the switching process becomes evident. The second and third terms of Equation 3-5 depict the influence of the SHE and AHE torque, respectively. Figure 3-3(b,c) demonstrates that when $H_x \ll H_{\text{EB}}$, $\boldsymbol{\sigma}_{\text{AHE}}$ is parallel to \mathbf{m}_{NiFe} . Similar to the orthogonality among \mathbf{m}_{Co} , $\boldsymbol{\sigma}_{\text{SHE}}$, and \mathbf{H}_C , \mathbf{m}_{Co} , $\boldsymbol{\sigma}_{\text{AHE}}$, and \mathbf{H}_x are also exhibit mutual orthogonality. According to the Type-Z switching scheme, now the AHE torque also capable to switch the perpendicular \mathbf{m}_{Co} .

By solving Equation 3-4, we obtain the hystereses depicted in Figure 3-3(e) in which, according to the literature [167], we assume that the efficiency of generating AHE spin current is consistent with that of generating SHE spin current, i.e., $\sigma_{\text{AHE}}/J_C = \sigma_{\text{SHE}}/J_C$. Our findings reveal two significant observations. First, the introduction of the AHE torque alters the switching polarity from clockwise (CW, -1) to counterclockwise (CCW, +1) when \mathbf{H}_x is large enough. Second, the switching

polarity remains consistent under $\pm \mathbf{H}_x$. Comparing Figure 3-3(b,c), it becomes evident that changing the sign of \mathbf{H}_x corresponds to a change in the sign of $\mathbf{m}_{\text{NiFe}} \times \mathbf{J}_C$, consequently leading to a sign change of σ_{AHE} . Type-Z switching scheme tells us, simultaneously changing the signs of both σ_{AHE} and \mathbf{H}_x will yields the same final magnetization state. Figure 3-3(f) summarizes the ΔM_z under different \mathbf{H}_x , where the sign of ΔM_z indicates the switching polarity. In the absence of AHE torque, the switching polarity remains negative under all \mathbf{H}_x . These two distinct characteristics serve as a benchmark for experimentally verifying the presence of the AHE torque.

Detailed derivation from Equation 3-3 to Equation 3-4 is as follows. Starting from Equation 3-3, the effective field \mathbf{H}_{eff} experienced by the perpendicular Co magnetization is obtained by:

$$E_{\text{Co}} = K \sin^2 \theta - \mathbf{H}_x \cdot \mathbf{m} - C(\mathbf{m} \cdot \mathbf{m}_{\text{NiFe}}). \quad (3-6)$$

Here, $\mathbf{m} = \sin \theta \cos \varphi \mathbf{x} + \sin \theta \sin \varphi \mathbf{y} + \cos \theta \mathbf{z}$ represents the unit vector of perpendicular Co magnetization. And $\mathbf{m}_{\text{NiFe}} = \cos \varphi_{\text{NiFe}} \mathbf{x} + \sin \varphi_{\text{NiFe}} \mathbf{y}$ denotes the unit vector of in-plane NiFe magnetization. C represents the coupling strength between these two magnetizations. Hence,

$$E_{\text{Co}} = K \sin^2 \theta - H_x \sin \theta \cos \varphi - C(\sin \theta \cos \varphi \cos \varphi_{\text{NiFe}} + \sin \theta \sin \varphi \sin \varphi_{\text{NiFe}}). \quad (3-7)$$

While $\mathbf{H}_{\text{eff}} = H_\theta \boldsymbol{\theta} + H_\varphi \boldsymbol{\varphi}$, therefore,

$$H_\theta = -\frac{\partial E_{\text{Co}}}{\partial \theta} = -2K \sin \theta \cos \theta + H_x \cos \theta \cos \varphi + C(\cos \theta \cos \varphi \cos \varphi_{\text{NiFe}} + \cos \theta \sin \varphi \sin \varphi_{\text{NiFe}}). \quad (3-8)$$

We define $H_K = 2K$ and $H_C = C$. Hence,

$$H_\theta = -H_K \sin \theta \cos \theta + (H_x + H_C \cos \varphi_{\text{NiFe}}) \cos \theta \cos \varphi + H_C \sin \varphi_{\text{NiFe}} \cos \theta \sin \varphi. \quad (3-9)$$

Meanwhile,

$$H_\varphi = -\frac{\partial E_{\text{Co}}}{\sin \theta \partial \varphi} = -(H_x + H_C \cos \varphi_{\text{NiFe}}) \sin \varphi + H_C \sin \varphi_{\text{NiFe}} \cos \varphi. \quad (3-10)$$

Next, $\boldsymbol{\sigma} = \boldsymbol{\sigma}_{\text{SHE}} + \boldsymbol{\sigma}_{\text{AHE}}$, and

$$\boldsymbol{\sigma}_{\text{SHE}} = \sigma_{\text{SHE}} \mathbf{x}, \quad (3-11)$$

$$\begin{aligned} \boldsymbol{\sigma}_{\text{AHE}} &= \sin\left(\frac{\pi}{4} - (2\pi - \varphi_{\text{NiFe}})\right) \sigma_{\text{AHE}} \mathbf{m}_{\text{NiFe}} = \cos \varphi_{\text{NiFe}} \sigma_{\text{AHE}} \mathbf{m}_{\text{NiFe}} = \\ &\sigma_{\text{AHE}} \cos^2 \varphi_{\text{NiFe}} \mathbf{x} + \sigma_{\text{AHE}} \cos \varphi_{\text{NiFe}} \sin \varphi_{\text{NiFe}} \mathbf{y}, \end{aligned} \quad (3-12)$$

$$\boldsymbol{\sigma} = \sigma_x \mathbf{x} + \sigma_y \mathbf{y} =$$

$$(\sigma_{\text{SHE}} + \sigma_{\text{AHE}} \cos^2 \varphi_{\text{NiFe}}) \mathbf{x} + \sigma_{\text{AHE}} \cos \varphi_{\text{NiFe}} \sin \varphi_{\text{NiFe}} \mathbf{y}. \quad (3-13)$$

Since the field-like torque is neglectable in the Pt/Co system, the LLGS equation is:

$$\frac{\partial \mathbf{m}}{\partial t} = -\gamma \mathbf{m} \times \mathbf{H}_{\text{eff}} + \alpha \mathbf{m} \times \frac{\partial \mathbf{m}}{\partial t} + \mathbf{m} \times \boldsymbol{\sigma} \times \mathbf{m}. \quad (3-14)$$

Each term is given by:

$$\begin{aligned} \mathbf{m} \times \boldsymbol{\sigma} &= \begin{vmatrix} i & j & k \\ \sin \theta \cos \varphi & \sin \theta \sin \varphi & \cos \theta \\ \sigma_x & \sigma_y & 0 \end{vmatrix} = \\ &\begin{bmatrix} -\cos \theta \sigma_y \\ \cos \theta \sigma_x \\ \sin \theta \cos \varphi \sigma_y - \sin \theta \sin \varphi \sigma_x \end{bmatrix}, \end{aligned} \quad (3-15)$$

$$\begin{aligned} \mathbf{m} \times \boldsymbol{\sigma} \times \mathbf{m} &= \begin{vmatrix} i & j & k \\ -\cos \theta \sigma_y & \cos \theta \sigma_x & \sin \theta \cos \varphi \sigma_y - \sin \theta \sin \varphi \sigma_x \\ \sin \theta \cos \varphi & \sin \theta \sin \varphi & \cos \theta \end{vmatrix} = \\ &\begin{bmatrix} (\cos^2 \theta + \sin^2 \theta \sin^2 \varphi) \sigma_x - \sin^2 \theta \sin \varphi \cos \varphi \sigma_y \\ -\sin^2 \theta \sin \varphi \cos \varphi \sigma_x + (\cos^2 \theta + \sin^2 \theta \cos^2 \varphi) \sigma_y \\ -\sin \theta \cos \varphi \cos \theta \sigma_x - \cos \theta \sin \theta \sin \varphi \sigma_y \end{bmatrix}, \end{aligned} \quad (3-16)$$

$$\mathbf{m} \times \mathbf{H}_{\text{eff}} = \begin{vmatrix} i & j & k \\ \sin \theta \cos \varphi & \sin \theta \sin \varphi & \cos \theta \\ H_\theta \cos \theta \cos \varphi - H_\varphi \sin \varphi & H_\theta \cos \theta \sin \varphi + H_\varphi \cos \varphi & -H_\theta \sin \theta \end{vmatrix} =$$

$$\begin{bmatrix} -H_\theta \sin \varphi - H_\varphi \cos \varphi \cos \theta \\ H_\theta \cos \varphi - H_\varphi \sin \varphi \cos \theta \\ H_\varphi \sin \theta \end{bmatrix}. \quad (3-17)$$

When the equilibrium position is arrived, $\partial \mathbf{m} / \partial t = 0$. Therefore,

$$0 = -\gamma \mathbf{m} \times \mathbf{H}_{\text{eff}} + \mathbf{m} \times \boldsymbol{\sigma} \times \mathbf{m}, \quad (3-18)$$

$$0 = -\gamma \begin{bmatrix} -H_\theta \sin \varphi - H_\varphi \cos \varphi \cos \theta \\ H_\theta \cos \varphi - H_\varphi \sin \varphi \cos \theta \\ H_\varphi \sin \theta \end{bmatrix} + \begin{bmatrix} (\cos^2 \theta + \sin^2 \theta \sin^2 \varphi) \sigma_x - \sin^2 \theta \sin \varphi \cos \varphi \sigma_y \\ -\sin^2 \theta \sin \varphi \cos \varphi \sigma_x + (\cos^2 \theta + \sin^2 \theta \cos^2 \varphi) \sigma_y \\ -\sin \theta \cos \varphi \cos \theta \sigma_x - \cos \theta \sin \theta \sin \varphi \sigma_y \end{bmatrix}. \quad (3-19)$$

To solve the relationship between θ , φ and σ . We focus on the third equation in Equation set 3-19 first:

$$-\gamma H_\varphi \sin \theta - \sin \theta \cos \varphi \cos \theta \sigma_x - \cos \theta \sin \theta \sin \varphi \sigma_y = 0. \quad (3-20)$$

Therefore,

$$h_\varphi \equiv \gamma H_\varphi = -\cos \varphi \cos \theta \sigma_x - \cos \theta \sin \varphi \sigma_y. \quad (3-21)$$

Substituting it into the first equation of Equation set 3-19,

$$\begin{aligned} \gamma H_\theta \sin \varphi + (-\cos \varphi \cos \theta \sigma_x - \cos \theta \sin \varphi \sigma_y) \cos \varphi \cos \theta + \\ (\cos^2 \theta + \sin^2 \theta \sin^2 \varphi) \sigma_x - \sin^2 \theta \sin \varphi \cos \varphi \sigma_y = 0. \end{aligned} \quad (3-22)$$

Simplify it, we have:

$$\sin \varphi (\gamma H_\theta + \sin \varphi \sigma_x - \cos \varphi \sigma_y) = 0. \quad (3-23)$$

Hence,

$$h_\theta \equiv \gamma H_\theta = -\sin \varphi \sigma_x + \cos \varphi \sigma_y. \quad (3-24)$$

Notice that H_θ and H_φ are already obtained in Equations 3-8 and 3-10. For simplicity, we set $\gamma = 1$. Therefore, Equations 3-24 and 3-21 becomes:

$$\begin{aligned} -\sin \varphi \sigma_x + \cos \varphi \sigma_y = -H_K \sin \theta \cos \theta + \\ (H_x + H_C \cos \varphi_{\text{NiFe}}) \cos \theta \cos \varphi + H_C \sin \varphi_{\text{NiFe}} \cos \theta \sin \varphi, \end{aligned} \quad (3-25a)$$

$$\begin{aligned}
 & -\cos \varphi \cos \theta \sigma_x - \cos \theta \sin \varphi \sigma_y = \\
 & -(H_x + H_C \cos \varphi_{\text{NiFe}}) \sin \varphi + H_C \sin \varphi_{\text{NiFe}} \cos \varphi. \quad (3-25b)
 \end{aligned}$$

Substituting the σ_x and σ_y from Equation 3-13, Equation 3-4 is obtained.

To determine the \mathbf{m} orientation for a given $\boldsymbol{\sigma}$, it is essential to numerically solve Equation 3-4. We can reformulate Equation 3-4 in its differential form while considering that $\sigma_{\text{SHE}} = \sigma$ and $\sigma_{\text{AHE}} = \eta \sigma_{\text{SHE}} = \eta \sigma$. Consequently, the rewritten equation becomes:

$$\begin{aligned}
 & \{-H_K \cos 2\theta - [(H_x + H_C \cos \varphi_{\text{NiFe}}) \sin \theta \cos \varphi] - H_C \sin \varphi_{\text{NiFe}} \sin \theta \sin \varphi\} d\theta + \\
 & \{- (H_x + H_C \cos \varphi_{\text{NiFe}}) \cos \theta \sin \varphi + \eta \sigma \sin \varphi \cos \varphi_{\text{NiFe}} \sin \varphi_{\text{NiFe}} \\
 & \quad + H_C \sin \varphi_{\text{NiFe}} \cos \theta \cos \varphi + (1 + \eta \cos^2 \varphi_{\text{NiFe}}) \cos \varphi \sigma\} d\varphi + \\
 & \{-\eta \cos \varphi \cos \varphi_{\text{NiFe}} \sin \varphi_{\text{NiFe}} + (1 + \eta \cos^2 \varphi_{\text{NiFe}}) \sin \varphi\} d\sigma = 0, \quad (3-26a)
 \end{aligned}$$

$$\begin{aligned}
 & \{-\eta \cos \varphi_{\text{NiFe}} \sin \varphi_{\text{NiFe}} \sin \theta \sin \varphi \sigma - (1 + \eta \cos^2 \varphi_{\text{NiFe}}) \sin \theta \cos \varphi \sigma\} d\theta + \\
 & \{- (H_x + H_C \cos \varphi_{\text{NiFe}}) \cos \varphi + \eta \cos \varphi_{\text{NiFe}} \sin \varphi_{\text{NiFe}} \cos \theta \cos \varphi \sigma \\
 & \quad - H_C \sin \varphi_{\text{NiFe}} \sin \varphi - (1 + \eta \cos^2 \varphi_{\text{NiFe}}) \cos \theta \sin \varphi \sigma\} d\varphi + \\
 & \{\eta \cos \varphi_{\text{NiFe}} \sin \varphi_{\text{NiFe}} \cos \theta \sin \varphi + (1 + \eta \cos^2 \varphi_{\text{NiFe}}) \cos \theta \cos \varphi\} d\sigma = 0. \quad (3-26b)
 \end{aligned}$$

Once the initial state of the system is defined, the application of a small current ($d\sigma$) enables the determination of the new equilibrium position of the system ($d\theta$ and $d\varphi$), as described by Equation 3-26. By iteratively running Equation 3-26, we are allowed to obtain the state (θ, φ) of the system as a function of the current σ once the initial state at zero current is preset. Subsequently, the switching hysteresis under all the applied current can be obtained accordingly, as shown in Figure 3-3(d,e).

3.3 Experimental results and discussions

To achieve Type-T magnetic multilayers with both in-plane and perpendicular anisotropy, it is crucial to optimize the spacer thickness. As depicted in Figure 3-4, when

only a 1 nm Pt spacer is present between the in-plane NiFe layer and the perpendicular Co layer, the coupling between these two magnetizations is overly strong, which suppresses the perpendicular anisotropy of Co. Conversely, the insertion of an additional 4 nm Ru layer between the in-plane NiFe layer and the perpendicular Co layer effectively preserves the perpendicular anisotropy of Co. However, this configuration results in weakened coupling between the two layers, which is unfavorable for the following experimental measurements. Eventually, we selected $\text{SiO}_2//\text{Ta}(2)/\text{IrMn}(8)/\text{NiFe}(3)/\text{Ru}(2)/\text{Pt}(1)/\text{Co}(1)/\text{Pt}(1 \text{ nm})$ as the main sample, wherein the 2 nm Ru spacer successfully preserves both the in-plane and perpendicular anisotropy well, while also ensures a significant perpendicular magnetization switching.

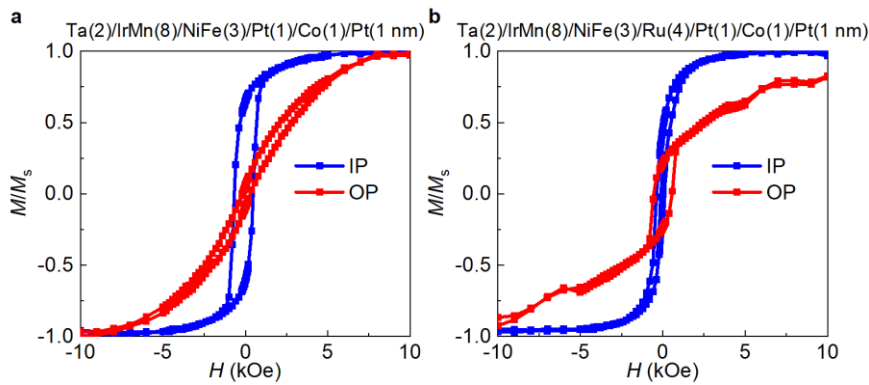


Figure 3-4 Optimization of the coupling layer thickness. (a) No Ru interlayer; (b) With 4 nm Ru interlayer.

The structural configuration of the main sample is illustrated in Figure 3-5(a). It consists of a three-layer film structure composed of $\text{Pt}(1)/\text{Co}(1)/\text{Pt}(1 \text{ nm})$, which induces perpendicular magnetic anisotropy. The presence of two Pt layers, with equal thickness, on both sides of Co generates spin currents that effectively cancel out and have no impact on Co. The Ru layer functions as a coupling layer, enabling Co to perceive the in-plane effective field generated by NiFe. This effective field facilitates the switching of perpendicular Co through SOTs generated by NiFe, eliminating the need for an external symmetry-breaking magnetic field. Additionally, the underlying

IrMn layer is employed to provide exchange coupling to NiFe while enhancing its in-plane magnetic anisotropy.

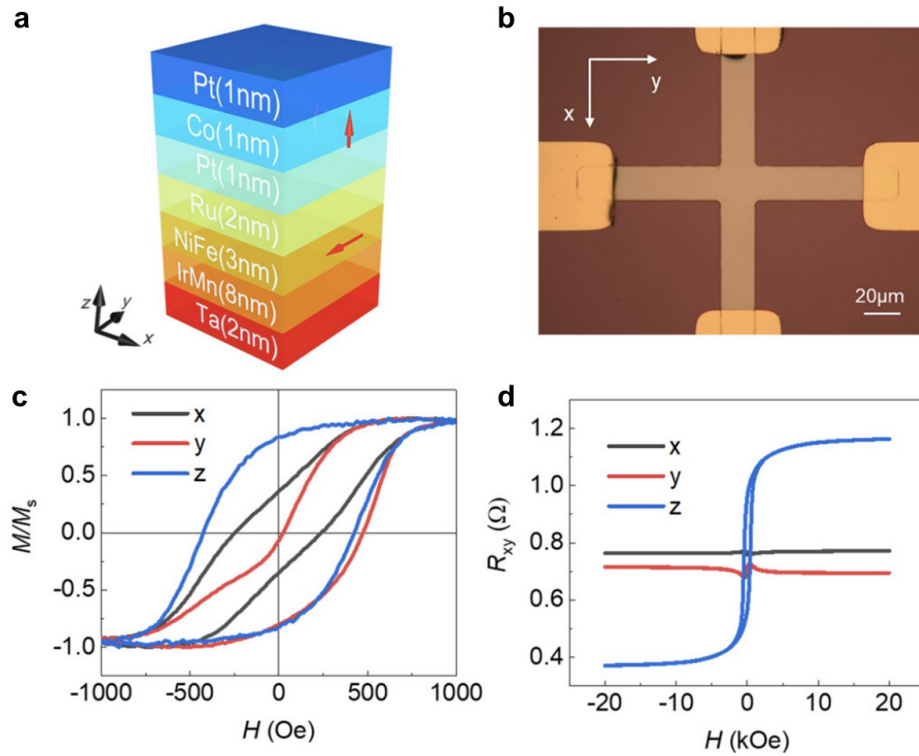


Figure 3-5 Structure and magnetization of the sample. (a) Element and thickness of each layer. (b) Image of the four-terminal Hall-bar device under a microscopy. (c) Hystereses of the sample film under a magnetic field in x , y and z direction. (d) Dependence of the Hall resistance of the device on a magnetic field in x , y and z direction [298].

The measurements are based on micro-size four-terminal Hall-bar devices, as depicted in Figure 3-5(b). Two terminals are utilized for current injection along either the x or y direction, while the remaining two terminals are employed to measure the Hall voltage along the y or x direction, accordingly. The Hall resistance V_H/I serves as an indicator to determine the orientation of the perpendicular Co magnetization \mathbf{m}_z . Due to the substantial thickness of the NiFe layer and the pinning by IrMn, its magnetization exhibits limited tilting when magnetic field is applied. Consequently, the PHE contribution from NiFe on the Hall resistance can be disregarded. The magnetization hysteresis of the sample is demonstrated in Figure 3-5(c,d), obtained through VSM and

Hall resistance measurements, respectively. The presence of \mathbf{m}_z is confirmed through both methods. Moreover, a H_{EB} of about 250 Oe in the y direction is also confirmed, which is crucial for achieving the field-free perpendicular magnetization switching.

Subsequently, we leverage the SOTs generated by NiFe to realize the switching of \mathbf{m}_z . A high or low value of R_{xy} corresponds to $\mathbf{m}_z > 0$ or $\mathbf{m}_z < 0$, respectively. As illustrated in Figure 3-6, our measurement procedure involves sweeping a y -direction current, I_y , while applying an external magnetic field, H_y , fixed at values ranging from +10 Oe to -10 Oe. In this configuration, the magnetization of NiFe aligns along the y -direction, and the torque is solely produced through the SHE mechanism. When $I_y > 20$ mA and $H_y > 0$, the final state $\mathbf{m}_z > 0$. Notably, individually switching I_y or H_y leads to the opposite final state $\mathbf{m}_z < 0$. This observation indicates that the sign of H_y determines the polarization of the SOT-induced switching, which aligns with the characteristics of Type-Z switching scheme.

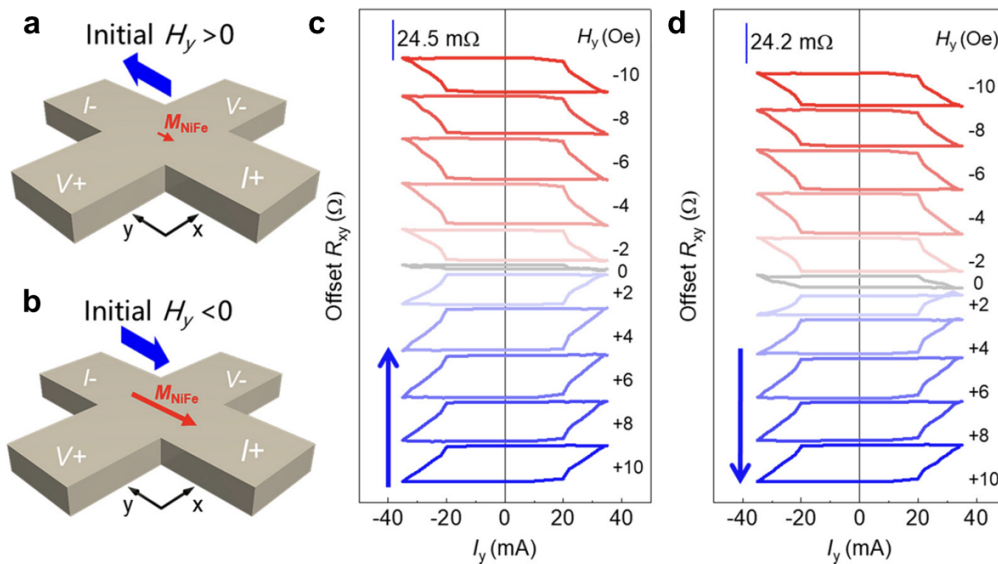


Figure 3-6 Perpendicular magnetization switching induced by SHE. (a-b) Measurement setups when the magnetic field is along the + y direction and - y direction, respectively. (c-d) Current dependence of the Hall resistance when the magnetic field sweep from the + y to - y direction and from the - y direction to the + y direction, respectively [298].

Figure 3-6(c,d) reveal that when $H_y = 0$, the polarity of the hysteresis loop is

consistently opposite to that observed when $H_y > 0$ and same as $H_y < 0$. Notably, when the magnetic field is swept from negative to positive, the amplitude of field-free switching is larger. In other words, the polarity of field-free switching is independent of the magnetization history, whereas the amplitude of field-free switching is determined by the magnetization history. These phenomena are attributed to the pinning of NiFe by IrMn in the $-y$ direction. When H_y decreases from a positive (negative) value to 0, the remanent magnetization of NiFe becomes very small (relatively large). Consequently, the effective field exerted by NiFe on Co becomes correspondingly small (relatively large), resulting in a small (large) amplitude of perpendicular magnetization switching. This phenomenon is consistent across a wider range of sweeping experiments, as depicted in Figure 3-7 and Figure 3-8, thereby demonstrating its reproducibility. Additionally, the fact that the switching polarity can be altered by an external magnetic field of ± 2 Oe indicates that the H_C between NiFe and Co is approximately 1 Oe.

The maximum ΔR_{xy} achieved through SOT-induced switching is 24 m Ω , which is smaller than the ΔR_{xy} obtained through field-driven switching (Figure 3-5). This discrepancy arises because ΔR_{xy} induced by magnetic field includes contributions from the in-plane NiFe magnetization tilted towards the z direction. Conversely, the ΔR_{xy} obtained from SOT-induced switching solely originates from the perpendicular Co magnetization switching. Consequently, the latter serves as the standard for assessing the switching amplitude obtained in the subsequent AHE experiments. As depicted in Figure 3-7 and Figure 3-8, it is observed that employing a larger external magnetic field only resulted in switching with the same or smaller amplitude.

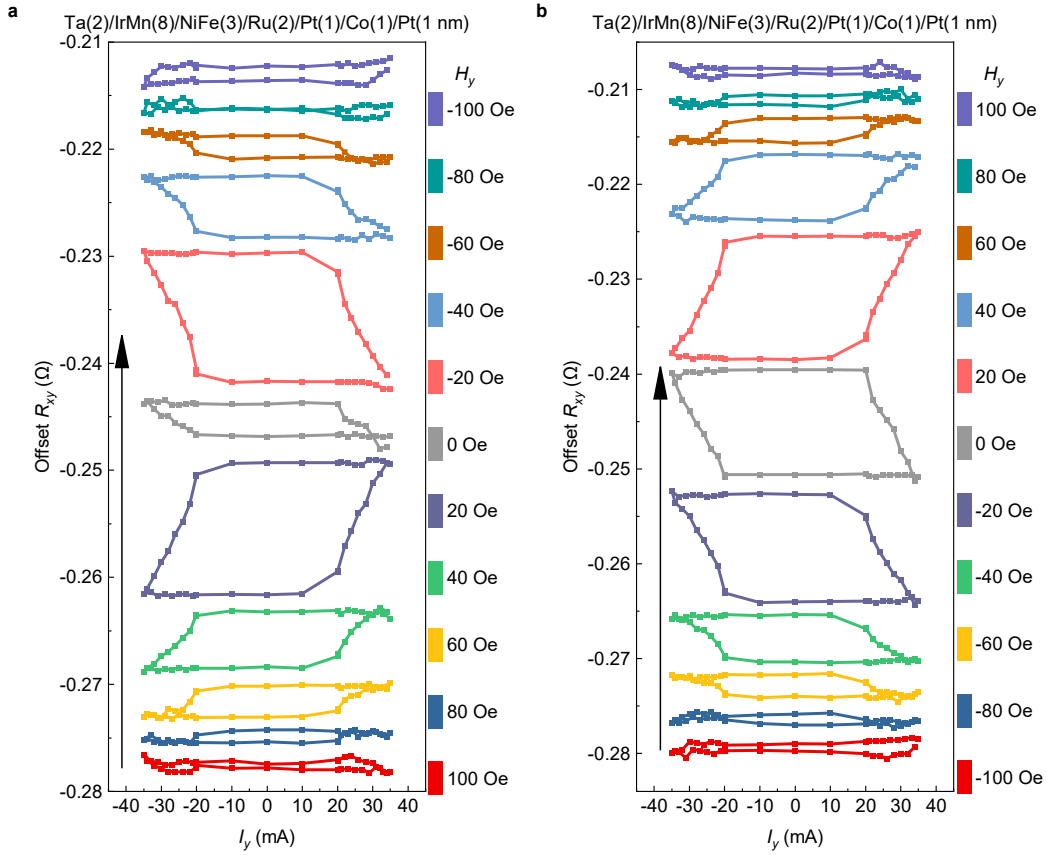


Figure 3-7 Perpendicular magnetization switching induced by SHE under 100 Oe magnetic field. Measurements when magnetic field sweep from the $+y$ ($-y$) to the $-y$ ($+y$) direction is shown in (a) and (b), respectively.

Same measurements are conducted on the control sample Ru/Pt/Co/Pt, wherein no SOT-induced switching is observed. This observation suggests that the spin current responsible for magnetization switching originates from IrMn/NiFe rather than Pt. Considering the much higher resistivity of IrMn compared to NiFe, along with the known spin diffusion length of NiFe being 2.5 nm [300–302], it further supports the conclusion that NiFe serves as the spin source. Recent experiments have also reported a considerable spin Hall angle in NiFe [169,171,303,304], providing additional evidence in supporting this conclusion.

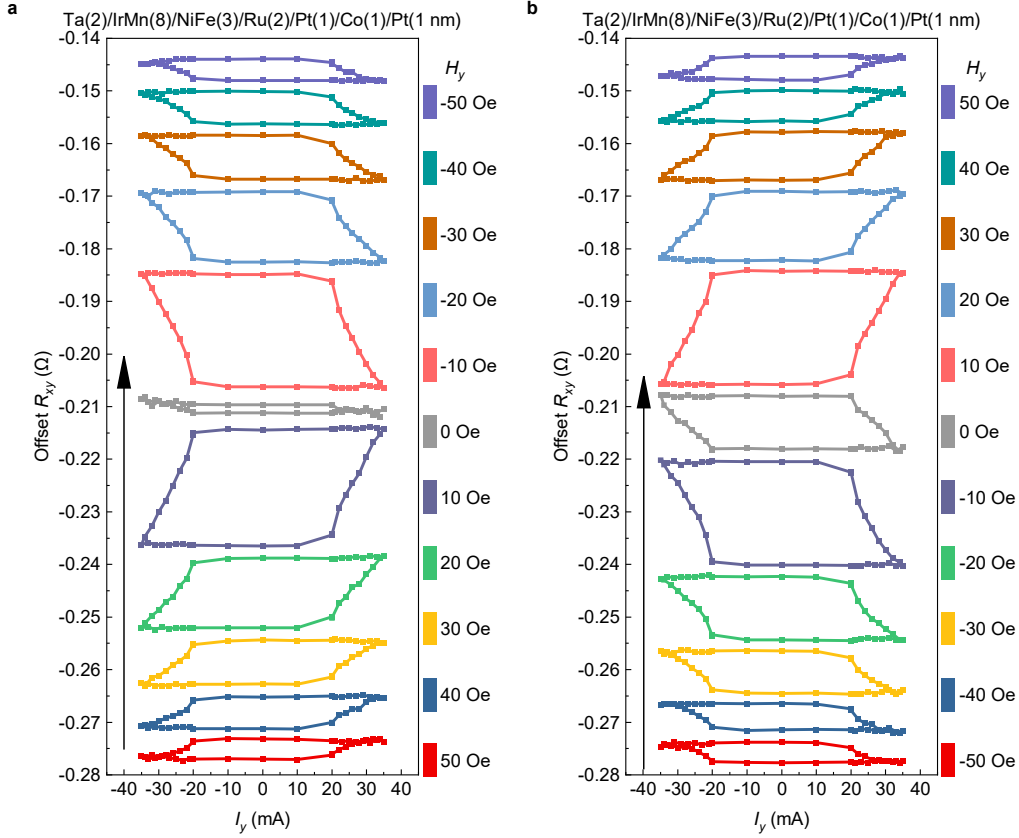


Figure 3-8 Perpendicular magnetization switching induced by SHE under 50 Oe magnetic field. Measurements when magnetic field sweep from the $+y$ ($-y$) to the $-y$ ($+y$) direction is shown in (a) and (b), respectively.

In Figure 3-9, when both a current I_y and an external magnetic field H_x are applied, an AHE torque is induced. Due to the pinning of NiFe in the y direction, robust field-free switching is achieved, with a clockwise (-1) switching polarity. The perpendicular magnetization switching is dominated by the SHE torque when the $H_x \approx 0$. Meanwhile, when $|H_x|$ exceeds a critical value (approximately 5 Oe in this experiment), the AHE torque becomes the dominant factor, leading to a change of switching polarity from clockwise (-1) to counterclockwise ($+1$). We defined $\Delta R_{xy} = R_{xy}(I_y = 0, \uparrow) - R_{xy}(0, \downarrow)$ when the switching is counterclockwise, and $\Delta R_{xy} = R_{xy}(I_y = 0, \downarrow) - R_{xy}(0, \uparrow)$ when the switching is clockwise. Hence, the dependence of ΔR_{xy} on H_x is summarized in Figure 3-9(c), which exhibits symmetry and polarity reversal characteristics consistent with the results of macrospin calculations (Figure

3-3). This result experimentally confirms the SHE and AHE competition during the perpendicular magnetization switching. As shown in Figure 3-10, the measurement is repeated 10 times to demonstrate the reproducibility of this phenomenon. Furthermore, the polarity reversal rules out the possibility of IrMn from dominating the SOT generation, as the polarity of the spin current generated by the SHE mechanism of IrMn would remain constant.

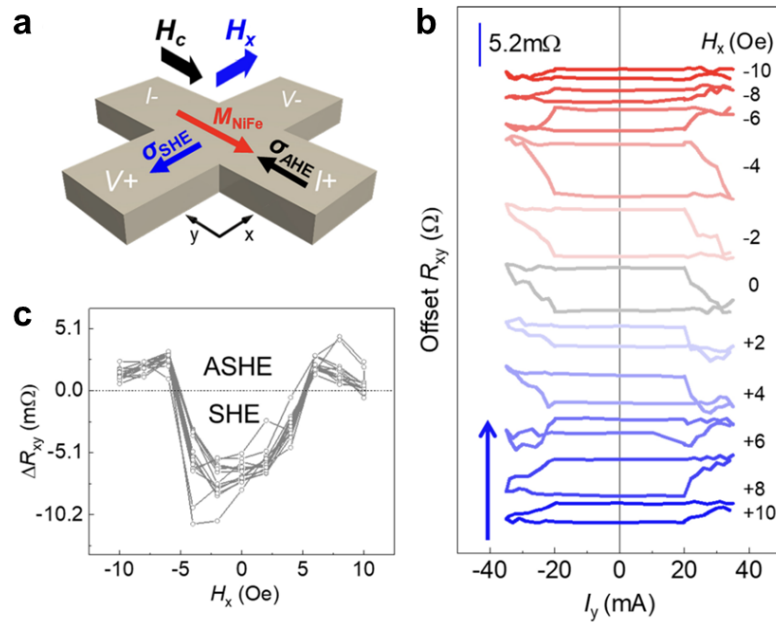


Figure 3-9 Perpendicular magnetization switching induced by AHE. (a) Schematic of the measurement setup. (b) Current dependence of the Hall resistance while sweeping the x -direction magnetic field. (c) Dependence of the polarity of the Hall resistance on the x -direction magnetic field. [298].

According to the VSM results presented in Figure 3-5, the H_K of the perpendicular Co layer is 420 Oe. Therefore, when the switching polarity changes, H_x/H_K is approximately 0.014-0.024 (Figure 3-9). However, based on the macrospin model depicted in Figure 3-3, the system should still be in the SHE switching range at this point. There are two origins of the discrepancy between the model and experimental results: (1) the macrospin model is primarily suitable for providing symmetry analysis and cannot give an accurate critical condition for the transition from SHE dominance

to AHE dominance, (2) Figure 3-9 reveals that the SHE switching amplitude is only about 20% compared to $\Delta R_{xy}(I = 0) = 24 \text{ m}\Omega$ shown in Figure 3-6. This smaller switching amplitude suggests that only a portion of the magnetic domains are switched, and these domains have lower perpendicular magnetic anisotropy compared to the bulk. Consequently, the magnetization switching initiates from these domain centers. In other words, when comparing Figure 3-9 and Figure 3-3, a lower H_K value of the domain centers should be considered instead of the bulk H_K value of 420 Oe. Thus, the H_x/H_K of 0.014-0.024 which calculated with the bulk H_K is underestimated compared to the real value.

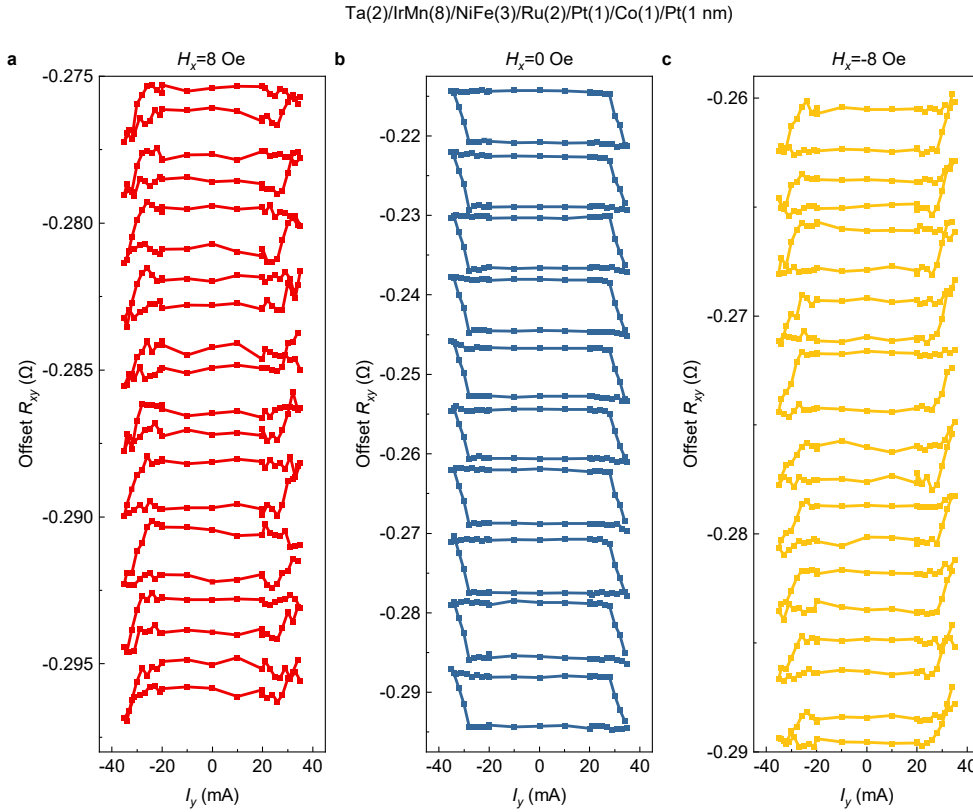


Figure 3-10 Reproducibility test of the AHE-induced perpendicular magnetization switching. Measurement of the y -direction current induced perpendicular magnetization switching with +8 Oe, 0 Oe and -8 Oe x -direction magnetic field for 10 times are shown in (a), (b) and (c), respectively.

In Figure 3-9, it is important to note that both AHE and SHE induce partial

switching. The observed switching amplitude is only 10% and 20% compared to $\Delta R_{xy}(I = 0) = 24 \text{ m}\Omega$ shown in Figure 3-6. This reduced switching amplitude can be attributed to the fact that both H_x and H_C are smaller than the DMI field in the Pt/Co/Pt structure [175].

Assuming that the switching is coherent and macrospin-like, the relative spin-conversion efficiency between AHE and SHE of NiFe can be estimated by using the critical current density. In this chapter, the average current required in SHE-induced magnetization switching is 27.4 mA, while the average current required in AHE-induced magnetization switching is 26.0 mA, resulting in a relative efficiency value of $\theta_{\text{AHE}}^{\text{NiFe}} / \theta_{\text{SHE}}^{\text{NiFe}} = 1.05$. This is close to the value of 1.28 reported in the literature [302]. However, it should be noticed that this estimation is based on the macrospin model, and the more reliable and accurate measurement of AHE efficiency in ferromagnetic materials is still needed.

Varying the thickness of NiFe with the same structure, similar phenomena can be observed with 5 nm NiFe sample (Figure 3-11 and Figure 3-12), while disappears with 1 nm NiFe sample (Figure 3-13 and Figure 3-14). This suggests that the AHE torque originates from the bulk NiFe rather than the Ru interface or bulk IrMn.

The thicker 5 nm in-plane NiFe provide a strong effective field ensuring the field-free switching, but it lacks good pinning by IrMn. Figure 3-11 illustrates, in contrast to the main sample (Figure 3-6), the polarity of the SHE-induced field-free switching now determined by the magnetization history. Additionally, the AHE-induced switching is also less clear due to this larger in-plane magnetization (Figure 3-12). On one hand, larger H_x is required to tilt the larger in-plane magnetization. Meanwhile increasing the H_x will tilt the perpendicular magnetization towards in-plane direction. Consequently, the measured curves are not as smooth as those obtained under H_y .

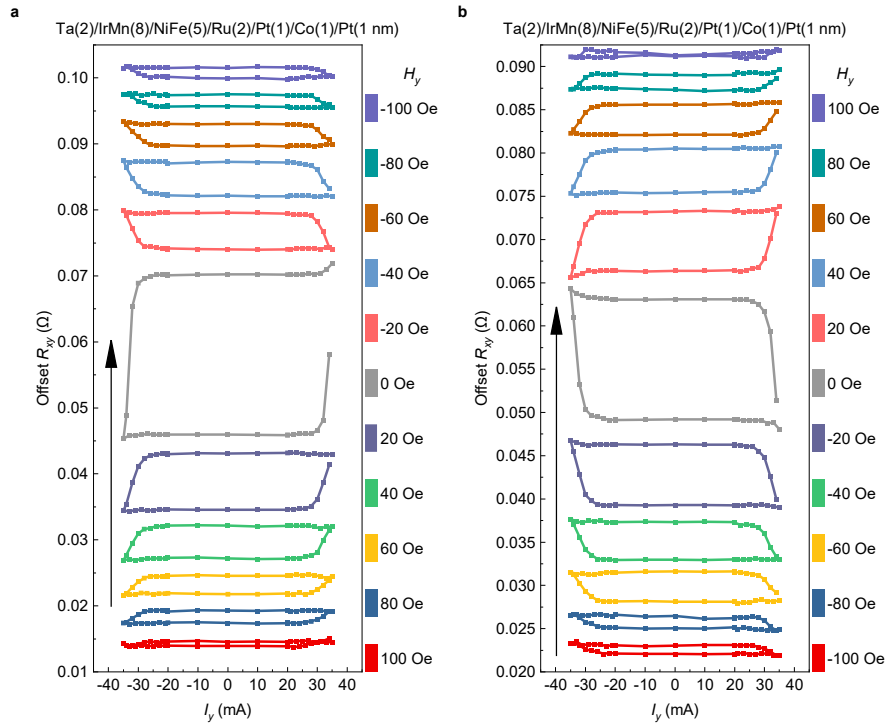


Figure 3-11 SHE-induced perpendicular magnetization switching of the sample with 5 nm NiFe. Results of magnetic field sweeping from +y (-y) to the -y (+y) direction is shown in (a) and (b), respectively.

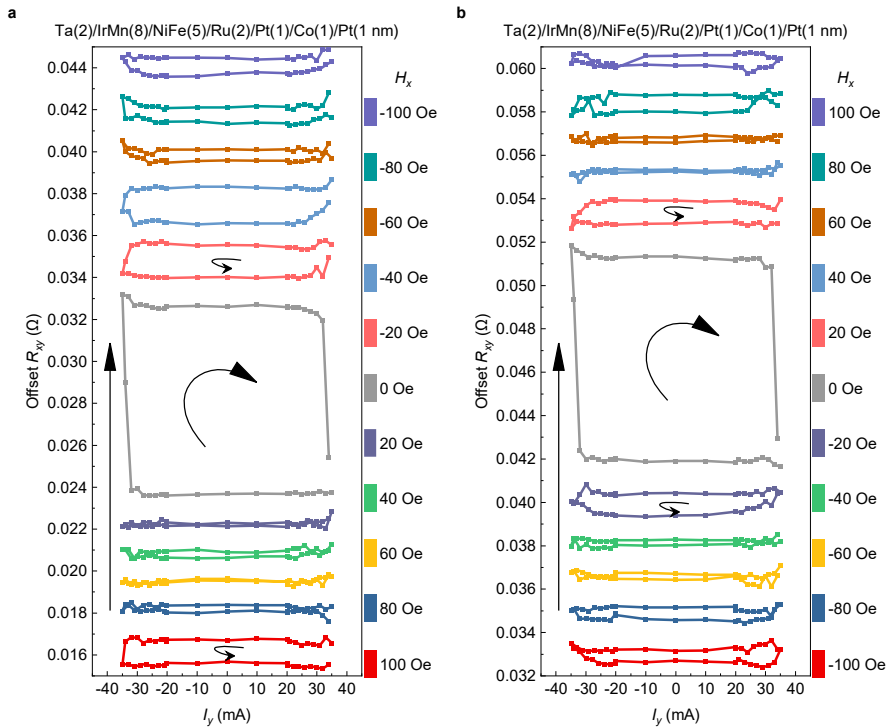


Figure 3-12 AHE-induced perpendicular magnetization switching of the sample with 5 nm NiFe. Results of magnetic field sweeping from the +x (-x) to the -x (+x) direction is shown in (a) and (b), respectively.

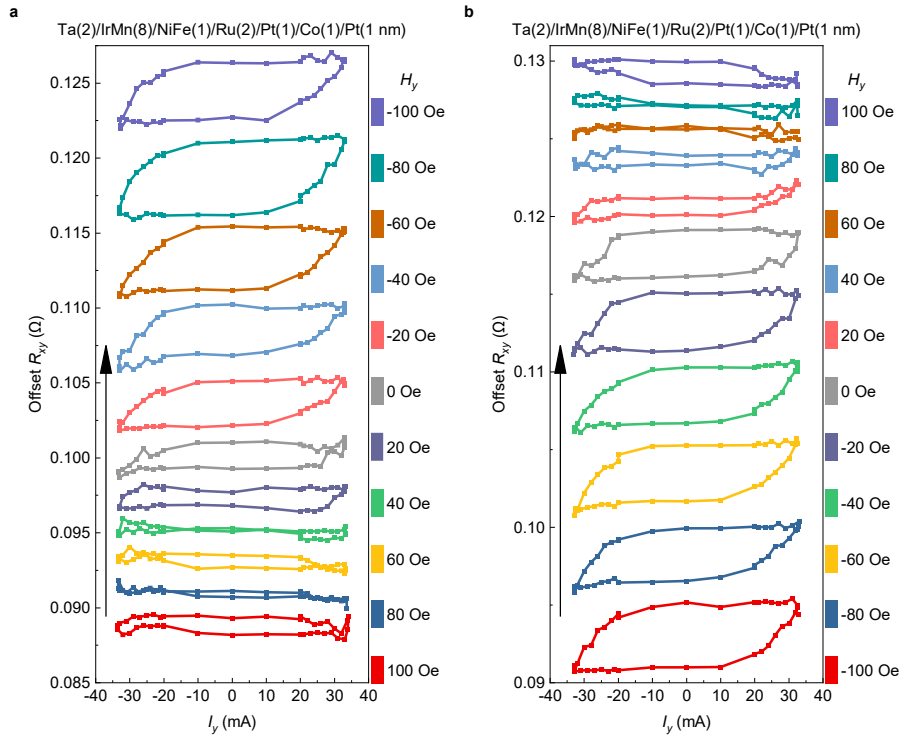


Figure 3-13 SHE-induced perpendicular magnetization switching of the sample with 1 nm NiFe. Results of magnetic field sweeping from $+y$ ($-y$) to the $-y$ ($+y$) direction is shown in (a) and (b), respectively.

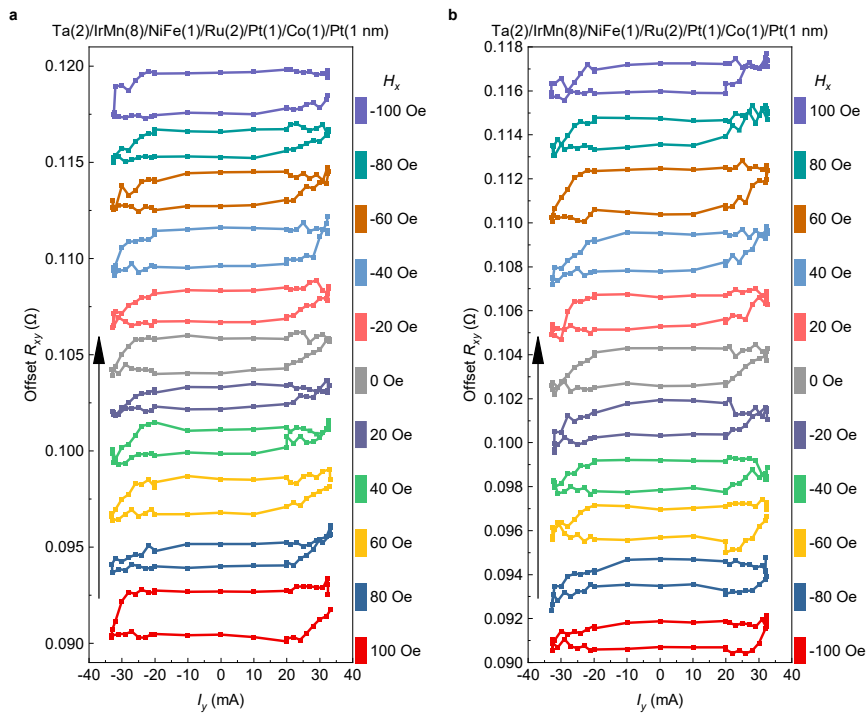


Figure 3-14 AHE-induced perpendicular magnetization switching of the sample with 1 nm NiFe. Results of magnetic field sweeping from the $+x$ ($-x$) to the $-x$ ($+x$) direction is shown in (a) and (b), respectively.

The thinner 1 nm in-plane NiFe layer also provide a sufficiently large effective field enabling the field-free switching, but it is excessively well pinned by IrMn. In Figure 3-13, it is clear now NiFe always provides a large effective field along the $-y$ direction. Consequently, the polarization of field-free switching is always same to the ones with $H_y < 0$. ΔR_{xy} increases as H_y increasing along the $-y$ direction; while ΔR_{xy} decreases as H_y increasing along the $+y$ direction. This behavior arises because a larger $+y$ -direction magnetic field is required for changing the switching polarization, which inevitably titles the perpendicular magnetization towards in-plane direction and leads to smaller ΔR_{xy} . Figure 3-14 illustrates that, with the strong pinning of NiFe, the H_x fails to sufficiently title the magnetization of NiFe away from the $-y$ direction. As a result, the switching is always dominated by the SHE since the AHE torque is not sufficient.

It is worth reiterating that Figure 3-3 presents the calculated outcomes of the macrospin model, which can solely offer a qualitative correspondence to the experimental findings depicted in Figure 3-9. The macrospin model lacks the ability to account for factors such as thermal activation, domain nucleation, and domain wall motion, all of which have the potential to decrease the critical current density and enable multistate switching. Conducting more accurate micromagnetic simulations that incorporate all these processes will significantly enhance our comprehension of AHE-induced magnetization switching.

The AHE in ferromagnets offers following advantages: (1) No heavy metals such as Pt are required, which reduces manufacture costs. (2) The AHE-induced spin current in magnetic materials allows for the manipulation of its spin polarization through magnetization, which enables the application of more flexible torques and multifunctional devices. (3) The coupling between the free layer and the pinned layer enables the desired field-free perpendicular magnetization switching. In summary, the

utilization of ferromagnets as spin sources not only reduce costs but also supports the advancement of field-free perpendicular MRAM technology.

3.4 Chapter summary

This chapter explores the generation of spin current through the AHE and SHE mechanisms in the ferromagnetic material NiFe, and demonstrates field-free perpendicular magnetization switching in a Ta/IrMn/NiFe/Ru/Pt/Co/Pt Type-T cross-shaped Hall-bar device. NiFe not only provides in-plane coupling fields, but also serves as the spin source. The polarities SHE- and AHE-induced switching are opposite, allowing for a clear understanding of the existence and contribution of the AHE torque. This research validates the various roles that ferromagnetic materials can play in spin current generation and magnetization switching, laying the foundation for the development of new heavy-metal free SOT-MRAMs and spin logic devices. The experimental procedure is as follows:

(1) A Type-T macrospin model containing in-plane and perpendicular magnetization is derived. Considering the coexistence of the SHE and AHE mechanisms within the in-plane magnetic layer, a method is proposed to verify the existence of the AHE spin current.

(2) Ta/IrMn/NiFe/Ru/Pt/Co/Pt Type-T multilayers are grown by magnetron sputtering, followed by the fabrication of Hall-bar devices through standard UV lithography and argon ion etching. The coexistence of perpendicular and in-plane magnetic anisotropy in the multilayers is verified through VSM measurements.

(3) The SHE-driven perpendicular magnetization switching is achieved when the applied magnetic field is aligned with the in-plane magnetization. With the symmetry-breaking effective field from the in-plane layer acting on the perpendicular

magnetization, the field-free switching is achieved.

(4) The perpendicular magnetization switching is also achieved when the applied magnetic field is perpendicular to the in-plane magnetization. When the field is small, the switching is dominated by the SHE mechanism, while when the field is large enough, the switching is now governed by the AHE mechanism.

This chapter of work is conducted with several colleges and their contributions are as follows: I grew the stacks, fabricated the devices, conducted magneto transport measurements, constructed the macrospin model and analyzed all the results. Xiao WANG and Wenlong YANG provided assistant during the stack growth. Chenyang GUO, Chi FANG and Mingkun ZHAO helped with the device fabrications. Jing DONG and Yu ZHANG contributes to the transport measurements. Caihua WAN and Xiufeng HAN led and was involved in all aspects of the research.

4 Effective perpendicular field induced by SOT in a magnetic trilayer

4.1 Research background

SOT is an essential means to achieve efficient magnetization switching, holding significant implications in the development of high-speed and long-endurance MRAMs. In common heavy metal/ferromagnet bilayers, the generation of SOT stems from the spin current generated in the heavy metal layer through the SHE mechanism. Due to symmetry constraints, the polarization direction of the spin current lies in the film plane, thus enabling only deterministic in-plane magnetization switching. However, to achieve the desired perpendicular magnetization switching for high-density storage, it is necessary to introduce fields that break the in-plane symmetry, such as the Oersted field, exchange bias, or interlayer coupling.

Meanwhile, effective perpendicular fields allow more efficient and convenient perpendicular magnetization switching. Numerous efforts have been devoted to utilizing SOT to create effective perpendicular fields. For instance, SOT can generate effective perpendicular fields on Néel-type domain walls (as shown in Figure 4-1) [175]; Interfacial spin-precessional scattering can generate perpendicular polarized spin currents and effective perpendicular fields [171]. Materials with low in-plane symmetry, such as WTe_2 [148] and Cu-Pt/Co-Pt [201], can also generate effective perpendicular fields when subjected to current injection. However, these mechanisms are limited to confined systems (such as domain walls or interfaces) or have strict substrate and crystal structure requirements.

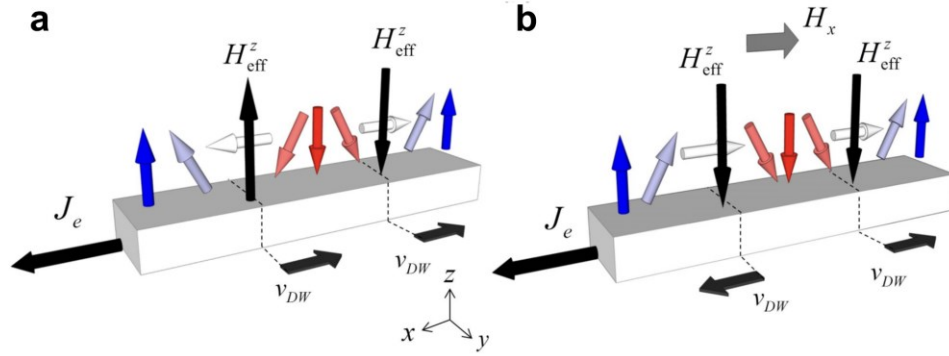


Figure 4-1 Effective perpendicular fields generated on Néel-type domain walls by SOT. (a) Magnetization orientation without magnetic fields. SHE-induced effective fields cancel out each other, resulting in domain movements. (b) Magnetization orientation with x-direction magnetic field. SHE-induced effective fields are aligned now, resulting in domain expansions [175].

This chapter demonstrates, both theoretically and experimentally, the natural generation of an SOT-induced effective perpendicular field in Type-T magnetic trilayers with interlayer coupling. When the two magnetic layers experience SOTs with same (opposite) polarity, the perpendicular effective field can facilitate (hinder) the SOT-induced perpendicular magnetization switching. This unique Type-T magnetic trilayer structure provides guidance for future designs of efficient SOT-MRAM. The main findings of this chapter have been published in Physical Review Applied [305].

4.2 Experimental and simulate methods

4.2.1 Construction and analyses of the macrospin model

Figure 4-2 illustrates the generation of the effective perpendicular field and the efficient SOT-induced perpendicular magnetization switching in the Type-T magnetic trilayer. The key factors are as follows: (1) interlayer coupling between perpendicular magnetization \mathbf{M}_1 and in-plane magnetization \mathbf{M}_2 ; (2) both \mathbf{M}_1 and \mathbf{M}_2 experiencing SOT with the same polarity. The second requirement is achieved by sandwiching the

two magnetic layers between two heavy metal layers (e.g., Pt and W) with opposite spin Hall angles. Assuming the current flows along the y direction, SHE in Pt and W generates two $+z$ and $-z$ spin currents σ_i , polarized along the $+x$ direction, which are injected into the two magnetic layers. Upon absorption, these spin currents induce a damping-like torque, $\mathbf{M}_i \times \sigma_i \times \mathbf{M}_i$, on each magnetic layer, resulting in an \mathbf{M}_2 tilting towards the perpendicular direction. Due to the presence of interlayer coupling, this perpendicular component generated by the tilting of \mathbf{M}_2 will provide an additional perpendicular effective field, H_{z1}^{eff} , to the perpendicular \mathbf{M}_1 . For simplicity, assuming that both ferromagnetic layers absorb spin currents of equal magnitude, σ_0 , and $K_2 \gg K_1$, the torque balance equation for \mathbf{M}_1 at steady state is given by Equation 4-1. The detailed derivation of this equation is provided at the end of this section.

$$H_{z1}^{\text{eff}} = -A \cos \theta_2 = A(\sigma_0/2K_2), \quad (4-1a)$$

$$K_1 \sin 2\theta_1 + A \cos \theta_1 + A\sigma_0/2K_2 \sin \theta_1 - \sigma_0 = 0. \quad (4-1b)$$

Here, A represents the interlayer coupling energy, M_i and K_i denote the saturation magnetization and effective anisotropy of the i -th layer, and θ_i is the polar angle. The first, second and fourth terms on the left-hand side of Equation 4-1b correspond to the torques induced by the perpendicular magnetic anisotropy field, the in-plane effective field provided by the in-plane layer, and the SOT, respectively. These three terms have been discussed in previous works [101]. The third term, proportional to SOT, represents the additional effective perpendicular field provided by the in-plane layer. Equation 4-1a clearly shows that this term originates from the SOT-induced perpendicular component of \mathbf{M}_2 and the interlayer coupling. The influence of this term on the \mathbf{M}_1 switching is depicted in Figure 4-2(b-e). With \mathbf{M}_2 initialized in the $+y$ direction, \mathbf{M}_1 can achieve field-free switching regardless of whether \mathbf{M}_1 and \mathbf{M}_2 experience SOT in the same or opposite directions. Meanwhile the switching polarity

depends on the torques involved in the switching process. Comparing Figure 4-2(b,c), when \mathbf{M}_1 and \mathbf{M}_2 experience SOT in opposite directions, H_{z1}^{eff} hinders \mathbf{M}_1 switching, resulting in a higher critical switching current density; while comparing Figure 4-2(d,e), when \mathbf{M}_1 and \mathbf{M}_2 experience SOT in the same direction, H_{z1}^{eff} assists \mathbf{M}_1 switching, leading to a lower critical current density.

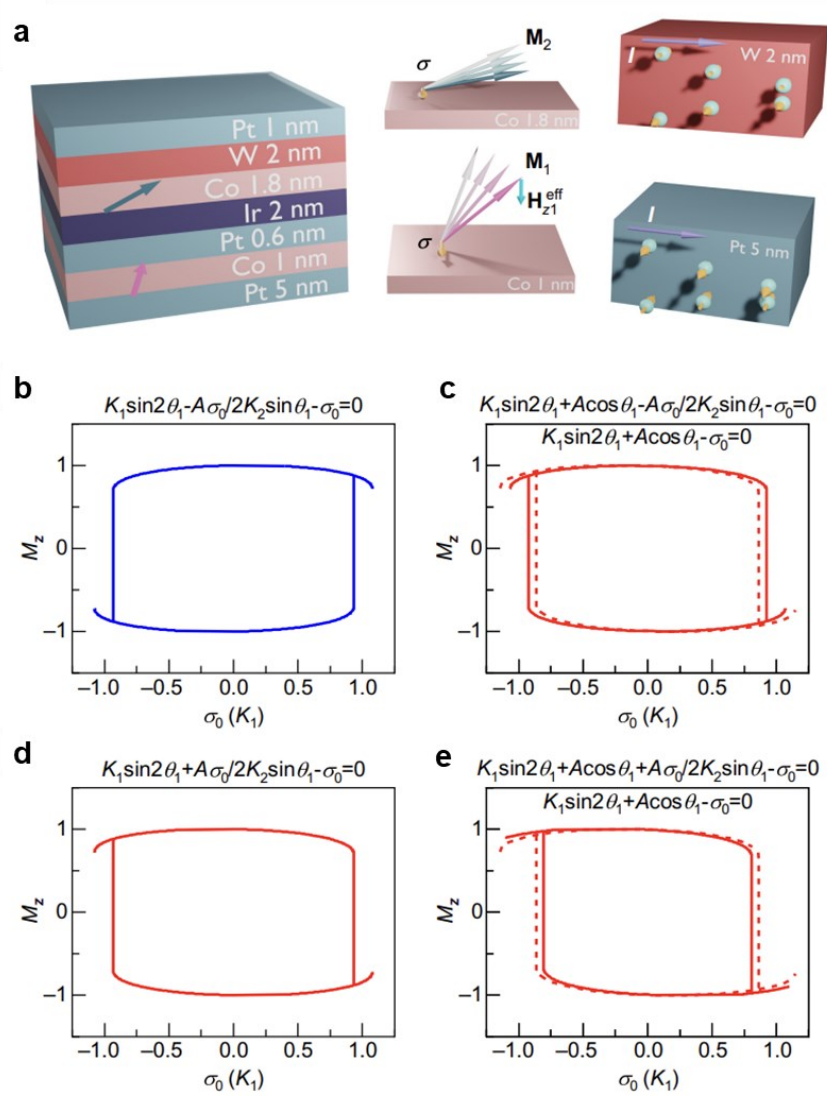


Figure 4-2 Creation of perpendicular effective field in the Type-T magnetic trilayer. (a) In-plane magnetization tilts towards the z-direction under SOT. Perpendicular Co experiences additional effective perpendicular field under interlayer coupling. (b-c) Simulations of the macrospin model when two magnetic layers experience SOTs with the opposite direction; (d-e) Simulation of the macrospin model when two magnetic layers experience SOTs with the same direction [305].

Please note that while micromagnetic models capable of simulating domain wall motion and domain nucleation can provide quantitative analysis and better reproduce the details of switching in micron-sized samples, they are not suitable for analyzing the detailed physical mechanisms of switching. On the contrary, the macrospin model employed here helps us grasp the physical essence of perpendicular magnetization switching in this Type-T magnetic trilayer system. The mathematical form of the third term, the effective perpendicular field term, in Equation 4-1b directly indicates its origin: the SOT-induced tilting of \mathbf{M}_2 in the perpendicular direction. Under the interlayer coupling between \mathbf{M}_1 and \mathbf{M}_2 , \mathbf{M}_1 experiences an additional effective perpendicular field whose direction is determined by the SOT experienced by \mathbf{M}_2 . This chapter's work highlights that in Type-T magnetic trilayer films with interlayer coupling, when both magnetization experience SOT in the same direction, the SOT-induced effective perpendicular field can reduce the critical current density. The macrospin model not only provides a clear characterization of the physical process but also reproduces key features observed in experimental data. Therefore, we have utilized the macrospin model in this study.

The derivation of the macrospin model is presented below.

Let χ represent the efficiency of generating an effective perpendicular field during the SOT-induced \mathbf{M}_1 switching. To better understand the generation of H_{z1}^{eff} , we introduce a macrospin model that supposes \mathbf{M}_1 and \mathbf{M}_2 experience the same or the opposite directions of SOTs. In Pt/Co multilayer systems, the field-like torque can be neglected [101]. At the same time, the current flows in the y direction, the in-plane magnetization \mathbf{M}_2 is oriented along the y direction, and magnetic fields are only applied in the y and z directions. Therefore, when SOT is small, the final states of this two-magnetization system are always confined in the yz plane, and the directions of \mathbf{M}_1 and

\mathbf{M}_2 can be described by two variables, θ_1 and θ_2 .

$$\mathbf{M}_i = M_i(\sin \theta_i \mathbf{y} + \cos \theta_i \mathbf{z}). \quad (4-2)$$

The total energy of the system is given by:

$$E = K_1 \sin^2 \theta_1 - (K_2 + \mu_0 M_2^2) \sin^2 \theta_2 + A \cos \beta - H_y M_1 \sin \theta_1 - H_y M_2 \sin \theta_2 - H_z M_1 \cos \theta_1 - H_z M_2 \cos \theta_2, \quad (4-3)$$

$$\cos \beta = \sin \theta_1 \sin \theta_2 + \cos \theta_1 \cos \theta_2. \quad (4-4)$$

Where K_1 and K_2 represent the magnetic anisotropy energy of the perpendicular Co and in-plane Co, respectively. θ_1 and θ_2 correspond to their polar angles. A and β denote the coupling energy between the two Co layers and the angle between them. μ_0 denotes the vacuum permeability. H_y and H_z denote the applied magnetic field along the y and z directions, respectively. M_1 and M_2 represent the saturation magnetization of the corresponding Co layers. The LLGS equation can be written as [102]:

$$\frac{1}{|\gamma|} \frac{d\mathbf{M}}{dt} = \boldsymbol{\tau}_{\text{tot}} + \frac{\alpha}{|\gamma|} \mathbf{M} \times \frac{d\mathbf{M}}{dt}. \quad (4-5)$$

When the system is stable, $d\mathbf{M}/dt = 0$. And $\alpha > 0$. Therefore, for each layer:

$$\boldsymbol{\tau}_{\text{tot}} = -\mathbf{M}_i \times \mathbf{H}_i^{\text{eff}} + \sigma_{0i}(\mathbf{M}_i \times \boldsymbol{\sigma}_i \times \mathbf{M}_i) = 0, \quad (4-6)$$

$$\mathbf{H}_i^{\text{eff}} = -\frac{\partial E}{M_i \partial \theta_i} \boldsymbol{\theta} \equiv H_i \boldsymbol{\theta}. \quad (4-7)$$

Here, we first derive \mathbf{M}_1 and \mathbf{M}_2 experience SOT of equal magnitude and in the same direction, namely:

$$\boldsymbol{\sigma}_1 = \boldsymbol{\sigma}_2 = \sigma_0 \mathbf{x}. \quad (4-8)$$

Therefore,

$$H_1 = -\frac{1}{M_1} (K_1 \sin 2\theta_1 - A \sin(\theta_1 - \theta_2) - H_y M_1 \cos \theta_1 + H_z M_1 \sin \theta_1), \quad (4-9a)$$

$$H_2 = -\frac{1}{M_2} (-(K_2 + \mu_0 M_2^2) \sin 2\theta_2 + A \sin(\theta_1 - \theta_2) - H_y M_2 \cos \theta_2 + H_z M_2 \sin \theta_2). \quad (4-9b)$$

Next, we proceed with the derivation of the formal torque balance equation and rewrite $\mathbf{H}_i^{\text{eff}}$ in Cartesian coordinates.

$$\mathbf{H}_i^{\text{eff}} \equiv H_i \boldsymbol{\theta} \equiv H_i \cos \theta_i \mathbf{y} - H_i \sin \theta_i \mathbf{z}. \quad (4-10)$$

$$\mathbf{M}_i \times \mathbf{H}_i^{\text{eff}} = \begin{vmatrix} i & j & k \\ 0 & \sin \theta_i & \cos \theta_i \\ 0 & H_i \cos \theta_i & -H_i \sin \theta_i \end{vmatrix} = -H_i \mathbf{x}. \quad (4-11)$$

$$\mathbf{M}_i \times \mathbf{x} \times \mathbf{M}_i = \mathbf{x}. \quad (4-12)$$

Hence,

$$\tau_{\text{tot}} = H_i + \sigma_i = 0. \quad (4-13)$$

Therefore,

$$-K_1 \sin 2\theta_1 + A \sin(\theta_1 - \theta_2) + H_y M_1 \cos \theta_1 - H_z M_1 \sin \theta_1 = -\sigma_0, \quad (4-14a)$$

$$(K_2 + \mu_0 M_2^2) \sin 2\theta_2 - A \sin(\theta_1 - \theta_2) + H_y M_2 \cos \theta_2 - H_z M_2 \sin \theta_2 = -\sigma_0. \quad (4-14b)$$

When \mathbf{M}_1 and \mathbf{M}_2 experience SOT of equal magnitude but in opposite directions, namely:

$$\boldsymbol{\sigma}_1 = -\boldsymbol{\sigma}_2 = \sigma_0 \mathbf{x}. \quad (4-15)$$

Now,

$$-K_1 \sin 2\theta_1 + A \sin(\theta_1 - \theta_2) + H_y M_1 \cos \theta_1 - H_z M_1 \sin \theta_1 = -\sigma_0, \quad (4-16a)$$

$$(K_2 + \mu_0 M_2^2) \sin 2\theta_2 - A \sin(\theta_1 - \theta_2) + H_y M_2 \cos \theta_2 - H_z M_2 \sin \theta_2 = \sigma_0. \quad (4-16b)$$

Note that, for the sake of simplifying calculations, the reduced values of K and A are used in Equations 4-14 and 4-16. Furthermore, to gain a clearer understanding of its physics, we assume that the in-plane magnetic anisotropy is significantly larger than the out-of-plane magnetic anisotropy, i.e., $K_2 \gg K_1$. Consequently, the perpendicular component of the \mathbf{M}_2 can be treated as a small one, denoted as:

$$\theta_2 = \pi/2 + \Delta\theta_2 \sim \pi/2, \quad (4-17)$$

$$\sin \theta_2 = \sin(\pi/2 + \Delta\theta_2) = \cos \Delta\theta_2 = 1. \quad (4-18)$$

If the perpendicular component of the \mathbf{M}_2 is minimally affected by the coupling

field induced by \mathbf{M}_1 and no external magnetic field is applied, Equation 4-14b can be simplified as:

$$2(K_2 + \mu_0 M_2^2) \cos \theta_2 = -\sigma_0 \quad (4-19)$$

By letting $K'_2 = K_2 + \mu_0 M_2^2$, we obtain Equation 4-1a, which can be simplified as:

$$-K_1 \sin 2\theta_1 + A(\sin \theta_1 \cos \theta_2 - \cos \theta_1 \sin \theta_2) = -\sigma_0. \quad (4-20)$$

$$-K_1 \sin 2\theta_1 - A \sin \theta_1 \sigma_0 / 2K'_2 - A \cos \theta_1 = -\sigma_0. \quad (4-21)$$

This is Equation 4-1b.

To calculate magnetization switching driven by the magnetic field while applying currents, we need to revisit Equations 4-14 and 4-16 and take differentials.

Thus, we have:

$$\begin{aligned} \begin{bmatrix} -1 \\ -1 \end{bmatrix} d\sigma &= \begin{bmatrix} -2K_1 \cos 2\theta_1 + A \cos(\theta_1 - \theta_2) - H_y M_1 \sin \theta_1 - H_z M_1 \cos \theta_1 \\ -A \cos(\theta_1 - \theta_2) \end{bmatrix} d\theta_1 + \\ &\begin{bmatrix} -A \cos(\theta_1 - \theta_2) \\ 2K'_2 \cos 2\theta_2 + A \cos(\theta_1 - \theta_2) - H_y M_2 \sin \theta_2 - H_z M_2 \cos \theta_2 \end{bmatrix} d\theta_2, \end{aligned} \quad (4-22a)$$

$$\begin{aligned} \begin{bmatrix} -1 \\ 1 \end{bmatrix} d\sigma &= \begin{bmatrix} -2K_1 \cos 2\theta_1 + A \cos(\theta_1 - \theta_2) - H_y M_1 \sin \theta_1 - H_z M_1 \cos \theta_1 \\ -A \cos(\theta_1 - \theta_2) \end{bmatrix} d\theta_1 + \\ &\begin{bmatrix} -A \cos(\theta_1 - \theta_2) \\ 2K'_2 \cos 2\theta_2 + A \cos(\theta_1 - \theta_2) - H_y M_2 \sin \theta_2 - H_z M_2 \cos \theta_2 \end{bmatrix} d\theta_2. \end{aligned} \quad (4-22b)$$

Figure 4-3 illustrates calculation results of \mathbf{M}_1 switching induced by the perpendicular magnetic field. Calculation parameters used here are $K_1 = 1$, $K'_2 = K_2 + \mu_0 M_2^2 = 2$, $M_1 = M_2 = 1$, and $A = -0.7$ representing ferromagnetic coupling, and $A = 0.7$ representing antiferromagnetic coupling.

It is important to note that during this calculation, the essence lies in finding the possible combinations of M_z , H_z , M_y , and σ . It is necessary to calculate the variation of θ with respect to σ at a very small H_z and examine if there is a discontinuity in θ between adjacent values to determine the critical value of σ . If σ is smaller than the critical value,

the state is valid, resulting in a set of M_z , H_z , M_y , and σ values. If σ is larger than the critical value, the state is prohibited. By classifying the states, we can obtain the dependence of M_z on H_z as shown in Figure 4-3. By further analyzing the horizontal shift of the hysteresis loop center, we can determine the efficiency of the SOT-induced effective perpendicular field.

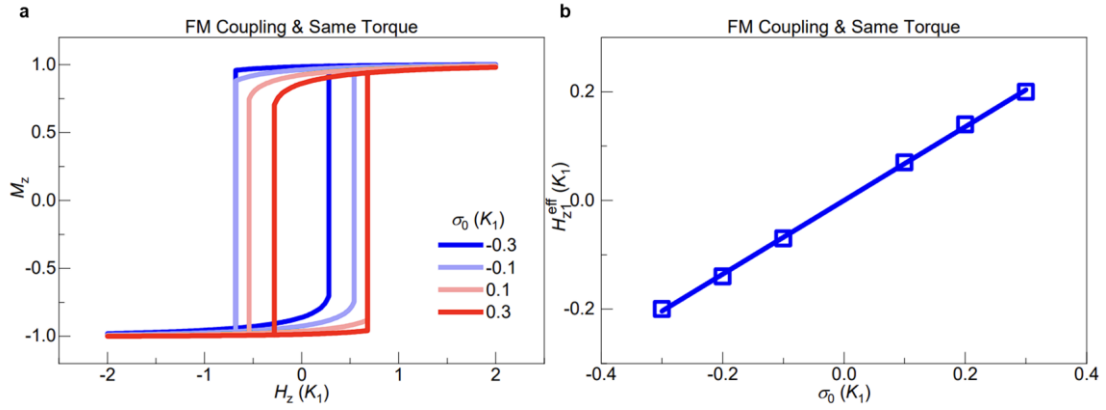


Figure 4-3 Calculations of the generation efficiency of the effective perpendicular field. Here, no y -direction magnetic fields are applied, and in-plane magnetization is initiated along the $+y$ direction. (a) Switching of perpendicular magnetization by z -direction magnetic field when the current is applied. (b) Efficiency of the current-generated effective perpendicular field [305].

4.2.2 Sample fabrication and measurements

The Type-T magnetic multilayers used in the study are as follows:

Sample A: SiO₂||Pt(5)/Co(1)/Pt(0.6)/Ir(2)/Co(1.8)/W(3)Pt(1 nm)

Sample B: SiO₂||Pt(5)/Co(1)/Pt(0.6)/W(0.6)/Co(1.8)/Ir(2)/Pt(1 nm)

Sample C (control sample): SiO₂||Pt(5)/Co(1)/Pt(0.6)/Ir(2)/W(2)/Pt(1 nm).

The multilayers are deposited using magnetron sputtering (ULVAC MPS-4000-HC7), with SiO₂ substrate. Subsequently, standard UV lithography and argon ion etching are employed to fabricate crossbar devices with a width of 20 μm and a length of 200 μm . Pt(5)/Au(80 nm) electrodes are deposited to connect the terminals of the Hall bars. VSM is used to measure the magnetic hysteresis loops of the multilayers.

Keithley 2400 is used to provide the current, Keithley 2182 is used to detect the Hall voltage, and a three-dimensional magnetic field probe station is used to apply the magnetic field. All measurements were conducted at room temperature.

Among all multilayers, the Pt(5)/Co(1)/Pt(0.6) segment is used to provide perpendicular magnetic anisotropy. Pt and W have significantly large but opposite spin Hall angles [101,136], while Ir, as a commonly used exchange coupling intermediate material, has a much smaller spin Hall angle [306] than to Pt and W. Consequently, the two Co magnetization in Sample *A* experience SOTs in the same direction, whereas the two Co magnetization in Sample *B* experience SOTs in opposite directions.

4.3 Experimental results and discussions

The atomic and magnetic structures of the samples are shown in Figure 4-4. Figure 4-4(a) presents a cross-sectional view of sample *A*, demonstrating the uniformity and flatness of each layer on a large scale. Figure 4-4(b) shows a high-angle angular dark field (HAADF) image obtained through scanning transmission electron microscopy (STEM). Figure 4-4(c-f) display the energy-dispersive spectrum (EDS) of each element, where the signals from the Co layers on either side of the Ir layer are prominent, with the upper Co layer being thicker than the lower Co layer. The positions of the Pt and W layers are consistent with the design. Figure 4-4(g-h) illustrate the magnetic hysteresis loops of sample *A* and sample *B*, providing evidence for the Type-T magnetic anisotropy of the samples.

The structures of samples *A*, *B*, and *C* are systematically optimized to achieve the desired magnetic anisotropy and interlayer coupling. Firstly, it is necessary to determine the appropriate thickness of the perpendicular Co layer and in-plane Co layer. For example, in the Type-T magnetic multilayer Pt(5)/Co(1)/Pt(1)/Ir(2)/Co(1.8)/W(1

nm), both perpendicular and in-plane magnetic anisotropy coexist. Next, while maintaining the Type-T magnetic anisotropy, it is necessary to finely adjust the thickness of the intermediate layers to achieve maximum interlayer coupling. This led to the final optimized structure of the main sample *A*: Pt(5)/Co(1)/Pt(0.6)/Ir(2)/Co(1.8)/W(2)/Pt(1 nm).

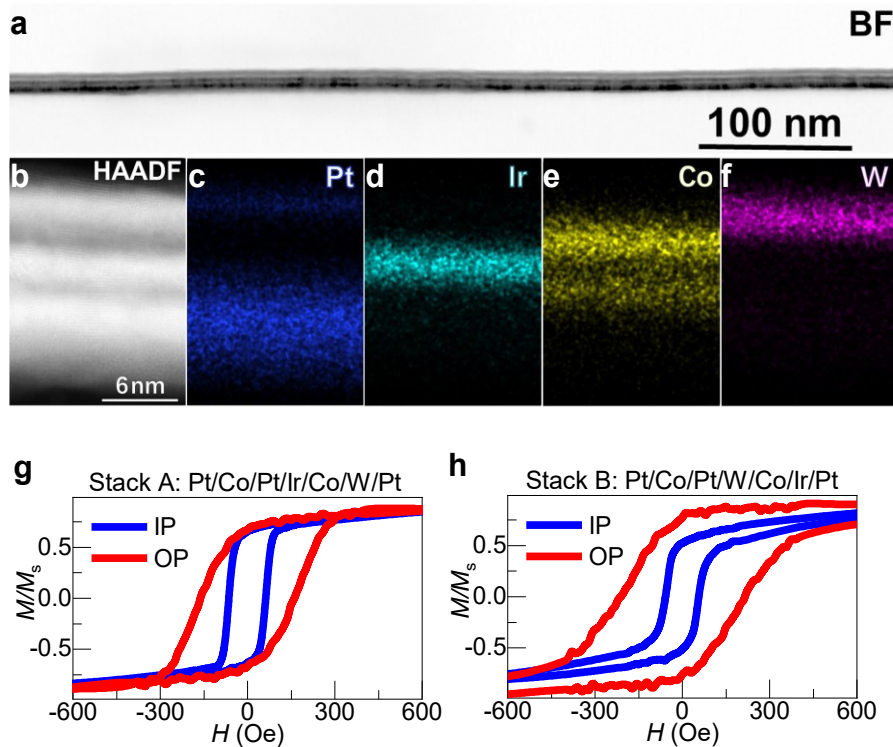


Figure 4-4 Atomic and magnetic structures of the Type-T magnetic multilayers. (a) Bright-field image of stack *A*. (b) HAADF image of stake *A*. (c-f) EDS mapping for each elements of stack *A*. (g) Hystereses of stake *A*. (h) Hystereses of stake *B* [305].

Subsequently, the in-plane anisotropy segment Ir/Co/W is transformed into W/Co/Ir to change the direction of SOT experienced by the in-plane layer. In this case, it is also necessary to optimize the thickness of W to enhance interlayer coupling while maintaining the Type-T magnetic anisotropy. Figure 4-5 illustrates the optimization process of the main sample.

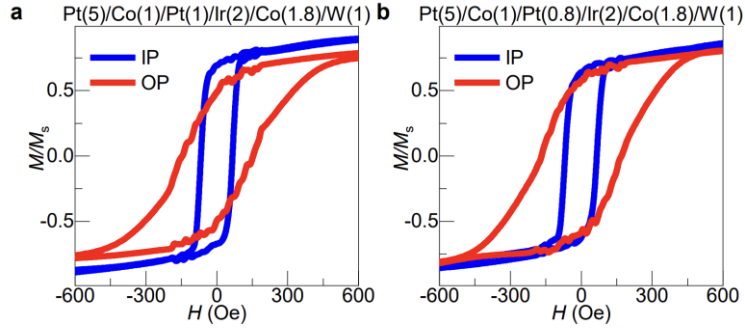


Figure 4-5 Optimization of sample magnetic structures. (a) Determination of the magnetic layers thicknesses. (b) Adjustment of the middle layers thicknesses. Notice that the Type-T magnetic anisotropy is preserved during these two optimization processes [305].

All multilayer films are fabricated into crossbar devices with a width of $20\ \mu\text{m}$ and a length of $200\ \mu\text{m}$ for SOT-induced perpendicular magnetization switching experiments. As shown in Figure 4-6, when an y -direction magnetic field, H_y is applied. A 50 ms pulse current, I_y , is swept between $\pm 35\ \text{mA}$, following by the application of a small current of $1\ \text{mA}$ to measure the AHE resistance, R_{xy} . The magnitude of R_{xy} is proportional to the z -component of \mathbf{M}_1 . This process is repeated while varying H_y between $\pm 340\ \text{Oe}$. For ease of analysis, the hysteresis loops corresponding to $H_y = 0$ and $\pm 300\ \text{Oe}$ are extracted from Figure 4-6, and the dependence of ΔR_{xy} on H_y at $I_y = 0$ is plotted in Figure 4-7. The positive and negative signs represent counterclockwise and clockwise magnetization switching, respectively.

As shown in Figure 4-7, both samples *A* and *B* achieved field-free switching. This is due to the in-plane \mathbf{M}_2 providing an in-plane effective field for the perpendicular \mathbf{M}_1 , fulfilling the requirements for Type-Z switching. The coupling type between \mathbf{M}_1 and \mathbf{M}_2 can be determined by analyzing the dependence of the field-free switching polarity on history.

When a sufficiently large in-plane magnetic field is applied (e.g., $\pm 300\ \text{Oe}$), the in-plane \mathbf{M}_2 aligns parallel to the field direction, and the switching polarity is determined by the applied magnetic field. As the field decreases from the large-field

regime to zero, the in-plane \mathbf{M}_2 maintains its orientation. Now, the switching polarity is determined by the in-plane effective field provided by the in-plane \mathbf{M}_2 .

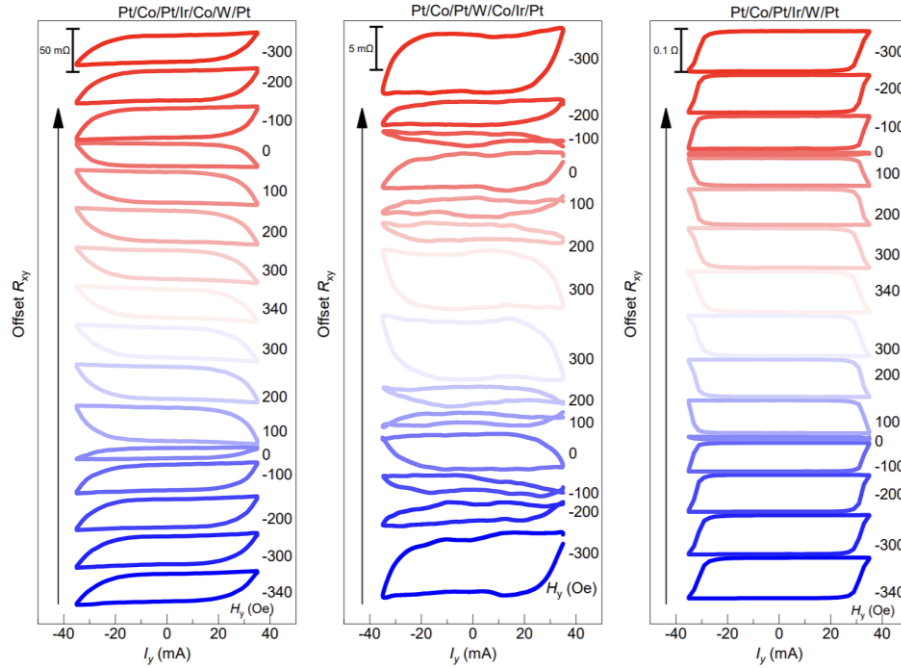


Figure 4-6 SOT-induced perpendicular magnetization switching in sample *A*, *B* and *C* [305].

In Figure 4-7(a), the polarity of the field-free hysteresis loop for sample *A* is the same as that of the previous loop, indicating that the in-plane effective field has the same direction as the previous applied magnetic field. This suggests ferromagnetic coupling between \mathbf{M}_1 and \mathbf{M}_2 . On the other hand, in Figure 4-7(b), the polarity of the field-free hysteresis loop for sample *B* is opposite to that of the previous large-field regime, indicating that the in-plane effective field is opposite to the previous applied magnetic field. This suggests antiferromagnetic coupling between \mathbf{M}_1 and \mathbf{M}_2 .

Interlayer coupling in metallic systems is generally attributed to the RKKY mechanism, which is highly sensitive to the interlayer spacing. Different thicknesses of intermediate layers, Pt(0.6)/Ir(2) for sample *A* and Pt(0.6)/W(0.6) for sample *B*, result in ferromagnetic and antiferromagnetic couplings, respectively.

As shown in Figure 4-7(c,d), by observing the intersection of the hysteresis

loops and the $\Delta R_{xy} = 0$ line, the in-plane effective fields for samples *A* and *B* are determined to be 10 Oe and 50 Oe, respectively. Although the hysteresis loops of samples *A* and *B* are not as steep as that of sample *C*, the switching is still deterministic. The smoothness of the hysteresis loops may be attributed to the non-uniform distribution of the perpendicular magnetic anisotropy across different parts of the device. To enhance the magnitude and speed of the switching, larger write currents can be applied. On the other hand, the smoothness of the hysteresis loops demonstrates the presence of many intermediate states, which can be utilized as artificial synapses for storing weight values in neuromorphic computing.

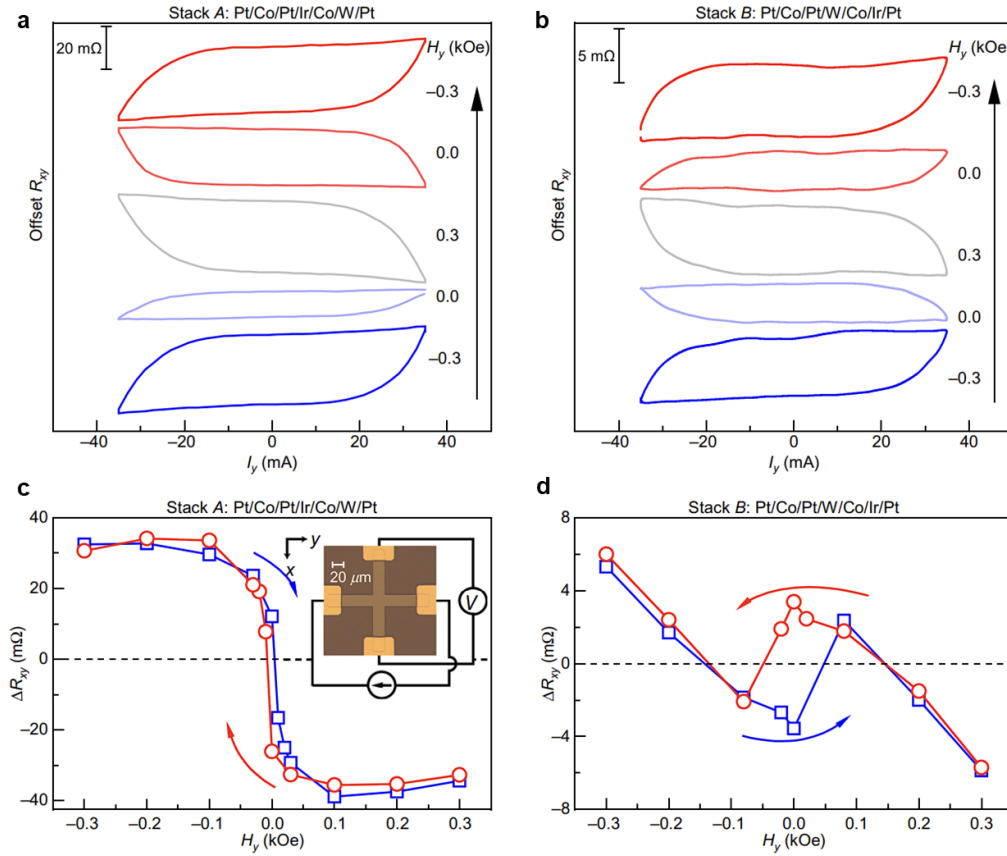


Figure 4-7 SOT-induced perpendicular magnetization switching in sample *A* and *B*. Current-induced changes of the Hall resistance of sample *A* and *B* under the *y*-direction magnetic field is shown in (a) and (b), respectively. Magnetic field dependence of changes of the Hall resistance of sample *A* and *B* is shown in (c) and (d), respectively. Clockwise switching is noted as negative and counterclockwise switching is noted as positive [305].

Next, the measurement of the effective perpendicular field in samples *A*, *B*, and the control sample *C* is conducted in the experiment of perpendicular magnetic field-driven perpendicular magnetization switching. Firstly, the applied field H_y is fixed (for example, +300 Oe as shown in Figure 4-8(a)), and then H_z is swept back and forth between ± 340 Oe while applying a larger current (for example, ± 20 mA) I_y to measure R_{xy} . The current-induced effective perpendicular field is manifested as a horizontal shift of the hysteresis loop, denoted as $H_z^{\text{eff}} \equiv (H_{c1} + H_{c2})/2$, where H_{c1} and H_{c2} are the coercive fields of the hysteresis loop. Figure 4-8(b) presents the parabolic dependence of the average coercive field $H_c \equiv (H_{c1} - H_{c2})/2$ on I_y and the linear dependence of the horizontal shift of the hysteresis loop H_z^{eff} on I_y , indicating that the effective perpendicular field is generated by SOT. By calculating the slope of $H_z^{\text{eff}} - I_y$, the efficiency χ of generating the effective perpendicular field by SOT can be obtained. The dependence of χ on H_y in samples *A*, *B*, and *C* is summarized in Figure 4-8(c-e).

In Figure 4-8(a), it appears that under large current, only one side of the hysteresis loop is decreasing while the other side remains nearly unchanged. This characteristic is also observed in the macrospin model simulation. This phenomenon arises from the influence of SOT on the horizontal shift of the loop, H_z^{eff} , and the average coercive field, H_c . H_z^{eff} linearly depends on the applied torque, while H_c exhibits a parabolic dependence on the applied torque. The latter is partly due to the torque reducing the coercive field, H_c , of the $R_{xy} - H_z$ loop and partly due to heating effects.

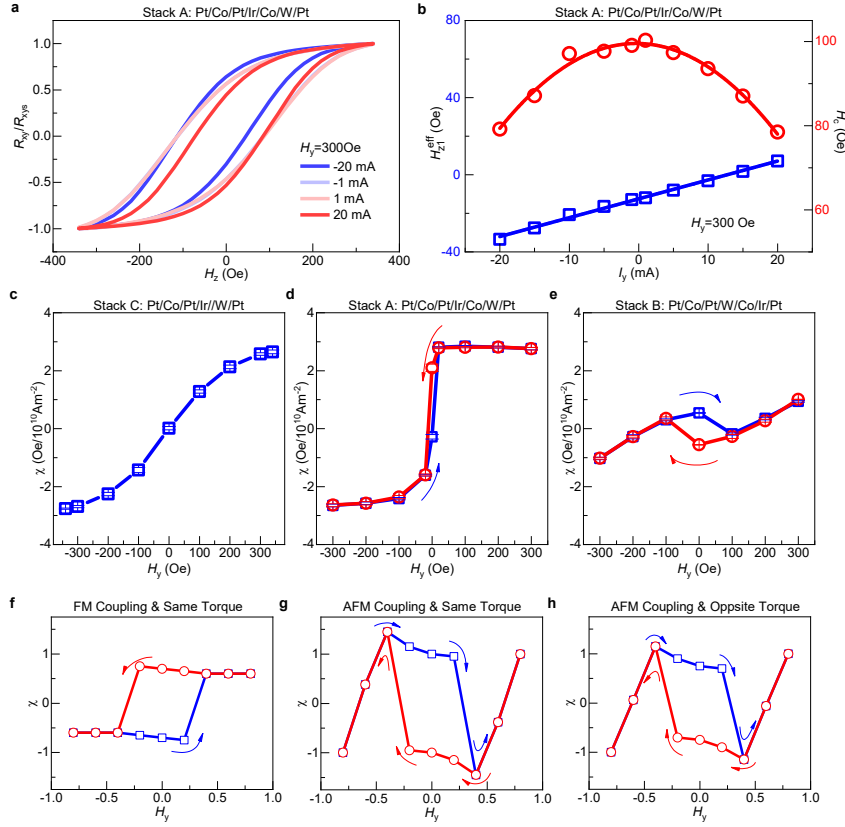


Figure 4-8 Measurements of the effective perpendicular field in *A* and *B*. (a) Perpendicular magnetization switching of sample *A* by the perpendicular magnetic field while applying currents and a 300 Oe *y*-direction field. (b) Currents dependence of the Hall resistance shift and the demagnetization field of sample *A* when the *y*-direction field is 300 Oe. (c-e) The *y*-direction field dependence of the current-induced effective perpendicular field efficiency of sample *A*, *B* and *C*, respectively. (f-h) Simulation of the current-induced effective perpendicular field efficiency in different scenarios [305].

For the control sample *C*, as H_y increases, χ initially increases and saturates when H_y approaches 300 Oe. Considering previous work [175], under the influence of DMI, Néel-type domain walls are formed in this system, and SOT acting on the Néel-type domain walls generates H_z^{eff} . When $H_y \geq H_{DMI}$, the domain wall uniform into the same form ($\uparrow \rightarrow \downarrow$ or $\downarrow \leftarrow \uparrow$), and the efficiency, χ , saturates. However, when $H_y = 0$, both forms of domain walls ($\uparrow \rightarrow \downarrow$ and $\downarrow \leftarrow \uparrow$) coexist in the system, and SOT applies H_z^{eff} with equal magnitude but opposite directions on these two types of domain walls, resulting in $\chi = 0$. These typical features can all be observed in sample *C*. It is worth

noting that in this experiment, the H_{DMI} of Pt/Co/Pt is approximately 300 Oe, while in the literature, the H_{DMI} of Pt/Co/MgO is about 5000 Oe [175]. Consequently, the H_{DMI} in our case is significantly reduced, and the χ generated by the in-plane magnetic coupling is not completely overshadowed by the DMI mechanism.

For samples *A* and *B*, χ depends on the history of H_y and exhibits a $\chi - H_y$ hysteresis loop. Comparing the loops of samples *A* and *C*, χ_A is significantly greater than χ_C when $H_y < 100$ Oe. When comparing samples *A* and *B*, the loops have opposite polarities at zero field due to the antiferromagnetic coupling between the two magnetic layers in sample *B*. To perform a quantitative analysis, χ can be divided into two components, namely χ_z and χ_{DMI} , representing the contributions from the SOT mechanism and the domain wall DMI mechanism, respectively. When $H_y = \pm 10$ Oe, the SOT switching in sample *A* disappears, which means that when $H_y = 0$, the in-plane effective field H_{y1}^{eff} experienced by the perpendicular Co is approximately ± 10 Oe. In the control sample *C*, only χ_{DMI} exists. Both sample *A* and sample *C* have the same Pt/Co/Pt perpendicular segment. Therefore, the χ_{DMI} at $H_y = 0$ in sample *A* is equal to the $\chi_{\text{DMI}} = 0.15$ and -0.13 Oe/ 10^{10} Am $^{-2}$ when $H_y = \pm 10$ Oe in sample *C*. Both values are much smaller than the total $\chi = 2.1$ and -0.28 Oe/ 10^{10} Am $^{-2}$ at $H_y = 0$ in sample *A*. This confirms that the SOT mechanism $\chi_z = \chi - \chi_{\text{DMI}} = 1.95$ and -0.15 Oe/ 10^{10} Am $^{-2}$ dominates the generation of effective perpendicular field. Furthermore, when $H_y = 0$, the signs of χ_z and χ_{DMI} in sample *A* are the same, demonstrating that when both magnetic layers experience SOTs in the same direction, the two mechanisms cooperate to enhance the switching efficiency.

For sample *B*, the in-plane effective field H_{y1}^{eff} experienced by the

perpendicular Co layer is approximately ± 50 Oe. The χ_{DMI} at $H_y = 0$ in sample *B* is equal to the $\chi_{\text{DMI}} = -0.71$ and 0.66 Oe/ 10^{10} Am $^{-2}$ at $H_y = \mp 50$ Oe in sample *C*. However, the total χ at $H_y = 0$ in sample *B* is $\chi = -0.56$ and 0.54 Oe/ 10^{10} Am $^{-2}$. Therefore, $\chi_z = \chi - \chi_{\text{DMI}} = 0.15$ and -0.12 Oe/ 10^{10} Am $^{-2}$, with the opposite sign to χ_{DMI} . This demonstrates that when the two magnetic layers in sample *B* experience SOTs in opposite directions, the two mechanisms counteract each other, leading to a higher critical current.

Figure 4-8(f-h) present the χ - H_y dependencies calculated based on Equation 4-22. The calculated results successfully reproduce (1) the dependence of χ on H_y in the Type-T magnetic trilayer, and (2) opposite polarities of hysteresis loops with ferromagnetic and antiferromagnetic couplings. The agreement between the calculations using the macrospin model and the experimental results validates the proposed SOT-induced effective perpendicular field mechanism in this chapter.

In this work, the maximum χ obtained in sample *A* at zero field is $\chi = 2.1$ Oe/ 10^{10} Am $^{-2}$. Comparing with previous measurements, the χ at 170 K in WTe $_2$ /Fe $_3$ GeTe $_2$ bilayer [148] is approximately 6.0 Oe/ 10^{10} Am $^{-2}$, in Cu-Pt/Co-Pt bilayer [201] is approximately 0.37 Oe/ 10^{10} Am $^{-2}$, and in ferromagnet/Ti/CoFeB/MgO systems [171] is approximately 0.6 Oe/ 10^{10} Am $^{-2}$. The results obtained in this chapter are in the same order of magnitude (1 Oe/ 10^{10} Am $^{-2}$) as those mentioned above and even larger than some of them. It is worth noting that in previous literature reports, H_z^{eff} significantly increases only when the current exceeds a certain critical value. However, in this work, H_z^{eff} linearly depends on the current, which not only indicates a different physical origin of the effective perpendicular field in this system compared to previous reports but also reveals the potential to achieve high SOT efficiency with small currents. Due to the completely different physical

origins, it is challenging to directly compare the numerical values of these χ . The reason for obtaining high χ in this work is that, in addition to the conventional mechanism of SOT generating H_z^{eff} (such as the DMI mechanism in the control sample), the in-plane layer is driven by SOT to tilt along the perpendicular direction, providing additional H_z^{eff} for the perpendicular layer under interlayer coupling. In sample *A*, the two mechanisms synergistically enhance χ , while in sample *B*, the two mechanisms counteract each other, reducing χ , as shown in Figure 4-8(c-e).

In this study, to simplify and clarify the physical picture, the two metallic layers, HM_i (Pt and W), on both sides of the magnetic layers are used to provide SOTs in the same direction to the two magnetic layers. To apply this mechanism in MTJs, we propose another structure of perpendicular layer/ HM_1 / HM_2 /in-plane layer, where the two metallic layers, HM_i (e.g., Pt and W), are used to provide SOTs in the same direction to the two magnetic layers, while utilizing exchange or dipole interaction to provide interlayer coupling. In this structure, the upper surface of the magnetic layers is freed, allowing it to be combined with MgO barriers and another magnetic electrode. Recently, Type-T magnetic multilayers with a structure of perpendicular layer/ HM /in-plane layer have been employed in field-free SOT-MRAM [248]. However, in that work, the two magnetic layers experience SOTs in opposite directions, which is not favorable to reduce the critical current density. This drawback can be overcome by utilizing the proposed dual-metal structure. Furthermore, in the Type-T magnetic multilayer, the ferromagnetic layer can also provide spin current, and several works have demonstrated its feasibility [171,172,298]. In this case, an intermediate layer such as Ru or Ir can only provide intermediate coupling, while the ferromagnetic layer is utilized to provide the spin current. In conclusion, the ideal scenario of both magnetic layers experiencing spin current with the same polarization direction is feasible through structural design and

material optimization.

4.4 Chapter summary

In this chapter, we mainly explore the generation of effective perpendicular field using SOT in Type-T magnetic trilayers. We achieve efficient SOT-driven field-free perpendicular magnetization switching in $\text{SiO}_2||\text{Pt}/\text{Co}/\text{Pt}/\text{Ir}/\text{Co}/\text{W}/\text{Pt}$ Type-T magnetic crossbars. The in-plane magnetic layer not only provides in-plane coupling field to assist field-free perpendicular magnetization switching but also contributes additional effective perpendicular field to facilitate efficient switching. By comparing with the control sample, which without any in-plane magnetic layer, we clearly observe the contribution of the effective perpendicular field. Our work demonstrates the tilting of in-plane magnetization driven by SOT under interlayer coupling, helps the perpendicular magnetization switching. This provides a foundation for the development of novel and efficient perpendicular SOT-MRAM and spin logic devices. The specific experimental procedure in this chapter is as follows:

(1) We construct a macrospin model for the Type-T magnetic anisotropy system, which clarify the deviation of the in-plane magnetization towards the perpendicular direction under SOT. With the interlayer coupling, the perpendicular magnetization experiences an additional effective perpendicular field, which depends on the direction of SOT experienced by the in-plane layer. When both the in-plane layer and the perpendicular layer experience SOTs in the same direction, the effective perpendicular field assists the perpendicular magnetization switching, thereby reducing the critical current density.

(2) The samples, namely Sample *A*: $\text{SiO}_2||\text{Pt}/\text{Co}/\text{Pt}/\text{Ir}/\text{Co}/\text{W}/\text{Pt}$, Sample *B*: $\text{SiO}_2||\text{Pt}/\text{Co}/\text{Pt}/\text{W}/\text{Co}/\text{Ir}/\text{Pt}$, and control sample *C*: $\text{SiO}_2||\text{Pt}/\text{Co}/\text{Pt}/\text{Ir}/\text{W}/\text{Pt}$, are grown

using magnetron sputtering deposition. The fabrication process involves standard UV lithography and argon ion etching to create micron-sized Hall bars. The magnetic anisotropy of the thin films is confirmed using a VSM.

(3) Due to the presence of the in-plane magnetic layer, the perpendicular magnetization experiences an in-plane effective field, which enables the SOT-driven field-free perpendicular magnetization switching.

(4) The total effective perpendicular field induced by SOT in the system is obtained by measuring the horizontal loop shift of the field-driven perpendicular magnetization switching hysteresis while applying currents. By varying the magnitude of the in-plane magnetic field, the dependence of the efficiency of SOT-induced effective perpendicular field on the in-plane magnetic field is determined. By comparing sample *A*, where the perpendicular and in-plane magnetizations experience the same direction SOT, with sample *B*, where they experience opposite directions SOT, and with sample *C*, which lacks an in-plane magnetic layer, the contribution of SOT-driven in-plane magnetization tilt to the generation of effective perpendicular field is distinguished. The results are further compared with the macrospin simulation, providing additional confirmation of the existence of SOT-induced effective perpendicular field.

This chapter of work is conducted with several colleges and their contributions are as follows: I grew the stacks, fabricated the devices, conducted magneto transport measurements, constructed the macrospin model and analyzed all the results. Jing DONG provided assistant during the stack growth. Chenyang GUO and Mingkun ZHAO helped with the device fabrications. Xiao WANG, Yu ZHANG and Guoqiang YU contributes to the transport measurements. Caihua WAN and Xiufeng HAN led and were involved in all aspects of the research.

5 Sign-changeable TMR effect in magnetic tunnel junctions

5.1 Research background

The TMR effect in MTJs is one of the cornerstones of spintronics, supporting extensive applications in MRAMs, magnetic sensors, spin logic devices, and neuromorphic computing. In 2003, Ney et al. [273] pioneered the use of single MTJ to create programmable logic gates, significantly advancing the development of spin logic devices. However, the implementation of logic functionality in this design requires specific magnetization configuration of both the free layer and the reference layer in the MTJ. Switching the reference layer not only consumes additional energy but also reduces the device's thermal stability. It is reported that the multifunctional logic gate can also be realized in magnetic heterostructures where the perpendicular magnetization of the free layer is switched by the spin-orbit torque and controlled by an effective in-plane field [118,119]. However, the readout of such gates relies on AHE and is less sensitive compared to TMR.

Recently, a novel proposal [307] emerges to build such spin logic devices by utilizing MTJs with voltage-controllable and sign-reversible TMR effect. Combining two of these MTJs and one current comparator, a real-time reprogrammable logic gate can be built, in which all four functions: AND, OR, NAND and NOR can be realized and switchable by initializing only the free-layer magnetization of the two MTJs [307]. To realize such spin logic function, a MTJ system with large sign-reversible TMR at RT is indispensable.

The sign-reversed TMR phenomena have been reported in several systems due to various mechanisms. For instance, the TMR ratio of the NiFe/composite

Ta₂O₅/Al₂O₃/NiFe MTJs varies from +1% to -4% with different bias at RT [308]. Its sign inversion is resulted from different densities of states (DOS) at two electrode/barrier interfaces. In Ni/NiO/Co nanowires, the TMR ratio can be inverted by voltage due to the matching of the energy of localized states in NiO, which is sensitive to the quality of the barrier, with the Fermi energy of ferromagnetic electrodes [309]. In La_{0.67}Sr_{0.33}MnO₃(LSMO)/SrTiO₃(STO)/SrO/Co MTJs, their TMR ratio varies from +8% to -15% with applied voltage at 85 K [310]. The sign of TMR ratio is found to be very sensitive to the interface spin polarization at SrTiO₃/Co interface with one atomic insertion layer of TiO₂ or SrO as well as the oxygen content in the barrier. In addition, MTJs with Fe₃O₄ electrode and MgO barrier also show a reversal TMR sign effect. Depending on the materials used for the second electrode (Co [311], CoFeB [312] and Fe [313]), the maximum negative TMR have been demonstrated to be -8.5%, -12% and -9.6% at RT, respectively. Recently, the multiferroic tunnel junctions (MFTJs) combining the ferroelectric tunnel barrier with ferromagnetic electrodes attract intensive interests. In such systems, TMR and tunneling electroresistance (TER) coexist and the sign of TMR can be modulated by changing the ferroelectric polarization of ferroelectric tunnel barrier. In Co/PbZr_{0.2}Ti_{0.8}O₃(PZT)/LSMO MFTJ, the TMR ratio varies from +4% to -3% with a ±3 V polarizing voltage pulse at 50 K (Figure 5-1) [90]. In LSMO/ Polyvinylidene fluoride(PVDF) or P(VDF-TrFE)/Co MFTJs, the TMR ratio varies from +8.3% to -12.5% with a ±1.5 V polarizing voltage pulse at 10 K [314,315]. Note that LSMO is usually chosen as the ferromagnetic electrode to obtain high spin polarization and well-defined ferromagnetic/ferroelectric interfaces. However, the low Curie temperature of LSMO hampers its room-temperature applications. Another issue for the MFTJ is that the TMR will be suppressed if the ferroelectric barrier is too thick, since the transport mechanisms are different from direct tunnelling [316]. Thus, a trade-

off relating to an optimized thickness of the ferroelectric barrier must be taken into account to keep both effects sizable [315].

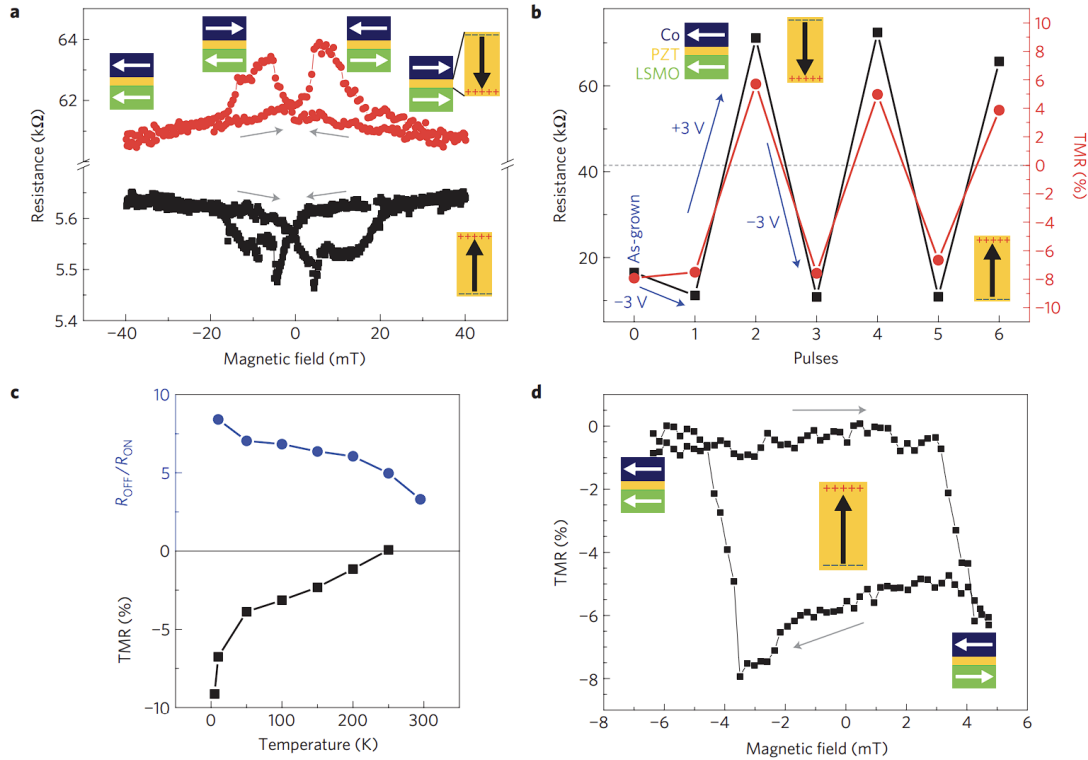


Figure 5-1 Tunnel magnetoresistance effect in MFTJ. There are four nonvolatile states in the Co/PZT/LSMO MFTJ since the TER and TMR effects are coupled in this system [90].

Although many systems have been demonstrated for the sign-reversal TMR effect, the amplitude of TMR is small and the operation temperature is low. Recently, Fe_4N has been demonstrated to have high negative spin-polarization [317–319], unique magnetic structure and low critical switching current density [235,236]. These merits co-make Fe_4N MTJs suitable for spintronic applications and also a potential candidate to achieve the sign-reversible TMR effect. In this chapter we have epitaxially grown $\text{Fe}/\text{MgAlO}_x/\text{Fe}_4\text{N}$ MTJ by molecular beam epitaxy (MBE). We have observed a voltage-dependent TMR ratio which can be modulated from +3.15% to -26.7% at RT, showing a superior performance than previous reported results. From first principal calculation, the sign-reversible TMR phenomenon is found to be relevant to the symmetry-dependent tunneling process between Fe and Fe_4N electrodes. The voltage-

controllable TMR signs and relatively large TMR ratios, especially at RT will contribute to develop the real-time reprogrammable spin logic gates for different spintronic applications. The main results of this chapter are now submitted and under review in ACS Appl. Electron. Mater.

5.2 Experimental and simulate results

5.2.1 Growth of high-quality multilayers

The MTJ stack consisting of MgO(001) substrate||MgO(10 nm)/Fe(45 nm)/MgAlO_x(3 monolayers, MLs)/Fe(7 nm)/MgAlO_x(12 MLs)/Fe₄N(3 nm)/Co(20 nm)/Au(10 nm) was deposited in a MBE system with a base pressure better than 1×10^{-10} torr. Firstly, the substrate was annealed at 700°C for 60 mins and 10 nm MgO seed layer was deposited. Then the first Fe layer was deposited at RT by e-beam evaporation and annealed *in situ* at 600°C for 30 mins to smooth the surface. The first 3 MLs (0.6 nm) thick MgAlO_x barrier was grown at about 70°C and the growth process was monitored by RHEED (Figure 5-2). Two-dimensional layer-by-layer growth of MgAlO_x was observed by RHEED intensity oscillation. The second 7 nm thick Fe layer was deposited at about 70°C and annealed *in situ* at 500°C for 20 mins follow by a second deposition of 12 MLs (2.5 nm) thick MgAlO_x barrier. For the growth of Fe₄N films, the Fe source was heated to 1250°C by Knudsen cell, and the substrate temperature was kept at 400°C; the nitrogen partial pressure in the chamber was set at 2×10^{-5} torr. The plasma cracker source (electron cyclotron resonance source) was used with the following characteristics: $V_{\text{anode}} = 400$ V, $V_{\text{extractor}} = -200$ V, $I_{\text{magnetron}} = 40$ mA. Finally, 20 nm Co layer was deposited above the Fe₄N to enhance the coercivity and 10 nm Au was used to prevent the films from oxidation. Another MTJ stack with MgO barrier consisting of MgO(001)||MgO(10 nm)/Fe(45 nm)/MgO(12

monolayer)/Fe₄N(3 nm)/Co(20 nm)/Au(10 nm) was also deposited through a similar procedure (Figure 5-3). More detailed MTJ growth conditions can be found elsewhere [56,57,320].

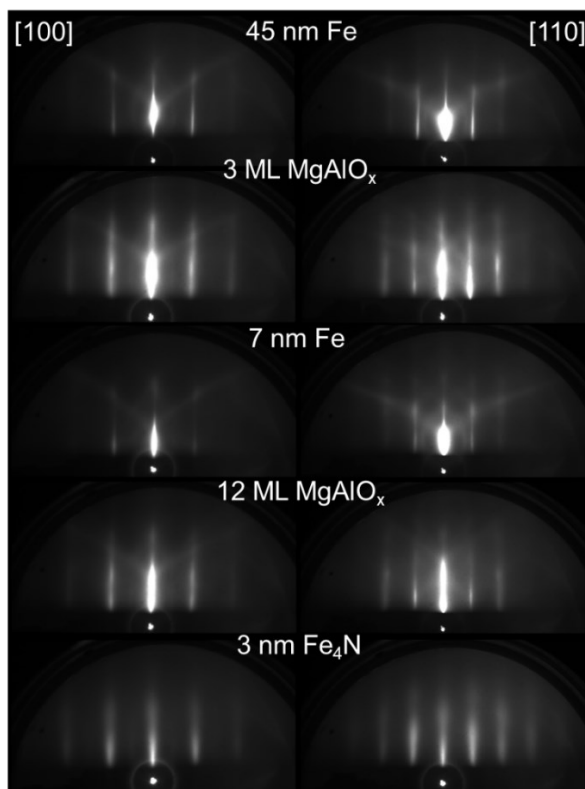


Figure 5-2 RHEED patterns of the MgAlO_x Fe₄N MTJ. Electron beam is injected along the [100] and [110] direction of the MgO substrate.

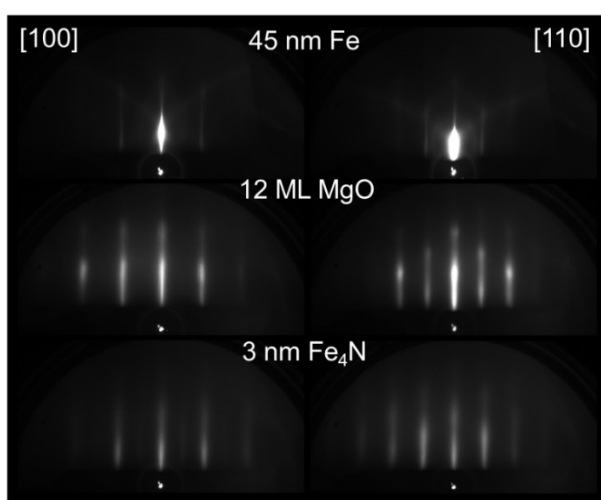


Figure 5-3 RHEED patterns of the MgO Fe₄N MTJ. Electron beam is injected along the [100] and [110] direction of the MgO substrate.

5.2.2 Structure analysis

I have collaborated with Xavier DEVAUX from IJL to characterize the structure of the samples using STEM. HR-STEM combined with spatially resolved electron energy loss spectroscopy (EELS) is performed by using a probe-corrected microscope JEOL ARM200F (cold FEG) equipped with a GATAN GIF quantum energy filter to reveal the structure and element distribution in the MTJ. The microscope is operated at 200 kV. High angle annular dark-field (HAADF), annular dark-field (ADF) and bright-field (BF) images are simultaneously recorded for investigating the heterostructure while only HAADF signal is recorded during EELS mapping. EELS spectrum images (SI) are recorded with a probe current of about 50 pA. Two EELS-SI are simultaneously recorded: one for the low-loss part containing the zero-loss, the other for the core loss, which allows advanced data post processing (correction of energy drift, multiple scattering corrections). A multivariate statistical analysis software (temDM MSA) is used to improve the quality of the STEM-EELS data by de-noising the core-loss SI before its processing to draw quantitative chemical maps [321]. Thin lamellas are extracted by focused ion beam (FIB) milling using an FEI Helios Nanolab 600i dual beam.

Figure 5-4(a-b) shows the HAADF images for MgAlO_x MTJ in a large and magnified scale, respectively. In Figure 5-4(a), one can observe sharp interfaces between MgAlO_x (in black contrast) and Fe or Fe_4N layers (in grey contrast). The MgAlO_x barrier layer appear quite flat and continuous, indicating a high quality of MTJ structure without any pinholes. The magnified image in Figure 5-4(b) further proves the epitaxial growth characters with well-aligned atomic arrays between Fe, MgAlO_x and Fe_4N layers. Bulk Fe_4N has a cubic antiperovskite structure, and the experimental lattice constant is 3.795 Å [322]. Despite the large lattice mismatch of 6.5% between

Fe_4N and MgAl_2O_4 (lattice constant 4.212\AA [322]), the crystalline orientation relationship can be determined to be $\text{Fe}[110]//\text{MgAlO}_x[100]//\text{Fe}_4\text{N}[100]$ combined with RHEED analysis (Figure 5-2). However, Co on Fe_4N exhibits large disorientated polycrystalline features. For MTJ with MgO barrier, one can also observe an epitaxial growth of Fe_4N on MgO (Figure 5-3 and Figure 5-5(a,b)), however the intensity of the RHEED appears weaker and more crystalline deformation can be found in the Fe_4N layer, which could be attributed to the larger lattice mismatch (11%) between Fe_4N and MgO.

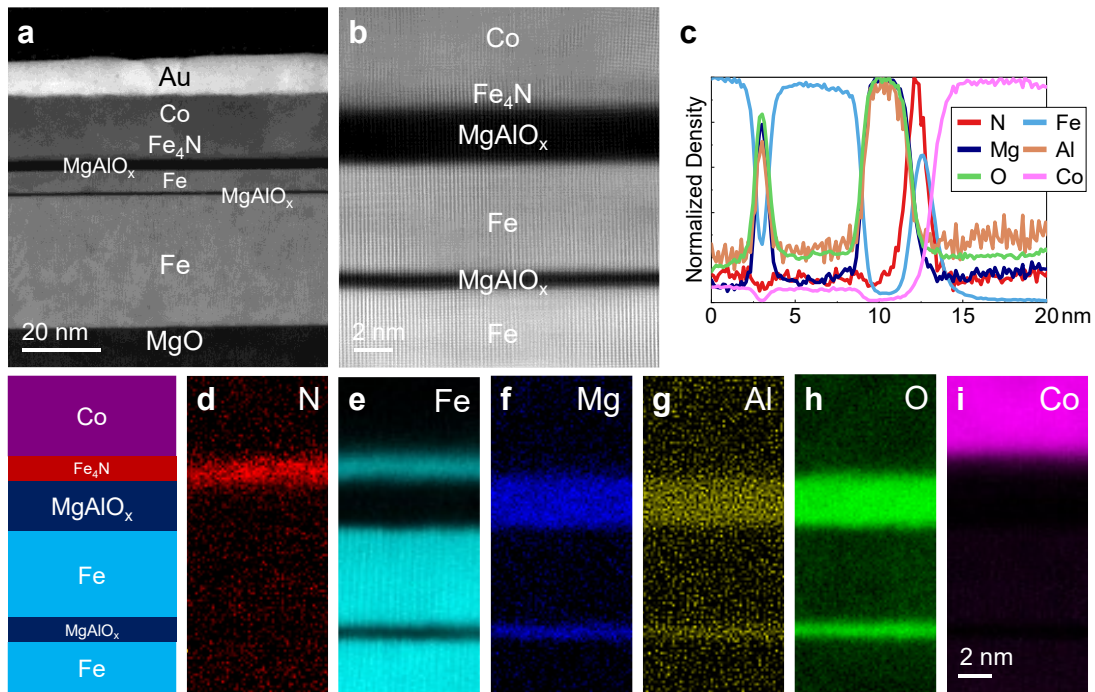


Figure 5-4 Atomic structures and chemical maps of the $\text{MgAlO}_x/\text{Fe}_4\text{N}$ MTJ. The STEM-HAADF images with different resolutions are shown in (a) and (b); The normalized elements density profile and elements maps extracted from STEM-EELS are shown in (c) and (d-i).

Figure 5-4(d-i) shows semi-quantitative chemical maps drawn by processing the EELS spectrum images. A sharp chemical interface is found between Fe and MgAlO_x layers. However, from the element mapping of N (Figure 5-4(d)), a partial N diffusion towards MgAlO_x barrier can be detected at $\text{MgAlO}_x/\text{Fe}_4\text{N}$ interface. This N diffusion can be also clearly evidenced by a large peak width (red line) in the element intensity

profiles compared with the Fe peak (blue line), as shown in Figure 5-4(c). For MgO MTJs, the situation of N diffusion is even pronounced. In Figure 5-5(d), one can observe that N can penetrate MgO barrier and reach bottom Fe/MgO interface. The diffusion of N could be attributed to the oxygen vacancy in the MgO and MgAlO_x barriers. Since the bond energy for Fe-N (350kJ/mol) < Mg-O (380kJ/mol) < Mg-N (400kJ/mol) < Al-O (510kJ/mol) < Al-N (650kJ/mol) [323], ionic N species tend to diffuse into MgO or MgAlO_x barrier to occupy oxygen vacancy position during Fe₄N growth. For MgAlO_x barrier, the formation of Al-N bonds can help to stop further diffusion of N inside the barrier. Nevertheless, the N diffusion can easily penetrate MgO barrier because of the low bond energy of Mg-N, which is comparable to Fe-N bond, thus resulting in an accumulation of N at the bottom Fe/MgO interface.

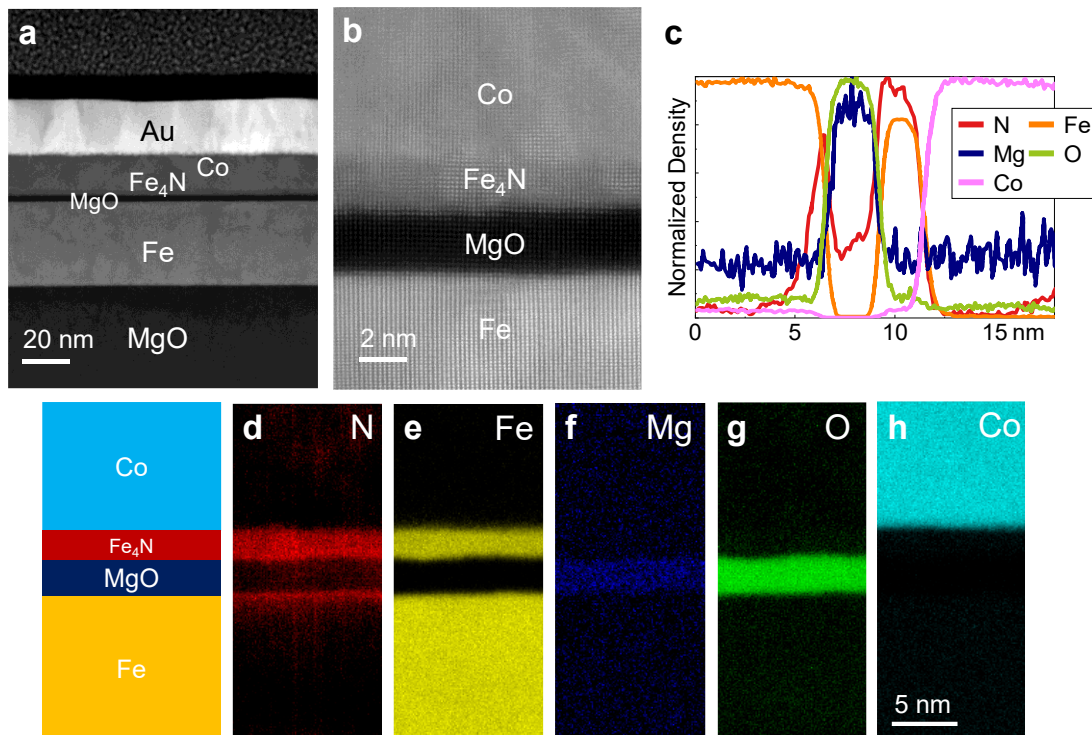


Figure 5-5 Atomic structures and chemical maps of the MgO Fe₄N MTJ. The STEM-HAADF images with different resolutions are shown in (a) and (b); The normalized elements density profile and elements maps extracted from STEM-EELS are shown in (c) and (d-h).

5.2.3 Transport measurements

The multilayers were patterned into junctions with the area size varying from $20 \times 20 \mu\text{m}^2$ (MgO junctions) to $30 \times 30 \mu\text{m}^2$ (MgAlO_x junctions) by standard ultraviolet lithography combined with Ar ion etching. The transport measurements were carried out in a cryostat (cooled by liquid Helium) with electrical magnets. A Keithley 2450 was used to apply the bias voltage to the MTJ and probe the current accordingly. The magneto-transport measurements have been performed by a dc two-probe configuration, where the negative bias corresponds to the electrons tunneling from the top to bottom electrode (Figure 5-6(a)).

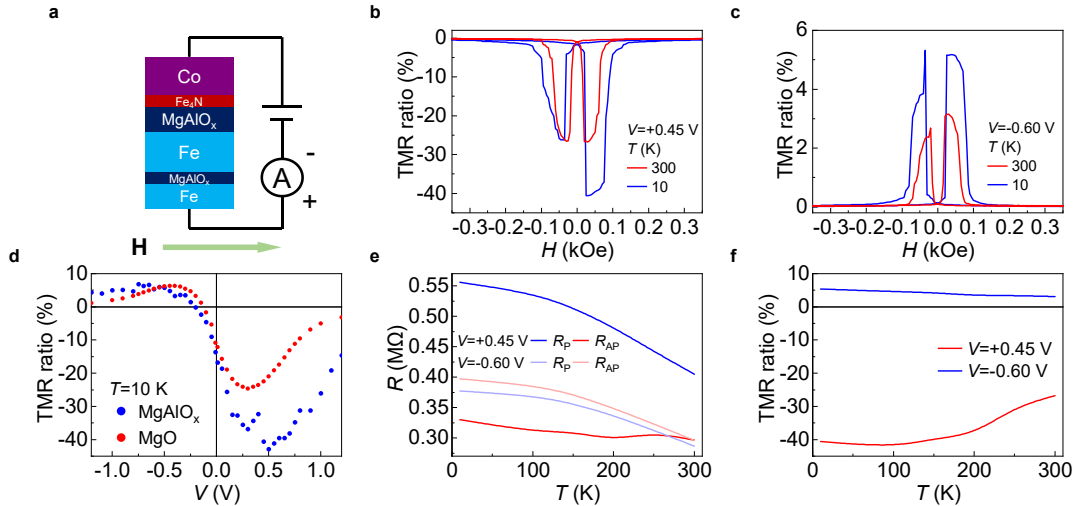


Figure 5-6 TMR measurement results of the MgAlO_x/Fe₄N MTJ. (a) Schematic of the measurement setup. (b-c) TMR curves measured at RT and 10 K for bias voltage $V = +0.45$ V and -0.60 V, respectively. (d) Voltage dependence of TMR ratios of Fe₄N MTJs with MgAlO_x and MgO barrier at 10 K. (e) Temperature dependence of the P and AP state resistance when $V = +0.45$ V and -0.60 V. (f) Temperature dependence of the TMR ratios when $V = +0.45$ V and -0.60 V.

Figure 5-6(b-c) shows the TMR curves measured at RT and 10K for bias voltage $V = +0.45$ V and $V = -0.6$ V, respectively. It is interesting to find that the TMR sign can be reversed with different voltage. At RT, the TMR can be modulated from -26% to $+3\%$. At 10K, the TMR sign reversal effect is quite enhanced from -40% to $+5\%$.

Here, both positive and negative TMR has been calculated by the definition of TMR ratio = $(R_{AP} - R_P)/R_P \times 100\%$, which limits the negative TMR ratio up to 100%. Our maximum negative TMR is approaching the reported highest negative TMR ratio (-36.5% at RT with the same TMR definition as ours) in CoFeB/MgO/Fe₄N MTJ [324,325]. However, no TMR sign change has been observed in that system. In the TMR curves at 10K, it is found that the AP plateaus are not well established with an asymmetric form at positive and negative magnetic field. This could be due to the complex magnetic structure in Fe₄N, which has a partial out-of-plane magnetic component [236]. Figure 5-6(e) shows the resistance in P and AP states as a function of temperature for $V=+0.45V$ and $V=-0.6V$. The corresponding variation of TMR as a function of temperature is shown in Figure 5-6(f). It is found that the resistance of junction gradually reduces with increase of temperature. However, the variation of resistance is lower than 25% for the largest case, which is an important signature to exclude either pinhole dominated tunneling for thin barrier (increased resistance with T) [326] or hopping dominated tunneling for thick barrier (reduced resistance with increasing T) [316]. Therefore, our TMR is dominated by coherent direct tunneling.

To have more insight on the TMR sign change for the Fe/MgAlO_x/Fe₄N MTJ, we measured TMR values at different bias at 10K, as shown in Figure 5-6(d) and Figure 5-7. It is clearly that TMR changes its sign at about $-0.2V$. Below this voltage, TMR almost keeps constant at positive TMR around $+5\%$. Above $-0.2V$, the TMR becomes negative and the value varies a lot with a maximum at $+0.5V$. For comparison, we have also plotted the TMR values from a Fe/MgO/Fe₄N MTJ, as illustrated in Figure 5-6(d) and Figure 5-8. Both samples show the same trend of TMR sign change, but the negative TMR ratio of MTJ with MgO barrier is only half of that of MTJ with MgAlO_x barrier. The superior performance of MgAlO_x based MTJ could be attributed to the

better lattice mismatch between $\text{Fe}_4\text{N}/\text{MgAlO}_x$ as well as less N diffusion inside the barrier which have been observed in STEM characterizations.

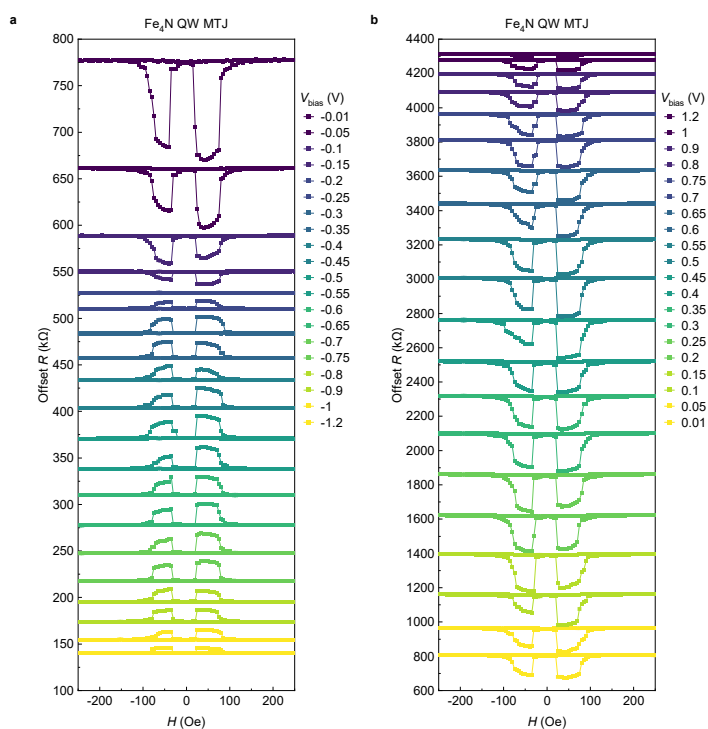


Figure 5-7 R - H measurements of the MgAlO_x Fe_4N MTJ under different bias at 10 K. Results with negative bias and positive bias are shown in (a) and (b), respectively.

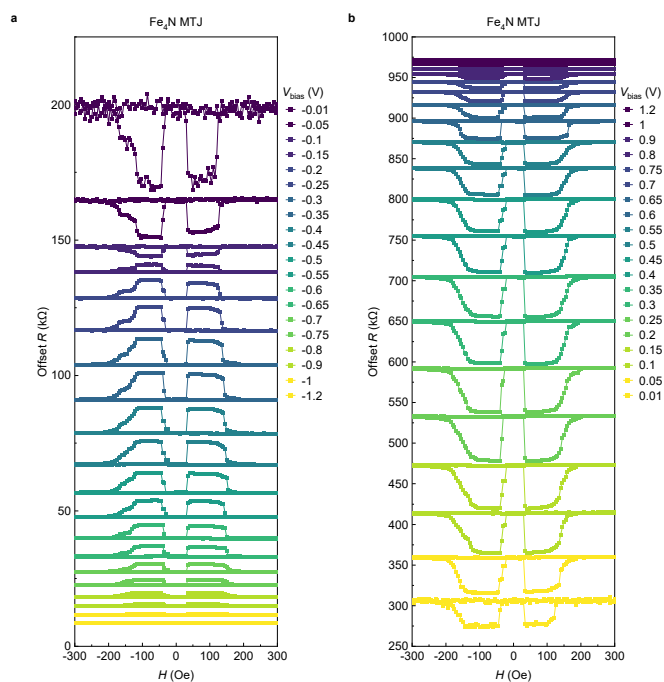


Figure 5-8 R - H measurements of the MgO Fe_4N MTJ under different bias at 10 K. Results with negative bias and positive bias are shown in (a) and (b), respectively.

To further understand the bias-dependent TMR, we set the MTJ into P and AP states respectively by applying appropriate in-plane field, and measured the bias dependence of differential conductance dI/dV at different temperatures (Figure 5-9(a-b)). All dI/dV curves in both states have been normalized by $G_P(V=0, T=10\text{K})$. Figure 5-9(c) shows the normalized differential conductance for both states at 10K. When $V < -0.1\text{ V}$, G_P is always higher than G_{AP} , resulting a positive TMR. However, when $0\text{ V} < V < 0.3\text{ V}$ G_{AP} increases much faster than G_P , resulting in a large negative TMR. At $V > 0.3\text{ V}$, the increase of G_P becomes more important than G_{AP} , which effectively reduces the negative TMR. Figure 5-9(d) displays the bias dependence of TMR deduced by the I - V curves ($R = V/I$) at different temperatures, showing a good agreement with the bias dependent TMR ratios measured directly from the R - H curves in Figure 5-6(d). The large attenuation of negative TMR with temperature can be found, which is mainly due to the large increase of G_P while G_{AP} almost keeps constant with the temperature, as shown in Figure 5-9(a-b).

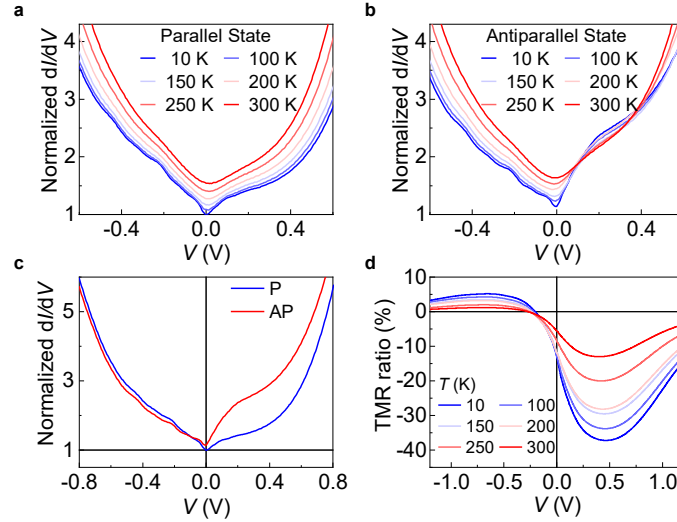


Figure 5-9 Bias dependence of the differential conductance dI/dV of the MgAlO_x Fe₄N MTJ. (a-b) Bias dependence of normalized dI/dV at different temperatures when the Fe₄N MTJ is in the P and AP state, respectively. (c) Bias dependence of normalized dI/dV for both states measured at 10 K. (d) Bias dependence of the TMR ratio at different temperatures deduced by the I - V measurements.

It is noticed that there are some small conductance oscillations appearing when $V < 0$ V in Figure 5-9(a-c) in both P and AP states. These oscillations could be explained by the electron tunneling in the QW states formed in the $\text{MgAlO}_x/\text{Fe}/\text{MgAlO}_x$ structure. However, the main origin of TMR sign change should not be related to the QW states since similar variation of conductance in P and AP states can also be evidenced in MgO based MTJ where there is no QW structure (Figure 5-8 and Figure 5-10).

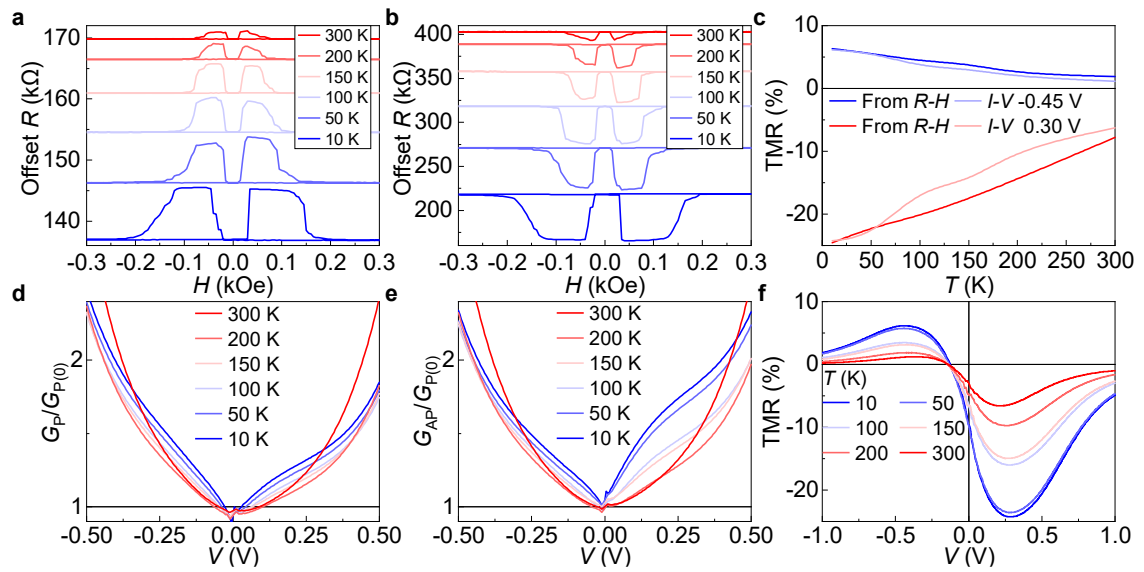


Figure 5-10 TMR measurements of the MgO Fe_4N MTJ at different temperatures.

Magnetic field dependences of the resistance when the bias voltage is -0.45 V and $+0.30$ V are shown in (a) and (b), respectively. (c) Temperature dependences of the TMR ratio when the bias voltage is -0.45 V and $+0.30$ V. Bias voltage V dependences of normalized differential conductance when the MTJ is in parallel state and antiparallel state are shown in (d) and (e). (f) Bias voltage dependences of TMR ratio summarized from I - V measurement.

5.2.4 *Ab initio* calculations

To understand the origin of the V dependence of TMR ratio, *ab initio* calculations have been performed to investigate the coherent tunneling in MTJ closely linked with the spin and symmetry of the electrons in both electrodes. The first-principles calculations in this chapter were conducted by Yu ZHU from Jilin University

using the projector-augmented-wave (PAW) method [327] as implemented in the Vienna ab initio simulation package (VASP) [328–330]. An energy cutoff of 500 eV and Perdew-Burke-Ernzerhof generalized-gradient approximation (GGA-PBE) [331] for the exchange-correlation functional were used throughout. A $21 \times 21 \times 21$ k -point mesh were performed for structural relaxations and self-consistent calculations for Fe_4N until the force on each atom is smaller than 0.01 eV/Å and the total energy converged to less than 1×10^{-5} eV. The bulk Fe_4N has a cubic antiperovskite structure and the experimental lattice constant is 3.795 Å. We also calculated the bcc Fe to analyze the tunneling between these two electrodes.

Figure 5-11(a) shows the symmetry and spin-resolved band structures along transport direction (Γ -X) for bulk Fe and Fe_4N . For bcc Fe, the majority-spin Δ_1 band crosses the Fermi level while minority-spin Δ_1 band situates well above E_F , which reveals a half-metal nature in terms of Δ_1 state along the transport direction [332]. For Fe_4N , the minority Δ_1 and Δ_5 bands cross the Fermi level, while no majority bands cross the Fermi level along the transport direction, which is in a good agreement with the calculation reported by Yang *et al.* [319] This indicates that Fe_4N also reveals a half-metal nature in terms of both Δ_1 and Δ_5 states. Since in single crystal Fe(001)/MgO/Fe [320] or Fe(001)/MgAl₂O₄/Fe [49] MTJs, MgO and MgAl₂O₄ tunneling barriers can efficiently filter electrons with other symmetries than Δ_1 and Δ_5 bands, it is reasonable to consider only the Δ_1 and Δ_5 bands are mainly involved in the tunneling process. Previous theoretical work in $\text{Fe}_4\text{N}/\text{MgO}/\text{Fe}_4\text{N}$ also reveals that not only the Δ_1 but also Δ_5 band electrons play an important role for the symmetry dependent coherent transmission [319].

To make the analysis clear, the symmetry and spin-resolved DOS of Fe and Fe_4N as a function of the energy is plotted in Figure 5-11(b-e). Generally, the conductance is

created by the electrons tunneling from an occupied band of one electrode to the unoccupied band of the other electrode. Therefore, the conductance of the P state is determined by: Majority (\uparrow) to Majority (\uparrow) and Minority (\downarrow) to Minority (\downarrow) while the conductance of the AP state is determined by: Majority (\uparrow) to Minority (\downarrow) and Minority (\downarrow) to Majority (\uparrow).

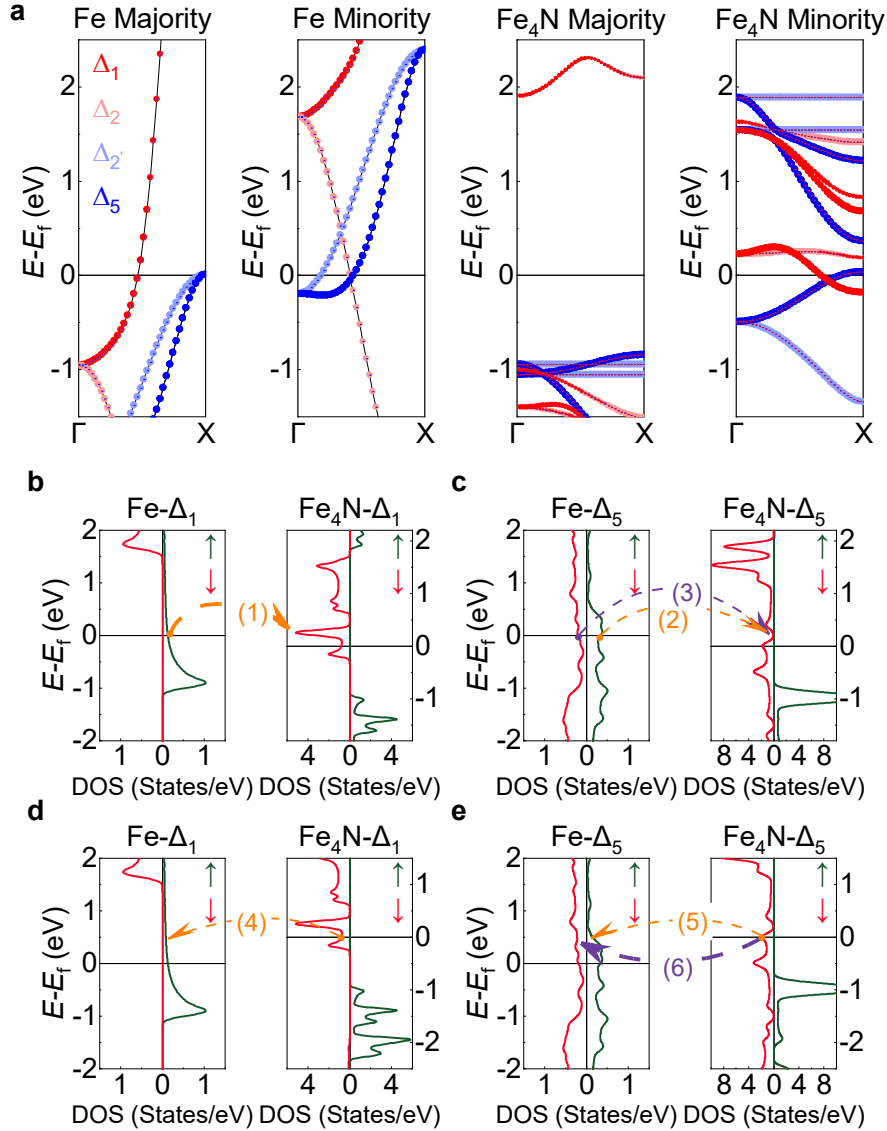


Figure 5-11 *Ab initio* calculations of bulk Fe and Fe₄N. (a) Symmetry and spin-resolved band structures of bulk Fe and Fe₄N along the transport direction (Γ-X). (b-e) Symmetry and spin-resolved DOS of bulk Fe and Fe₄N as a function of the energy. Dash lines represent tunneling channels.

5.3 Discussions

Figure 5-11(b-c) show the tunneling under positive bias through Δ_1 and Δ_5 bands, respectively. Since there are no DOS near the Fermi energy for the majority bands of Fe_4N , the tunneling channels when $V > 0\text{V}$ are mainly from: (1) $\text{Fe } \Delta_1\uparrow$ to $\text{Fe}_4\text{N } \Delta_1\downarrow$, (2) $\text{Fe } \Delta_5\uparrow$ to $\text{Fe}_4\text{N } \Delta_5\downarrow$ for AP conductance and (3) $\text{Fe } \Delta_5\downarrow$ to $\text{Fe}_4\text{N } \Delta_5\downarrow$ for P conductance. From Figure 5-9(c), we know that the normalized dI/dV in the AP state increases fast first when $0 < V < 0.2\text{V}$, then slows down when $0.2\text{V} < V < 0.4\text{V}$, and finally increase fast again when $V > 0.4\text{V}$. This fast-slow-fast increase of conductance is well attributed to the strong $\text{Fe}_4\text{N } \Delta_1\downarrow$ peak around 0.2V in the AP tunneling channel (1), as shown in Figure 5-11(b). Notice that the channel (2) is less important since the DOS of $\text{Fe}_4\text{N } \Delta_5\downarrow$ near E_F is much smaller than that of $\text{Fe}_4\text{N } \Delta_1\downarrow$. The low DOS intensity in $\text{Fe}_4\text{N } \Delta_5\downarrow$ also limit the P conductance channel (3). This can well explain the observed large negative TMR ratio. In Figure 5-9(a-b), the temperature dependence of conductance shows that AP conductance almost keeps constant, while P conductance increases with temperature at positive bias. This results in the rapid decrease of negative TMR, which can be understood as following. Since the thermal effect induces the phonon scattering, the distribution of DOS as a function of the energy will be smeared. Therefore, the conductance in channel (1) reduces while that in channel (2) increases, so that they compensate together resulting in a small variation of AP conductance.

When $V < 0$, the tunneling channels are mainly from: (4) $\text{Fe}_4\text{N } \Delta_1\downarrow$ to $\text{Fe } \Delta_1\uparrow$ and (5) $\text{Fe}_4\text{N } \Delta_5\downarrow$ to $\text{Fe } \Delta_5\uparrow$ for AP conductance and (6) $\text{Fe}_4\text{N } \Delta_5\downarrow$ to $\text{Fe } \Delta_5\downarrow$ for P conductance. From Figure 5-9(c), the changes of the normalized dI/dV are similar in the AP state and P state, and the normalized dI/dV in the P state is slightly higher than that in the AP state. From Figure 5-11(d-e), the AP conductance is mainly determined by the channel (5) since the DOS of $\text{Fe } \Delta_1\uparrow$ in channel (4) decreases rapidly with higher

energy. By comparison of channel (5) and (6) for AP and P conductance, the DOS of the Fe $\Delta_5\uparrow$ (Fe $\Delta_5\downarrow$) keeps decreasing (increasing) with higher energy. This can explain the higher P conductance observed in normalized dI/dV curves in Figure 5-9(c), which results in the positive TMR ratio. However, since there is no distinguished DOS peak in Fe $\Delta_5\downarrow$, the positive TMR ratio is less pronounced than the negative TMR ratio. Here, we can qualitatively explain the experimental observation by the simple analyses based on the band structure of bulk Fe₄N and Fe. A more rigorous model should take into account the electrode, barrier and the interfaces together, which will give more insight of the transport process.

5.4 Chapter summary

This chapter primarily investigates the phenomenon of the sign-changeable TMR effect in Fe₄N MTJs. The voltage-controlled and sign-reversible TMR effect is demonstrated from 10 K to 300 K. The positive TMR ratio = +3.15% at $V = -0.6$ V can be changed to the negative TMR ratio = -26.7% (-36.5% under the optimistic definition) at $V = +0.45$ V at RT. The voltage-dependence of TMR ratio can be well explained by a simple model taking account of the symmetry and spin-resolved band structures of Fe and Fe₄N. This new freedom of TMR turnability paves a way for new spintronics devices, especially for real-time reprogrammable spin logic gates. The main contents of this chapter include:

(1) High-quality MgAlO_x-barrier Fe₄N MTJs and MgO-barrier Fe₄N MTJs are grown using MBE. Real-time monitoring of the growth process is conducted with RHEED, and *in-situ* annealing is employed to improve crystal quality.

(2) From bias dependent TMR measurements, we have demonstrated the sign-changeable TMR effect. MgAlO_x barrier can significantly block the N atoms from

diffusion, which leads to higher crystal quality and TMR ratios compared to MTJ with MgO barrier.

(3) First-principles calculations are performed to obtain the symmetry-dependent band structure and DOS of Fe and Fe₄N near the Fermi level. The changes in conductance are explained by analyzing the variation of the tunneling channels under different bias voltage, thereby elucidating the mechanism behind this sign-changeable TMR effect.

This chapter of work is conducted with several colleagues and their contributions are as follows: I grew the stacks, fabricated the devices, conducted magneto transport measurements and analyzed all the results. Yu ZHU and Yu YAN conducted the *ab initio* calculations. Pambiang Abel DAINONE optimized the growth condition of Fe₄N. Tongxin CHEN helped with the transport measurements and analysis of STEM results. Xavier DEVAUX conducted the STEM measurements. Sylvie MIGOT and Pambiang Abel DAINONE performed the FIB milling to provide the thin lamellas for STEM. Gwladys LENGAINNE provided help during the device fabrication. Caihua WAN and Michel VERGNAT engaged with the data analyze. Yuan LU and Xiufeng HAN led and was involved in all aspects of the research.

6 Impact of interfacial structural and chemical disorders on the resonant oscillation in QW based MTJs

6.1 Research background

Double barrier MTJs (DMTJs), featuring additional metallic or insulating barrier compared to the standard MTJ structure, allows the formation of quantum well (QW) between these two barriers and enables the resonant tunneling of electrons if the energy of injected electrons matches the discrete QW energy levels. As shown in Figure 6-1, the discrete QW states established between two insulating layers enable a resonant tunneling of Δ_1 electrons when the Fermi level of the top electrode aligns with the QW states, which leads to a sizable oscillation of conductance when varying the bias voltage.

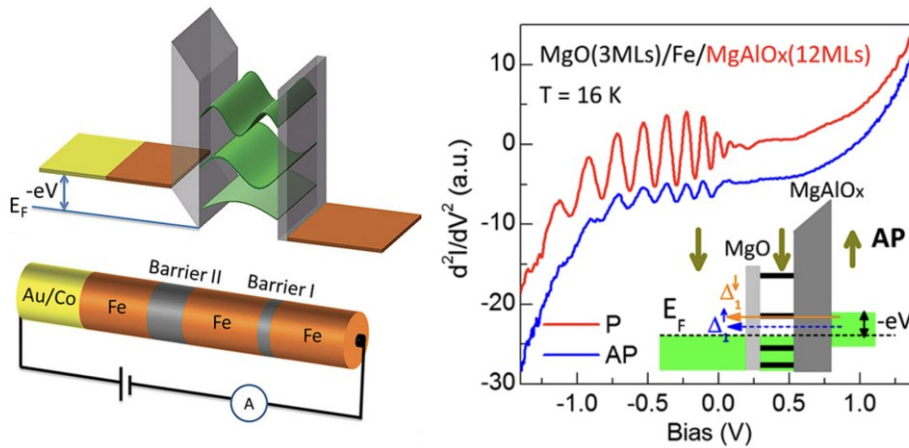


Figure 6-1 Resonant oscillation of conductance in the QW MTJ [56].

In previous works, both metallic barrier (Cr) with desired symmetry dependent band structure [54,333–337] and insulating barrier (Al_2O_3 or MgO) with much higher barrier height [51,53,55] have been studied to achieve the resonant tunneling. However, the QW thickness are limited to 1-2 nm to avoid electron dephasing in the QW. By replacing MgO barrier with MgAlO_x barrier, the lattice mismatch between the barrier

and the Fe electrode has been minimized (<1%), which allows to observe clear resonant oscillation of conductance in a 12 nm thick Fe metallic QW even at room temperature [56,57]. In order to achieve higher conductance quantum oscillation, it is important to keep a good phase coherence at the two metal/insulator interfaces inside the QW to minimize the dephasing mechanisms due to the interface chemical and structure disorders. It is reported that the interface Co insertion can lead to a large enhancement of TMR up to 410% at RT in epitaxial Co/MgO/Co MTJs [338] and 300% at RT in FeCo_x/MgO/FeCo_x MTJs [46,47]. The reason revealed by *ab initio* calculations is that Co only possesses majority-spin Δ_1 states near the Fermi level [339], which quite significantly increases the interface spin polarization. It will be quite interesting to know if the interface Co insertion could also enhance the QW MTJ TMR as well as the conductance oscillation. However, the structural and chemical disorders introduced by Co insertion could also cause a significant dephasing of electrons, which makes obtaining high oscillation amplitude challenging. Therefore, it requires a systematic investigation on the interfacial optimization to study the impact of chemical disorder on the QW resonant oscillation.

In this chapter, we experimentally show the impact of interfacial chemical and structural disorders on the resonant oscillation by introducing Co and Fe monolayers at the QW/barrier interface. It is found that the insertion of Co outside of QW doesn't influence on the conductance oscillation, however the Co insertion inside QW generates chemical disorder at interface leading to a significant reduction of oscillation amplitude by half. In contrast, the structural disorder introduced by Fe monolayers completely suppresses all resonant oscillation. Our finding highlights the critical role of interface structural and chemical disorder on QW phase coherence and the physical understanding of it will greatly promote the development of spin-dependent quantum

tunneling applications.

6.2 Experimental results

6.2.1 Sample preparation

Two serials of samples were grown by MBE system on single crystal MgO(001) substrates to separately investigate the effect of Co insertion. The first series of samples consists of Samples *A*, *B* and *C*, in which Co insertion is on the top of the MgAlO_x/Fe/MgAlO_x QW. The second series samples consist of Samples *D*, *E* and *F*. Besides of Co insertion on the top of QW, Co or Fe monolayers are also introduced inside the QW at QW/barrier interface. The detailed sample structures are listed as follows (Figure 6-2):

Sample *A*: MgO(10 nm)/Fe(45 nm)/MgAlO_x(3 MLs)/Fe(10 nm)/MgAlO_x(12 MLs)/Fe(10 nm)/Co(20 nm)/Au(15 nm),

Sample *B*: MgO(10 nm)/Fe(45 nm)/MgAlO_x(3 MLs)/Fe(10 nm)/MgAlO_x(12 MLs)/Co(4 MLs)/Fe(10 nm)/Co(20 nm)/Au(15 nm),

Sample *C*: MgO(10 nm)/Fe(45 nm)/MgAlO_x(3 MLs)/Fe(7 nm)/MgAlO_x(12 MLs)/Fe₄N(3 nm)/Co(20 nm)/Au(10 nm),

Sample *D*: MgO(10 nm)/Fe(45 nm)/MgAlO_x(3 MLs)/Fe(10 nm)/Co(4 MLs)/MgAlO_x(12 MLs)/Co(4 MLs)/Fe(10 nm)/Co(20 nm)/Au(15 nm),

Sample *E*: MgO(10 nm)/Fe(45 nm)/MgAlO_x(3 MLs)/Fe(10 nm)/Co(2 MLs)/MgAlO_x(12 MLs)/Co(4 MLs)/Fe(10 nm)/Co(20 nm)/Au(15 nm),

Sample *F*: MgO(10 nm)/Fe(45 nm)/MgAlO_x(3 MLs)/Fe(10 nm)/Fe(2 MLs)/MgAlO_x(12 MLs)/Co(4 MLs)/Fe(10 nm)/Co(20 nm)/Au(15 nm).

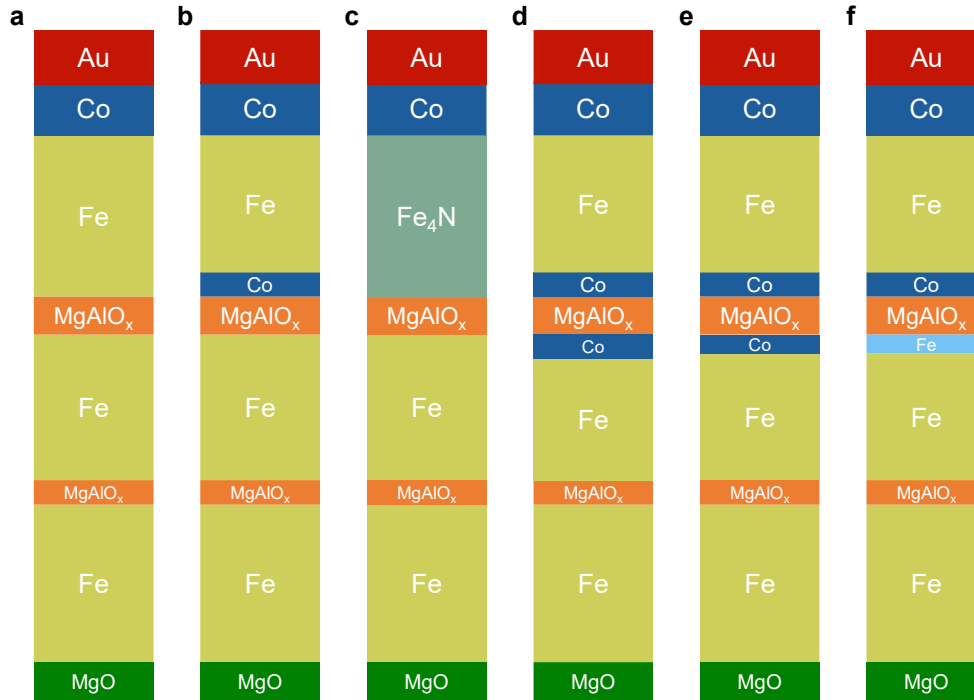


Figure 6-2 Schematics of samples' structure. (a-f) represents the structure of Sample A-F, respectively.

Take the growth process of Sample *D* as an example. Firstly, the substrate was annealed at 650°C for 30 mins and 10 nm MgO seed layer was deposited. Then the first Fe layer was deposited at RT by e-beam evaporation and annealed *in situ* at 500°C for 30 mins to smooth the surface. The first MgAlO_x barrier was grown at about 80°C and the growth process was monitored by RHEED. Two-dimensional layer-by-layer growth mode of MgAlO_x is observed by the oscillation of RHEED intensity, The second Fe layer was deposited at about 70°C and annealed *in situ* at 400°C for 20 mins followed by the deposition of 4 MLs thick Co insertion at about 80°C and then the deposition of second thick MgAlO_x barrier at about 80°C. Sequentially, a second deposition of 4 MLs Co layer at about 70°C is performed, followed by a third deposition of 10 nm thick Fe at about 70°C and an annealing *in situ* at 250°C for 30 mins (except at 400°C for Sample *A*). Finally, 20 nm Co layer is deposited above the Fe layer to enhance the coercivity and 15 nm Au is used to prevent the films from oxidation. Figure 6-3 and Figure 6-4,

show the RHEED patterns and intensity oscillation obtained during the growth of the first 4 MLs Co, 12 MLs MgAlO_x and second 4 MLs Co for Sample *D*. One can observe strong oscillations during the growth of the bottom Co (Figure 6-3(a)) and the middle MgAlO_x, (Figure 6-3(b)) indicating a desired two-dimensional layer-by-layer growth mode. The bright streaks and Kikuchi lines observed in the RHEED patterns further confirms their good epitaxial growth. In contrast, the upper Co grown on the MgAlO_x is no longer layer-by-layer due to the wetting property of metal on oxide. The spot pattern observed in Figure 6-3(c) indicates that the growth of Co on MgAlO_x follows a 3D mode and the Co surface becomes very rough. After deposition of top Fe and following in-situ annealing, the surface roughness becomes smooth again (Figure 6-4). Figure 6-5 shows the RHEED patterns and intensity oscillation obtained during the growth of Sample *F*.

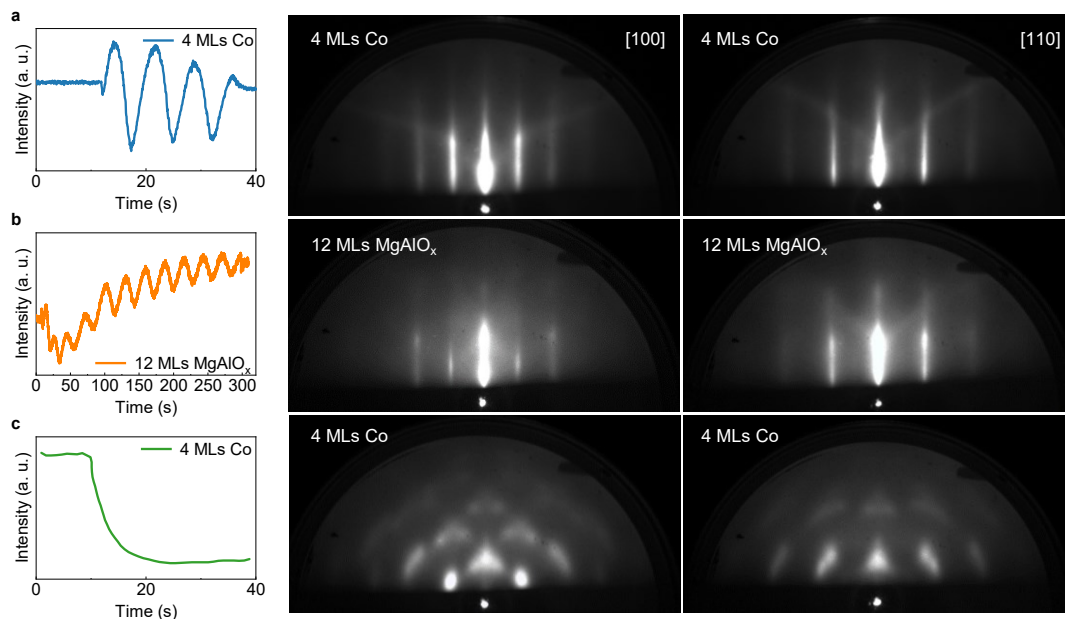


Figure 6-3 RHEED patterns of Sample *D* in different growth steps. RHEED intensity and patterns of (a) 4 MLs Co, (b) 12 MLs MgAlO_x and (c) 4 MLs Co along [100] and [110] azimuths of MgO substrate, respectively.

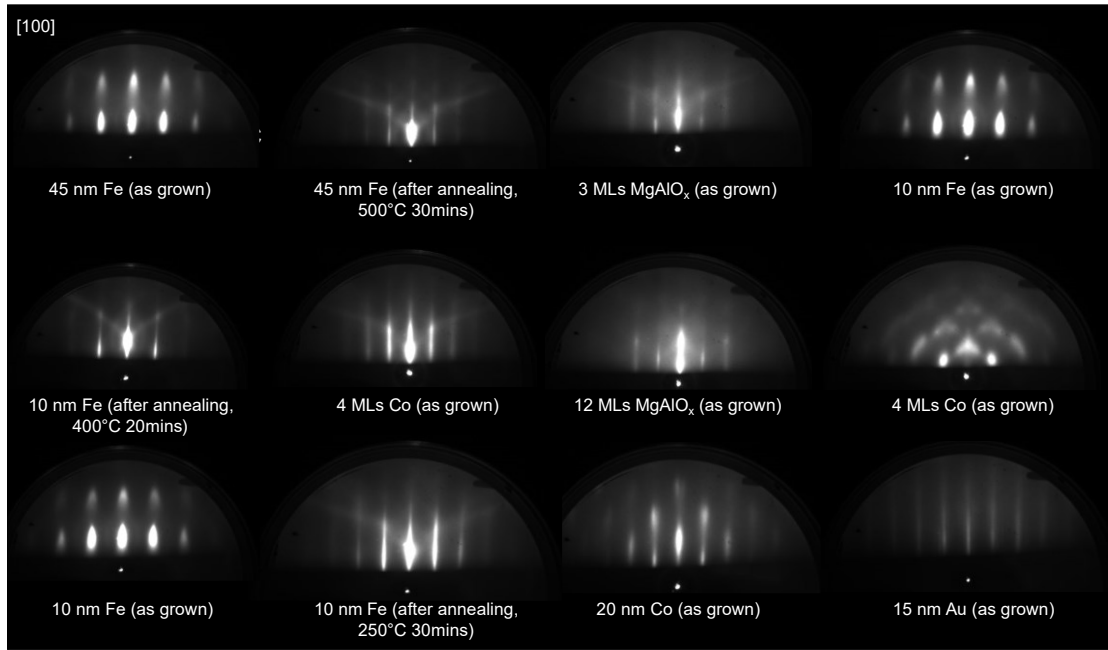


Figure 6-4 RHEED patterns of Sample *D* in different growth steps along the [100] azimuths of MgO substrate.

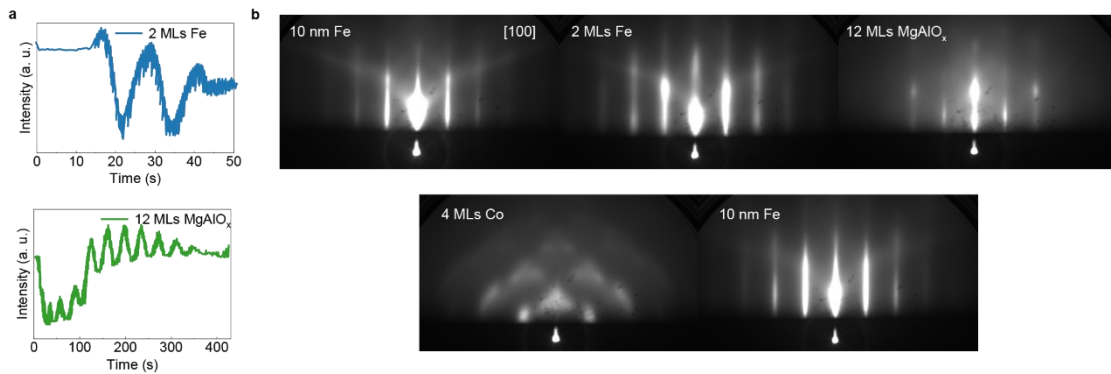


Figure 6-5 RHEED patterns and intensity oscillation of Sample *F* in different growth steps along the [100] azimuths of MgO substrate.

To elucidate the effect of outer Co insertion and exclude any difference conditions during the growth, an additional control stack Sample *G*: MgO(10 nm)/Fe(45 nm)/MgAlO_x(3 MLs)/Fe(10 nm)/MgAlO_x(12 MLs)/Co(4 MLs, half covered by shutter)/Fe(10 nm)/Co(20 nm)/Au(15 nm) was grown. During the growth of top Co(4 MLs) layer, a shutter was utilized to cover half of the substrate, which enables us to fabricate two types of MTJs with exactly the same condition for bottom structures

(see Figure 6-6 for RHEED patterns). The growth details of Sample *C* with Fe₄N electrode are already presented in Chapter 5.

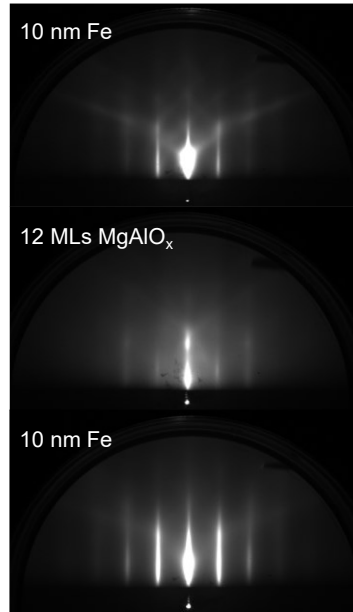


Figure 6-6 RHEED patterns of the control stack in different growth steps along the [100] azimuth of MgO substrate.

6.2.2 Structural and chemical characterization

HR-STEM characterizations are performed by Xavier DEVAUX from IJL to verify the structure of the DMTJs, and the technical details of STEM-EELS measurements are presented in Chapter 5. Figure 6-7(a) shows the HAADF images for Sample *D* in a large and magnified scale, in which artificial colors are added to improve the readability. Sharp interfaces between the Co (in grey and orange contrast) and MgAlO_x (in black and blue contrast) can be observed. Two MgAlO_x barriers are flat and continuous, indicating a high quality of the stack structure. The magnified images further prove the epitaxial growth characters with well-aligned atomic arrays between Fe, MgAlO_x and Co layers. In Figure 6-7(a), no structural disorder can be found at the top and bottom QW/barrier interfaces after Co insertion.

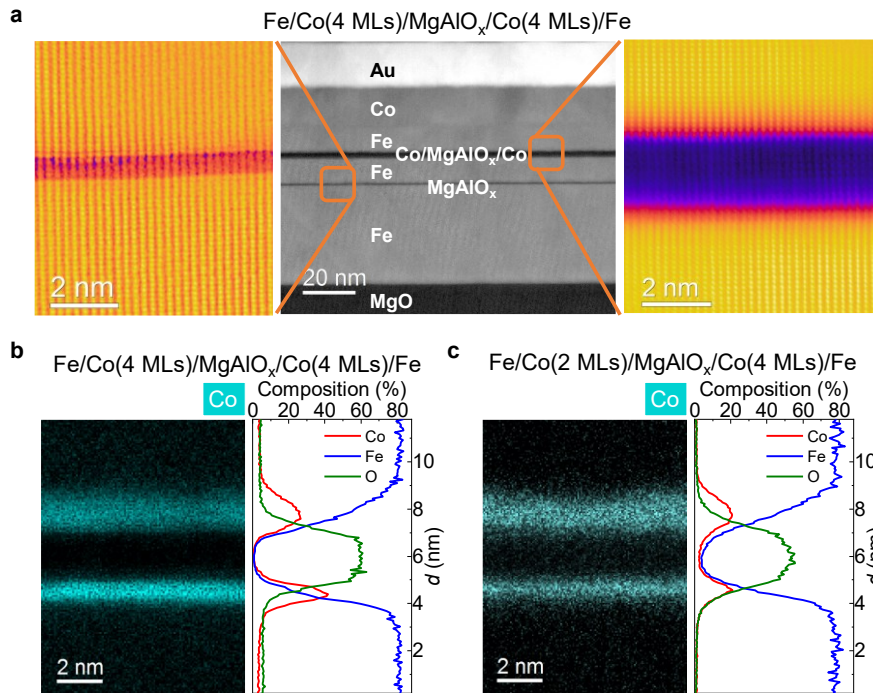


Figure 6-7 Interfacial structures and chemical maps of MTJ stacks. STEM-HAADF images of Sample *D* with different scales are shown in (a). Artificial colors are added to improve the readability. The Co map and elements density profiles extracted from STEM-EELS of Samples *D* and *E* are shown in (b) and (c), respectively.

To check the chemical disorder at the interface, the element distribution analyses were performed by STEM combined with spatially resolved EELS characterizations. Figure 6-7(b,c) presents semi-quantitative chemical maps drawn by processing the EELS spectrum images and the element intensity profiles of the Samples *D* and *E* (additional chemical maps can be found in Figure 6-8, Figure 6-9 and Figure 6-10 for Samples *B*, *D*, *E*, respectively). From the element mapping of Co, it is evident that in both samples, the bottom Co layer is well-confined, in contrast to the wider distribution of the top Co layer, which is attributed to the larger roughness of the top Co layer. The 4 MLs of bottom Co almost has the same thickness distribution as the 2 MLs Co, but with higher Co intensity. These two features are more visible in the element intensity profiles. The insertion of Co layer with different thickness does not introduce a structure disorder, however it results in the formation of $\text{Co}_x\text{Fe}_{1-x}$ alloy at the interface with

different Fe-Co concentration [46], which generates a chemical disorder at the Fe/MgAlO_x interface.

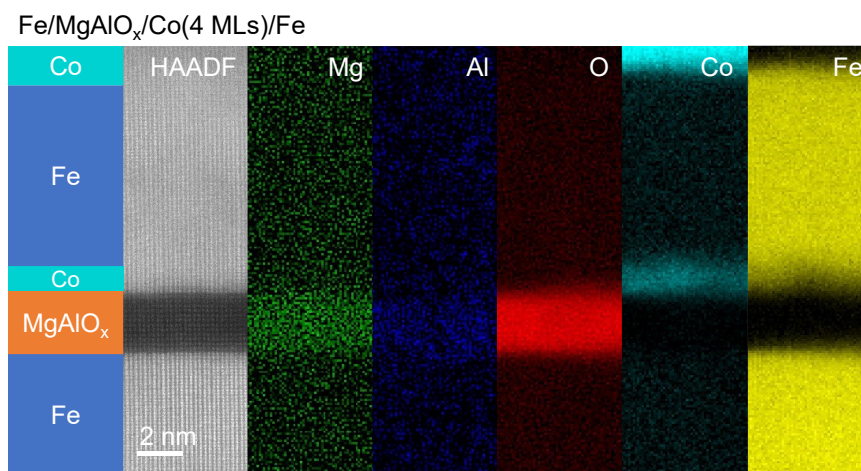


Figure 6-8 STEM-HAADF images and elements maps extracted from STEM-EELS measurements of Sample *B*.

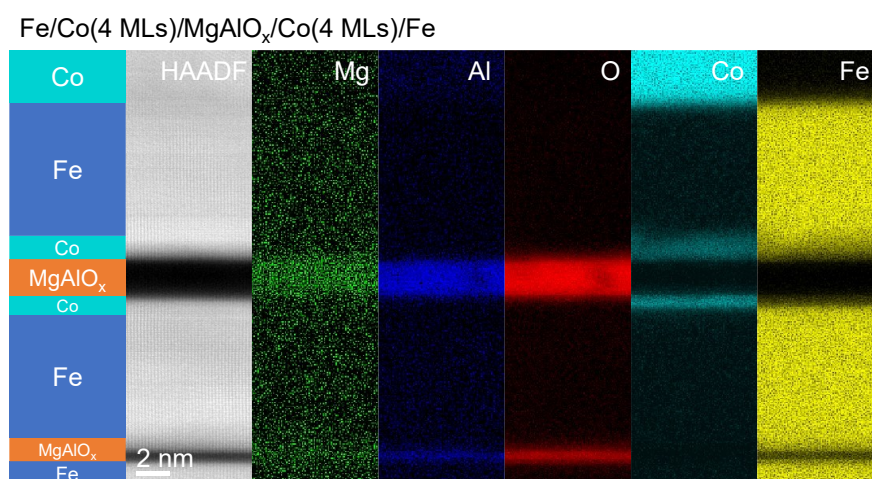


Figure 6-9 STEM-HAADF images and elements maps extracted from STEM-EELS measurements of Sample *D*.

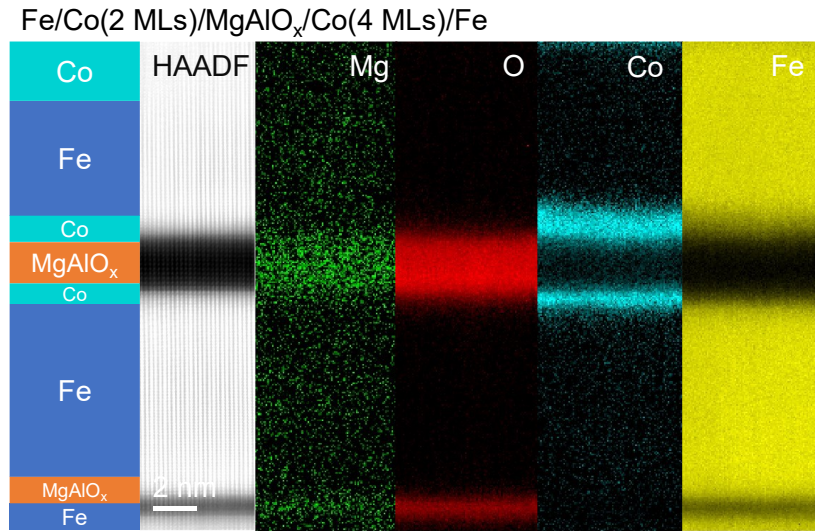


Figure 6-10 STEM-HAADF images and elements maps extracted from STEM-EELS measurements of Sample *E*.

6.2.3 Magneto-transport measurements

The magneto-transport measurements have been performed using a dc two-probe configuration, where the negative bias corresponds to the electrons tunneling from the top to bottom electrode. Although there are two MgAlO_x insulating barriers in the stacks, the junction resistance is mainly induced by the thicker one. Figure 6-11 and Figure 6-12 show the bias dependence of differential conductance dI/dV and secondary differential conductance d^2I/dV^2 for samples with outer modification (Samples *A-C*) and inner insertion (Samples *D-F*), respectively. The corresponding TMR curves are shown in the insets of each figure. The measurement results are summarized in Table 6-1. All dI/dV curves have been normalized by corresponding G_P (0 V, 10 K).

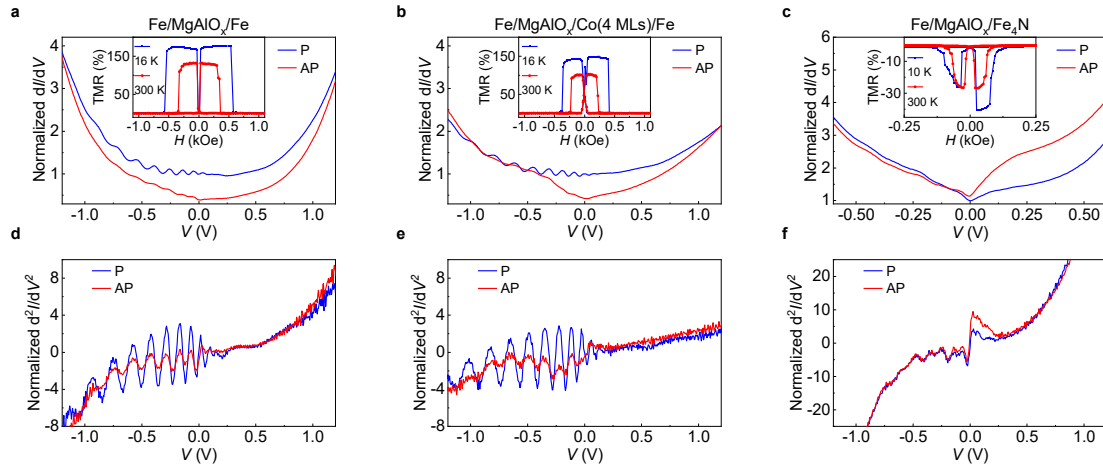


Figure 6-11 Bias dependence of differential conductance dI/dV and secondary differential conductance d^2I/dV^2 of samples with outer insertion. Bias dependence of normalized dI/dV (divided by $G_P(0\text{ V}, 10\text{ K})$) at LT of Samples *A*, *B* and *C* are shown in (a-c), respectively. Bias dependence of normalized d^2I/dV^2 at LT of Samples *A*, *B* and *C* are shown in (d-f), respectively. Insets in (a-c) show the TMR curves measured at LT and RT of corresponding samples.

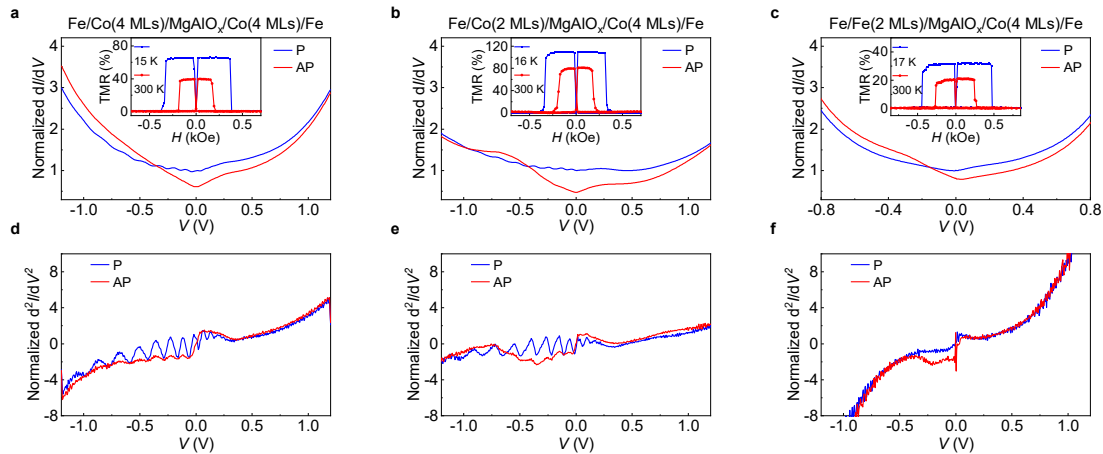


Figure 6-12 Bias dependence of differential conductance dI/dV and secondary differential conductance d^2I/dV^2 of samples with inner insertion. Bias dependence of normalized dI/dV (divided by $G_P(0\text{ V}, 10\text{ K})$) at LT of Samples *D*, *E* and *F* are shown in (a-c), respectively. Bias dependence of normalized d^2I/dV^2 at LT of Samples *D*, *E* and *F* are shown in (d-f), respectively. Insets in (a-c) show the TMR curves measured at LT and RT of corresponding samples.

Table 6-1. Summary of experimental results for samples with different insertions.

Sample	Inner insertion (MLs)	Outer insertion (MLs)	Oscillation amplitude (a. u.) P	Oscillation amplitude (a. u.) AP	TMR (10 mV) LT	TMR (10 mV) RT
<i>A</i>	-	-	6.49	2.34	176%	133%
<i>B</i>	-	Co 4	6.99	2.49	149%	103%
<i>C</i>	-	Fe ₄ N (bulk)	3.28	3.86	-41% (450 mV)	-27% (450 mV)
<i>D</i>	Co 4	Co 4	2.35	0.55	66%	40%
<i>E</i>	Co 2	Co 4	2.13	0.97	110%	81%
<i>F</i>	Fe 2	Co 4	-	-	32%	21%

It is found that the insertion of top 4 MLs Co results in a reduction of TMR (10 K) from 176% to 149%. This is because of the increase of conductance in AP states, which is due to the minority Δ_1 interface state close to E_F at Fe_{1-x}Co_x/MgAlO_x interface [46]. Comparing Figure 6-11(d,e), it is clear that the outer insertion of Co (4 MLs) almost has no influence on the oscillation amplitude. To avoid any different growth conditions of the Fe QW and MgAlO_x barrier for Samples *A* and *B* in comparison, we have also examined the control Sample *G* in which the half substrate was covered by the shutter during the growth of top 4 MLs Co layer. As shown in Figure 6-13(c), the conductance oscillation period and amplitude for the DMTJs on the part with and without 4 MLs top Co layer are exactly the same. These results firmly conclude that the insertion of Co on the top of QW has no influence on the QW oscillation although the majority Δ_1 DOS in Fe_{1-x}Co_x alloy is reduced compared to the Fe electrode. Therefore, the oscillation amplitude is mainly determined by the sharpness of the Fe QW states in the case of outer Co insertion.

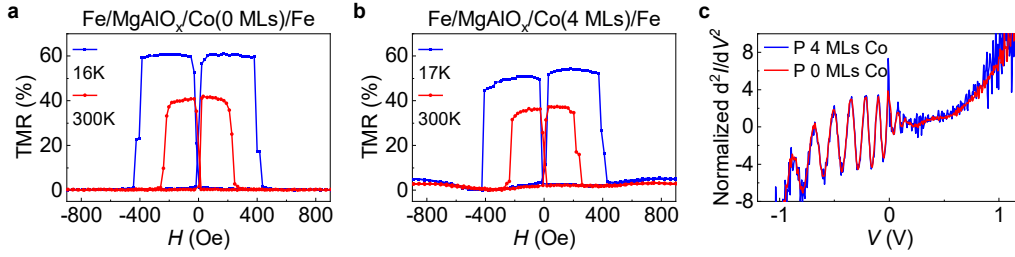


Figure 6-13 Bias dependence of d^2I/dV^2 of MTJs fabricated on the same control stack. TMR curves measured at LT and RT of MTJs with and without Co insertion are shown in (a) and (b), respectively. The corresponding bias dependence of normalized d^2I/dV^2 in P state are shown in (c).

For Sample C, by replacing the top Fe electrode with Fe_4N electrode, we have observed a large negative TMR up to -40% at 10 K, 0.45 V (Figure 6-11(c)). As mentioned in Chapter 5, the minority Δ_1 and Δ_5 bands of Fe_4N cross the Fermi level, while no majority bands of Fe_4N cross E_F along the transport direction [319]. The negative TMR is mainly due to the strong Fe_4N minority Δ_1 peak around 0.2 V in the AP tunneling channel. It is found that the QW oscillations are much attenuated and the amplitude is almost equal in P and AP states (Figure 6-11(f)). Since Fe QW states are formed by Fe majority Δ_1 states, the lack of majority Δ_1 states can explain the attenuation of oscillation amplitude in P state. However, in AP state, we should expect a much higher oscillation amplitude than that in P state because of the minority Δ_1 states at Fermi level in Fe_4N band. However, it is not the case. This implies that in order to generate a strong QW oscillation, the electrons should not only fulfill the symmetry and spin conditions to match the QW states, but also should match k condition. Since the QW is formed between two barriers perfectly parallel to the sample plane, only electrons having $k_{\parallel} = 0$ can conserve coherent phase when reflecting between the two potential barriers. As discussed in Chapter 5, since there is a large lattice mismatch of 6.5% between Fe_4N (3.795\AA) and $MgAl_2O_4$ (4.212\AA) [322], the electrons injected in the QW could have a large distribution of k_{\parallel} . Therefore, the oscillation amplitude in

Fe₄N based DMTJ is low even in AP configuration.

For the second series samples, we fix the outer insertion of Co (4 MLs) and focus on the influence of inner insertion on the oscillation amplitude. As shown in Figure 6-12(a,b), it is found that the TMR ratios of Sample *D* and *E* with Co insertion in both sides become even smaller than that of the Sample *B* with only one side Co insertion. This is completely different than what have been observed in normal MTJ with Co insertion [338]. In fact, it is found that the G_{AP} continues increasing with the increase of the inserted Co thickness. As observed by spatial resolved EELS, the increase of Co thickness results in a higher Co concentration, which will push minority Δ_1 DOS close to E_F , thus enhancing G_{AP} and reducing the TMR ratio [46].

As shown in Figure 6-12(d,e), for Samples *D* and *E*, the inner Co insertion has largely reduced the oscillation amplitude by half in the P and AP state, while the insertion thickness is less relevant. The decrease of oscillation amplitude demonstrates that the chemical disorder (Figure 6-7(b,c)) introduced inside the QW has a negative impact on the sharpness of the QW states. Notably, a fine structure of the resonant oscillation of Sample *E* can be observed, as shown in Figure 6-14(d). The small steps feature in the oscillation are confirmed by repeated measurements that we will discuss later.

Surprisingly, when we grow additional 2 MLs of Fe on the top of Fe QW, which introduce no chemical disorder, no oscillation can be observed anymore. This indicates that the structural disorder introduced by the growth of Fe (2 MLs) is so profound that eliminates all oscillation completely. Notably, during the growth of Samples *D-F*, the post annealing temperature after the growth of top Co is 250°C, which is enough to smooth Co layer and obtain high-quality Co/MgAlO_x interface (Figure 6-7(a)) [338]. In contrast, Fe usually requires a 350°C-400°C annealing to ensure a flat surface [45,56],

which is not satisfied in the growth of Sample *F*. Therefore, the quantum oscillation is more sensitive to the interface structural disorder than the chemical disorder.

6.2.4 *Ab initio* calculations

To further clarify the influence of interfacial chemical disorders on the QW states. An *ab initio* calculation was carried out to exam the difference of QW states formed by pure Fe or Fe with 2 MLs of Co interface, using the Vienna ab-initio simulation package (VASP) [328–330]. In all calculations, the exchange-correlation potentials were treated with the generalized gradient approximation (GGA) of Perdew-Burke-Ernzerhof (PBE) function. The cutoff energy is set to 420 eV. A Γ -centered $9 \times 9 \times 1$ k -mesh was used in the structure relaxation, and the quantum well states were extracted at Γ point. The convergence energy and force of the heterostructure were 10^{-7} eV and 0.001 eV/Å, respectively. More details of the calculation can be found in our previous work [56].

Figure 6-14(a,b) show the calculated s -resolved partial DOS of Co and Fe at the Γ point in a Fe/MgO(7 MLs)/Fe(45 MLs)/Co(2 MLs)/MgO(7 MLs) stack from -0.5 eV to 1.5 eV, respectively. The spikes in DOS demonstrate the QW states formed between two barriers and mainly with majority states. Notably, the position of the QW states is identical for the interfacial Co and inner Fe, which means if the Co are perfectly covered the Fe, sharp QW states will still form, resulting identical oscillation amplitude as the sample without Co insertion. For comparison, we have also calculated the band structure of stack Fe/MgO(7 MLs)/Fe(47 MLs)/MgO(7 MLs), which has the same thickness of QW as the stack with 2 MLs Co insertion, as shown in Figure 6-14(c). It is interesting to find the total set of QW peaks shift 0.05 eV to higher energy in the QW without Co insertion.

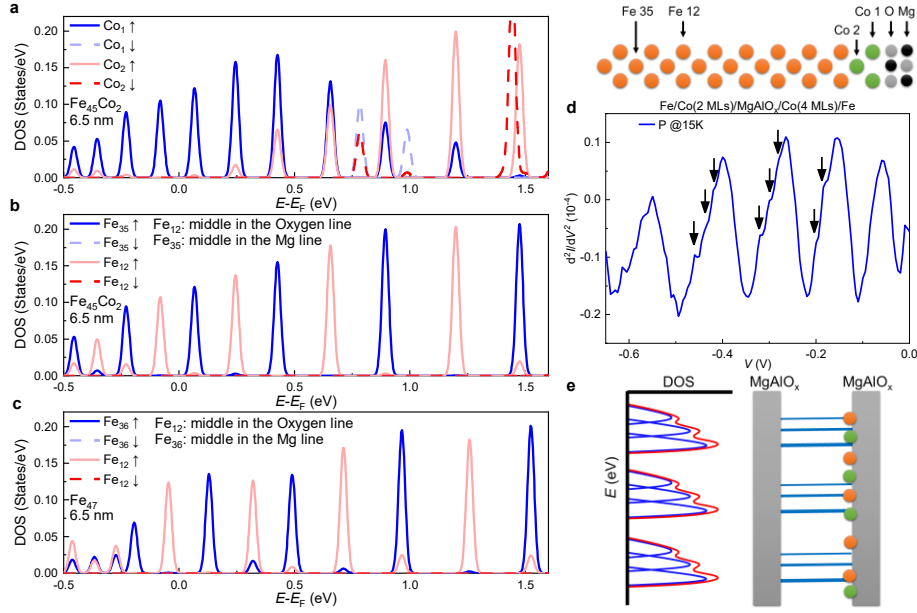


Figure 6-14 QW states formed in Fe and Fe/Co. (a-b) s -resolved partial DOS at the $\bar{\Gamma}$ point for central Fe and interface Co in the QW of MgO/Fe/Co/MgO. (c) s -resolved partial DOS at the $\bar{\Gamma}$ point for central Fe in the QW of MgO/Fe/MgO. In both cases the total thickness of ferromagnetic layer is 47 ML. (d) Fine structure of dI/dV of Sample *E*. The sub-steps are shown by the arrows. (e) Schematics of the DOS distribution with two set of QW states in QW MTJ with both Fe and Co at the QW/barrier interface.

6.3 Discussions

The QW states obtained from experimental results can be directly and qualitatively compared with a simple phase accumulation model (PAM) [340]. The PAM describes the quantization condition for the existence of a QW state as:

$$2k_{\perp}d - \Phi_1 - \Phi_2 - \Phi_{\text{inf}} = 2\pi n, \quad (6-1)$$

where $k_{\perp} = \sqrt{2m^*(E - E_L)}/\hbar$ is the crystal momentum wave vector in the film perpendicular to the interface, d is the QW thickness, and $\Phi_1 = \Phi_2 = 2 \sin^{-1} \sqrt{(E - E_L)/(E_U - E_L)} - \pi$ is the reflection phase shift at the two Fe(Co)/MgAlO_x interfaces. Furthermore, m^* is the effective mass of the majority Δ_1 electron in Fe, while E_L and E_U are the energies of the lower and upper edges of the barrier band gap. Here, we set $E_L = -1.0$ eV and $E_U = -1.0$ eV similar to the

previous work [35]. Φ_{inf} is an important parameter to account for the additional phase shift at interfaces due to other effects such as structure, chemical disorders, impurities, strain inhomogeneity and so on. Since the collected current is from a two-dimensional spatial integration in the whole junction area, if the electron changes its phase with the same Φ_{inf} everywhere, strong QW oscillations can still be obtained but with a shift of energy positions. Therefore, the reduction of QW amplitude is due to a large distribution of $\langle\Phi_{\text{inf}}\rangle$. As shown in the *ab initio* calculation, the QWs with and without Co insertion have different energy positions, which can effectively generate a spatial distribution of $\langle\Phi_{\text{inf}}\rangle$ if the chemical disorder exists at the interface. From STEM-EELS analysis, it is clear that different Co layer insertion results in a CoFe alloy layer with different concentration at the interface. Interesting, Sample *E* with 2 MLs Co insertion has a different shape of the oscillation peak than that of Sample *D* with 4 MLs Co insertion. In Figure 6-14(d), the small steps feature (indicated by the black arrows) implies that there are several sets of QW states mixed in the tunneling conductance. As schematically shown in Figure 6-14(e), with a large distribution of $\langle\Phi_{\text{inf}}\rangle$ induced by the chemical disorder at the interface, the QW energy position will also have a large distribution within the same QW index at different spatial locations. As a consequence, this smears the contrast of the current intensity as a function of bias and gives rise to the decrease of QW oscillation amplitude. Compared to chemical disorder, the interface structure disorder will not only introduce a large $\langle\Phi_{\text{inf}}\rangle$, but also effectively modify the QW thickness d , which is more detrimental to conserve the phase coherence for resonant oscillation.

It is found that the TMR in our QW MTJ with Co insertion is much smaller than the normal MTJ with Co insertion [338]. There are two possible reasons. Firstly, the annealing of top electrode is at 250°C for QW MTJ in order to avoid creating large

chemical disorder in the QW, while the annealing temperature is 400°C for normal MTJ usually. The difference of annealing temperature can significantly influence on the TMR ratio. Secondly, the band structure of QW with Co insertion is different than that of the normal MTJ with Co insertion. This especially reflects on the formation of interface states at the CoFe/MgAlO_x interface [46], which can play an important role on the symmetry dependent tunneling and influence on TMR ratio.

6.4 Chapter Summary

Building on the insights gained from prior material optimization studies of MTJs, this chapter undertakes a systematic investigation to elucidate the impact of structural and chemical disorders on the oscillation amplitude in QWs. We achieve this by introducing Co and Fe monolayers at the inner Fe QW/MgAlO_x and outer MgAlO_x/Fe interfaces. Our findings reveal that the oscillation amplitude remains stable when inserting Co out of the QW. However, introducing chemical disorder through Co insertion within the QW leads to a significant reduction in oscillation amplitude. Furthermore, structural disorder introduced by Fe insertion within the QW completely destroys the oscillations. The discernible sensitivity of resonant tunneling to both structural and chemical factors underscore the importance of comprehensive material optimization for the future design of QW devices.

This chapter of work is conducted with several colleges and their contributions are as follows: I grew the stacks, fabricated the devices, conducted magneto transport measurements of Sample C and analyzed all the experimental and theoretical results. Bingshan TAO grew the stacks, fabricated the devices, conducted magneto transport measurements of the rest of samples. Hongxin YANG conducted the *ab initio* calculations. Xavier DEVAUX conducted the STEM measurements. Yuan LU and

Xiufeng HAN led and was involved in all aspects of the research.

7 Summary

7.1 Conclusion of the dissertation

Magnetic materials serve as vital carriers for non-volatile storage. Manipulating and detecting the magnetization orientations in these materials through electrical means are crucial for the development of the next generation of in-memory computing technologies. In this dissertation, a series of investigations are conducted, focusing on current-driven magnetization switching and current detection of magnetization orientation. The summarized research findings are as follows:

(1) A Type-T magnetic macrospin model, which consists an in-plane ferromagnetic layer, an interlayer and a perpendicular ferromagnetic layer, is established. When a current passes through the in-plane ferromagnetic layer, spin currents are generated through the SHE and AHE mechanism. Upon absorption of these spin currents by the perpendicular ferromagnetic layer, its magnetization is switched. The polarity of this magnetization switching depends on the polarization direction of the spin current and the in-plane effective field. In the experimental design described here, the polarity of the SHE-driven perpendicular magnetization switching is opposite to that of the AHE-driven switching. Thus, the variation in switching polarity simultaneously confirms the presence of both effects. In the experiment, a Type-T magnetic multilayer of $\text{SiO}_2||\text{Ta}/\text{IrMn}/\text{NiFe}/\text{Ru}/\text{Pt}/\text{Co}/\text{Pt}$ is grown by magnetron sputtering, and microfabrication techniques are employed to fabricate micron-sized crossbar devices. In the electrical transport measurements, a small in-plane magnetic field transverse to the in-plane magnetization is applied. It is observed that when this magnetic field is small, the perpendicular magnetization switching is driven by SHE,

while for a larger magnetic field, AHE torque is enhanced, resulting in AHE-driven perpendicular magnetization switching. This research demonstrates that magnetic materials can generate significant spin currents similar to heavy metals, and the polarity of this spin current can be modulated, laying the foundation for designing heavy-metal, free cheap spin logic devices.

(2) A Type-T magnetic macrospin model is established. Notice that under the influence of SOT, the in-plane magnetization tilts along the perpendicular direction. The in-plane ferromagnetic layer and the perpendicular ferromagnetic layer are coupled, enabling the perpendicular ferromagnetic layer to simultaneously experience the in-plane effective field and an additional perpendicular effective field provided by the in-plane ferromagnetic layer. The former allows for field-free switching of the perpendicular magnetization, while the latter can assist in the switching and reduce the critical switching current density. The model reveals that when both the in-plane ferromagnetic layer and the perpendicular ferromagnetic layer experience spin currents with the same polarization direction, the perpendicular effective field assists the switching. Conversely, when the two layers sense spin currents with opposite polarization directions, the perpendicular effective field impedes the switching. In the experiments, Sample *A*: $\text{SiO}_2||\text{Pt}/\text{Co}/\text{Pt}/\text{Ir}/\text{Co}/\text{W}/\text{Pt}$, Sample *B*: $\text{SiO}_2||\text{Pt}/\text{Co}/\text{Pt}/\text{W}/\text{Co}/\text{Ir}/\text{Pt}$, and control Sample *C*: $\text{SiO}_2||\text{Pt}/\text{Co}/\text{Pt}/\text{Ir}/\text{W}/\text{Pt}$ are grown by magnetron sputtering, and the efficiency of current-induced perpendicular effective field is measured by observing the horizontal shift of the field-driven perpendicular magnetization switching hysteresis loop. This research demonstrates that in Type-T magnetic multilayers, by employing appropriate designs, it is possible to utilize effective perpendicular fields for field-free perpendicular magnetization switching and further reduce the critical switching current density.

(3) A series of high-quality Fe₄N MTJs are grown using MBE, and experimental observations reveal voltage-induced changes in the amplitude and sign of TMR ratio. Positive bias voltage leads to negative TMR ratios, while negative bias voltage leads to positive TMR ratios. By comparing the MgO barrier with the MgAlO_x barrier, it is found that the MgAlO_x barrier exhibits superior capability in suppressing N atom impurities, resulting in higher TMR ratios. Due to the high crystal quality and low interfacial roughness, a quantum well is formed between the double MgAlO_x barriers, and oscillations in differential conductance are observed. MTJs with changeable TMR sign hold significant importance in constructing spin logic circuits, and this research lays the groundwork for further advancements in spin logic.

(4) Two serials of epitaxial Fe/MgAlO_x/Fe/MgAlO_x/Fe DMTJs with Co insertion out of the QW or inside the QW are grown by MBE. And we found that the chemical and structural disorders within the QW have great impact on the QW states. The oscillation amplitude is determined by the sharpness of the QW states rather than the DOS of outer electrode. The chemical disorder introduced inside the QW greatly decrease the oscillation amplitude while the structural disorder completely eliminates all the oscillation. Additionally, a fine structure of resonant oscillation is observed, which further highlights the influence of chemical disorder on the oscillation amplitude. This investigation systematically analyses the dependence resonant oscillation amplitude on the interface, and paves ways for the development of new spintronics devices with both high oscillation amplitude and high TMR ratio.

7.2 Future research outlook

This dissertation focuses on current-driven magnetization switching and current detection of magnetization orientation, which correspond to the write and read aspects

of MRAM. The GMR and TMR effects enable the characterization of magnetization orientation through electrical currents, while STT and SOT allow for the manipulation of it through electrical currents. The combination of these two approaches has made the development of MRAM possible, and further advancements in MRAM will undoubtedly rely on progress in these two areas.

Currently, the room temperature TMR ratio of MTJs typically ranges from 100% to 200%. However, the on-off ratio still needs to be further improved compared to resistive or phase-change memories. Exploring new materials with higher spin polarization or even searching for new magneto-resistive mechanisms will enhance the advantages of MRAM. On the other hand, voltage-controlled TMR effect or the development of MFTJs will provide more degrees of freedom for MTJs, facilitating the development of spin logic devices with more functionalities.

Compared to STT, SOT offers advantages such as read-write separation and barrier protection. However, additional design considerations are needed to switch the perpendicular magnetization. Searching for materials with low in-plane symmetry will further simplify the multilayer structure, enabling large-scale production. Additionally, the efficiency of SOT still needs to be improved to reduce the critical switching current density. Research on new materials such as ferromagnetic materials, two-dimensional materials, topological insulators, as well as new mechanisms such as orbital Hall effect, holds the promise of addressing these issues and significantly advancing the development of spintronics.

Spintronics devices also possess unique advantages in the development of novel computing modes. By reducing the barrier height of MTJs, probability-adjustable random number generators can be obtained, and probability computing networks can be constructed accordingly. Magnetic domains and domain walls exist in Hall-bar

devices, enabling multi-state storage in single device and also cascaded logic operations. Spin nano-oscillators exhibit rich nonlinear outputs and memory effects, finding wide applications in neural networks. Further exploration of the advantages of spintronics devices and the identification of suitable computing modes will drive the integration of spintronics with emerging paradigms such as neural networks and probabilistic computing.

Bibliography

- [1] A. Sebastian, M. Le Gallo, R. Khaddam-Aljameh, and E. Eleftheriou, *Memory Devices and Applications for In-Memory Computing*, Nat. Nanotechnol. **15**, 529 (2020).
- [2] Z. Guo, J. Yin, Y. Bai, D. Zhu, K. Shi, G. Wang, K. Cao, and W. Zhao, *Spintronics for Energy-Efficient Computing: An Overview and Outlook*, Proc. IEEE **109**, 1398 (2021).
- [3] M. Baibich, J. Broto, A. Fert, F. Vandau, F. Petroff, P. Eitenne, G. Creuzet, A. Friederich, and J. Chazelas, *Giant Magnetoresistance of (001)Fe/(001)Cr Magnetic Superlattices*, Phys. Rev. Lett. **61**, 2472 (1988).
- [4] G. Binasch, P. Grunberg, F. Saurenbach, and W. Zinn, *Enhanced Magnetoresistance in Layered Magnetic-Structures with Antiferromagnetic Interlayer Exchange*, Phys. Rev. B **39**, 4828 (1989).
- [5] S. N. Mao et al., *Commercial TMR Heads for Hard Disk Drives: Characterization and Extendibility at 300 Gbit/in(2)*, IEEE Trans. Magn. **42**, 97 (2006).
- [6] M. Takagishi, K. Yamada, H. Iwasaki, H. N. Fuke, and S. Hashimoto, *Magnetoresistance Ratio and Resistance Area Design of CPP-MR Film for 2-5 Tb/in(2) Read Sensors*, IEEE Trans. Magn. **46**, 2086 (2010).
- [7] H. N. Fuke, S. Hashimoto, M. Takagishi, H. Iwasaki, S. Kawasaki, K. Miyake, and M. Sahashi, *Magnetoresistance of FeCo Nanocontacts with Current-Perpendicular-to-Plane Spin-Valve Structure*, IEEE Trans. Magn. **43**, 2848 (2007).
- [8] H. J. Richter, *The Transition from Longitudinal to Perpendicular Recording*, J. Phys. D-Appl. Phys. **40**, R149 (2007).
- [9] M. H. Kryder, E. C. Gage, T. W. Mcdaniel, W. A. Challener, R. E. Rottmayer, G. Ju, Y.-T. Hsia, and M. F. Erden, *Heat Assisted Magnetic Recording*, Proc. IEEE **96**, 1810 (2008).
- [10] M. A. Seigler et al., *Integrated Heat Assisted Magnetic Recording Head: Design and Recording Demonstration*, IEEE Trans. Magn. **44**, 119 (2008).
- [11] G. Ju et al., *High Density Heat-Assisted Magnetic Recording Media and Advanced Characterization-Progress and Challenges*, IEEE Trans. Magn. **51**, 3201709 (2015).
- [12] J.-G. Zhu, X. Zhu, and Y. Tang, *Microwave Assisted Magnetic Recording*, IEEE Trans. Magn. **44**, 125 (2008).
- [13] T. Seki, K. Utsumiya, Y. Nozaki, H. Imamura, and K. Takanashi, *Spin Wave-Assisted Reduction in Switching Field of Highly Coercive Iron-Platinum Magnets*, Nat. Commun. **4**, 1726 (2013).
- [14] B. Dieny et al., *Opportunities and Challenges for Spintronics in the Microelectronics Industry*, Nat. Electron. **3**, 446 (2020).
- [15] Y. M. Huai, F. Albert, P. Nguyen, M. Pakala, and T. Valet, *Observation of Spin-Transfer Switching in Deep Submicron-Sized and Low-Resistance Magnetic Tunnel Junctions*, Appl. Phys. Lett. **84**, 3118 (2004).
- [16] J. Hayakawa, S. Ikeda, Y. M. Lee, R. Sasaki, T. Meguro, F. Matsukura, H. Takahashi, and H. Ohno, *Current-Induced Magnetization Switching in MgO Barrier Based Magnetic Tunnel Junctions with CoFeB/Ru/CoFeB Synthetic*

- Ferrimagnetic Free Layer*, Jpn. J. Appl. Phys. Part 2 - Lett. Express Lett. **45**, L1057 (2006).
- [17] M. K. Zhao, R. Zhang, C. H. Wan, X. M. Luo, Y. Zhang, W. Q. He, Y. Z. Wang, W. L. Yang, G. Q. Yu, and X. F. Han, *Type-Y Magnetic Tunnel Junctions with CoFeB Doped Tungsten as Spin Current Source*, Appl. Phys. Lett. **120**, 182405 (2022).
- [18] S. Mangin, D. Ravelosona, J. A. Katine, M. J. Carey, B. D. Terris, and E. E. Fullerton, *Current-Induced Magnetization Reversal in Nanopillars with Perpendicular Anisotropy*, Nat. Mater. **5**, 210 (2006).
- [19] M. Nakayama, T. Kai, N. Shimomura, M. Amano, E. Kitagawa, T. Nagase, M. Yoshikawa, T. Kishi, S. Ikegawa, and H. Yoda, *Spin Transfer Switching in TbCoFe/CoFeB/MgO/CoFeB/TbCoFe Magnetic Tunnel Junctions with Perpendicular Magnetic Anisotropy*, J. Appl. Phys. **103**, 07A710 (2008).
- [20] S. Ikeda, K. Miura, H. Yamamoto, K. Mizunuma, H. D. Gan, M. Endo, S. Kanai, J. Hayakawa, F. Matsukura, and H. Ohno, *A Perpendicular-Anisotropy CoFeB-MgO Magnetic Tunnel Junction*, Nat. Mater. **9**, 721 (2010).
- [21] N. Nishimura, T. Hirai, A. Koganei, T. Ikeda, K. Okano, Y. Sekiguchi, and Y. Osada, *Magnetic Tunnel Junction Device with Perpendicular Magnetization Films for High-Density Magnetic Random Access Memory*, J. Appl. Phys. **91**, 5246 (2002).
- [22] K. C. Chun, H. Zhao, J. D. Harms, T.-H. Kim, J.-P. Wang, and C. H. Kim, *A Scaling Roadmap and Performance Evaluation of In-Plane and Perpendicular MTJ Based STT-MRAMs for High-Density Cache Memory*, IEEE J. Solid-State Circuit **48**, 598 (2013).
- [23] T. Ohsawa, H. Koike, S. Miura, H. Honjo, K. Kinoshita, S. Ikeda, T. Hanyu, H. Ohno, and T. Endoh, *A 1 Mb Nonvolatile Embedded Memory Using 4T2MTJ Cell With 32 b Fine-Grained Power Gating Scheme*, IEEE J. Solid-State Circuit **48**, 1511 (2013).
- [24] M.-C. Shih et al., *Reliability Study of Perpendicular STT-MRAM as Emerging Embedded Memory Qualified for Reflow Soldering at 260 Degrees C*, in *2016 IEEE Symposium on VLSI Technology* (IEEE, New York, 2016).
- [25] Y. J. Song et al., *Highly Functional and Reliable 8Mb STT-MRAM Embedded in 28nm Logic*, in *2016 IEEE International Electron Devices Meeting (IEDM)* (IEEE, New York, 2016), p. 27.2.
- [26] D. Saida et al., *1x-to 2x-Nm Perpendicular MTJ Switching at Sub-3-Ns Pulses Below 100 μ A for High-Performance Embedded STT-MRAM for Sub-20-Nm CMOS*, IEEE Trans. Electron Devices **64**, 427 (2017).
- [27] P.-K. Wang, *STT-MRAM for Embedded Memory Applications from ENVM to Last Level Cache*, in *2018 International Symposium on VLSI Technology, Systems and Application (VLSI-TSA)* (IEEE, New York, 2018).
- [28] O. Golonzka et al., *MRAM as Embedded Non-Volatile Memory Solution for 22FFL FinFET Technology*, in *2018 IEEE International Electron Devices Meeting (IEDM)* (IEEE, New York, 2018).
- [29] Q. Dong, Z. Wang, J. Lim, Y. Zhang, M. E. Sinangil, Y.-C. Shih, Y.-D. Chih, J. Chang, D. Blaauw, and D. Sylvester, *A 1-Mb 28-Nm 1T1MTJ STT-MRAM With Single-Cap Offset-Cancelled Sense Amplifier and In Situ Self-Write-Termination*, IEEE J. Solid-State Circuit **54**, 231 (2019).
- [30] S. Ikegawa, F. B. Mancoff, J. Janesky, and S. Aggarwal, *Magnetoresistive Random Access Memory: Present and Future*, IEEE Trans. Electron Devices **67**, 1407 (2020).

- [31] X. Han, X. Wang, C. Wan, G. Yu, and X. Lv, *Spin-Orbit Torques: Materials, Physics, and Devices*, Appl. Phys. Lett. **118**, 120502 (2021).
- [32] M. Julliere, *Tunneling Between Ferromagnetic-Films*, Phys. Lett. A **54**, 225 (1975).
- [33] J. Slonczewski, *Conductance and Exchange Coupling of 2 Ferromagnets Separated by a Tunneling Barrier*, Phys. Rev. B **39**, 6995 (1989).
- [34] T. Miyazaki and N. Tezuka, *Giant Magnetic Tunneling Effect in Fe/Al₂O₃/Fe Junction*, J. Magn. Magn. Mater. **139**, L231 (1995).
- [35] J. Moodera, L. Kinder, T. Wong, and R. Meservey, *Large Magnetoresistance at Room-Temperature in Ferromagnetic Thin-Film Tunnel-Junctions*, Phys. Rev. Lett. **74**, 3273 (1995).
- [36] H. X. Wei, Q. H. Qin, M. Ma, R. Sharif, and X. F. Han, *80% Tunneling Magnetoresistance at Room Temperature for Thin Al-O Barrier Magnetic Tunnel Junction with CoFeB as Free and Reference Layers*, J. Appl. Phys. **101**, 09B501 (2007).
- [37] W. H. Butler, X. G. Zhang, T. C. Schulthess, and J. M. MacLaren, *Spin-Dependent Tunneling Conductance of Fe Vertical Bar MgO Vertical Bar Fe Sandwiches*, Phys. Rev. B **63**, 054416 (2001).
- [38] J. Mathon and A. Umerski, *Theory of Tunneling Magnetoresistance of an Epitaxial Fe/MgO/Fe(001) Junction*, Phys. Rev. B **63**, 220403 (2001).
- [39] F. Bonell, S. Andrieu, C. Tiusan, F. Montaigne, E. Snoeck, B. Belhadji, L. Calmels, F. Bertran, P. Le Fevre, and A. Taleb-Ibrahimi, *Influence of Misfit Dislocations on the Magnetoresistance of MgO-Based Epitaxial Magnetic Tunnel Junctions*, Phys. Rev. B **82**, 092405 (2010).
- [40] A. Duluard, C. Bellouard, Y. Lu, M. Hehn, D. Lacour, F. Montaigne, G. Lengaigne, S. Andrieu, F. Bonell, and C. Tiusan, *Enhanced Magnetoresistance by Monoatomic Roughness in Epitaxial Fe/MgO/Fe Tunnel Junctions*, Phys. Rev. B **91**, 174403 (2015).
- [41] X. G. Zhang, W. H. Butler, and A. Bandyopadhyay, *Effects of the Iron-Oxide Layer in Fe-FeO-MgO-Fe Tunneling Junctions*, Phys. Rev. B **68**, 092402 (2003).
- [42] H. L. Meyerheim, R. Popescu, N. Jedrecy, M. Vedpathak, M. Sauvage-Simkin, R. Pinchaux, B. Heinrich, and J. Kirschner, *Surface X-Ray Diffraction Analysis of the MgO/Fe(001) Interface: Evidence for an FeO Layer*, Phys. Rev. B **65**, 144433 (2002).
- [43] Q. L. Ma, S. G. Wang, J. Zhang, Y. Wang, R. C. C. Ward, C. Wang, A. Kohn, X.-G. Zhang, and X. F. Han, *Temperature Dependence of Resistance in Epitaxial Fe/MgO/Fe Magnetic Tunnel Junctions*, Appl. Phys. Lett. **95**, 052506 (2009).
- [44] S. S. P. Parkin, C. Kaiser, A. Panchula, P. M. Rice, B. Hughes, M. Samant, and S. H. Yang, *Giant Tunneling Magnetoresistance at Room Temperature with MgO (100) Tunnel Barriers*, Nat. Mater. **3**, 862 (2004).
- [45] S. Yuasa, T. Nagahama, A. Fukushima, Y. Suzuki, and K. Ando, *Giant Room-Temperature Magnetoresistance in Single-Crystal Fe/MgO/Fe Magnetic Tunnel Junctions*, Nat. Mater. **3**, 868 (2004).
- [46] F. Bonell et al., *Spin-Polarized Electron Tunneling in Bcc FeCo/MgO/FeCo(001) Magnetic Tunnel Junctions*, Phys. Rev. Lett. **108**, 176602 (2012).
- [47] S. Andrieu, L. Calmels, T. Hauet, F. Bonell, P. Le Fevre, and F. Bertran, *Spectroscopic and Transport Studies of CoxFe1-x/MgO(001)-Based Magnetic Tunnel Junctions*, Phys. Rev. B **90**, 214406 (2014).
- [48] T. Scheike, Z. Wen, H. Sukegawa, and S. Mitani, *Enhanced Tunnel Magnetoresistance in Fe/Mg₄Al-O-x/Fe(001) Magnetic Tunnel Junctions*, Appl.

- Phys. Lett. **120**, 032404 (2022).
- [49] Y. Miura, S. Muramoto, K. Abe, and M. Shirai, *First-Principles Study of Tunneling Magnetoresistance in Fe/MgAl₂O₄/Fe(001) Magnetic Tunnel Junctions*, Phys. Rev. B **86**, 024426 (2012).
- [50] Q. Xiang, H. Sukegawa, M. Belmoubarik, M. Al-Mahdawi, T. Scheike, S. Kasai, Y. Miura, and S. Mitani, *Realizing Room-Temperature Resonant Tunnel Magnetoresistance in Cr/Fe/MgAl₂O₄ Quasi-Quantum Well Structures*, Adv. Sci. **6**, 1901438 (2019).
- [51] A. Iovan, S. Andersson, Y. G. Naidyuk, A. Vedyayev, B. Dieny, and V. Korenivski, *Spin Diode Based on Fe/MgO Double Tunnel Junction*, Nano Lett. **8**, 805 (2008).
- [52] Z. Y. Lu, X. G. Zhang, and S. T. Pantelides, *Spin-Dependent Resonant Tunneling through Quantum-Well States in Magnetic Metallic Thin Films*, Phys. Rev. Lett. **94**, 207210 (2005).
- [53] T. Nozaki, N. Tezuka, and K. Inomata, *Quantum Oscillation of the Tunneling Conductance in Fully Epitaxial Double Barrier Magnetic Tunnel Junctions*, Phys. Rev. Lett. **96**, 027208 (2006).
- [54] T. Niizeki, N. Tezuka, and K. Inomata, *Enhanced Tunnel Magnetoresistance Due to Spin Dependent Quantum Well Resonance in Specific Symmetry States of an Ultrathin Ferromagnetic Electrode*, Phys. Rev. Lett. **100**, 047207 (2008).
- [55] R. S. Liu et al., *CoFe Alloy as Middle Layer for Strong Spin Dependent Quantum Well Resonant Tunneling in MgO Double Barrier Magnetic Tunnel Junctions*, Phys. Rev. B **87**, 024411 (2013).
- [56] B. S. Tao et al., *Long-Range Phase Coherence in Double-Barrier Magnetic Tunnel Junctions with a Large Thick Metallic Quantum Well*, Phys. Rev. Lett. **115**, 157204 (2015).
- [57] B. Tao et al., *Coherent Resonant Tunneling through Double Metallic Quantum Well States*, Nano Lett. **19**, 3019 (2019).
- [58] Y. Wang, Z.-Y. Lu, X.-G. Zhang, and X. F. Han, *First-Principles Theory of Quantum Well Resonance in Double Barrier Magnetic Tunnel Junctions*, Phys. Rev. Lett. **97**, 087210 (2006).
- [59] L. Schwee, *Proposal on Cross-Tie Wall and Bloch Line Propagation in Thin Magnetic-Films*, IEEE Trans. Magn. **MAG8**, 405 (1972).
- [60] Z. G. Wang and Y. Nakamura, *Spin Tunneling Random Access Memory (STram)*, IEEE Trans. Magn. **32**, 4022 (1996).
- [61] J. M. Daughton, *Magnetic Tunneling Applied to Memory*, J. Appl. Phys. **81**, 3758 (1997).
- [62] R. Scheuerlein, W. Gallagher, S. Parkin, A. Lee, S. Ray, R. Robertazzi, and W. Reohr, *A 10 Ns Read and Write Non-Volatile Memory Array Using a Magnetic Tunnel Junction and FET Switch in Each Cell*, in *2000 IEEE International Solid-State Circuits Conference. Digest of Technical Papers (Cat. No.00CH37056)* (2000), pp. 128–129.
- [63] M. Durlam, P. Naji, M. DeHerrera, S. Tehrani, G. Kerszykowski, and K. Kyler, *Nonvolatile RAM Based on Magnetic Tunnel Junction Elements*, in *2000 IEEE International Solid-State Circuits Conference. Digest of Technical Papers (Cat. No.00CH37056)* (2000), pp. 130–131.
- [64] M. Durlam et al., *A 0.18 μ m 4Mb Toggling MRAM*, in *IEEE International Electron Devices Meeting 2003* (2003), p. 34.6.1-34.6.3.
- [65] B. N. Engel et al., *A 4-Mb Toggle MRAM Based on a Novel Bit and Switching Method*, IEEE Trans. Magn. **41**, 132 (2005).
- [66] Y. Iwata et al., *A 16Mb MRAM with FORK Wiring Scheme and Burst Modes*, in

- 2006 IEEE International Solid State Circuits Conference - Digest of Technical Papers (2006), pp. 477–486.
- [67] J. DeBrosse et al., *A High-Speed 128-Kb MRAM Core for Future Universal Memory Applications*, IEEE J. Solid-State Circuit **39**, 678 (2004).
- [68] B. Dieny and M. Chshiev, *Perpendicular Magnetic Anisotropy at Transition Metal/Oxide Interfaces and Applications*, Rev. Mod. Phys. **89**, 025008 (2017).
- [69] D. C. Worledge, G. Hu, D. W. Abraham, J. Z. Sun, P. L. Trouilloud, J. Nowak, S. Brown, M. C. Gaidis, E. J. O’Sullivan, and R. P. Robertazzi, *Spin Torque Switching of Perpendicular Ta Vertical Bar CoFeB Vertical Bar MgO-Based Magnetic Tunnel Junctions*, Appl. Phys. Lett. **98**, 022501 (2011).
- [70] D. C. Worledge, G. Hu, D. W. Abraham, P. L. Trouilloud, and S. Brown, *Development of Perpendicularly Magnetized Ta Vertical Bar CoFeB Vertical Bar MgO-Based Tunnel Junctions at IBM (Invited)*, J. Appl. Phys. **115**, 172601 (2014).
- [71] R. Q. Zhang, G. Y. Shi, J. Su, Y. X. Shang, J. W. Cai, L. Y. Liao, F. Pan, and C. Song, *Tunable Spin-Orbit Torque Switching in Antiferromagnetically Coupled CoFeB/Ta/CoFeB*, Appl. Phys. Lett. **117**, 212403 (2020).
- [72] K. Lee, J. J. Sapan, S. H. Kang, and E. E. Fullerton, *Perpendicular Magnetization of CoFeB on Single-Crystal MgO*, J. Appl. Phys. **109**, 123910 (2011).
- [73] J. W. Koo, S. Mitani, T. T. Sasaki, H. Sukegawa, Z. C. Wen, T. Ohkubo, T. Niizeki, K. Inomata, and K. Hono, *Large Perpendicular Magnetic Anisotropy at Fe/MgO Interface*, Appl. Phys. Lett. **103**, 192401 (2013).
- [74] C.-H. Lambert, A. Rajanikanth, T. Hauet, S. Mangin, E. E. Fullerton, and S. Andrieu, *Quantifying Perpendicular Magnetic Anisotropy at the Fe-MgO(001) Interface*, Appl. Phys. Lett. **102**, 122410 (2013).
- [75] A. Koziol-Rachwal, T. Slezak, K. Matlak, P. Kuswik, M. Urbaniak, F. Stobiecki, L. D. Yao, S. van Dijken, and J. Korecki, *Tunable Magnetic Properties of Monoatomic Metal-Oxide Fe/MgO Multilayers*, Phys. Rev. B **90**, 045428 (2014).
- [76] A. Manchon et al., *Analysis of Oxygen Induced Anisotropy Crossover in Pt/Co/MOx Trilayers*, J. Appl. Phys. **104**, 043914 (2008).
- [77] S. Monso, B. Rodmacq, S. Auffret, G. Casali, F. Fettar, B. Gilles, B. Dieny, and P. Boyer, *Crossover from In-Plane to Perpendicular Anisotropy in Pt/CoFe/AlOx Sandwiches as a Function of Al Oxidation: A Very Accurate Control of the Oxidation of Tunnel Barriers*, Appl. Phys. Lett. **80**, 4157 (2002).
- [78] B. Carvello, C. Ducruet, B. Rodmacq, S. Auffret, E. Gautier, G. Gaudin, and B. Dieny, *Sizable Room-Temperature Magnetoresistance in Cobalt Based Magnetic Tunnel Junctions with out-of-Plane Anisotropy*, Appl. Phys. Lett. **92**, 102508 (2008).
- [79] J.-H. Park, C. Park, T. Jeong, M. T. Moneck, N. T. Nufer, and J.-G. Zhu, *Co/Pt Multilayer Based Magnetic Tunnel Junctions Using Perpendicular Magnetic Anisotropy*, J. Appl. Phys. **103**, 07A917 (2008).
- [80] K. Mizunuma, S. Ikeda, J. H. Park, H. Yamamoto, H. Gan, K. Miura, H. Hasegawa, J. Hayakawa, F. Matsukura, and H. Ohno, *MgO Barrier-Perpendicular Magnetic Tunnel Junctions with CoFe/Pd Multilayers and Ferromagnetic Insertion Layers*, Appl. Phys. Lett. **95**, 232516 (2009).
- [81] B. Huang et al., *Layer-Dependent Ferromagnetism in a van Der Waals Crystal down to the Monolayer Limit*, Nature **546**, 270 (2017).
- [82] B. Huang et al., *Electrical Control of 2D Magnetism in Bilayer CrI₃*, Nat. Nanotechnol. **13**, 544 (2018).
- [83] H. Y. Song et al., *Van Der Waals Electride: Toward Intrinsic Two-Dimensional*

- Ferromagnetism of Spin-Polarized Anionic Electrons*, Mater. Today Phys. **20**, 100473 (2021).
- [84] Y. Deng et al., *Gate-Tunable Room-Temperature Ferromagnetism in Two-Dimensional Fe₃GeTe₂*, Nature **563**, 94 (2018).
- [85] X. Wang et al., *Current-Driven Magnetization Switching in a van Der Waals Ferromagnet Fe₃GeTe₂*, Sci. Adv. **5**, eaaw8904 (2019).
- [86] M. Alghamdi, M. Lohmann, J. Li, P. R. Jothi, Q. Shao, M. Aldosary, T. Su, B. P. T. Fokwa, and J. Shi, *Highly Efficient Spin-Orbit Torque and Switching of Layered Ferromagnet Fe₃GeTe₂*, Nano Lett. **19**, 4400 (2019).
- [87] T. Song et al., *Voltage Control of a van Der Waals Spin-Filter Magnetic Tunnel Junction*, Nano Lett. **19**, 915 (2019).
- [88] Y. Wei, S. Matzen, C. P. Quinteros, T. Maroutian, G. Agnus, P. Lecoeur, and B. Noheda, *Magneto-Ionic Control of Spin Polarization in Multiferroic Tunnel Junctions*, Npj Quantum Mater. **4**, 62 (2019).
- [89] Y. Wei, S. Matzen, T. Maroutian, G. Agnus, M. Salverda, P. Nukala, Q. Chen, J. Ye, P. Lecoeur, and B. Noheda, *Magnetic Tunnel Junctions Based on Ferroelectric Hf_{0.5}Zr_{0.5}O₂ Tunnel Barriers*, Phys. Rev. Appl. **12**, 031001 (2019).
- [90] D. Pantel, S. Goetze, D. Hesse, and M. Alexe, *Reversible Electrical Switching of Spin Polarization in Multiferroic Tunnel Junctions*, Nat. Mater. **11**, 289 (2012).
- [91] J. C. Slonczewski, *Current-Driven Excitation of Magnetic Multilayers*, J. Magn. Magn. Mater. **159**, L1 (1996).
- [92] L. Berger, *Emission of Spin Waves by a Magnetic Multilayer Traversed by a Current*, Phys. Rev. B **54**, 9353 (1996).
- [93] E. B. Myers, D. C. Ralph, J. A. Katine, R. N. Louie, and R. A. Buhrman, *Current-Induced Switching of Domains in Magnetic Multilayer Devices*, Science **285**, 867 (1999).
- [94] M. Hosomi et al., *A Novel Nonvolatile Memory with Spin Torque Transfer Magnetization Switching: Spin-RAM*, in *IEEE International Electron Devices Meeting 2005, Technical Digest* (IEEE, New York, 2005), pp. 473–476.
- [95] G. Schmidt, D. Ferrand, L. W. Molenkamp, A. T. Filip, and B. J. van Wees, *Fundamental Obstacle for Electrical Spin Injection from a Ferromagnetic Metal into a Diffusive Semiconductor*, Phys. Rev. B **62**, R4790 (2000).
- [96] Y. Nagamine, H. Maehara, K. Tsunekawa, D. D. Djayaprawira, N. Watanabe, S. Yuasa, and K. Ando, *Ultralow Resistance-Area Product of 0.4 $\Omega\mu\text{m}^2$ and High Magnetoresistance above 50% in CoFeB/MgO/CoFeB Magnetic Tunnel Junctions*, Appl. Phys. Lett. **89**, 162507 (2006).
- [97] K. Watanabe, B. Jinnai, S. Fukami, H. Sato, and H. Ohno, *Shape Anisotropy Revisited in Single-Digit Nanometer Magnetic Tunnel Junctions*, Nat. Commun. **9**, 663 (2018).
- [98] N. Perrissin, S. Lequeux, N. Strelkov, A. Chavent, L. Vila, L. D. Buda-Prejbeanu, S. Auffret, R. C. Sousa, I. L. Prejbeanu, and B. Dieny, *A Highly Thermally Stable Sub-20 Nm Magnetic Random-Access Memory Based on Perpendicular Shape Anisotropy*, Nanoscale **10**, 12187 (2018).
- [99] N. Cacoilo, S. Lequeux, B. M. S. Teixeira, B. Dieny, R. C. Sousa, N. A. Sobolev, O. Fruchart, I. L. Prejbeanu, and L. D. Buda-Prejbeanu, *Spin-Torque-Triggered Magnetization Reversal in Magnetic Tunnel Junctions with Perpendicular Shape Anisotropy*, Phys. Rev. Appl. **16**, 024020 (2021).
- [100] K.-S. Lee, S.-W. Lee, B.-C. Min, and K.-J. Lee, *Threshold Current for Switching of a Perpendicular Magnetic Layer Induced by Spin Hall Effect*, Appl. Phys. Lett.

- 102**, 112410 (2013).
- [101] L. Liu, O. J. Lee, T. J. Gudmundsen, D. C. Ralph, and R. A. Buhrman, *Current-Induced Switching of Perpendicularly Magnetized Magnetic Layers Using Spin Torque from the Spin Hall Effect*, Phys. Rev. Lett. **109**, 096602 (2012).
- [102] L. Liu, T. Moriyama, D. C. Ralph, and R. A. Buhrman, *Spin-Torque Ferromagnetic Resonance Induced by the Spin Hall Effect*, Phys. Rev. Lett. **106**, 036601 (2011).
- [103] L. Liu, C.-F. Pai, Y. Li, H. W. Tseng, D. C. Ralph, and R. A. Buhrman, *Spin-Torque Switching with the Giant Spin Hall Effect of Tantalum*, Science **336**, 555 (2012).
- [104] I. Mihai Miron, G. Gaudin, S. Auffret, B. Rodmacq, A. Schuhl, S. Pizzini, J. Vogel, and P. Gambardella, *Current-Driven Spin Torque Induced by the Rashba Effect in a Ferromagnetic Metal Layer*, Nat. Mater. **9**, 230 (2010).
- [105] I. Mihai Miron, K. Garello, G. Gaudin, P.-J. Zermatten, M. V. Costache, S. Auffret, S. Bandiera, B. Rodmacq, A. Schuhl, and P. Gambardella, *Perpendicular Switching of a Single Ferromagnetic Layer Induced by In-Plane Current Injection*, Nature **476**, 189 (2011).
- [106] U. H. Pi, K. W. Kim, J. Y. Bae, S. C. Lee, Y. J. Cho, K. S. Kim, and S. Seo, *Tilting of the Spin Orientation Induced by Rashba Effect in Ferromagnetic Metal Layer*, Appl. Phys. Lett. **97**, 162507 (2010).
- [107] I. Mihai Miron et al., *Fast Current-Induced Domain-Wall Motion Controlled by the Rashba Effect*, Nat. Mater. **10**, 419 (2011).
- [108] X. Wang and A. Manchon, *Diffusive Spin Dynamics in Ferromagnetic Thin Films with a Rashba Interaction*, Phys. Rev. Lett. **108**, 117201 (2012).
- [109] D. A. Pesin and A. H. MacDonald, *Quantum Kinetic Theory of Current-Induced Torques in Rashba Ferromagnets*, Phys. Rev. B **86**, 014416 (2012).
- [110] P. M. Haney, H.-W. Lee, K.-J. Lee, A. Manchon, and M. D. Stiles, *Current Induced Torques and Interfacial Spin-Orbit Coupling: Semiclassical Modeling*, Phys. Rev. B **87**, 174411 (2013).
- [111] K.-W. Kim, S.-M. Seo, J. Ryu, K.-J. Lee, and H.-W. Lee, *Magnetization Dynamics Induced by In-Plane Currents in Ultrathin Magnetic Nanostructures with Rashba Spin-Orbit Coupling*, Phys. Rev. B **85**, 180404 (2012).
- [112] A. Chernyshov, M. Overby, X. Liu, J. K. Furdyna, Y. Lyanda-Geller, and L. P. Rokhinson, *Evidence for Reversible Control of Magnetization in a Ferromagnetic Material by Means of Spin-Orbit Magnetic Field*, Nat. Phys. **5**, 656 (2009).
- [113] Y. Du, S. Takahashi, and J. Nitta, *Spin Current Related Magnetoresistance in Epitaxial Pt/Co Bilayers in the Presence of Spin Hall Effect and Rashba-Edelstein Effect*, Phys. Rev. B **103**, 094419 (2021).
- [114] K. Garello et al., *SOT-MRAM 300nm Integration for Low Power and Ultrafast Embedded Memories*, in *2018 IEEE Symposium on VLSI Circuits* (IEEE, New York, 2018), pp. 81–82.
- [115] Y. Shiota, T. Nozaki, F. Bonell, S. Murakami, T. Shinjo, and Y. Suzuki, *Induction of Coherent Magnetization Switching in a Few Atomic Layers of FeCo Using Voltage Pulses*, Nat. Mater. **11**, 39 (2012).
- [116] H. Yoda et al., *Voltage-Control Spintronics Memory (VoCSM) Having Potentials of Ultra-Low Energy-Consumption and High-Density*, in *2016 IEEE International Electron Devices Meeting (IEDM)* (IEEE, New York, 2016), p. 27.6.
- [117] D. Chiba, S. Fukami, K. Shimamura, N. Ishiwata, K. Kobayashi, and T. Ono,

- Electrical Control of the Ferromagnetic Phase Transition in Cobalt at Room Temperature*, Nat. Mater. **10**, 853 (2011).
- [118] C. Wan, X. Zhang, Z. Yuan, C. Fang, W. Kong, Q. Zhang, H. Wu, U. Khan, and X. Han, *Programmable Spin Logic Based on Spin Hall Effect in a Single Device*, Adv. Electron. Mater. **3**, 1600282 (2017).
- [119] X. Wang et al., *Field-Free Programmable Spin Logics via Chirality-Reversible Spin-Orbit Torque Switching*, Adv. Mater. **30**, 1801318 (2018).
- [120] W. J. Kong, C. H. Wan, X. Wang, B. S. Tao, L. Huang, C. Fang, C. Y. Guo, Y. Guang, M. Irfan, and X. F. Han, *Spin-Orbit Torque Switching in a T-Type Magnetic Configuration with Current Orthogonal to Easy Axes*, Nat. Commun. **10**, 233 (2019).
- [121] G. J. Lim, D. Chua, W. Gan, C. Murapaka, and W. S. Lew, *Programmable Spin-Orbit-Torque Logic Device with Integrated Bipolar Bias Field for Chirality Control*, Adv. Electron. Mater. **6**, 1901090 (2020).
- [122] J. Sinova, S. O. Valenzuela, J. Wunderlich, C. H. Back, and T. Jungwirth, *Spin Hall Effects*, Rev. Mod. Phys. **87**, 1213 (2015).
- [123] S. Murakami, N. Nagaosa, and S. C. Zhang, *Dissipationless Quantum Spin Current at Room Temperature*, Science **301**, 1348 (2003).
- [124] J. Sinova, D. Culcer, Q. Niu, N. A. Sinitsyn, T. Jungwirth, and A. H. MacDonald, *Universal Intrinsic Spin Hall Effect*, Phys. Rev. Lett. **92**, 126603 (2004).
- [125] L. Berger, *Side-Jump Mechanism for the Hall Effect of Ferromagnets*, Physical Review B **2**, 4559 (1970).
- [126] J. E. Hirsch, *Spin Hall Effect*, Phys. Rev. Lett. **83**, 1834 (1999).
- [127] S. F. Zhang, *Spin Hall Effect in the Presence of Spin Diffusion*, Phys. Rev. Lett. **85**, 393 (2000).
- [128] X. Zhang, C. H. Wan, Z. H. Yuan, Q. T. Zhang, H. Wu, L. Huang, W. J. Kong, C. Fang, U. Khan, and X. F. Han, *Electrical Control over Perpendicular Magnetization Switching Driven by Spin-Orbit Torques*, Phys. Rev. B **94**, 174434 (2016).
- [129] W. Zhang, W. Han, X. Jiang, S.-H. Yang, and S. S. P. Parkin, *Role of Transparency of Platinum-Ferromagnet Interfaces in Determining the Intrinsic Magnitude of the Spin Hall Effect*, Nat. Phys. **11**, 496 (2015).
- [130] Y. Zhou et al., *Current-Induced In-Plane Magnetization Switching in a Biaxial Ferrimagnetic Insulator*, Phys. Rev. Appl. **13**, 064051 (2020).
- [131] M. Yang et al., *All-Linear Multistate Magnetic Switching Induced by Electrical Current*, Phys. Rev. Appl. **15**, 054013 (2021).
- [132] L. Zhu, L. Zhu, M. Sui, D. C. Ralph, and R. A. Buhrman, *Variation of the Giant Intrinsic Spin Hall Conductivity of Pt with Carrier Lifetime*, Sci. Adv. **5**, eaav8025 (2019).
- [133] C.-Y. Hu and C.-F. Pai, *Benchmarking of Spin-Orbit Torque Switching Efficiency in Pt Alloys*, Adv. Quantum Technol. **3**, 2000024 (2020).
- [134] L. Zhu, D. C. Ralph, and R. A. Buhrman, *Highly Efficient Spin-Current Generation by the Spin Hall Effect in Au1-XPtx*, Phys. Rev. Appl. **10**, 031001 (2018).
- [135] L. Zhu, L. Zhu, S. Shi, M. Sui, D. C. Ralph, and R. A. Buhrman, *Enhancing Spin-Orbit Torque by Strong Interfacial Scattering From Ultrathin Insertion Layers*, Phys. Rev. Appl. **11**, 061004 (2019).
- [136] C.-F. Pai, L. Liu, Y. Li, H. W. Tseng, D. C. Ralph, and R. A. Buhrman, *Spin Transfer Torque Devices Utilizing the Giant Spin Hall Effect of Tungsten*, Appl. Phys. Lett. **101**, 122404 (2012).

- [137] G. Yu et al., *Switching of Perpendicular Magnetization by Spin-Orbit Torques in the Absence of External Magnetic Fields*, Nat. Nanotechnol. **9**, 548 (2014).
- [138] C. Zhang, S. Fukami, K. Watanabe, A. Ohkawara, S. DuttaGupta, H. Sato, F. Matsukura, and H. Ohno, *Critical Role of W Deposition Condition on Spin-Orbit Torque Induced Magnetization Switching in Nanoscale W/CoFeB/MgO*, Appl. Phys. Lett. **109**, 192405 (2016).
- [139] W. Chen, G. Xiao, Q. Zhang, and X. Zhang, *Temperature Study of the Giant Spin Hall Effect in the Bulk Limit of Beta-W*, Phys. Rev. B **98**, 134411 (2018).
- [140] K. K. V. Sethu, S. Ghosh, S. Couet, J. Swerts, B. Soree, J. De Boeck, G. S. Kar, and K. Garello, *Optimization of Tungsten Beta-Phase Window for Spin-Orbit-Torque Magnetic Random-Access Memory*, Phys. Rev. Appl. **16**, 064009 (2021).
- [141] L. Zhu, K. Sobotkiewich, X. Ma, X. Li, D. C. Ralph, and R. A. Buhrman, *Strong Damping-Like Spin-Orbit Torque and Tunable Dzyaloshinskii-Moriya Interaction Generated by Low-Resistivity Pd1-XPtx Alloys*, Adv. Funct. Mater. **29**, 1805822 (2019).
- [142] R. Ramaswamy, X. Qiu, T. Dutta, S. D. Pollard, and H. Yang, *Hf Thickness Dependence of Spin-Orbit Torques in Hf/CoFeB/MgO Heterostructures*, Appl. Phys. Lett. **108**, 202406 (2016).
- [143] C. Cao et al., *Spin-Orbit Torque and Dzyaloshinskii-Moriya Interaction in 4d Metal Rh-Based Magnetic Heterostructures*, Appl. Phys. Lett. **118**, 112402 (2021).
- [144] S. Dutta, A. Bose, A. A. Tulapurkar, R. A. Buhrman, and D. C. Ralph, *Interfacial and Bulk Spin Hall Contributions to Fieldlike Spin-Orbit Torque Generated by Iridium*, Phys. Rev. B **103**, 184416 (2021).
- [145] S. Fukami, C. Zhang, S. DuttaGupta, A. Kurenkov, and H. Ohno, *Magnetization Switching by Spin-Orbit Torque in an Antiferromagnet-Ferromagnet Bilayer System*, Nat. Mater. **15**, 535 (2016).
- [146] Y.-W. Oh et al., *Field-Free Switching of Perpendicular Magnetization through Spin-Orbit Torque in Antiferromagnet/Ferromagnet/Oxide Structures*, Nat. Nanotechnol. **11**, 878 (2016).
- [147] W. J. Kong et al., *Field-Free Spin Hall Effect Driven Magnetization Switching in Pd/Co/IrMn Exchange Coupling System*, Appl. Phys. Lett. **109**, 132402 (2016).
- [148] D. MacNeill, G. M. Stiehl, M. H. D. Guimaraes, R. A. Buhrman, J. Park, and D. C. Ralph, *Control of Spin-Orbit Torques through Crystal Symmetry in WTe₂/Ferromagnet Bilayers*, Nat. Phys. **13**, 300 (2017).
- [149] S. Shi et al., *All-Electric Magnetization Switching and Dzyaloshinskii-Moriya Interaction in WTe₂/Ferromagnet Heterostructures*, Nat. Nanotechnol. **14**, 945 (2019).
- [150] H. Xu et al., *High Spin Hall Conductivity in Large-Area Type-II Dirac Semimetal PtTe₂*, Adv. Mater. **32**, 2000513 (2020).
- [151] C. K. Safeer, J. Ingla-Aynes, F. Herling, J. H. Garcia, M. Vila, N. Ontoso, M. Reyes Calvo, S. Roche, L. E. Hueso, and F. Casanova, *Room-Temperature Spin Hall Effect in Graphene/MoS₂ van Der Waals Heterostructures*, Nano Lett. **19**, 1074 (2019).
- [152] M. H. D. Guimaraes, G. M. Stiehl, D. MacNeill, N. D. Reynolds, and D. C. Ralph, *Spin-Orbit Torques in NbSe₂/Permalloy Bilayers*, Nano Lett. **18**, 1311 (2018).
- [153] G. M. Stiehl et al., *Layer-Dependent Spin-Orbit Torques Generated by the Centrosymmetric Transition Metal Dichalcogenide Beta-MoTe₂*, Phys. Rev. B **100**, 184402 (2019).
- [154] H. Wang, J. Kally, J. S. Lee, T. Liu, H. Chang, D. R. Hickey, K. A. Mkhoyan, M.

- Wu, A. Richardella, and N. Samarth, *Surface-State-Dominated Spin-Charge Current Conversion in Topological-Insulator-Ferromagnetic-Insulator Heterostructures*, Phys. Rev. Lett. **117**, 076601 (2016).
- [155] H. Wu et al., *Magnetic Memory Driven by Topological Insulators*, Nat. Commun. **12**, 6251 (2021).
- [156] D. C. Mahendra et al., *Room-Temperature High Spin-Orbit Torque Due to Quantum Confinement in Sputtered BixSe(1-x) Films*, Nat. Mater. **17**, 800 (2018).
- [157] S. Z. Rahaman et al., *Size-Dependent Switching Properties of Spin-Orbit Torque MRAM With Manufacturing-Friendly 8-Inch Wafer-Level Uniformity*, IEEE J. Electron Devices Soc. **8**, 163 (2020).
- [158] J. Han, A. Richardella, S. A. Siddiqui, J. Finley, N. Samarth, and L. Liu, *Room-Temperature Spin-Orbit Torque Switching Induced by a Topological Insulator*, Phys. Rev. Lett. **119**, 077702 (2017).
- [159] P. Li et al., *Magnetization Switching Using Topological Surface States*, Sci. Adv. **5**, eaaw3415 (2019).
- [160] A. R. Mellnik et al., *Spin-Transfer Torque Generated by a Topological Insulator*, Nature **511**, 449 (2014).
- [161] H. Wu et al., *Spin-Orbit Torque Switching of a Nearly Compensated Ferrimagnet by Topological Surface States*, Adv. Mater. **31**, 1901681 (2019).
- [162] K.-U. Demasius, T. Phung, W. Zhang, B. P. Hughes, S.-H. Yang, A. Kellock, W. Han, A. Pushp, and S. S. P. Parkin, *Enhanced Spin-Orbit Torques by Oxygen Incorporation in Tungsten Films*, Nat. Commun. **7**, 10644 (2016).
- [163] Y. Fan et al., *Magnetization Switching through Giant Spin-Orbit Torque in a Magnetically Doped Topological Insulator Heterostructure*, Nat. Mater. **13**, 699 (2014).
- [164] N. H. D. Khang, Y. Ueda, and P. N. Hai, *A Conductive Topological Insulator with Large Spin Hall Effect for Ultralow Power Spin-Orbit Torque Switching*, Nat. Mater. **17**, 808 (2018).
- [165] N. Nagaosa, J. Sinova, S. Onoda, A. H. MacDonald, and N. P. Ong, *Anomalous Hall Effect*, Rev. Mod. Phys. **82**, 1539 (2010).
- [166] T. Taniguchi, J. Grollier, and M. D. Stiles, *Spin-Transfer Torques Generated by the Anomalous Hall Effect and Anisotropic Magnetoresistance*, Phys. Rev. Appl. **3**, 044001 (2015).
- [167] S. Iihama, T. Taniguchi, K. Yakushiji, A. Fukushima, Y. Shiota, S. Tsunegi, R. Hiramatsu, S. Yuasa, Y. Suzuki, and H. Kubota, *Spin-Transfer Torque Induced by the Spin Anomalous Hall Effect*, Nat. Electron. **1**, 120 (2018).
- [168] V. P. Amin and M. D. Stiles, *Spin Transport at Interfaces with Spin-Orbit Coupling: Formalism*, Phys. Rev. B **94**, 104419 (2016).
- [169] K. S. Das, J. Liu, B. J. van Wees, and I. J. Vera-Marun, *Efficient Injection and Detection of Out-of-Plane Spins via the Anomalous Spin Hall Effect in Permalloy Nanowires*, Nano Lett. **18**, 5633 (2018).
- [170] C. Safranski, E. A. Montoya, and I. N. Krivorotov, *Spin-Orbit Torque Driven by a Planar Hall Current*, Nat. Nanotechnol. **14**, 27 (2019).
- [171] S. C. Baek, V. P. Amin, Y.-W. Oh, G. Go, S.-J. Lee, G.-H. Lee, K.-J. Kim, M. D. Stiles, B.-G. Park, and K.-J. Lee, *Spin Currents and Spin-Orbit Torques in Ferromagnetic Trilayers*, Nat. Mater. **17**, 509 (2018).
- [172] H. Wu, S. A. Razavi, Q. Shao, X. Li, K. L. Wong, Y. Liu, G. Yin, and K. L. Wang, *Spin-Orbit Torque from a Ferromagnetic Metal*, Phys. Rev. B **99**, 184403 (2019).
- [173] T. Seki, S. Iihama, T. Taniguchi, and K. Takanashi, *Large Spin Anomalous Hall Effect in $L1(0)$ -FePt: Symmetry and Magnetization Switching*, Phys. Rev. B **100**,

- 144427 (2019).
- [174] J. D. Gibbons, D. MacNeill, R. A. Buhrman, and D. C. Ralph, *Reorientable Spin Direction for Spin Current Produced by the Anomalous Hall Effect*, Phys. Rev. Appl. **9**, 064033 (2018).
- [175] C.-F. Pai, M. Mann, A. J. Tan, and G. S. D. Beach, *Determination of Spin Torque Efficiencies in Heterostructures with Perpendicular Magnetic Anisotropy*, Phys. Rev. B **93**, 144409 (2016).
- [176] O. J. Lee, L. Q. Liu, C. F. Pai, Y. Li, H. W. Tseng, P. G. Gowtham, J. P. Park, D. C. Ralph, and R. A. Buhrman, *Central Role of Domain Wall Depinning for Perpendicular Magnetization Switching Driven by Spin Torque from the Spin Hall Effect*, Phys. Rev. B **89**, 024418 (2014).
- [177] C.-F. Pai, Y. Ou, L. H. Vilela-Leao, D. C. Ralph, and R. A. Buhrman, *Dependence of the Efficiency of Spin Hall Torque on the Transparency of Pt/Ferromagnetic Layer Interfaces*, Phys. Rev. B **92**, 064426 (2015).
- [178] L. Zhu, D. C. Ralph, and R. A. Buhrman, *Lack of Simple Correlation between Switching Current Density and Spin-Orbit-Torque Efficiency of Perpendicularly Magnetized Spin-Current-Generator-Ferromagnet Heterostructures*, Phys. Rev. Appl. **15**, 024059 (2021).
- [179] J. Kim, J. Sinha, M. Hayashi, M. Yamanouchi, S. Fukami, T. Suzuki, S. Mitani, and H. Ohno, *Layer Thickness Dependence of the Current-Induced Effective Field Vector in Ta Vertical Bar CoFeB Vertical Bar MgO*, Nat. Mater. **12**, 240 (2013).
- [180] M. Hayashi, J. Kim, M. Yamanouchi, and H. Ohno, *Quantitative Characterization of the Spin-Orbit Torque Using Harmonic Hall Voltage Measurements*, Phys. Rev. B **89**, 144425 (2014).
- [181] Q. Shao, G. Yu, Y.-W. Lan, Y. Shi, M.-Y. Li, C. Zheng, X. Zhu, L.-J. Li, P. K. Amiri, and K. L. Wang, *Strong Rashba-Edelstein Effect-Induced Spin-Orbit Torques in Monolayer Transition Metal Dichalcogenide/Ferromagnet Bilayers*, Nano Lett. **16**, 7514 (2016).
- [182] M. Harder, Z. X. Cao, Y. S. Gui, X. L. Fan, and C.-M. Hu, *Analysis of the Line Shape of Electrically Detected Ferromagnetic Resonance*, Phys. Rev. B **84**, 054423 (2011).
- [183] Y. Wang, R. Ramaswamy, and H. Yang, *FMR-Related Phenomena in Spintronic Devices*, J. Phys. D-Appl. Phys. **51**, 273002 (2018).
- [184] J. Sklenar, W. Zhang, M. B. Jungfleisch, W. Jiang, H. Chang, J. E. Pearson, M. Wu, J. B. Ketterson, and A. Hoffmann, *Driving and Detecting Ferromagnetic Resonance in Insulators with the Spin Hall Effect*, Phys. Rev. B **92**, 174406 (2015).
- [185] A. Okada, Y. Takeuchi, K. Furuya, C. Zhang, H. Sato, S. Fukarni, and H. Ohno, *Spin-Pumping-Free Determination of Spin-Orbit Torque Efficiency from Spin-Torque Ferromagnetic Resonance*, Phys. Rev. Appl. **12**, 014040 (2019).
- [186] J. Sklenar, W. Zhang, M. B. Jungfleisch, H. Saglam, S. Grudichak, W. Jiang, J. E. Pearson, J. B. Ketterson, and A. Hoffmann, *Unidirectional Spin-Torque Driven Magnetization Dynamics*, Phys. Rev. B **95**, 224431 (2017).
- [187] L. Bai, Z. Feng, P. Hyde, H. F. Ding, and C.-M. Hu, *Distinguishing Spin Pumping from Spin Rectification in a Pt/Py Bilayer through Angle Dependent Line Shape Analysis*, Appl. Phys. Lett. **102**, 242402 (2013).
- [188] C. Du, H. Wang, P. C. Hammel, and F. Yang, *Y₃Fe₅O₁₂ Spin Pumping for Quantitative Understanding of Pure Spin Transport and Spin Hall Effect in a Broad Range of Materials*, J. Appl. Phys. **117**, 172603 (2015).

- [189] H. Zhou, X. Fan, L. Ma, Q. Zhang, L. Cui, S. Zhou, Y. S. Gui, C.-M. Hu, and D. Xue, *Spatial Symmetry of Spin Pumping and Inverse Spin Hall Effect in the Pt/Y3Fe5O12 System*, Phys. Rev. B **94**, 134421 (2016).
- [190] T. L. Gilbert, *A Phenomenological Theory of Damping in Ferromagnetic Materials*, IEEE Trans. Magn. **40**, 3443 (2004).
- [191] S. Fukami, T. Anekawa, C. Zhang, and H. Ohno, *A Spin-Orbit Torque Switching Scheme with Collinear Magnetic Easy Axis and Current Configuration*, Nat. Nanotechnol. **11**, 621 (2016).
- [192] J. Lourembam, L. Huang, B. Chen, J. Qiu, H. J. Chung, S. L. K. Yap, Q. J. Yap, S. K. Wong, and S. T. Lim, *Multi-State Magnetic Tunnel Junction Programmable by Nanosecond Spin-Orbit Torque Pulse Sequence*, Adv. Electron. Mater. **7**, 2001133 (2021).
- [193] Y.-T. Liu, C.-C. Huang, K.-H. Chen, Y.-H. Huang, C.-C. Tsai, T.-Y. Chang, and C.-F. Pai, *Anatomy of Type-x Spin-Orbit-Torque Switching*, Phys. Rev. Appl. **16**, 024021 (2021).
- [194] A. Razavi, H. Wu, Q. Shao, C. Fang, B. Dai, K. Wong, X. Han, G. Yu, and K. L. Wang, *Deterministic Spin-Orbit Torque Switching by a Light-Metal Insertion*, Nano Lett. **20**, 3703 (2020).
- [195] L. You, O. Lee, D. Bhowmik, D. Labanowski, J. Hong, J. Bokor, and S. Salahuddin, *Switching of Perpendicularly Polarized Nanomagnets with Spin Orbit Torque without an External Magnetic Field by Engineering a Tilted Anisotropy*, Proc. Natl. Acad. Sci. U. S. A. **112**, 10310 (2015).
- [196] Y. Cao, Y. Sheng, K. W. Edmonds, Y. Ji, H. Zheng, and K. Wang, *Deterministic Magnetization Switching Using Lateral Spin-Orbit Torque*, Adv. Mater. **32**, 1907929 (2020).
- [197] K. Cai et al., *Electric Field Control of Deterministic Current-Induced Magnetization Switching in a Hybrid Ferromagnetic/Ferroelectric Structure*, Nat. Mater. **16**, 712 (2017).
- [198] M. Tang et al., *Bulk Spin Torque-Driven Perpendicular Magnetization Switching in $L1(0)$ FePt Single Layer*, Adv. Mater. **32**, 2002607 (2020).
- [199] H. Wu et al., *Chiral Symmetry Breaking for Deterministic Switching of Perpendicular Magnetization by Spin-Orbit Torque*, Nano Lett. **21**, 515 (2021).
- [200] Z. Zheng et al., *Field-Free Spin-Orbit Torque-Induced Switching of Perpendicular Magnetization in a Ferrimagnetic Layer with a Vertical Composition Gradient*, Nat. Commun. **12**, 4555 (2021).
- [201] L. Liu et al., *Symmetry-Dependent Field-Free Switching of Perpendicular Magnetization*, Nat. Nanotechnol. **16**, 277 (2021).
- [202] A. van den Brink, G. Vermeij, A. Solignac, J. Koo, J. T. Kohlhepp, H. J. M. Swagten, and B. Koopmans, *Field-Free Magnetization Reversal by Spin-Hall Effect and Exchange Bias*, Nat. Commun. **7**, 10854 (2016).
- [203] Y. Hibino, K. Hasegawa, T. Koyama, and D. Chiba, *Spin-Orbit Torque Generated by Spin-Orbit Precession Effect in Py/Pt/Co Tri-Layer Structure*, APL Mater. **8**, (2020).
- [204] V. P. Amin and M. D. Stiles, *Spin Transport at Interfaces with Spin-Orbit Coupling: Phenomenology*, Phys. Rev. B **94**, 104420 (2016).
- [205] L. Zhu and R. A. Buhrman, *Absence of Significant Spin-Current Generation in Ti/Fe-Co-B Bilayers with Strong Interfacial Spin-Orbit Coupling*, Phys. Rev. Appl. **15**, L031001 (2021).
- [206] Y.-C. Lau, D. Betto, K. Rode, J. M. D. Coey, and P. Stamenov, *Spin-Orbit Torque Switching without an External Field Using Interlayer Exchange Coupling*, Nat.

- Nanotechnol. **11**, 758 (2016).
- [207] Y. Sheng, K. W. Edmonds, X. Ma, H. Zheng, and K. Wang, *Adjustable Current-Induced Magnetization Switching Utilizing Interlayer Exchange Coupling*, Adv. Electron. Mater. **4**, 1800224 (2018).
- [208] S. Parkin, *Systematic Variation of the Strength and Oscillation Period of Indirect Magnetic Exchange Coupling Through the 3d, 4d, and 5d Transition-Metals*, Phys. Rev. Lett. **67**, 3598 (1991).
- [209] W. He et al., *Field-Free Spin-Orbit Torque Switching Enabled by the Interlayer Dzyaloshinskii-Moriya Interaction*, Nano Lett. **22**, 6857 (2022).
- [210] R. Chen et al., *Reducing Dzyaloshinskii-Moriya Interaction and Field-Free Spin-Orbit Torque Switching in Synthetic Antiferromagnets*, Nat. Commun. **12**, 3113 (2021).
- [211] A. Fert and P. Levy, *Role of Anisotropic Exchange Interactions in Determining the Properties of Spin-Glasses*, Phys. Rev. Lett. **44**, 1538 (1980).
- [212] I. Dzyaloshinsky, *A Thermodynamic Theory of Weak Ferromagnetism of Antiferromagnetics*, J. Phys. Chem. Solids **4**, 241 (1958).
- [213] K. Xia, W. Y. Zhang, M. Lu, and H. R. Zhai, *Noncollinear Interlayer Exchange Coupling Caused by Interface Spin-Orbit Interaction*, Phys. Rev. B **55**, 12561 (1997).
- [214] A. Crepieux and C. Lacroix, *Dzyaloshinsky-Moriya Interactions Induced by Symmetry Breaking at a Surface*, J. Magn. Magn. Mater. **182**, 341 (1998).
- [215] T. Kim, I. H. Cha, Y. J. Kim, G. W. Kim, A. Stashkevich, Y. Roussigne, M. Belmeguenai, S. M. Cherif, A. S. Samardak, and Y. K. Kim, *Ruderman-Kittel-Kasuya-Yosida-Type Interfacial Dzyaloshinskii-Moriya Interaction in Heavy Metal/Ferromagnet Heterostructures*, Nat. Commun. **12**, 3280 (2021).
- [216] Q. Zhang et al., *Quantifying the Dzyaloshinskii-Moriya Interaction Induced by the Bulk Magnetic Asymmetry*, Phys. Rev. Lett. **128**, 167202 (2022).
- [217] G. Yu et al., *Room-Temperature Skyrmions in an Antiferromagnet-Based Heterostructure*, Nano Lett. **18**, 980 (2018).
- [218] W. Jiang et al., *Blowing Magnetic Skyrmion Bubbles*, Science **349**, 283 (2015).
- [219] M. Sapozhnikov, N. S. Gusev, S. A. Gusev, D. A. Tatarskiy, Y. Petrov, A. G. Temiryazev, and A. A. Fraerman, *Direct Observation of Topological Hall Effect in Co/Pt Nanostructured Films*, Phys. Rev. B **103**, 054429 (2021).
- [220] H. Zhang, D. Zhu, W. Kang, Y. Zhang, and W. Zhao, *Stochastic Computing Implemented by Skyrmionic Logic Devices*, Phys. Rev. Appl. **13**, 054049 (2020).
- [221] M. Song, M. G. Park, S. Ko, S. K. Jang, M. Je, and K.-J. Kim, *Logic Device Based on Skyrmion Annihilation*, IEEE Trans. Electron Devices **68**, 1939 (2021).
- [222] S. Luo, M. Song, X. Li, Y. Zhang, J. Hong, X. Yang, X. Zou, N. Xu, and L. You, *Reconfigurable Skyrmion Logic Gates*, Nano Lett. **18**, 1180 (2018).
- [223] A. Fernandez-Pacheco, E. Vedmedenko, F. Ummelen, R. Mansell, D. Petit, and R. P. Cowburn, *Symmetry-Breaking Interlayer Dzyaloshinskii-Moriya Interactions in Synthetic Antiferromagnets*, Nat. Mater. **18**, 679 (2019).
- [224] E. Y. Vedmedenko, P. Riego, J. Ander Arregi, and A. Berger, *Interlayer Dzyaloshinskii-Moriya Interactions*, Phys. Rev. Lett. **122**, 257202 (2019).
- [225] D.-S. Han et al., *Long-Range Chiral Exchange Interaction in Synthetic Antiferromagnets*, Nat. Mater. **18**, 703 (2019).
- [226] C. O. Avci, C.-H. Lambert, G. Sala, and P. Gambardella, *Chiral Coupling between Magnetic Layers with Orthogonal Magnetization*, Phys. Rev. Lett. **127**, 167202 (2021).
- [227] K. Wang, L. Qian, S.-C. Ying, and G. Xiao, *Spin-Orbit Torque Switching of*

- Chiral Magnetization across a Synthetic Antiferromagnet*, Commun. Phys. **4**, 10 (2021).
- [228] A. van den Brink, S. Cosemans, S. Cornelissen, M. Manfrini, A. Vaysset, W. Van Roy, T. Min, H. J. M. Swagten, and B. Koopmans, *Spin-Hall-Assisted Magnetic Random Access Memory*, Appl. Phys. Lett. **104**, 012403 (2014).
- [229] Z. Wang, W. Zhao, E. Deng, J.-O. Klein, and C. Chappert, *Perpendicular-Anisotropy Magnetic Tunnel Junction Switched by Spin-Hall-Assisted Spin-Transfer Torque*, J. Phys. D-Appl. Phys. **48**, 065001 (2015).
- [230] W. Cai et al., *Sub-Ns Field-Free Switching in Perpendicular Magnetic Tunnel Junctions by the Interplay of Spin Transfer and Orbit Torques*, IEEE Electron Device Lett. **42**, 704 (2021).
- [231] C. Zhang, Y. Takeuchi, S. Fukami, and H. Ohno, *Field-Free and Sub-Ns Magnetization Switching of Magnetic Tunnel Junctions by Combining Spin-Transfer Torque and Spin-Orbit Torque*, Appl. Phys. Lett. **118**, 092406 (2021).
- [232] S. Z. Peng, J. Q. Lu, W. X. Li, L. Z. Wang, H. Zhang, X. Li, K. L. Wang, and W. S. Zhao, *Field-Free Switching of Perpendicular Magnetization through Voltage-Gated Spin-Orbit Torque*, in *2019 IEEE International Electron Devices Meeting (IEDM)* (IEEE, New York, 2019).
- [233] A. Deka, B. Rana, R. Anami, K. Miura, H. Takahashi, Y. Otani, and Y. Fukuma, *Electric-Field Control of Interfacial in-Plane Magnetic Anisotropy in CoFeB/MgO Junctions*, Phys. Rev. B **101**, 174405 (2020).
- [234] J. W. Lee, J. Y. Park, J. M. Yuk, and B.-G. Park, *Spin-Orbit Torque in a Perpendicularly Magnetized Ferrimagnetic Tb-Co Single Layer*, Phys. Rev. Appl. **13**, 044030 (2020).
- [235] H. Li et al., *Spin-Orbit Torque-Induced Magnetization Switching in Epitaxial Au/Fe₄N Bilayer Films*, Appl. Phys. Lett. **114**, 092402 (2019).
- [236] H. Li et al., *Field-Free Deterministic Magnetization Switching with Ultralow Current Density in Epitaxial Au/Fe₄N Bilayer Films*, ACS Appl. Mater. Interfaces **11**, 16965 (2019).
- [237] M. Jiang, H. Asahara, S. Sato, S. Ohya, and M. Tanaka, *Suppression of the Field-like Torque for Efficient Magnetization Switching in a Spin-Orbit Ferromagnet*, Nat. Electron. **3**, 751 (2020).
- [238] M. Filianina, Z. Wang, L. Baldrati, K. Lee, M. Vafaei, G. Jakob, and M. Klauwi, *Impact of the Interplay of Piezoelectric Strain and Current-Induced Heating on the Field-like Spin-Orbit Torque in Perpendicularly Magnetized Ta/Co₂₀Fe₆₀B₂₀/Ta/MgO Film*, Appl. Phys. Lett. **118**, 032401 (2021).
- [239] Y. Shi, K. Chi, Z. Li, W. Zhang, Y. Xing, H. Meng, and B. Liu, *Reconfigurable Spin Orbit Logic Device Using Asymmetric Dzyaloshinskii-Moriya Interaction*, Appl. Phys. Lett. **117**, 072401 (2020).
- [240] J. Zhang, Z. Guo, S. Zhang, Z. Cao, R. Li, J. Cao, M. Song, M. Wan, J. Hong, and L. You, *Spin-Orbit Torque-Based Reconfigurable Physically Unclonable Functions*, Appl. Phys. Lett. **116**, 192406 (2020).
- [241] H. Chen, M. Song, Z. Guo, R. Li, Q. Zou, S. Luo, S. Zhang, Q. Luo, J. Hong, and L. You, *Highly Secure Physically Unclonable Cryptographic Primitives Based on Interfacial Magnetic Anisotropy*, Nano Lett. **18**, 7211 (2018).
- [242] S. Fukami, T. Anekawa, A. Ohkawara, C. Zhang, and H. Ohno, *A Sub-Ns Three-Terminal Spin-Orbit Torque Induced Switching Device*, in *2016 IEEE Symposium on VLSI Technology* (IEEE, New York, 2016).
- [243] H. Honjo et al., *First Demonstration of Field-Free SOT-MRAM with 0.35 Ns Write Speed and 70 Thermal Stability under 400 Degrees C Thermal Tolerance*

- by Canted SOT Structure and Its Advanced Patterning/SOT Channel Technology, in *2019 IEEE International Electron Devices Meeting (IEDM)* (IEEE, New York, 2019).
- [244] M. Natsui et al., *Dual-Port Field-Free SOT-MRAM Achieving 90-MHz Read and 60-MHz Write Operations under 55-Nm CMOS Technology and 1.2-V Supply Voltage*, in *2020 IEEE Symposium on VLSI Circuits* (IEEE, New York, 2020).
- [245] S. Z. Rahaman et al., *Pulse-Width and Temperature Effect on the Switching Behavior of an Etch-Stop-on-MgO-Barrier Spin-Orbit Torque MRAM Cell*, *IEEE Electron Device Lett.* **39**, 1306 (2018).
- [246] K. Garello et al., *Manufacturable 300mm Platform Solution for Field-Free Switching SOT-MRAM*, in *2019 Symposium on VLSI Circuits* (IEEE, New York, 2019), pp. T194–T195.
- [247] K. Garello, F. Yasin, and G. S. Kar, *Spin-Orbit Torque MRAM for Ultrafast Embedded Memories: From Fundamentals to Large Scale Technology Integration*, in *2019 IEEE 11th International Memory Workshop (IMW 2019)* (IEEE, New York, 2019), pp. 101–104.
- [248] W. J. Kong, C. H. Wan, C. Y. Guo, C. Fang, B. S. Tao, X. Wang, and X. F. Han, *All-Electrical Manipulation of Magnetization in Magnetic Tunnel Junction via Spin-Orbit Torque*, *Appl. Phys. Lett.* **116**, (2020).
- [249] S. Baillet, *Magnetoencephalography for Brain Electrophysiology and Imaging*, *Nat. Neurosci.* **20**, 327 (2017).
- [250] M. Oogane et al., *Sub-PT Magnetic Field Detection by Tunnel Magneto-Resistive Sensors*, *Appl. Phys. Express* **14**, 123002 (2021).
- [251] Z. Jin, Y. Wang, K. Fujiwara, M. Oogane, and Y. Ando, *Detection of Small Magnetic Fields Using Serial Magnetic Tunnel Junctions with Various Geometrical Characteristics*, *Sensors* **20**, 5704 (2020).
- [252] G. Prenat et al., *Ultra-Fast and High-Reliability SOT-MRAM: From Cache Replacement to Normally-Off Computing*, *IEEE Trans. Multi-Scale Comput. Syst.* **2**, 49 (2016).
- [253] S. I. Kiselev, J. C. Sankey, I. N. Krivorotov, N. C. Emley, R. J. Schoelkopf, R. A. Buhrman, and D. C. Ralph, *Microwave Oscillations of a Nanomagnet Driven by a Spin-Polarized Current*, *Nature* **425**, 380 (2003).
- [254] T. J. Silva and W. H. Rippard, *Developments in Nano-Oscillators Based upon Spin-Transfer Point-Contact Devices*, *J. Magn. Magn. Mater.* **320**, 1260 (2008).
- [255] A. M. Deac, A. Fukushima, H. Kubota, H. Maehara, Y. Suzuki, S. Yuasa, Y. Nagamine, K. Tsunekawa, D. D. Djayaprawira, and N. Watanabe, *Bias-Driven High-Power Microwave Emission from MgO-Based Tunnel Magnetoresistance Devices*, *Nat. Phys.* **4**, 803 (2008).
- [256] W. H. Rippard, M. R. Pufall, S. Kaka, T. J. Silva, and S. E. Russek, *Current-Driven Microwave Dynamics in Magnetic Point Contacts as a Function of Applied Field Angle*, *Phys. Rev. B* **70**, 100406 (2004).
- [257] H. Kubota et al., *Spin-Torque Oscillator Based on Magnetic Tunnel Junction with a Perpendicularly Magnetized Free Layer and In-Plane Magnetized Polarizer*, *Appl. Phys. Express* **6**, 103003 (2013).
- [258] H. Maehara et al., *High Q Factor over 3000 Due to Out-of-Plane Precession in Nano-Contact Spin-Torque Oscillator Based on Magnetic Tunnel Junctions*, *Appl. Phys. Express* **7**, 023003 (2014).
- [259] R. Lebrun et al., *Mutual Synchronization of Spin Torque Nano-Oscillators through a Long-Range and Tunable Electrical Coupling Scheme*, *Nat. Commun.* **8**, 15825 (2017).

- [260] R. N. S. Rajapakse, Z. M. Zeng, and H. W. Jiang, *High-Frequency Microwave Emission of a Trilayer Magnetic Tunnel Junction in the Absence of External Magnetic Bias Field*, Phys. Rev. Appl. **14**, 014040 (2020).
- [261] W. A. Borders, H. Akima, S. Fukami, S. Moriya, S. Kurihara, Y. Horio, S. Sato, and H. Ohno, *Analogue Spin-Orbit Torque Device for Artificial-Neural-Network-Based Associative Memory Operation*, Appl. Phys. Express **10**, 013007 (2017).
- [262] W. A. Borders, A. Z. Pervaiz, S. Fukami, K. Y. Camsari, H. Ohno, and S. Datta, *Integer Factorization Using Stochastic Magnetic Tunnel Junctions*, Nature **573**, 390 (2019).
- [263] J. Grollier, D. Querlioz, K. Y. Camsari, K. Everschor-Sitte, S. Fukami, and M. D. Stiles, *Neuromorphic Spintronics*, Nat. Electron. **3**, 360 (2020).
- [264] Z. Lu, C. Xiong, H. Mou, Z. Luo, C. Fang, C. Wan, H. Wu, X. Zhang, and X. Zhang, *Nonvolatile Magnetic Half Adder Combined with Memory Writing*, Appl. Phys. Lett. **118**, 182402 (2021).
- [265] L. Ji, R. Zhao, C. Hu, W. Chen, Y. Li, K. Ren, Y. Chen, and X. Zhang, *Logical Devices Based on the Antiferromagnetic-Antimeron in a Ferromagnet Nanodot with Gain*, Appl. Phys. Lett. **118**, 172410 (2021).
- [266] T. Wakamura, N. J. Wu, A. D. Chepelienskii, S. Gueron, M. Och, M. Ferrier, T. Taniguchi, K. Watanabe, C. Mattevi, and H. Bouchiat, *Spin-Orbit-Enhanced Robustness of Supercurrent in Graphene/WS₂ Josephson Junctions*, Phys. Rev. Lett. **125**, 266801 (2020).
- [267] M. W. Johnson et al., *Quantum Annealing with Manufactured Spins*, Nature **473**, 194 (2011).
- [268] J. Linder and J. W. A. Robinson, *Superconducting Spintronics*, Nat. Phys. **11**, 307 (2015).
- [269] A. P. Petrovic et al., *Skyrmion-(Anti)Vortex Coupling in a Chiral Magnet-Superconductor Heterostructure*, Phys. Rev. Lett. **126**, 117205 (2021).
- [270] B. Li, N. Roschewsky, B. A. Assaf, M. Eich, M. Epstein-Martin, D. Heiman, M. Muenzenberg, and J. S. Moodera, *Superconducting Spin Switch with Infinite Magnetoresistance Induced by an Internal Exchange Field*, Phys. Rev. Lett. **110**, 097001 (2013).
- [271] M. S. Wornle, P. Welter, M. Giraldo, T. Lottermoser, M. Fiebig, P. Gambardella, and C. L. Degen, *Coexistence of Bloch and Neel Walls in a Collinear Antiferromagnet*, Phys. Rev. B **103**, 094426 (2021).
- [272] S. H. Liang et al., *Large and Robust Electrical Spin Injection into GaAs at Zero Magnetic Field Using an Ultrathin CoFeB/MgO Injector*, Phys. Rev. B **90**, 085310 (2014).
- [273] A. Ney, C. Pampuch, R. Koch, and K. H. Ploog, *Programmable Computing with a Single Magnetoresistive Element*, Nature **425**, 485 (2003).
- [274] Z. Luo et al., *Chirally Coupled Nanomagnets*, Science **363**, 1435 (2019).
- [275] Z. Luo, A. Hrabec, T. P. Dao, G. Sala, S. Finizio, J. Feng, S. Mayr, J. Raabe, P. Gambardella, and L. J. Heyderman, *Current-Driven Magnetic Domain-Wall Logic*, Nature **579**, 214 (2020).
- [276] Z. Luo et al., *Field- and Current-Driven Magnetic Domain-Wall Inverter and Diode*, Phys. Rev. Appl. **15**, 034077 (2021).
- [277] M. A. Zidan, Y. Jeong, J. Lee, B. Chen, S. Huang, M. J. Kushner, and W. D. Lu, *A General Memristor-Based Partial Differential Equation Solver*, Nat. Electron. **1**, 411 (2018).
- [278] K. Yang, Q. Duan, Y. Wang, T. Zhang, Y. Yang, and R. Huang, *Transiently Chaotic Simulated Annealing Based on Intrinsic Nonlinearity of Memristors for*

- Efficient Solution of Optimization Problems*, Sci. Adv. **6**, eaba9901 (2020).
- [279] Q. Duan, Z. Jing, X. Zou, Y. Wang, K. Yang, T. Zhang, S. Wu, R. Huang, and Y. Yang, *Spiking Neurons with Spatiotemporal Dynamics and Gain Modulation for Monolithically Integrated Memristive Neural Networks*, Nat. Commun. **11**, 3399 (2020).
- [280] J. Cai, B. Fang, L. Zhang, W. Lv, B. Zhang, T. Zhou, G. Finocchio, and Z. Zeng, *Voltage-Controlled Spintronic Stochastic Neuron Based on a Magnetic Tunnel Junction*, Phys. Rev. Appl. **11**, 034015 (2019).
- [281] J. Yun, Q. Bai, Z. Yan, M. Chang, J. Mao, Y. Zuo, D. Yang, L. Xi, and D. Xue, *Tailoring Multilevel-Stable Remanence States in Exchange-Biased System through Spin-Orbit Torque*, Adv. Funct. Mater. **30**, 1909092 (2020).
- [282] W. A. Borders, S. Fukami, and H. Ohno, *Characterization of Spin-Orbit Torque-Controlled Synapse Device for Artificial Neural Network Applications*, Jpn. J. Appl. Phys. **57**, 1002B2 (2018).
- [283] S. Liu, T. P. Xiao, C. Cui, J. A. C. Incorvia, C. H. Bennett, and M. J. Marinella, *A Domain Wall-Magnetic Tunnel Junction Artificial Synapse with Notched Geometry for Accurate and Efficient Training of Deep Neural Networks*, Appl. Phys. Lett. **118**, 202405 (2021).
- [284] J. Zhou, T. Zhao, X. Shu, L. Liu, W. Lin, S. Chen, S. Shi, X. Yan, X. Liu, and J. Chen, *Spin-Orbit Torque-Induced Domain Nucleation for Neuromorphic Computing*, Adv. Mater. **33**, 2103672 (2021).
- [285] J. Li, C. Ge, J. Du, C. Wang, G. Yang, and K. Jin, *Reproducible Ultrathin Ferroelectric Domain Switching for High-Performance Neuromorphic Computing*, Adv. Mater. **32**, 1905764 (2020).
- [286] A. Kurenkov, S. DuttaGupta, C. Zhang, S. Fukami, Y. Horio, and H. Ohno, *Artificial Neuron and Synapse Realized in an Antiferromagnet/Ferromagnet Heterostructure Using Dynamics of Spin-Orbit Torque Switching*, Adv. Mater. **31**, 1900636 (2019).
- [287] J. Torrejon et al., *Neuromorphic Computing with Nanoscale Spintronic Oscillators*, Nature **547**, 428 (2017).
- [288] M. Riou et al., *Temporal Pattern Recognition with Delayed-Feedback Spin-Torque Nano-Oscillators*, Phys. Rev. Appl. **12**, 024049 (2019).
- [289] A. Welbourne, A. L. R. Levy, M. O. A. Ellis, H. Chen, M. J. Thompson, E. Vasilaki, D. A. Allwood, and T. J. Hayward, *Voltage-Controlled Superparamagnetic Ensembles for Low-Power Reservoir Computing*, Appl. Phys. Lett. **118**, 202402 (2021).
- [290] M. Romera et al., *Vowel Recognition with Four Coupled Spin-Torque Nano-Oscillators*, Nature **563**, 230 (2018).
- [291] K. Y. Camsari, P. Debashis, V. Ostwal, A. Z. Pervaiz, T. Shen, Z. Chen, S. Datta, and J. Appenzeller, *From Charge to Spin and Spin to Charge: Stochastic Magnets for Probabilistic Switching*, Proc. IEEE **108**, 1322 (2020).
- [292] G. Braeuer, B. Szyszka, M. Vergoehl, and R. Bandorf, *Magnetron Sputtering - Milestones of 30 Years*, Vacuum **84**, 1354 (2010).
- [293] P. J. Kelly and R. D. Arnell, *Magnetron Sputtering: A Review of Recent Developments and Applications*, Vacuum **56**, 159 (2000).
- [294] S. Hasegawa, *Reflection High-Energy Electron Diffraction*, in *Characterization of Materials*, Second Edition (John Wiley & Sons, Inc, 2012), pp. 1925–1938.
- [295] C. Kittel, *Introduction to Solid State Physics*, Eighth Edition (John Wiley & Sons, Inc, 2005).
- [296] S. Foner, *Versatile and Sensitive Vibrating-Sample Magnetometer*, Rev. Sci.

- Instrum. **30**, 548 (1959).
- [297] V. P. Amin, J. Li, M. D. Stiles, and P. M. Haney, *Intrinsic Spin Currents in Ferromagnets*, Phys. Rev. B **99**, 220405 (2019).
- [298] T. Y. Ma, C. H. Wan, X. Wang, W. L. Yang, C. Y. Guo, C. Fang, M. K. Zhao, J. Dong, Y. Zhang, and X. F. Han, *Evidence of Magnetization Switching by Anomalous Spin Hall Torque in NiFe*, Phys. Rev. B **101**, 134417 (2020).
- [299] J. Z. Sun, *Spin-Current Interaction with a Monodomain Magnetic Body: A Model Study*, Phys. Rev. B **62**, 570 (2000).
- [300] V. Tshitoyan, C. Ciccarelli, A. P. Mihai, M. Ali, A. C. Irvine, T. A. Moore, T. Jungwirth, and A. J. Ferguson, *Electrical Manipulation of Ferromagnetic NiFe by Antiferromagnetic IrMn*, Phys. Rev. B **92**, 214406 (2015).
- [301] S. Dubois, L. Piraux, J. M. George, K. Ounadjela, J. L. Duvail, and A. Fert, *Evidence for a Short Spin Diffusion Length in Permalloy from the Giant Magnetoresistance of Multilayered Nanowires*, Phys. Rev. B **60**, 477 (1999).
- [302] K. S. Das, W. Y. Schoemaker, B. J. van Wees, and I. J. Vera-Marun, *Spin Injection and Detection via the Anomalous Spin Hall Effect of a Ferromagnetic Metal*, Phys. Rev. B **96**, 220408 (2017).
- [303] H. Wu, C. H. Wan, Z. H. Yuan, X. Zhang, J. Jiang, Q. T. Zhang, Z. C. Wen, and X. F. Han, *Observation of Pure Inverse Spin Hall Effect in Ferromagnetic Metals via Ferromagnetic/Antiferromagnetic Exchange-Bias Structures*, Phys. Rev. B **92**, 054404 (2015).
- [304] W. L. Yang, J. W. Wei, C. H. Wan, Y. W. Xing, Z. R. Yan, X. Wang, C. Fang, C. Y. Guo, G. Q. Yu, and X. F. Han, *Determining Spin-Torque Efficiency in Ferromagnetic Metals via Spin-Torque Ferromagnetic Resonance*, Phys. Rev. B **101**, 064412 (2020).
- [305] T. Ma, C. Wan, J. Dong, C. Guo, M. Zhao, X. Wang, Y. Zhang, G. Yu, and X. Han, *Efficient Spin-Orbit-Torque Switching Assisted by an Effective Perpendicular Field in a Magnetic Trilayer*, Phys. Rev. Appl. **16**, 014016 (2021).
- [306] T. Fache, J. C. Rojas-Sanchez, L. Badie, S. Mangin, and S. Petit-Watelot, *Determination of Spin Hall Angle, Spin Mixing Conductance, and Spin Diffusion Length in CoFeB/Ir for Spin-Orbitronic Devices*, Phys. Rev. B **102**, 064425 (2020).
- [307] A. Thomas, D. Meyners, D. Ebke, N.-N. Liu, M. D. Sacher, J. Schmalhorst, G. Reiss, H. Ebert, and A. Huetten, *Inverted Spin Polarization of Heusler Alloys for Spintronic Devices*, Appl. Phys. Lett. **89**, 012502 (2006).
- [308] M. Sharma, S. X. Wang, and J. H. Nickel, *Inversion of Spin Polarization and Tunneling Magnetoresistance in Spin-Dependent Tunneling Junctions*, Phys. Rev. Lett. **82**, 616 (1999).
- [309] E. Y. Tsymbal, A. Sokolov, I. F. Sabirianov, and B. Doudin, *Resonant Inversion of Tunneling Magnetoresistance*, Phys. Rev. Lett. **90**, 186602 (2003).
- [310] I. J. Vera Marun, F. M. Postma, J. C. Lodder, and R. Jansen, *Tunneling Magnetoresistance with Positive and Negative Sign in La_{0.67}Sr_{0.33}MnO₃/SrTiO₃/Co Junctions*, Phys. Rev. B **76**, 064426 (2007).
- [311] F. Greullet, E. Snoeck, C. Tiusan, M. Hehn, D. Lacour, O. Lenoble, C. Magen, and L. Calmels, *Large Inverse Magnetoresistance in Fully Epitaxial Fe/Fe₃O₄/MgO/Co Magnetic Tunnel Junctions*, Appl. Phys. Lett. **92**, 053508 (2008).
- [312] L. Marnitz et al., *Sign Change in the Tunnel Magnetoresistance of Fe₃O₄/MgO/Co-Fe-B Magnetic Tunnel Junctions Depending on the Annealing Temperature and the Interface Treatment*, AIP Adv. **5**, 047103 (2015).

- [313] S. Yasui, S. Honda, J. Okabayashi, T. Yanase, T. Shimada, and T. Nagahama, *Large Inverse Tunnel Magnetoresistance in Magnetic Tunnel Junctions with an Fe₃O₄ Electrode*, Phys. Rev. Appl. **15**, 034042 (2021).
- [314] S. Liang et al., *Ferroelectric Control of Organic/Ferromagnetic Spinterface*, Adv. Mater. **28**, 10204 (2016).
- [315] S. Liang et al., *Quenching of Spin Polarization Switching in Organic Multiferroic Tunnel Junctions by Ferroelectric “Ailing-Channel” in Organic Barrier*, ACS Appl. Mater. Interfaces **10**, 30614 (2018).
- [316] Y. Lu, M. Tran, H. Jaffrès, P. Seneor, C. Deranlot, F. Petroff, J.-M. George, B. Lépine, S. Ababou, and G. Jézéquel, *Spin-Polarized Inelastic Tunneling through Insulating Barriers*, Phys. Rev. Lett. **102**, 176801 (2009).
- [317] S. Kokado, N. Fujima, K. Harigaya, H. Shimizu, and A. Sakuma, *Theoretical Analysis of Highly Spin-Polarized Transport in the Iron Nitride Fe₄N*, Phys. Rev. B **73**, 172410 (2006).
- [318] H. Li, X. Li, D. Kim, G. Zhao, D. Zhang, Z. Diao, T. Chen, and J.-P. Wang, *High Spin Polarization in Epitaxial Fe₄N Thin Films Using Cr and Ag as Buffer Layers*, Appl. Phys. Lett. **112**, 162407 (2018).
- [319] B. Yang, L. Tao, L. Jiang, W. Chen, P. Tang, Y. Yan, and X. Han, *Ultrahigh Tunneling-Magnetoresistance Ratios in Nitride-Based Perpendicular Magnetic Tunnel Junctions from First Principles*, Phys. Rev. Appl. **9**, 54019 (2018).
- [320] Y. Lu et al., *Spin-Orbit Coupling Effect by Minority Interface Resonance States in Single-Crystal Magnetic Tunnel Junctions*, Phys. Rev. B **86**, 184420 (2012).
- [321] P. Potapov, *Why Principal Component Analysis of STEM Spectrum-Images Results in “Abstract”, Uninterpretable Loadings?*, Ultramicroscopy **160**, 197 (2016).
- [322] W. B. Mi, Z. B. Guo, X. P. Feng, and H. L. Bai, *Reactively Sputtered Epitaxial Gamma'-Fe₄N Films: Surface Morphology, Microstructure, Magnetic and Electrical Transport Properties*, Acta Mater. **61**, 6387 (2013).
- [323] W. M. Haynes, *CRC Handbook of Chemistry and Physics* (CRC press, 2016).
- [324] K. Sunaga, M. Tsunoda, K. Komagaki, Y. Uehara, and M. Takahashi, *Inverse Tunnel Magnetoresistance in Magnetic Tunnel Junctions with an Fe₄N Electrode*, J. Appl. Phys. **102**, 013917 (2007).
- [325] Y. Komasaki, M. Tsunoda, S. Isogami, and M. Takahashi, *75% Inverse Magnetoresistance at Room Temperature in Fe₄N/MgO/CoFeB Magnetic Tunnel Junctions Fabricated on Cu Underlayer*, J. Appl. Phys. **105**, 07C928 (2009).
- [326] J. J. Åkerman, R. Escudero, C. Leighton, S. Kim, D. A. Rabson, R. W. Dave, J. M. Slaughter, and I. K. Schuller, *Criteria for Ferromagnetic-Insulator-Ferromagnetic Tunneling*, Journal of Magnetism and Magnetic Materials **240**, 86 (2002).
- [327] P. Blochl, *Projector Augmented-Wave Method*, Phys. Rev. B **50**, 17953 (1994).
- [328] G. Kresse and J. Hafner, *Ab Initio Molecular Dynamics for Liquid Metals*, Phys. Rev. B **47**, 558 (1993).
- [329] G. Kresse and J. Furthmuller, *Efficiency of Ab-Initio Total Energy Calculations for Metals and Semiconductors Using a Plane-Wave Basis Set*, Comput. Mater. Sci. **6**, 15 (1996).
- [330] G. Kresse and J. Furthmuller, *Efficient Iterative Schemes for Ab Initio Total-Energy Calculations Using a Plane-Wave Basis Set*, Phys. Rev. B **54**, 11169 (1996).
- [331] J. P. Perdew, K. Burke, and M. Ernzerhof, *Generalized Gradient Approximation Made Simple*, Phys. Rev. Lett. **77**, 3865 (1996).

- [332] E. Kisker, K. Schröder, W. Gudat, and M. Campagna, *Spin-Polarized Angle-Resolved Photoemission Study of the Electronic Structure of Fe(100) as a Function of Temperature*, Phys. Rev. B **31**, 329 (1985).
- [333] S. Yuasa, T. Nagahama, and Y. Suzuki, *Spin-Polarized Resonant Tunneling in Magnetic Tunnel Junctions*, Science **297**, 234 (2002).
- [334] T. Nagahama, S. Yuasa, Y. Suzuki, and E. Tamura, *Quantum Size Effect in Magnetic Tunnel Junctions with Ultrathin Fe(001) Electrodes*, J. Appl. Phys. **91**, 7035 (2002).
- [335] F. Greullet, C. Tiusan, F. Montaigne, M. Hehn, D. Halley, O. Bengone, M. Bowen, and W. Weber, *Evidence of a Symmetry-Dependent Metallic Barrier in Fully Epitaxial MgO Based Magnetic Tunnel Junctions*, Phys. Rev. Lett. **99**, 187202 (2007).
- [336] P. Sheng, F. Bonell, S. Miwa, T. Nakamura, Y. Shiota, S. Murakami, D. D. Lam, S. Yoshida, and Y. Suzuki, *Detailed Analysis of Spin-Dependent Quantum Interference Effects in Magnetic Tunnel Junctions with Fe Quantum Wells*, Appl. Phys. Lett. **102**, 032406 (2013).
- [337] J. M. Teixeira, J. D. Costa, J. Ventura, J. B. Sousa, P. Wisniowski, and P. P. Freitas, *Observation of Spin-Dependent Quantum Well Resonant Tunneling in Textured CoFeB Layers*, Appl. Phys. Lett. **104**, 112414 (2014).
- [338] S. Yuasa, A. Fukushima, H. Kubota, Y. Suzuki, and K. Ando, *Giant Tunneling Magnetoresistance up to 410% at Room Temperature in Fully Epitaxial Co/MgO/Co Magnetic Tunnel Junctions with Bcc Co(001) Electrodes*, Appl. Phys. Lett. **89**, 042505 (2006).
- [339] X. G. Zhang and W. H. Butler, *Large Magnetoresistance in Bcc Co/MgO/Co and FeCo/MgO/FeCo Tunnel Junctions*, Phys. Rev. B **70**, 172407 (2004).
- [340] N. Smith, N. Brookes, Y. Chang, and P. Johnson, *Quantum-Well and Tight-Binding Analyses of Spin-Polarized Photoemission from Ag/Fe(001) Overlayers*, Phys. Rev. B **49**, 332 (1994).

Acknowledgements

This study was conducted as part of a co-supervised PhD program between the Institute of Physics, Chinese Academy of Sciences, and the Institut Jean Lamour, Université de Lorraine. The Chinese version of this dissertation has already been submitted to the University of Chinese Academy of Sciences, in partial fulfillment of the requirements for the degree of Doctor of Science in Condensed Matter Physics. I am immensely grateful for the guidance and encouragement I have received from Prof. Xiufeng HAN, Prof. Yuan LU, and numerous colleagues throughout this endeavor. This opportunity has been invaluable, and I would like to express my deepest gratitude to everyone who has supported and guided me. Thank you!

I extend my sincere appreciation to my Chinese supervisor, Prof. Xiufeng HAN. Prof. HAN is an exceptionally diligent individual, always striving for excellence. Under his leadership, our entire research group undertook and successfully completed many important projects. Prof. HAN not only provided us with outstanding experimental environment but also offered invaluable ideas and insights. His supervision has formed the very foundation of this study.

Many thanks to my French supervisor, Prof. Yuan LU. The one-year experience in Prof. LU's team has been truly remarkable. Prof. LU is a true gentleman who treats everyone with genuine care. As an expert in spintronics, every discussion with Prof. LU has been incredibly helpful and inspiring. His guidance has transformed my academic journey, and with his instruction, the pursuit of knowledge has taken on a whole new dimension. I am motivated to continue striving for what I truly desire.

I am grateful to my co-supervisor, Prof. Michel VERGNAT, for his valuable discussions and many help on the administration procedure. I also wish to express my

gratitude to Prof. Hervé RINNERT and Prof. Mathieu STOFFEL for their assistance throughout our daily work. Thanks to Prof. Hongxin YANG for his support in first-principles calculations. Special thanks go to Prof. Xavier DEVAUX for his invaluable help and meticulous analysis of the STEM measurements, and to Prof. Sylvie MIGOT for her support during the preparation of STEM samples. I am also indebted to Engineer Gwladys LENGAIGNE and Laurent BADIE for their careful training in nanofabrication, as well as to Engineer Ludovic PASQUIER and Claudia DE MELO SACHEZ for their assistance during the thin-film deposition. I would like to acknowledge the insightful discussions with Prof. Jeanmarie GEORGE and Prof. Henri JAFFRES from CNRS-Thales. Furthermore, I extend my appreciation to Miss Juliette BARBAT, Miss Christine SARTORI and Mr. Georges BILLANT for their help with visa applications, enrollment and dissertation defense.

I would like to express my gratitude to everyone in Prof. LU's team, whose collaboration and support have been invaluable. Special thanks go to Dr. Tongxin CHEN for his assistance in both work and daily life, and to Dr. Priyanka TYAGI and Mr. Pambiang Abel DAINONE for their insightful discussions.

I extend my thanks to everyone who has worked or studied in Prof. HAN's group, including Prof. Guoqiang YU, A. Prof. Caihua WAN, Dr. Leina Jiang, Dr. Hongjun XU, Dr. Jinwu WEI, Engineer Lin YIN, and A. Prof. Jiafeng FENG, as well as, for their invaluable support. I am also grateful to Dr. Xiao WANG, Dr. Chi FANG, and Dr. Chenyang GUO for their care and assistance. Additionally, I would like to acknowledge the long-standing collaboration with Mr. Yu ZHANG, Mr. Jing DONG, Mr. Mingkun ZHAO, Mr. Yu ZHU, and Mr. Chen CHENG over the past five years.

Special thanks go to my father, Mr. Ximin MA, and my mother, Mrs. Lizhi ZHANG. Your unwavering love and encouragement have been a constant source of

support throughout my journey.

Lastly, I extend my heartfelt gratitude to everyone who has provided assistance and support along the way. Your contributions have been invaluable, and I am truly thankful.

Tianyi MA

June 2023

Beijing

Curriculum vitae and list of publications

Curriculum vitae:

Tianyi was born on April 7, 1996 in Heilongjiang, China. He started his study of Physics at Jilin University in 2014. After obtaining his Bachelor degree in 2018, Tianyi started pursuing his Doctoral degree of Condensed Matter Physics in a co-supervised program between the Institute of Physics, Chinese Academy of Sciences and the Institut Jean Lamour, Université de Lorraine.

Publications:

[*] **T. Y. Ma**, Y. Zhu, P. A. Dainone, T. X. Chen, X. Devaux, C. H. Wan, S. Migot, G. Lengaigne, M. Vergnat, Y. Yan, X. F. Han and Y. Lu, *Large sign-reversal of tunneling magnetoresistance in epitaxial Fe/MgAlO_x/Fe₄N magnetic tunnel junction*, under review in ACS Appl. Electron. Mater.

[1] **T. Y. Ma**, C. H. Wan, X. Wang, W. L. Yang, C. Y. Guo, C. Fang, M. K. Zhao, J. Dong, Y. Zhang and X. F. Han, *Evidence of magnetization switching by anomalous spin Hall torque in NiFe*, Phys. Rev. B **101**, 134417 (2020).

[2] **T. Y. Ma**, C. H. Wan, J. Dong, C. Y. Guo, M. K. Zhao, X. Wang, Y. Zhang, G. Q. Yu, and X. F. Han, *Efficient Spin-Orbit-Torque Switching Assisted by an Effective Perpendicular Field in a Magnetic Trilayer*, Phys. Rev. Appl. **16**, 014016 (2021).

[3] W. L. Yang, C. H. Wan, Z. R. Yan, X. Zhang, Maksim E. Stebliy, X. Wang, C. Fang, C. Y. Guo, Y. W. Xing, **T. Y. Ma**, Alexey V. Ognev, Alexander S. Samardak, Mean-Jue Tung, G. Q. Yu and X. F. Han. *Chirality-Reversible Multistate Switching via Two Orthogonal Spin-Orbit Torques in a Perpendicularly Magnetized System*. Phys. Rev. Appl. **13**, 024052 (2020).

[4] X. Wang, C. H. Wan, Y. Z. Liu, Q. M. Shao, H. Wu, C. Y. Guo, C. Fang,

Y. Guang, W. L. Yang, C. L. He, B. S. Tao, X. M. Zhang, **T. Y. Ma**, J. Dong, Y. Zhang, J. F. Feng, J. Xiao, K. L. Wang, G. Q. Yu and X. F. Han. *Spin transmission in IrMn through measurements of spin Hall magnetoresistance and spin-orbit torque*. Phys. Rev. B **101**, 144412 (2020).

[5] Y. Zhang, H. J. Xu, C. J. Yi, X. Wang, Y. Huang, J. Tang, J. L. Jiang, C. L. He, M. K. Zhao, **T. Y. Ma**, J. Dong, C. Y. Guo, J. F. Feng, C. H. Wan, H. X. Wei, H. F. Du, Y. G. Shi, G. Q. Yu, G. Y. Zhang and X. F. Han. *Exchange bias and spin-orbit torque in the Fe₃GeTe₂-based heterostructures prepared by vacuum exfoliation approach*. Appl. Phys. Lett. **118**, 262406 (2021).

[6] C. Y. Guo, C. H. Wan, M. K. Zhao, C. Fang, **T. Y. Ma**, X. Wang, Z. R. Yan, W. Q. He, Y. W. Xing, J. F. Feng, and X. F. Han. *Switching the perpendicular magnetization of a magnetic insulator by magnon transfer torque*. Phys. Rev. B **104**, 094412 (2021).

[7] M. K. Zhao, C. H. Wan, X. M. Luo, Y. Z. Wang, **T. Y. Ma**, W. L. Yang, Y. Zhang, L. Yin, G. Q. Yu and X. F. Han. *Field-free programmable spin logics based on spin Hall effect*. Appl. Phys. Lett. **119**, 212405 (2021).

[8] W. Q. He, C. H. Wan*, C. X. Zheng, Y. Z. Wang, X. Wang, **T. Y. Ma**, Y. Q. Wang, C. Y. Guo, X. M. Luo, M. E. Stebliy, G. Q. Yu, Y. W. Liu, A. V. Ognev, A. S. Samardak and X. F. Han. *Field-Free Spin-Orbit Torque Switching Enabled by the Interlayer Dzyaloshinskii-Moriya Interaction*. Nano Lett. **22**, 6857-6865 (2022)